Measurement of the Proton Structure Function F_2 at Low Q^2 at HERA

Vom Fachbereich Physik
der Universität Dortmund
zur Erlangung des akademischen Grades eines
Doktors der Naturwissenschaften
genehmigte

D I S S E R T A T I O N

von
Diplom-Physiker Olaf Behrendt
aus Lünen

Dortmund
August 2006

Abstract

A measurement of the inclusive deep inelastic positron proton scattering cross-section at low momentum transfers squared Q^2 between $0.2\,\mathrm{GeV^2}$ and $3.5\,\mathrm{GeV^2}$ and values of Bjorken x down to $3 \cdot 10^{-5}$ is presented. Based on this the proton structure function F_2, parameterising the quark composition of the proton, is extracted. Measurements at these low values of Q^2 are particularly interesting since perturbative calculations based on Quantum Chromodynamics, the theory of the strong interaction, can no longer be performed and only phenomenological models are able to describe the proton structure.

Experimentally this transition region can be accessed by shifting the interaction point of positrons and protons into the direction of the incoming proton. This possibility has been exploited in the year 2000 during a special running period of the HERA collider. The present analysis is based on data recorded with the H1 detector at that time. Compared to a similar data taking period in 1995 the statistical error of the data sample is smaller by a factor of two. Due to a detailed investigation of the systematic uncertainties affecting the measurement it has been possible to reduce the total error by almost the same amount. The improved precision should allow for a better constraint of the available phenomenological models.

Kurzfassung

In der vorliegenden Arbeit wird eine Messung des inklusiven Wirkungsquerschnitts der tiefinelastischen Positron-Proton-Streuung bei kleinen Viererimpulsübertragsquadraten Q^2 zwischen $0.2\,\mathrm{GeV^2}$ und $3.5\,\mathrm{GeV^2}$ vorgestellt. Der minimal erreichbare Wert der Bjorken Skalenvariablen x beträgt dabei $3 \cdot 10^{-5}$. Mit Hilfe der Meßergebnisse wird die Protonstrukturfunktion F_2 bestimmt, die den Quarkinhalt des Protons parametrisiert. Der analysierte Teil des Phasenraums ist von besonderem Interesse, da bei hinreichend kleinen Werten von Q^2 störungstheoretische Vorhersagen im Rahmen der Quantenchromodynamik, der Theorie der starken Wechselwirkung, versagen und phänomenologische Modelle zur Beschreibung der Protonstruktur herangezogen werden müssen.

Um diesen Übergangsbereich experimentell zugänglich zu machen, wurde der Wechselwirkungspunkt von Positronen und Protonen am HERA-Beschleuniger während einer speziellen Datennahmeperiode im Jahr 2000 in Richtung des einlaufenden Protons verschoben. Die mit dem H1-Detektor in diesem Zeitraum aufgezeichneten Daten bilden die Grundlage der durchgeführten Messung. Der statistische Fehler des Datensatzes ist um einen Faktor zwei kleiner als für eine entsprechende Datennahmeperiode im Jahr 1995. Aufgrund einer detaillierten Untersuchung der systematischen Unsicherheiten konnte der totale Meßfehler um nahezu den gleichen Wert verringert werden. Die Meßergebnisse sollen dazu beitragen, die freien Parameter der verfügbaren phänomenologischen Modelle mit höherer Präzision zu bestimmen.

Contents

Preface

Spectroscopic measurements and scattering experiments are the two basic methods to investigate the structure of matter. Among the latter the exploration of nuclei and afterwards nucleons with a lepton as a point-like probe has played and continues to play a key role. According to Heisenberg's uncertainty principle the negative squared momentum transfer between the lepton and the target Q^2 defines the scale $\lambda \simeq \hbar/\sqrt{Q^2}$ to which the target structure can be resolved. The higher the energy in the centre of mass system of the interacting particles the larger values of Q^2 that can be reached and the finer structures of the target that can be resolved. Therefore the development of new experiments aims for a continuous increase of the centre of mass energy.

With the Stanford Linear Accelerator for electrons proposed in 1957 [Gin57] energies large enough to probe the substructure of the proton in a *deep-inelastic scattering* (DIS) experiment were reached. The striking feature of the first SLAC data published in 1969 was that the *structure function F_2* parametrising the structure of the proton showed almost no dependence on Q^2, i.e. the resolution power of the electron [Blo69, Bre69]. Such a scale invariant behaviour, simply called *scaling*, had already been predicted by Bjorken [Bjo69a]. Feynman gave a simple physical interpretation of the result in the so-called *parton model* [Fey69] where the proton is assumed to consist of non-interacting and point-like constituents (partons), on which the electron scatters incoherently. One then expects no dependence of F_2 on Q^2 since the scattering centre is a point. It only depends on a variable commonly referred to as Bjorken x, which can be interpreted as the fraction of the proton's momentum carried by the struck parton. Finally Bjorken and Paschos associated the partons with quarks [Bjo69b], resulting in the *quark-parton model*. Quarks had been introduced to explain the large number of meson and baryon resonances observed in hadron spectroscopy [GM64, Zwe64].

Despite many successful applications severe difficulties arose for the quark parton model in the following years: It was observed in neutrino-nucleon experiments that the quarks carry only about half of the momentum of the nucleon [Per75]. This was evidence for the existence of additional constituents in the proton not interacting with the leptonic probe. The other major problem was the non-observation of quarks in the final state. This imposes a conceptual problem on the quark parton model: While the non-existence of free quarks implies strong forces between them the scaling behaviour is successfully described assuming no interactions between the partons.

Both problems were solved with the development of Quantum Chromodynamics (QCD), the gauge theory of the strong interaction, in the early 1970s. It describes the interaction between the quarks via the exchange of *gluons*, which carry the missing momentum fraction of the proton. It was discovered that due to the non-Abelian structure of QCD the strength of the interaction between the quarks decreases towards small distances (large Q^2) [Gro73b, Pol73], such that the quarks in DIS experiments are

quasi-free. This behaviour is referred to as *asymptotic freedom* and allows perturbative methods to be employed to make quantitative predictions. At large distances (small Q^2) the strength of the interaction rises such that *confinement* of the quarks within the hadrons takes place. Apart from providing a theoretical justification for the parton model QCD predicted the breaking of Bjorken scaling. Indeed a Q^2 dependence of the structure function F_2 was observed in muon-nucleon scattering experiments [Fox74].

With the HERA accelerator at DESY in Hamburg starting operation in 1991 a new class of experiments was realised: lepton-hadron collider experiments. Electrons or positrons and protons are accelerated and brought to collision inside the multi-purpose detectors of the H1 and ZEUS collaborations. Compared to the previous fixed target experiments the centre of mass energy is significantly increased, allowing for a large extension of the kinematic range in x and Q^2 and thus enabling extensive QCD tests.

One of the most important results of the H1 and ZEUS experiments so far is the observation of a steep rise of the proton structure function F_2 towards low values of Bjorken x at fixed Q^2 [Abt93, Der93a], which is caused by the gluonic content of the proton and is successfully described by perturbative QCD (pQCD) calculations [Glü92]. Moreover, it turned out that the Q^2 evolution of the proton structure function $F_2(x, Q^2)$ is well described by pQCD down to low values of Q^2 of only a few GeV^2.

At even lower Q^2 values around $1\,\text{GeV}^2$ a transition takes place into a domain in which quark confinement effects start to dominate and hadrons become the relevant degrees of freedom instead of quarks. Since pQCD is no longer applicable the description of the transition region constitutes a challenge for the theory and a field for phenomenological models. Successful predictions should improve the understanding of quark confinement. If the results of pQCD or most of the phenomenological models are extrapolated towards smaller values of x the growth of F_2 would violate unitarity. Therefore the rise of F_2 at low x is expected to be tamed, an effect referred to as *saturation*. The lowest values of x are reached at HERA for small values of Q^2.

To test the available models and to search for signs of saturation high precision data in the transition region are essential. Collecting them requires dedicated experimental techniques since with the scattered electron being detected in the main detector of H1 or ZEUS standard DIS events can only be reconstructed for $Q^2 > 2\,\text{GeV}^2$. One possibility is to extend the acceptance of the existing detector components towards lower values of Q^2 by shifting the interaction region of leptons and protons in the direction of the incoming proton. This has been done during a special running period of the HERA collider in the year 2000, called the *shifted vertex run*. The subject of the present thesis is the measurement of the proton structure function F_2 using the data collected by the H1 experiment in this time interval.

The thesis is organised as follows: In chapter 1 the theoretical concepts concerning deep inelastic scattering and the structure of the proton are introduced. Chapter 2 is concerned with the experimental foundations of the measurement, namely the relevant aspects of the HERA accelerator and the H1 detector. Following these prerequisites the basic principles of the cross-section determination and the extraction of the structure function F_2 are presented in chapter 3. The chapter also serves to distinguish the present work from complementary analyses. All details about the data analysis are covered in chapter 4. Finally, chapter 5 is devoted to the results of the measurement and the comparison to other experimental results and to theoretical predictions.

1 Deep Inelastic Scattering

The present chapter provides the theoretical basis for the measurement of the proton structure functions F_2 and F_L in deep inelastic electron[1]-proton scattering at low values of Q^2. After the basic variables describing the event kinematics are introduced the parameterisation of the inclusive electron-proton scattering cross-section in terms of proton structure functions is discussed. Subsequently, predictions of their behaviour by the quark parton model, perturbative Quantum Chromodynamics and various phenomenological models are presented. It turns out that also a class of processes referred to as *radiative electron-proton scattering* is relevant for the measurement. Therefore the corresponding experimental configurations are introduced.

The chapter can only provide a short overview of the individual topics. A detailed discussion can be found in [Dev04] and [Bro95].

1.1 Event Kinematics

The interaction of electron (e) and proton (p) can be described in lowest order perturbation theory via the exchange of virtual gauge bosons. If a neutral gauge boson is exchanged, i.e. a photon (γ) or a Z^0, the electron is scattered off the proton and a hadronic final state X is produced. In case the gauge boson carries a charge ($W^\pm$) the final state consists of a neutrino and the hadronic system X. Figure 1.1 shows the corresponding Feynman diagram.

At a fixed centre of mass energy $\sqrt{s}$ the event kinematics are fully determined by two of the three Lorentz invariant variables Q^2, x and y. They are defined by the four-momenta of the particles involved in the scattering process: the four-momenta of the incoming electron and proton are denoted by $\mathbf{k}$ and $\mathbf{P}$, respectively, $\mathbf{k}'$ corresponds to the scattered electron. Finally, $\mathbf{q}$ denotes the four-momentum of the exchanged boson. Neglecting the electron and the proton mass the squared centre of mass energy is determined by the energies of the incoming electron E_e^0 and the incoming proton E_p^0:

$$s = (\mathbf{P} + \mathbf{k})^2 \approx 4E_e^0 E_p^0 \tag{1.1}$$

The negative four momentum transfer squared at the electron vertex is defined as

$$Q^2 = -\mathbf{q}^2 = -(\mathbf{k} - \mathbf{k}')^2 \tag{1.2}$$

It is also referred to as the virtuality of the exchanged boson.

Furthermore, the Bjorken scale variable x and the inelasticity y are used to describe the event kinematics:

$$x = \frac{Q^2}{2\,\mathbf{P} \cdot \mathbf{q}}, \qquad y = \frac{\mathbf{P} \cdot \mathbf{q}}{\mathbf{P} \cdot \mathbf{k}} \tag{1.3}$$

---

[1]Unless otherwise stated, the term 'electron' is used in this thesis to generically denote electrons or positrons.
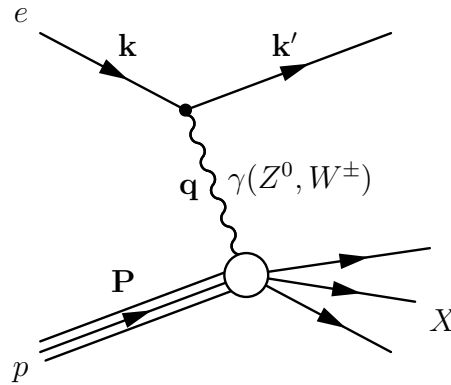
Figure 1.1: *Lowest order Feynman graph for the electron-proton scattering process.*

In the quark-parton model x is interpreted as the fraction of the proton's momentum carried by the struck quark (see section 1.3). The inelasticity y corresponds to the relative energy transfer of the incoming electron to the proton in the rest frame of the latter. Correspondingly, both variables are dimensionless and limited to the range $0 \leq x, y \leq 1$.

Neglecting the particle masses the previously defined quantities are related by:

$$Q^2 \approx xys \tag{1.4}$$

Finally the invariant mass of the hadronic final state is given by

$$W^2 = (\mathbf{P} + \mathbf{q})^2 = \frac{1 - x}{x} Q^2 + m_p^2 \tag{1.5}$$

with m_p denoting the proton mass.

The values of Q^2 relevant to this analysis are small compared to the large masses of the Z^0 and $W^\pm$ bosons ($m_W \approx 80 \, \text{GeV}$, $m_{Z^0} \approx 91 \, \text{GeV}$). Therefore Z^0 and $W^\pm$ exchange can be neglected and only the photon exchange is considered in the following. In the limit $Q^2 \to 0 \, \text{GeV}^2$ the ep scattering process can be interpreted as an interaction of a real photon with the proton. The corresponding events are called *photoproduction events* in contrast to DIS events.

1.2 DIS Cross-Section

At lowest order in electroweak theory (Born approximation) the DIS cross-section can be expressed in terms of a tensor product:

$$d\sigma \sim L_{\mu\nu} W^{\mu\nu} \tag{1.6}$$

The leptonic tensor $L_{\mu\nu}$ describes the interaction of the electron with the exchanged virtual gauge boson and can be precisely calculated in the electroweak theory treating the electron as a point-like particle. Correspondingly, the interaction of the gauge boson and the proton is represented by the hadronic tensor $W^{\mu\nu}$. Since the internal structure of the proton is unknown the precise form of $W^{\mu\nu}$ cannot be specified. Instead, the most general Lorentz invariant form is assumed. Considering the photon exchange

only and employing current conservation at the hadron vertex $W^{\mu\nu}$ can be expressed in terms of two unknown functions.

Hence the inclusive differential ep cross-section at low Q^2 can be expressed in terms of two independent proton structure functions F_2 and F_L:

$$\frac{d^2\sigma}{dxdQ^2} = \frac{2\pi\alpha^2}{Q^4x}Y_+ \left(F_2(x,Q^2) - \frac{y^2}{Y_+} \cdot F_L(x,Q^2) \right) \quad \text{with } Y_+ = 1 + (1-y)^2 \quad (1.7)$$

A simultaneous measurement of both structure functions is only possible if the inelasticity y is varied for fixed values of x and Q^2. According to equation 1.4 this requires a variation of the centre of mass energy $\sqrt{s}$. The latter can be achieved either by changing the beam energies of the HERA collider or by analysing events for which the energy of the electron available for the interaction with the proton is reduced due to photon radiation (see section 1.7). However, at sufficiently low values of y the contribution of F_L to the cross-section is strongly suppressed due the factor y^2. Since this is the case for the bulk of the phase space accessible at HERA the structure function F_2 can be directly determined from the differential DIS cross-section even at fixed s.

It turns out to be convenient to define the so-called *reduced cross-section* σ_r derived from equation 1.7 by absorbing the common factor of both structure functions:

$$\sigma_r = F_2(x,Q^2) - \frac{y^2}{Y_+} \cdot F_L(x,Q^2) \quad (1.8)$$

The ep scattering process at low Q^2 can be interpreted as the interaction of a flux of virtual photons with the proton. Due to their effective mass virtual photons can have a longitudinal as well as a transverse polarisation. Hence the differential ep cross-section in the Born approximation can be decomposed accordingly:

$$\frac{d^2\sigma}{dxdQ^2} = \Gamma(y,Q^2) \left(\sigma_T(x,Q^2) + \epsilon(y)\sigma_L(x,Q^2) \right) \quad (1.9)$$

Here σ_T and σ_L denote the cross-section for the absorption of transversely and longitudinally polarised photons by the proton, respectively, $\Gamma(y,Q^2) = \alpha Y_+/(2\pi Q^2 x)$ describes the photon flux and $\epsilon(y) = 2(1-y)/Y_+$ is the photon polarisation[2].

Comparing equations 1.7 and 1.9 one obtains:

$$F_2(x,Q^2) = \frac{Q^2}{4\pi^2\alpha} \left(\sigma_T(x,Q^2) + \sigma_L(x,Q^2) \right) \quad (1.10)$$

$$F_L(x,Q^2) = \frac{Q^2}{4\pi^2\alpha} \sigma_L(x,Q^2) \quad (1.11)$$

Due to its relation to the cross-section for longitudinally polarised photons F_L is called *longitudinal structure function*. The condition that both the longitudinal and the transverse cross-section have to be positive imposes the following constraint on the proton structure functions:

$$0 \leq F_L(x,Q^2) \leq F_2(x,Q^2) \quad (1.12)$$

---

[2]It should be emphasised that there is a certain amount of freedom in the definition of the flux factor since the only constraint is the correct description of the real photon flux in the photoproduction limit ($Q^2 \to 0\,\text{GeV}^2$). Here the convention of Hand is used [Han63]. The quoted formulae for $\Gamma(y,Q^2)$ and $\epsilon(y)$ are approximations valid for $W^2 \gg m_p^2$.
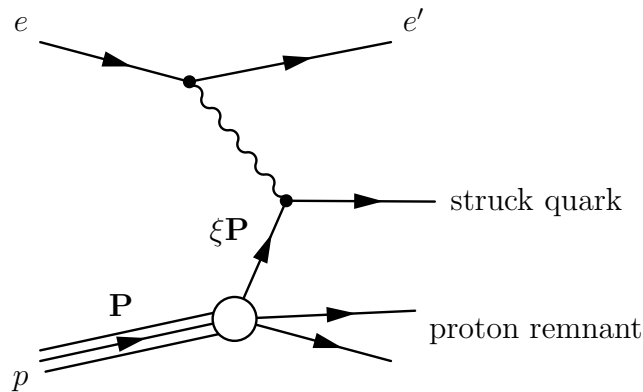
Figure 1.2: *Deep inelastic scattering in the quark parton model.*

1.3 Quark Parton Model

The quark parton model has been the first approach to provide a reasonable interpretation of the SLAC measurements mentioned in the preface. In the quark parton model the proton is assumed to consist of point-like spin-$\frac{1}{2}$ particles (partons) that can be identified with the three quarks necessary to explain the quantum numbers of the proton. The interaction of electron and proton is viewed in the *infinite momentum frame* in which the transverse momenta of the quarks are neglected and $Q^2 \gg m_p^2$. In this frame relativistic time dilatation slows down the rate at which the partons interact with each other, i.e. during the short time the virtual photon interacts with the proton the quarks are essentially free. Hence deep inelastic ep scattering can be viewed as an incoherent sum of electron-quark scattering processes as displayed in figure 1.2.

Accordingly, the differential ep cross-section is expressed as a sum of elastic eq scattering cross-sections

$$\frac{d^2\sigma}{dxdQ^2} = \sum_i \int_0^1 d\xi q_i(\xi) \left(\frac{d^2\sigma}{dxdQ^2}\right)_{eq_i \to eq_i} \tag{1.13}$$

where the *parton density function* $q_i(\xi)$ is the probability to find a quark i carrying the fraction ξ of the proton's momentum before entering the scattering process. The cross-section for electron-quark elastic scattering can be calculated in QED to

$$\left(\frac{d^2\sigma}{dxdQ^2}\right)_{eq_i \to eq_i} = \frac{4\pi\alpha^2}{Q^4}e_i^2\frac{1}{2}(1+(1-y)^2)\delta(x-\xi) \tag{1.14}$$

The result implies that the momentum fraction ξ of the struck quark is identical to the dimensionless variable Bjorken x introduced in section 1.1. Equation 1.13 illustrates the basic concept of the quark parton model, namely the splitting of the DIS cross-section into an calculable hard process and a parton density function to be determined by the experiment.

Inserting equation 1.14 in 1.13 and comparing the result to 1.7 yields:

$$F_2(x, Q^2) = \sum_i e_i^2 x q_i(x) \tag{1.15}$$

$$F_L(x, Q^2) = 0 \tag{1.16}$$

From these equations the following predictions of the quark parton model can be derived: the structure function F_2 is scale invariant, i.e. it does not depend on Q^2 but only on x. This behaviour is called *scaling* and was observed in the first DIS experiments at SLAC for $x \approx 0.25$ in 1969 [Blo69, Bre69]. The longitudinal structure function F_L is predicted to vanish. Equation 1.16 is also known as Callan-Gross relation. It follows from the helicity conservation for massless spin-$\frac{1}{2}$ partons [Cal69]. In the same year when it was derived (1969) it was confirmed in a combined analysis of SLAC and DESY [Alb69, Tay69] giving strong evidence for the spin-$\frac{1}{2}$ structure of the quarks.

1.4 Quantum Chromodynamics

As already pointed out in the preface the experimental observation that the quarks carry only about 50% of the proton's momentum cannot be explained within the quark parton model. Nor can it account for free quarks not being observed in the final state of any particle reaction while in DIS experiments quarks appear to be quasi-free. Further problems occurred in the classification of the hadron spectra: to explain the quantum numbers of the Δ^{++} resonance it is assumed to consist out of three u quarks. Since quarks are spin-$\frac{1}{2}$ particles the Fermi statistics seems to be violated.

In first instance to overcome the latter caveat a new quantum number, *colour*, was introduced [Han65, Gre64]. Each quark carries one of the colours red, green or blue. The idea of extending the colour model to a gauge theory obeying SU(3) symmetry led to the development of *Quantum Chromodynamics* (QCD), the theory of the strong interaction [Fri73, Gro73a, Wei73]. The gauge bosons of QCD are eight massless *gluons* mediating the interaction between the quarks. They carry the missing fraction of the proton's momentum. Due to the non-Abelian structure of the SU(3) group they have themselves a colour and an anticolour allowing for gluon self interactions. The colour plays the same role for the strong interaction as the charge for QED. However, the Abelian structure of the U(1) symmetry group allows no photon self couplings in QED.

The vacuum polarisation in QED leads to a screening of a charge to be probed and the coupling constant α increases with decreasing distance (increasing Q^2). On the contrary, in QCD the self coupling of the gluons causes an antiscreening effect leading to a decrease of the strong coupling constant α_s with increasing Q^2. This behaviour is referred to as *running of α_s* and quantified in the renormalisation group equation given in leading order by

$$\alpha_s(Q^2) = \frac{12\pi}{(33 - 2n_f) \ln \frac{Q^2}{\Lambda_{QCD}^2}} \tag{1.17}$$

where n_f denotes the number of active quark flavours, i.e. those with $m_q^2 < Q^2$. The parameter Λ_{QCD} determines the scale at which α_s becomes large. For Q^2 values much larger than Λ_{QCD}^2 the coupling constant α_s becomes small and the quarks inside the hadrons are quasi-free. The discovery of this property of QCD [Gro73b, Pol73], called *asymptotic freedom*, allows to conduct perturbative calculations. Approaching Λ_{QCD}^2 with Q^2 implies α_s getting large. Hence the quarks start to be tightly bound in the hadrons and perturbative methods cannot be used. Either $\alpha_s(Q^2)$ or Λ_{QCD} has to be determined from experimental data. The latter is of the order of a few hundred MeV.
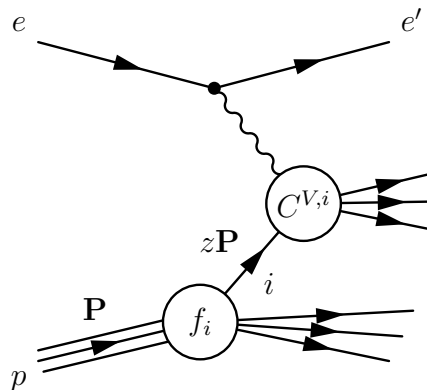
Figure 1.3: *Illustration of the factorisation theorem for deep inelastic ep scattering.*

One of the achievements of perturbative QCD (pQCD), applicable in the domain of asymptotic freedom, is the field theoretical justification of the parton model. This is realised by the *factorisation theorem* of deep inelastic scattering [Col89]. It states that for the general case of lepton-hadron scattering the interaction of the exchanged vector boson with the hadron can be divided into two independent parts, a *short distance* part which is perturbatively calculable and a *long distance* part to be determined experimentally. It is a direct transfer of the basic assumption of the quark parton model to separate the DIS cross-section into a hard scattering process and a parton density function. Formally, factorisation implies to express the structure function $F_2^{V,h}$ as convolution of a *coefficient function* $C_2^{V,i}$ and a parton density $f_{i/h}$ summing over all partons i (quarks q, antiquarks $\bar{q}$, gluons g):

$$F_2^{V,h}(x, Q^2) = \sum_{i=q,\bar{q},g} \int_x^1 dz\, C_2^{V,i}\left(\frac{x}{z}, \frac{Q^2}{\mu_r^2}, \frac{\mu_f^2}{\mu_r^2}, \alpha_s(\mu_r^2)\right) f_{i/h}(z, \mu_r^2, \mu_f^2) \qquad (1.18)$$

The coefficient function $C_2^{V,i}$ describes the interaction of the exchanged vector boson V with a parton i. It is independent of the long distance effects and in particular independent of the identity of the hadron h. For a particular exchanged boson V it can be expanded in a power series of α_s and perturbatively calculated. The parton density $f_{i/h}(z)$ is a direct generalisation of the parton model quark distribution, i.e. it corresponds to the probability to find a parton i carrying a fraction z of the hadron's momentum. It is specific to the hadron h, but *universal*, that is, independent of the particular hard scattering process. Two scales are present: the factorisation scale parameter μ_f defines the boundary between the short and long distance part and μ_r is the so-called renormalisation scale parameter used to absorb divergent parts of the perturbation theory. Figure 1.3 shows an illustration of the factorisation theorem for deep inelastic *ep* scattering[3].

The separation between the coefficient functions and parton density functions is not unique. To eliminate this ambiguity a specific *factorisation scheme* has to be applied. The two most commonly used schemes are the DIS [Alt79] and the modified minimal subtraction scheme $\overline{\text{MS}}$ [Bar78] scheme. In the DIS scheme the structure function F_2

---

[3]As this thesis is concerned with *ep* scattering in a region of the kinematic phase space in which the photon exchange dominates the indices V and h are omitted in the following implicitly assuming that they correspond to γ and p.
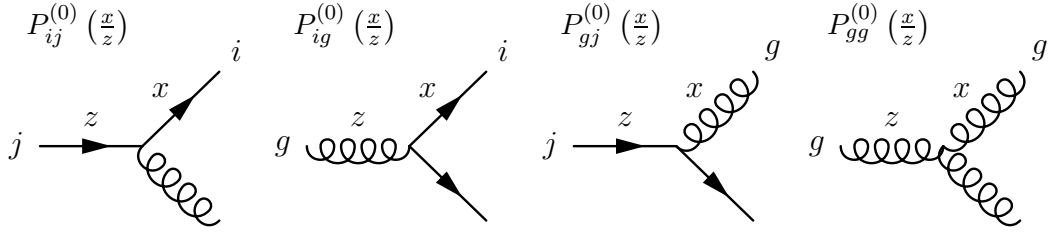
Figure 1.4: *Diagrams of the leading order DGLAP slitting functions. $P_{\alpha\beta}^{(0)}(x/z)$ denotes the probability that a parton α carrying a fraction x of the proton's momentum originates from a parton β with a momentum fraction z.*

is given by the quark parton model equation 1.15 to all orders in perturbation theory, just that the quark densities are scale dependent. Choosing $\mu_r = \mu_f = Q$ one obtains:

$$F_2(x, Q^2) = \sum_{i=q,\bar{q}} e_i^2 x f_i(x, Q^2) \tag{1.19}$$

In case of the $\overline{\text{MS}}$ scheme the parton density functions are defined directly in terms of hadronic matrix elements. The latter scheme is more useful for theoretical calculations while the former is the natural choice for DIS experiments.

A remarkable consequence of factorisation is that measuring the parton density functions at one scale μ allows their prediction for any other scale μ' given that both scales are large enough for α_s at each of them to be small. This possibility increases the predictive power of pQCD enormously and is referred to as *evolution* of the parton densities. The underlying evolution equations can be derived from equation 1.18 by requiring that the structure functions as measurable quantities should be independent of the factorisation and renormalisation scale. Choosing again $\mu_r = \mu_f = Q$ one obtains the DGLAP evolution equations named after Dokshitzer, Gribov, Lipatov, Altarelli and Parsisi [Gri72, Dok77, Alt77]:

$$\frac{dq_i(x, Q^2)}{d\ln Q^2} = \frac{\alpha_s(Q^2)}{2\pi} \int_x^1 \frac{dz}{z} \left[\sum_j q_j(z, Q^2) P_{ij}\left(\frac{x}{z}\right) + g(z, Q^2) P_{ig}\left(\frac{x}{z}\right) \right] \tag{1.20}$$

$$\frac{dg(x, Q^2)}{d\ln Q^2} = \frac{\alpha_s(Q^2)}{2\pi} \int_x^1 \frac{dz}{z} \left[\sum_j q_j(z, Q^2) P_{gj}\left(\frac{x}{z}\right) + g(z, Q^2) P_{gg}\left(\frac{x}{z}\right) \right] \tag{1.21}$$

Here $q_j(z, Q^2)$ and $g(x, Q^2)$ denote the quark and gluon density functions, respectively. Like the coefficient functions the so-called *splitting functions* $P_{\alpha\beta}$ are calculable in pQCD expanding them into a power series in α_s:

$$P_{\alpha\beta}(z, \alpha_s(Q^2)) = \frac{\alpha_s}{2\pi} P_{\alpha\beta}^{(0)}(z) + \left(\frac{\alpha_s}{2\pi}\right)^2 P_{\alpha\beta}^{(1)}(z) + \dots \tag{1.22}$$

The leading order splitting functions $P_{\alpha\beta}^{(0)}(x/z)$ have a simple physical interpretation: they correspond to the probability that a parton α carrying a fraction x of the proton's momentum originates from a parton β with a momentum fraction z. Figure 1.4 shows the graphs for all leading order splitting functions.

Since the momentum fraction of the radiated parton is always smaller or equal to that of the parent parton, the integration in equations 1.20 and 1.21 is restricted to the interval $x \leq z \leq 1$. Hence the evolution of the parton density functions can be predicted without having to know them to arbitrary small values of x.

This allows for a determination of the parton density functions from experimental data according to the following procedure: the parton density functions are parameterised by smooth analytical functions at a low starting scale Q_0^2 as a function of x with a certain number of free parameters. They are evolved in Q^2 using the DGLAP equations. Afterwards predictions for structure functions and cross-sections are calculated. The free parameters are determined by performing a χ^2 fit to the data. Several constraints are imposed during this procedure.

For an accurate determination of the parton density functions the coefficient and splitting functions have to be precisely known as they govern the calculation of the structure functions (see equation 1.18) and the evolution (see equations 1.20 and 1.21), respectively. Since 2005 all of them are known to next-to-next-to-leading order (NNLO) [Moc04, Vog04, Ver05].

Global QCD analyses applying the fitting procedure outlined above to the data of different experiments have been carried out by several theoretical groups, resulting in a large set of available parameterisations for the parton density functions. Among them are the ones from Glück, Reya and Vogt (GRV) [Glü98], from Martin, Roberts, Stirling and Thorne (MRST) [Mar02, Mar03] and the CTEQ collaboration [Pum02].

Also the H1 collaboration has performed a QCD fit (H1 PDF 2000) based on positron-proton neutral and charged current events recorded with the H1 detector in the years 1994 to 2000 [Adl03]. The parton densities have been evolved according to the DGLAP equations in next to leading order. Figure 1.5 compares the H1PDF 2000 fit to the data used for its derivation as well as to data from the ZEUS collaboration and the fixed target experiments BCDMS and NMC. The structure function F_2 is displayed as a function of Q^2 for various values of x. Good agreement between the data and the fit is observed except for the BCDMS data at $x = 0.65$. This implies that pQCD successfully describes the data over almost five orders of magnitude in x and Q^2 including the scaling violation of F_2 explained in the following.

The structure function F_2 rises (decreases) with Q^2 at small (large) values of x, i.e. the scaling behaviour predicted by the quark parton model and observed in the first DIS experiments at SLAC [Blo69, Bre69] is violated for the bulk of the phase space. Only in the region of $x \approx 0.25$ where the SLAC measurements have been performed scaling is still found. The scaling violations are caused by gluon radiation: by radiating a gluon with a momentum fraction x'' the original momentum fraction x of the quark is reduced to $x' < x$ because of $x = x' + x''$. In addition gluons can split into quark antiquarks pairs[4] carrying a relatively small momentum fraction. With increasing resolution, i.e. larger values of Q^2, more of such processes can be resolved by the photon. Therefore one expects the quark density functions to rise with Q^2 at low x and to decrease with it at high x. Since the structure function F_2 is the charged weighted sum of the quark densities (see formula 1.19) this behaviour directly leads to the observed scaling violations.

---

[4]The quarks and antiquarks originating from gluon splittings are called *sea quarks* in contrast to the three *valence quarks* necessary to explain the quantum numbers of the proton.
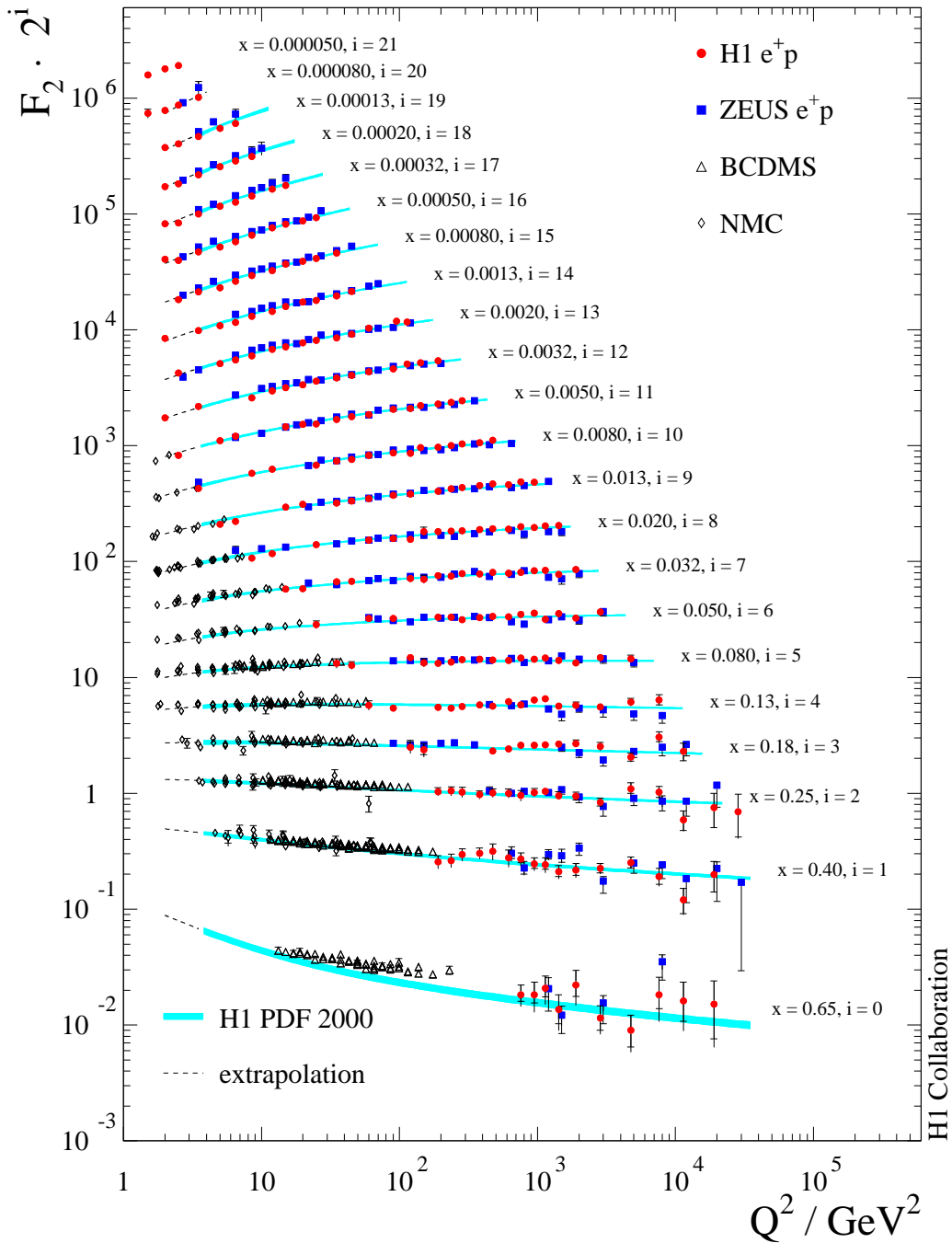
Figure 1.5: *Proton structure function F_2 as a function of Q^2 for various values of x measured by the H1 and ZEUS collaborations as well as the fixed target experiments BCDMS and NMC (figure taken from [New04]). The results are compared to the H1 PDF 2000 fit represented by the error bands. The width of the latter contains the experimental uncertainty as derived from the fit and the model uncertainty added in quadrature. In case of the data points the inner error bars indicate the statistical errors, the outer ones the statistical and systematic errors added in quadrature. For a better visibility the values of the structure function F_2 are multiplied by 2^i with i depending on the particular value of x.*

1.5 The Rise of F_2 towards Low x

It has been already mentioned in the preface that one of the first observations at HERA was a substantial rise of F_2 with decreasing x at fixed Q^2 [Abt93, Der93a]. Such a behaviour is expected in pQCD: the DGLAP equations can be solved in the so-called double leading log approximation predicting F_2 to rise approximately as a power of x towards low x [DR74, Bal94]. The rise is a reflection of the gluon density and the sea quark densities getting larger with decreasing x. However, for sufficiently small x the power-like growth of F_2 causes the cross-section to violate unitarity. Hence one expects the rise of F_2 to be tamed as $x \to 0$, an effect referred to as *saturation*. One possible explanation for saturation are gluon recombinations in the nucleon [Gri81, Gri83]. Concerning the event kinematics it is most promising to search for saturation effects in the low Q^2 regime[5] since in this region the lowest values of x are reached according to equation 1.4.

It has been suggested [Nav94] to measure the derivative

$$\lambda(x, Q^2) = - \left. \frac{\partial F_2(x, Q^2)}{\partial \ln x} \right|_{Q^2} \tag{1.23}$$

in order to investigate the behaviour of F_2 at low x. The H1 collaboration has determined this quantity for various data sets [Adl01b, Laš02a, Pet04]. It was found that $\lambda(x, Q^2)$ is independent of x at fixed Q^2 for $x \lesssim 0.01$ within the experimental accuracy. This implies that the structure function F_2 at low x can be parameterised as

$$F_2 = c(Q^2) \cdot x^{-\lambda(Q^2)} \tag{1.24}$$

Hence the x dependence of F_2 at low x is indeed consistent with a power law as predicted by pQCD and there is no evidence for a taming of this rise. Both H1 and ZEUS have subjected their data to fits of the function 1.24 for $x < 0.01$ [Bre99, Adl01b, Laš02a]. The results for $\lambda(Q^2)$ are shown in figure 1.6. Two distinct regions can be distinguished: for $Q^2 \gtrsim 3\,\text{GeV}^2$ where partons are the relevant degrees of freedom, λ depends logarithmically on Q^2. This behaviour is well reproduced by DGLAP based QCD fits. In contrast, for $Q^2 \lesssim 1\,\text{GeV}^2$, $\lambda(Q^2)$ deviates from the logarithmic dependence on Q^2 and tends to the value of 0.08 known from fits to hadron-hadron and photoproduction total cross-sections based on Regge phenomenology (see next section). In this region α_s is large and due to the confinement hadrons are the relevant degrees of freedom. Since perturbative methods are not applicable in this regime a reasonable description of the transition between quasi-real photoproduction and DIS remains one of the biggest challenges in QCD. Presently the best description is provided by phenomenological models. Three of them are discussed in the coming section.

1.6 Phenomenological Models at Low Q^2

A large fraction of the phenomenological models describing the transition from high to low values of Q^2 make use of the fact that the *ep* scattering process can be interpreted

---

[5]At very low values of Q^2 gluon self-interactions cannot be used as an explanation for the taming of the rise of F_2 since individual partons are not resolved any more.
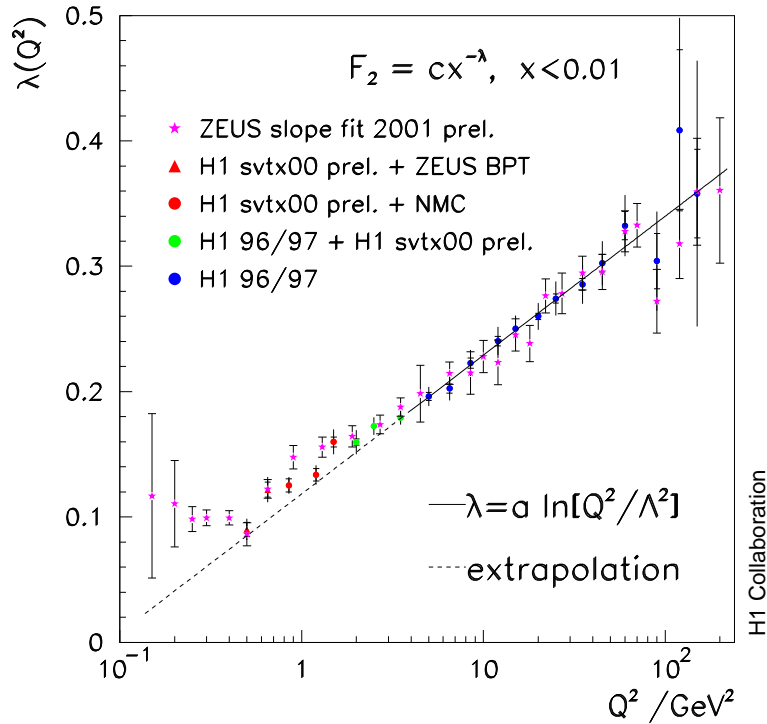
Figure 1.6: *Exponent $\lambda(Q^2)$ obtained from fits of the function 1.24 to H1 and ZEUS structure function data for $x < 0.01$ [Bre99, Adl01b, Laš02a] (figure taken from [New04]). The inner error bars illustrate the statistical errors, the outer error bars indicate the statistical and systematic errors added in quadrature. The straight line represents a fit of the form $\lambda(Q^2) = a \ln(Q^2/\Lambda^2)$ using data for $Q^2 \geq 3.5\,\mathrm{GeV}^2$, the dashed line shows an extrapolation of this fit to lower values of Q^2.*

as the interaction of a virtual photon with the proton (see section 1.2). They provide a smooth fit of the structure functions or equally the photoabsorption cross-sections ensuring that in the limit $Q^2 \to 0$ the corresponding photoproduction values are reached. Since real photons can have no longitudinal polarisation this implies for σ_T and σ_L:

$$\sigma_T \to \sigma_{\gamma p}, \qquad \sigma_L \to 0 \tag{1.25}$$

According to equations 1.10 and 1.11 this implies that the structure functions F_2 and F_L have to vanish in the photoproduction limit.

At very low values of Q^2 the exchanged photon becomes almost real and it can fluctuate into a virtual quark-antiquark pair. The lifetime of this state can become large and comparable to the photon-proton interaction time since the virtuality is small. Thus it is possible to interpret the photon-proton scattering as a hadron-hadron interaction.

ALLM Parameterisation

The ALLM parameterisation is inspired by the Regge theory which has been developed well in advance of QCD to describe hadron-hadron interactions [Reg59, Reg60, Che61].

Due to the hadronic nature of quasi real photons mentioned above it can be used to describe *ep* scattering at small values of Q^2. In Regge theory the interaction of two hadrons is described by the exchange of collective states of colour neutral particles, all of them having the same quantum numbers apart from the spin. The spin depends approximately linearly on the particle mass squared t. The corresponding straight line is called *Regge trajectory* and parameterised as follows

$$\alpha(t) = \alpha(0) + \alpha' \cdot t \tag{1.26}$$

with $\alpha(0)$ being the intercept and α' the slope of the trajectory.

Using this approach Donnachie and Landshoff [Don92] have fitted pp and $p\bar{p}$ total cross-sections by the form

$$\sigma_i^{tot} = A_i^{I\!P} s^{\alpha_{I\!P}(0)-1} + A_i^{I\!R} s^{\alpha_{I\!R}(0)-1} \tag{1.27}$$

The coefficients $A_i^{I\!P}$ and $A_i^{I\!R}$ are process dependent constants whereas the intercepts $\alpha_{I\!P}(0)$ and $\alpha_{I\!R}(0)$ are universal and have been determined to be $\alpha_{I\!P}(0) = 1.0808$ and $\alpha_{I\!R}(0) = 0.5475$. The trajectory $I\!R$ is an effective trajectory comprising several trajectories of known mesons (reggeon trajectories). It describes the decrease of the cross-section as a function of s at low s. To account for the observed increase of σ_i^{tot} at larger values of s, the so-called pomeron trajectory $I\!P$ has been introduced which has the quantum numbers of the vacuum.

It has been shown that equation 1.27 also describes other hadronic total cross-section data including that of real photoproduction on protons. In addition it directly implies F_2 to rise as $F_2 \sim x^{1-\alpha_{I\!P}(0)}$ or $F_2 \sim x^{-0.08}$ towards small values of x [Don94]. This is in agreement with the observations in the last section.

In contrast, the given parameterisation fails to to reproduce DIS data. To achieve a description of the entire Q^2 range the ansatz of Donnachie and Landshoff has been extended by several authors. In the parameterisation of Abramowicz, Levin, Levy and Moar (ALLM) [Abr91] the structure function F_2 is composed of a pomeron ($F_2^{I\!P}$) and a reggeon ($F_2^{I\!R}$) contribution:

$$F_2(x, Q^2) = \frac{Q^2}{Q^2 + m_0^2} \left(F_2^{I\!P}(x, Q^2) + F_2^{I\!R}(x, Q^2) \right) \tag{1.28}$$

The basic difference between this model and equation 1.27 is the introduction of Q^2 dependent intercepts. The version of the parameterisation employed for the present analysis has been obtained in 1997 by fitting its 23 free parameters to DIS data of HERA and fixed target experiments together with total pp and γp cross-sections [Abr97].

Saturation Model

The saturation model of Golec-Biernat and Wüsthoff [GB99a, GB99b] is intended to provide a description of the transition between the high and low Q^2 regime in inclusive *ep* scattering at low x. It is based on the colour dipole model. The latter has a physical interpretation in the proton rest frame (see figure 1.7 a)): the virtual photon γ^* splits into a quark-antiquark pair, i.e. a colour dipole, long before the interaction with the proton since the formation time, $\tau_{q\bar{q}} \sim 1/(x m_p)$, is large. Subsequently the
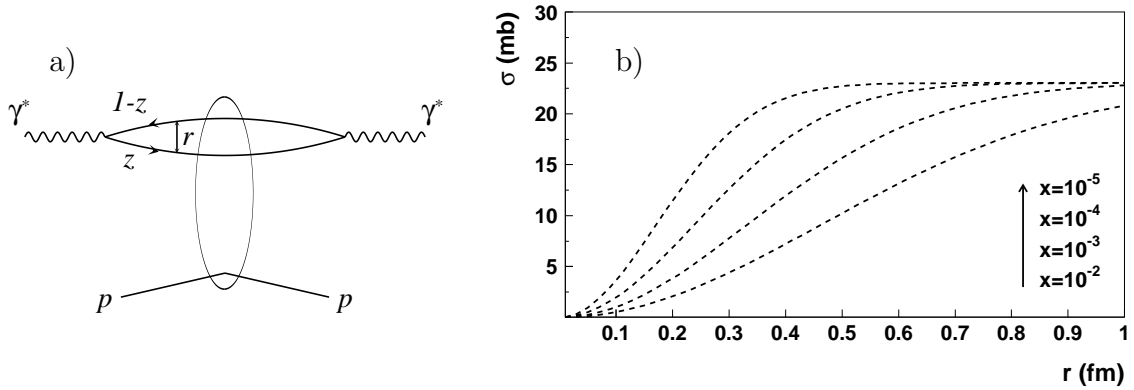
Figure 1.7: a) *Illustration of the photon-proton scattering process within the dipole model. b) Dipole cross-section $\hat{\sigma}(x, r^2)$ as a function of the transverse separation r of the $q\bar{q}$ pair according to equation 1.30 for different values of x (both figures taken from [GB99b]).*

$q\bar{q}$ pair scatters coherently off the proton in a time which is short compared to $\tau_{q\bar{q}}$. The dissociation of the photon into the $q\bar{q}$ pair is described by QED while the strong interaction is contained in the cross-section for the dipole-proton interaction. It is assumed that the transverse separation r of quark and antiquark remains constant during the interaction. Quark and antiquark carry the fraction z and $1 - z$ of the photon's momentum, respectively.

The idea of the dipole model is expressed formally by factorising the absorption cross-sections for transversely and longitudinally polarised photons in the following way:

$$\sigma_{T,L}(x, Q^2) = \int d^2\mathbf{r} \int_0^1 dz \, |\Psi_{T,L}(z, \mathbf{r})|^2 \, \hat{\sigma}(x, r^2) \qquad (1.29)$$

The photon wave functions Ψ_T and Ψ_L describe the photon dissociation in a $q\bar{q}$ pair and are calculable in QED. In contrast, the dipole cross-section $\hat{\sigma}(x, r^2)$ is substantially influenced by non-perturbative contributions and needs to be modelled.

In the saturation model [GB99a, GB99b] the dipole cross-section is assumed to have the form

$$\hat{\sigma}(x, r^2) = \sigma_0 \left[1 - \exp\left(-\frac{r^2}{4R_0^2(x)} \right) \right] \qquad (1.30)$$

where the x dependent *saturation radius* $R_0(x)$ is given by

$$R_0(x) = \frac{1}{Q_0} \left(\frac{x}{x_0} \right)^{\frac{\lambda}{2}} \qquad (1.31)$$

To ensure a smooth transition to the photoproduction limit ($Q^2 \to 0$) x is modified to be

$$x = x_B \left(1 + \frac{4m_q^2}{Q^2} \right) \qquad (1.32)$$

with x_B denoting Bjorken x in its original definition according to equation 1.3 and m_q being an effective quark mass.

Fixing Q_0 to $1\,\text{GeV}$ and m_q to $140\,\text{MeV}$ three model parameters remain which have been determined from fits to DIS data for $x < 10^{-2}$ [GB99a]:

$$\sigma_0 = 23\,\text{mb}, \quad \lambda = 0.29, \quad x_0 = 3 \cdot 10^{-4} \tag{1.33}$$

The resulting dipole cross-section $\hat{\sigma}(x, r^2)$ as a function of the transverse separation r is depicted in figure 1.7 b) for different values of x. For small values of r the dipole cross-section rises like r^2 while for large values of r it saturates. Saturation sets in at $r \sim 2R_0$, i.e. it is governed by R_0. The characteristic size of the dipoles is given by $r \sim 1/\sqrt{Q^2}$. Hence $\hat{\sigma}(x, r^2)$ rises with decreasing values of Q^2 and finally saturates if low values of Q^2 are approached[6]. This feature of the dipole model can explain the change in the behaviour of λ at very low values of Q^2 (see section 1.5). The dipole model predicts a pomeron intercept of $\alpha_{I\!P}(0) \approx 1.08$ if the parameterisation obtained from fits to DIS data is extrapolated to the photoproduction regime. This result is in perfect agreement with the model of Donnachie and Landshoff [Don92] as well as the experimental results for λ obtained at HERA (see figure 1.6).

Due to the x dependence of the saturation radius R_0 given by equation 1.31 the dipole cross-section $\hat{\sigma}(x, r^2)$ saturates at smaller values of r and hence larger values of Q^2 as x decreases. For a fixed value of r, i.e. Q^2, it saturates as a function of x when approaching low values of x. In this way the saturation model incorporates the saturation of F_2 expected at small x. The saturation sets in at larger values of x when Q^2 decreases.

While being very successful in describing the experimental observations at low Q^2 the saturation model undershoots the measured structure function F_2 for $Q^2 > 20\,\text{GeV}^2$. This is caused by the fact that it does not include any scaling violations. Therefore the saturation model has been extended by incorporating leading order DGLAP evolution [Bar02]. In order to preserve the good agreement with the data at low Q^2 the dipole cross-section is only modified at small values of r while at large r is still shows saturation:

$$\hat{\sigma}(x, r^2) = \sigma_0 \left[1 - \exp\left(-\frac{\pi^2\, r^2\, \alpha_s(\mu^2)\, xg(x, \mu^2)}{3\,\sigma_0} \right) \right] \tag{1.34}$$

The scale μ^2 is assumed to have the form $\mu^2 = \mu_0^2 + C/r^2$ with μ_0^2 and C being parameters to be determined from a fit to the data. Since the model is intended to describe the data at low x, only the gluon density $g(x, Q^2)$ is included in the leading order DGLAP evolution, because it is the dominating parton density in this regime. The modified saturation model with four additional parameters describes the Q^2 dependence of λ as observed at HERA (see figure 1.6) remarkably well over the whole Q^2 range [Bar02].

Fractal Fit

At small values of x the proton structure function F_2 is almost solely determined by the sea quarks. In QCD their behaviour is driven by gluon emissions and splittings. The larger values of Q^2 are reached the more of these emissions and splittings

---

[6]The saturation of the dipole cross-section as a function of Q^2 has to be distinguished from the saturation as a function of x which is described below and leads to the small x saturation of F_2 introduced in section 1.5.
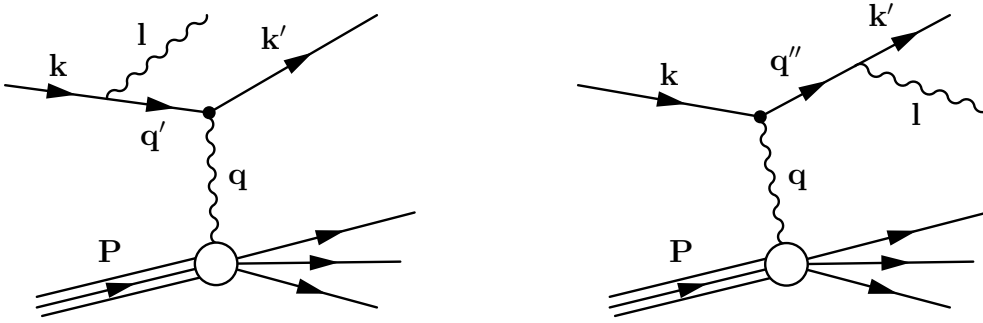
Figure 1.8: *Lowest order Feynman diagrams for the process* $ep \to e\gamma X$ *with photon emission from the electron line.*

can be observed. In [Laš02b] it has therefore been attempted to parametrise F_2 assuming a self-similar structure of the proton, i.e. expecting that the proton reveals a fractal nature at low x. Two magnification scales are used: $1/x$ and $1 + Q^2/Q_0^2$. Including Q_0^2 the parameterisation contains five free parameters. They have been determined using results from the H1 and ZEUS experiments at $0.045 \leq Q^2 \leq 120\,\mathrm{GeV}^2$ and $6.2 \cdot 10^{-7} \leq x \leq 0.01$. The parameterisation, which is referred to as *fractal fit* in the following, provides a good description of the data in the kinematic region given.

1.7 Radiative ep Scattering

Figure 1.1 depicts the ep scattering process to lowest order perturbation theory (Born approximation). The corresponding Born cross-section is given in equation 1.7 taking only the photon exchange into account. At higher orders various radiative processes have to be considered which are discussed in section 3.7. The present section focuses solely on their dominant contribution to the cross-section at low Q^2, the radiation of a real photon from the incoming or outgoing electron. For these process class several configurations can be experimentally observed and are important for the analysis as outlined in the following.

The lowest order Feynman diagrams for the photon emission from the lepton line are shown in figure 1.8. Also the notation for the particle four-momenta to be used in the following can be inferred from there. The amplitudes of both diagrams and the interference term between them contribute to the scattering cross-section. Hence it is impossible to attribute a single event to either the one or the other diagram. The amplitudes for the first and second diagram are inversely proportional to $(\mathbf{q'}^2 - m_e^2)\,\mathbf{q}^2$ and $(\mathbf{q''}^2 - m_e^2)\,\mathbf{q}^2$, respectively. Correspondingly, the differential cross-section exhibits several maxima when one or both of these term approach zero. These peaks correspond to the following experimental configurations:

- *Radiative DIS events* correspond to the maxima of the cross-section reached for $\mathbf{q'}^2 \simeq 0$ or $\mathbf{q''}^2 \simeq 0$, but $\mathbf{q}^2$ still being finite. This implies that the radiated photon is emitted collinear either with the incoming ($\mathbf{q'}^2 \simeq 0$) or the scattered ($\mathbf{q''}^2 \simeq 0$) electron while the virtuality $Q^2 = -\mathbf{q}^2$ of the exchanged photon is large enough for the scattered electron to be detected in the main detector.

  In the first case the Feynman diagram shown in figure 1.8 a) dominates the

cross-section. Such events are called *Initial State Radiation* (ISR) events. Due to the photon radiation the energy of the electron available for the interaction with the proton is lowered and hence an ISR event can be interpreted as a non-radiative *ep* scattering event at a reduced centre of mass energy $\sqrt{s}$. According to equation 1.4 this allows on the one hand to extract the structure function F_2 at lower values of Q^2 for a given x or at larger values x for a given Q^2 [Ahm95, Der96, ZEU03, İşs00]. In addition the lowered centre of mass energy in ISR events can be exploited to measure the proton structure function F_L [ZEU03, İşs00] (see section 1.2). Also the present analysis makes use of ISR events to extend the accessible kinematic phase space for the F_2 measurement, but in contrast to the previous measurements the radiated photon is not explicitely detected.

In the second case the main contribution stems from the Feynman diagram of figure 1.8 b), the corresponding events are referred to as *Final State Radiation* (FSR) events. For them the opening angle between the scattered electron and the radiated photon is typically too small for the two particles to be separately reconstructed in the calorimeter. Therefore they usually cannot be distinguished from non-radiative events.

- A further peak of the radiative cross-section is reached for $\mathbf{q}^2 \simeq 0$, but $\mathbf{q'}^2$ and $\mathbf{q''}^2$ finite. For this configuration electron and photon have a sizeable transverse momentum and are almost back-to-back in azimuth. Since the virtuality of the exchanged photon is small the process can be interpreted as the scattering of a quasi-real photon off an electron. For this reason the process is called *QED Compton Scattering* (QEDC). Due to the sizeable transverse momenta of the outgoing particles QEDC events can be rather easily identified experimentally. Therefore they are ideally suited to measure the proton structure function F_2 at small values of Q^2 [Akt04, Len01]. Furthermore they can be employed for the detector alignment by making use of their property to be back-to-back in azimuth (see section 4.4).

- Due to the maximum of the cross-section in the limit $\mathbf{q}^2 \simeq 0$, $\mathbf{q'}^2 \simeq 0$ and $\mathbf{q''}^2 \simeq 0$ most of the radiative events are characterised by both electron and radiated photon being scattered at very small angles. Hence they leave the main detector through the beam pipe without being detected. The majority of these events are elastic scattering processes called *Bethe-Heitler events* [Bet34]. Their cross-section can be precisely calculated in QED and is insensitive to the internal proton structure. For these reasons the Bethe-Heitler process is used as reference for the luminosity measurement of the H1 experiment (see section 2.5).

2 The H1 Experiment

The data for the measurement of the structure function F_2 to be presented in this thesis has been collected in the year 2000 with the H1 experiment situated at the HERA collider. After a short overview of the accelerator this chapter concentrates on the description of the H1 detector putting special focus on the relevant subdetectors and the online event selection.

2.1 HERA Accelerator

The HERA (Hadron-Elektron-Ring-Anlage) collider located at DESY (Deutsches-Elektronen-Synchrotron) in Hamburg is the first storage ring for electrons or positrons[1] and protons ever built. It started operation in 1991. The beam energies are 27.6 GeV for the electrons and 920 GeV for the protons[2], respectively. This corresponds to a centre of mass energy available for electron-proton collisions of $\sqrt{s} \approx 320$ GeV which is more than ten times larger than in fixed target experiments performed beforehand.

The particles are accelerated in two separate beam lines located in a tunnel of 6.3 km circumference. The electron (proton) ring is equipped with normal conducting (superconducting) dipole magnets having a maximum field strength of 0.17 T (4.7 T). The magnetic field strength limits the reachable proton energy. The maximum energy of the electron beam is defined by the power of the radiofrequency system which is responsible for the acceleration and thus has to compensate the energy losses due to synchrotron radiation. Synchrotron radiation losses are negligible in the case of the protons since they have a mass being more than three orders of magnitude larger than the electron mass. Before the particles reach the HERA machine they pass a system of several pre-accelerators as depicted in figure 2.1. The last pre-accelerator before the injection into HERA is PETRA (Positron-Elektron-Tandem-Ring-Anlage) accelerating electrons and protons to energies of 12 GeV and 40 GeV, respectively.

The counter rotating beams collide head-on at the North and South interaction regions where the multi-purpose detectors H1 and ZEUS are located. Two additional experiments make use of only one of the two beams: the HERA-B experiment has been designed to study the interaction of protons with the nuclei of target wires positioned in the halo of the proton beam aiming for a measurement of the CP violation in decays of B mesons. It stopped data taking at the end of 2003. The second experiment, HERMES, explores the spin structure of the nucleons by scattering longitudinally polarised electrons off polarised gas atoms (hydrogen, deuterium, helium-3).

The HERA accelerator stores electrons and protons in 220 bunches of 10^{10} to 10^{11} particles each. This beam structure defines the collision rate of 10.4 MHz corresponding

---

[1] In the year 2000 relevant for this analysis positrons have been accelerated.

[2] An increase of the proton beam energy from 820 GeV to 920 GeV was achieved at the beginning of 1998.
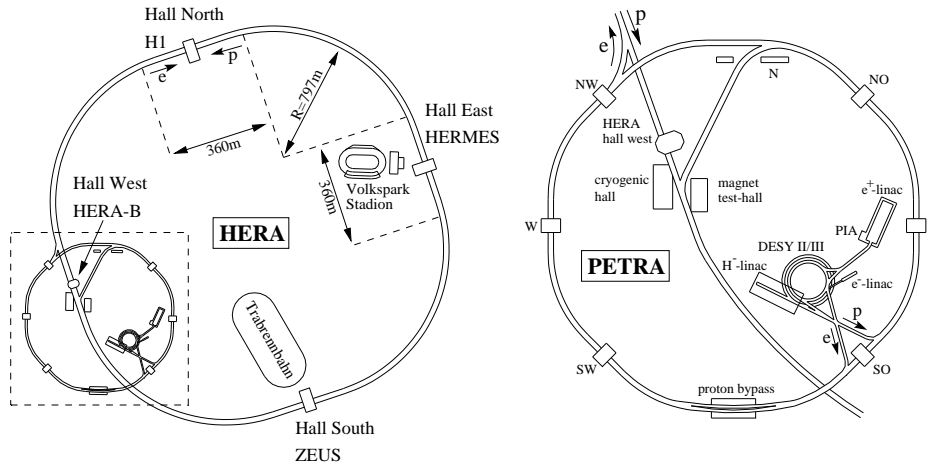
Figure 2.1: *The HERA collider facility and its pre-accelerator system.*

to a time interval of 96 ns between two bunch crossings. During the data taking period relevant for the analysis on average 174 colliding bunches were filled. The remaining bunches are either not filled or have an empty partner bunch. They can be used to study the beam induced background (see section 3.4).

In September 2000 the first running phase of the HERA collider ended with a long shut down to allow for a major upgrade of the machine and the colliding beam experiments. The major goal of the upgrade was a fivefold increase in instantaneous luminosity[3] to further enhance the physics potential of the experiments. The ongoing running phase that started in 2002 is referred to as HERA-II.

2.2 Detector Overview

The H1 detector [Abt97a, Abt97b] has been designed for a precise identification and reconstruction of the particles emerging from the *ep* interactions. It provides a hermetic coverage of almost the entire solid angle as can be seen in figure 2.2 which shows a schematic view of the main setup.

A right-handed Cartesian coordinate system (see figure 2.2) defined by the Central Tracker (see below) is used to describe the signatures of detected particles. The positive z-axis points into the proton beam direction, the positive x-axis towards the centre of HERA. The geometrical centre of the Central Tracker constitutes the origin. For the parameterisation of particle trajectories polar coordinates are usually employed: the distance r from the origin in the xy-plane, the azimuthal angle ϕ in the xy-plane w.r.t. the x-axis and the polar angle θ w.r.t. the z-axis. The region of small (large) polar angles is referred to as forward (backward) region. The H1 detector is arranged symmetrically around the beam pipe, the asymmetric instrumentation in z-direction accounts for the different beam energies causing a large fraction of the hadronic final state particles to occupy the forward region.

A detailed description of the H1 detector can be found in [Abt97a, Abt97b]. In the

---

[3]The luminosity is a measure for the number of observable *ep* scattering processes as is explained in section 2.5.
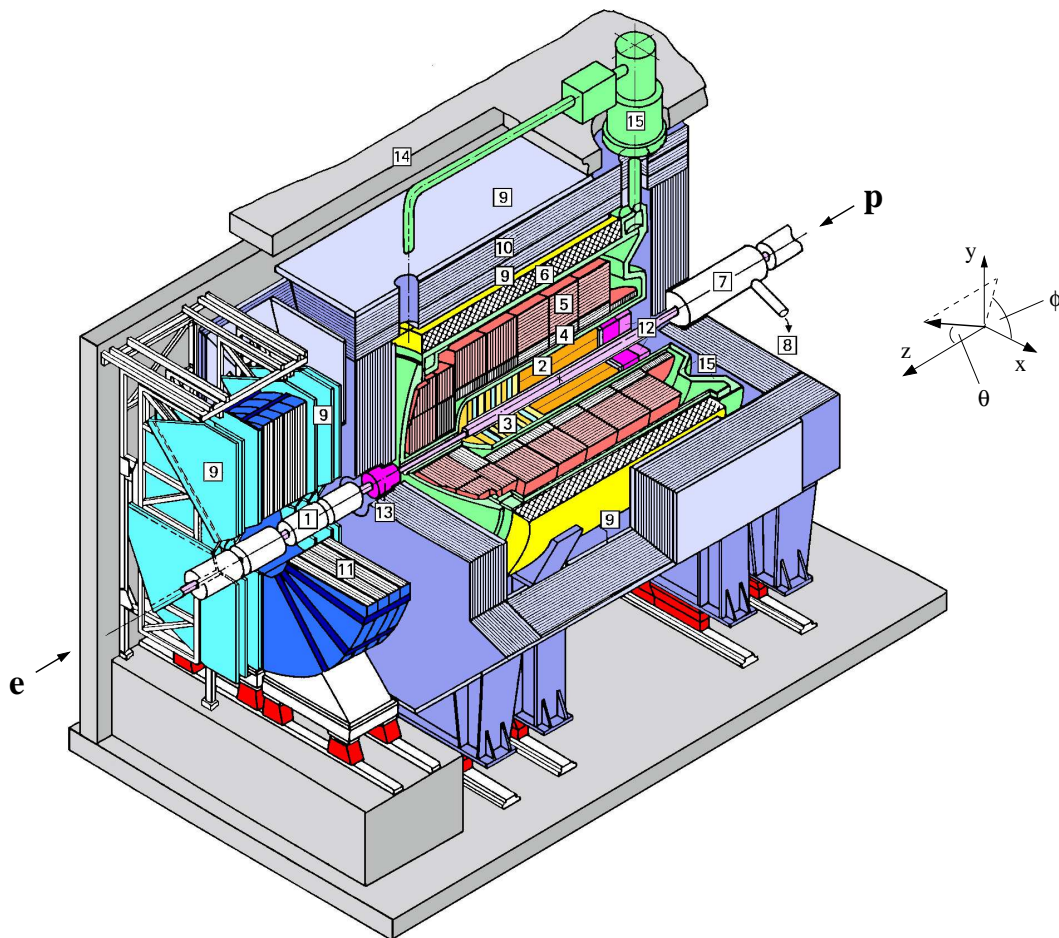
Figure 2.2: *Schematic 3-dimensional view of the H1 detector. References to particular items of this figure are indicated by boxes in the text.*

following only the detector components most relevant for this analysis are discussed after a short overview of the general layout. The numbers given below refer to the labels in figure 2.2.

The interaction region is surrounded by the tracking system of the H1 detector used for the identification and momentum determination of charged particles. The tracking system consists of two separate modules: the forward $\boxed{3}$ and the central $\boxed{2}$ tracking device having a polar angle acceptance[4] of $7° < \theta < 25°$ and $15° < \theta < 165°$, respectively. The central tracking device is shortly referred to as Central Tracker in the following. Its wire chambers are complemented by the Central Silicon Tracker (CST) situated closest to the interaction region. The CST covers the polar angle range $30° < \theta < 150°$ and provides precise information concerning the vertex position allowing to separate vertices from primary interaction products and decay particles. The backward region of the tracking system is equipped with two subdetectors dedicated to the reconstruc-

---

[4]All polar angle acceptances quoted in this chapter refer to $z = 0$, i.e. the nominal z-position of the interaction vertex for standard running conditions of the HERA collider. Note however that for the data taking period analysed in this thesis the interaction vertex has been shifted resulting in a nominal vertex position of approximately $70\,\mathrm{cm}$ (see section 3.1). This causes a shift of the acceptance intervals towards larger polar angles.

tion of the scattered electron, the Backward Silicon Tracker (BST) and the Backward Drift Chamber (BDC).

The trackers are enclosed by a calorimeter system used to measure the energy of the final state particles. The bulk of the acceptance ($4° < \theta < 154°$) is occupied by a liquid argon calorimeter (LAr calorimeter) that is composed of an electromagnetic [4] and a hadronic section [5] and is contained in a cryogenic vessel [15]. The Spaghetti Calorimeter (SpaCal) [12] in the backward region ($153° < \theta < 177.5°$) has been designed for an accurate energy determination of the scattered electron. An additional PLUG calorimeter [13] is installed in the forward direction close to the beam pipe.

All detector components mentioned so far are surrounded by a superconducting solenoid [6] providing a homogeneous magnetic field of $1.16\,$T parallel to the beam axis. It causes the trajectories of charged particles to bend allowing for a measurement of their momenta. Since the solenoid is located outside of the calorimeters the amount of dead material influencing the energy measurement is minimised.

The magnetic field lines are closed by the iron return yoke [10] which is instrumented with streamer tubes. Together with two additional sets of three layers of streamer tubes [9] mounted at its inside and outside the instrumented iron constitutes the central muon detector. Apart from the reconstruction of muon tracks it allows to measure the energy leakage from hadrons not fully contained in the calorimeters. High energetic muons with polar angles $3° < \theta < 17°$ are detected in the forward muon detector consisting of two sets of three double layers of drift chambers [9] at the front and back side of a toroidal magnet [11].

In order to reduce the background caused by interactions of the beam particles with residual gas atoms in the beam pipe or the beam pipe material the H1 detector is equipped with a time-of-flight system [Wis98]. Several combinations of scintillators inside and outside of the main detector provide timing information with high precision allowing to distinguish background and signal events by the definition of narrow time intervals.

The luminosity system is installed in negative z-direction close to the electron beam pipe in the HERA tunnel. It consists of a photon detector and an electron tagger to reconstruct the radiated photon and the scattered electron of Bethe-Heitler events. The data delivered by the individual subdetectors are processed by the trigger and data acquisition systems.

2.3 Tracking Detectors

For the measurement of the polar angle of the scattered electron either the BST or a combination of Central Tracker and BDC is employed. Apart from measuring the position of the interaction vertex the Central Tracker provides information for the reconstruction of the hadronic final state.

Central Tracker

The main components for the track reconstruction in the central region of the H1 detector are the two central jet chambers CJC1 and CJC2 (see figure 2.3). These are
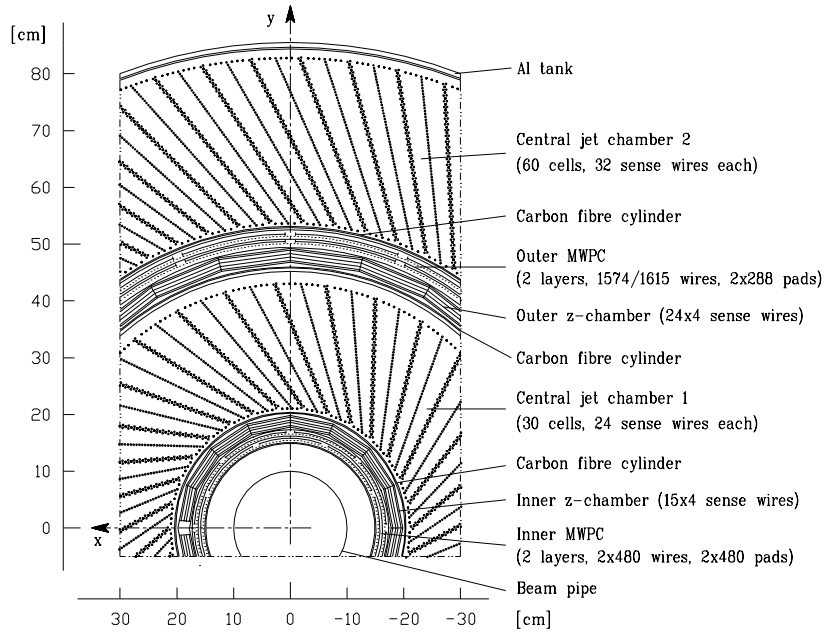
Figure 2.3: *View of the central tracking device in the rφ-plane.*

two concentric drift chambers having an active length of $220\,\mathrm{cm}$ and a radial extension of $20.3\,\mathrm{cm} \leq r \leq 45.1\,\mathrm{cm}$ (CJC1) and $53.0\,\mathrm{cm} \leq r \leq 84.4\,\mathrm{cm}$ (CJC2).

The track reconstruction is based on the ionisation of a gas mixture $(\mathrm{Ar} - \mathrm{CO_2} - \mathrm{CH_4})$ by the charged particles originating from the collision. The free electrons being produced in the course of the ionisation are detected on 2640 signal wires strung parallel to the z-axis and organised in 30 (CJC1) and 60 (CJC2) drift cells, respectively. The drift cells are inclined by about $30°$ w.r.t. the radial direction. This causes the ionisation electrons in the presence of the magnetic field to drift approximately perpendicular to high momentum tracks originating from the beam axis which guarantees an optimal track resolution.

The spatial reconstruction in the $r\phi$-plane is based on the measurement of the drift time of the ionisation electrons. A charge division technique is used to determine the z-coordinate. The 3-dimensional space point corresponding to the information of a single wire is referred to as *hit*. The achieved resolutions for the hit coordinates are $\sigma_{r\phi} = 170\,\mu\mathrm{m}$ and $\sigma_z = 4\,\mathrm{cm}$ [Tlu99], respectively.

In addition to the track reconstruction the central jet chambers provide information for the particle identification by measuring the specific energy loss of charged particles dE/dx with a resolution of $\sigma_{dE/dx}/(dE/dx) \approx 8\%$ [Ste99].

Two thin drift chambers CIZ (central inner z-chamber) and COZ (central outer z-chamber) are attached to the inside and outside of the CJC1, respectively. Their wires are strung in polygonal support structures around the beam axis (see figure 2.3). In z-direction the CIZ (COZ) is separated in 15 (24) rings of $12\,\mathrm{cm}$ ($9\,\mathrm{cm}$) width containing 4 layers of sense wires each. Since the wires are oriented perpendicular to the beam axis the chambers are ideally suited for the reconstruction of the z-coordinate. The corresponding resolution $\sigma_z = 300\,\mu\mathrm{m}$ is significantly better than the one for the central jet chambers. Therefore the signals of the two jet chambers and the two z-chambers are subjected to a combined track reconstruction (see section 3.3). This
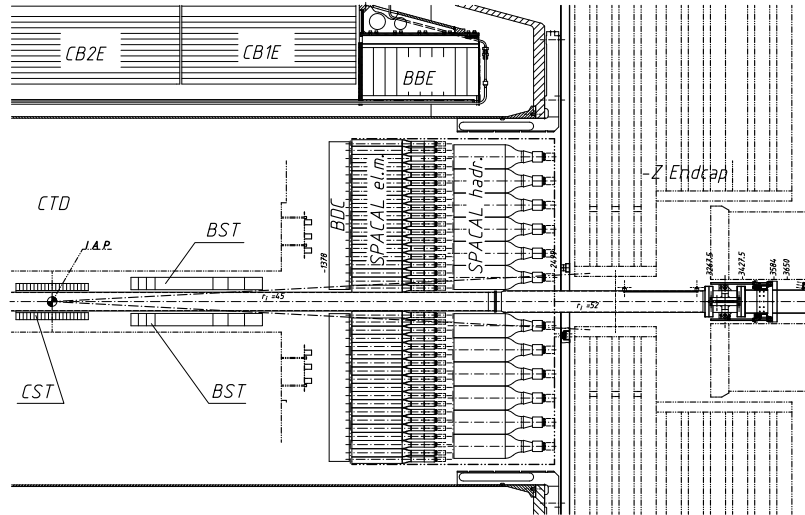
Figure 2.4: *Backward region of the H1 detector in the rz-plane. The nominal interaction point (IAP) is indicated.*

yields a resolution of the z-coordinate of the interaction vertex of $1\,\text{cm}$ [Gla98a] and a momentum resolution $\sigma_p/p = 0.01\,\text{GeV}^{-1}p$.

Furthermore the Central Tracker comprises two multiwire proportional chambers, the CIP (central inner proportional chamber) and the COP (central outer proportional chamber). The CIP is the wire chamber sitting closest to the beam line at an average radial distance of $16.2\,\text{cm}$ covering the polar angle acceptance $9° < \theta < 171°$. Its two layers are equipped with 480 cathode pads each, 60 pads in z-direction and 8 pads in azimuth. They collect the charge induced by crossing charged particles. The layout of the COP is similar to the one of the CIP. It is divided into 18 sectors along the z-axis and 16 sectors in azimuth and detects charged particles in the polar angle range $25° < \theta < 155°$.

Both multiwire proportional chambers deliver a fast timing signal with a resolution better than the time interval of $96\,\text{ns}$ between two successive HERA bunch crossings. These signals are used in combination with the first proportional chamber FPC (Forward Proportional Chamber) of the forward tracking device to select events online based on charged particle trajectories originating from the nominal interaction vertex.

Backward Drift Chamber

The Backward Drift Chamber [Sch96b] has been designed to complement the reconstruction of the scattered electron in the SpaCal (see next section) with track information in order to improve the precision of the polar angle measurement. Figure 2.4 indicates the position of the BDC in the backward region of the H1 detector. It is mounted in front of the SpaCal at $z = -145\,\text{cm}$ having the same polar angle acceptance of $153° < \theta < 177.5°$. Four double layers subdivided into eight octants are the basic construction units of the BDC, i.e. a charged particle can cause up to eight hits on a distance of approximately $7\,\text{cm}$.

In total 2048 wires are strung octagonal in planes perpendicular to the beam line. This implies that the ionisation electrons drift in radial direction and thus the chamber

Figure 2.5: *Part of one BDC double layer in the rz-plane. The numbers indicate the radial distance from the beam line in* mm.
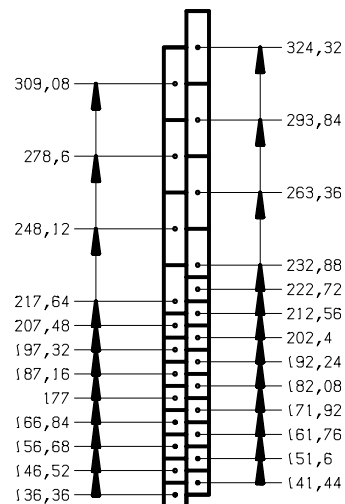
geometry is optimised for an accurate reconstruction of the polar angle θ. The stereo effect of the four double layers which are rotated by $11.25°$ w.r.t. each other is employed for a coarse measurement of the azimuthal angle ϕ. Since the event rate rapidly increases with increasing polar angles drift cells of different size are used in the inner and outer part of the BDC (see figure 2.5) to keep the fraction of overlaying events in the chamber (pile-up) as small as possible. The radial wire spacing is 1 cm for the inner and 3 cm for the outer cells. The intermediate region is covered by a transition cell of 2 cm size which has a special field configuration since the wire position is not centred w.r.t. the cell. From figure 2.5 it can be inferred in addition that that wires in the neighbouring planes of a double layer are shifted by half the cell size in radial direction. This allows to resolve left-right ambiguities of the drift origin. For the reconstruction of the polar angle θ the BDC information is combined with the position of interaction vertex determined by the Central Tracker (see section 3.3). The resulting resolution amounts to 0.57 mrad [Gla98b, Kel98].

Backward Silicon Tracker

The Backward Silicon Tracker measures the polar angle of the scattered electron with high precision and is able to reconstruct the interaction vertex independently of the Central Tracker.

Figure 2.6 a) depicts the BST [Ark00, Eck02] in its configuration of the years 1998-2000. It comprises eight detector planes which are oriented perpendicular to the beam axis and cover the z-interval $-95.6 \,\mathrm{cm} \leq z \leq -35.8 \,\mathrm{cm}$. They are arranged in two groups of four detector planes each. The first group (BST1) was installed in the H1 detector already in 1996, the second group (BST2) has been added in 1998 to enlarge the BST acceptance towards larger values of Q^2.

Each plane is equipped with 16 wedge shaped silicon strip detectors, called *r-sensors*. According to figure 2.6 b) their readout strips are segments of a circle concentric to the beam line. The active material is $280 \,\mu$m thick n-type silicon. About 20000 electron-hole pairs are produced by a single minimal ionising particle scattered in the active volume of a sensor. The wedges overlap in ϕ-direction by 3 mm providing some redundancy for the track reconstruction and a hermetic coverage of the azimuthal angle.
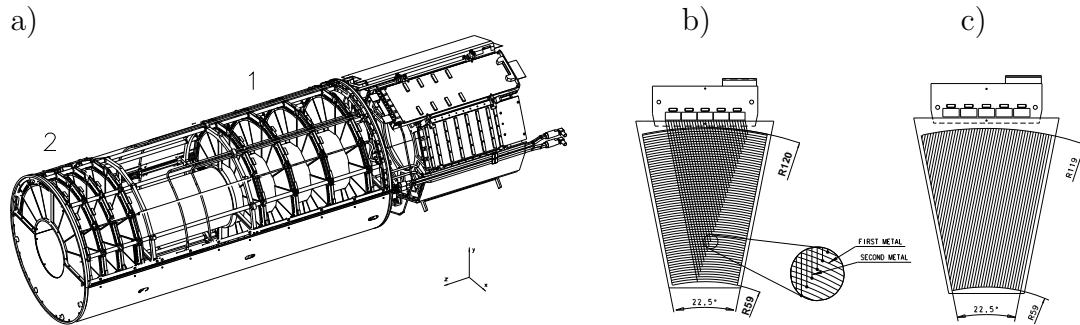
Figure 2.6: a) Layout of the BST in the years 1998-2000. Following the z-axis in positive direction one can distinguish the readout electronics and the two groups of detector planes BST1 and BST2. Each detector plane is equipped with 16 r-sensors b) and one u-sensor c).

They extend in radial direction from 5.9 cm to 12.0 cm allowing to reconstruct charged particles in the polar angle range $164° < \theta < 176°$ with an uncertainty of 0.2 mrad [H1].

One ϕ-sector $(45° < \phi < 67.5°)$ of each wheel is equipped with an additional *u-sensor*. For this sensor type the readout strips are parallel to one of the detector edges. By combining the information of *r*- and *u*-sensors it is possible to measure the transverse momentum and the charge of a track. Both sensor types have 640 readout strips each. In order to minimise the attenuation of the small signals five pre-amplifiers are directly bonded to the readout strips on each sensor.

2.4 Calorimetry

The energy measurement of the H1 experiment is based on the LAr calorimeter in the central and forward region and the SpaCal in the backward region. For the present analysis the former is employed to reconstruct the hadronic final state while the main purpose of the latter is the energy measurement of the scattered electron. In addition the SpaCal provides information for the online event selection.

Spaghetti Calorimeter

The Spaghetti calorimeter covers the polar angle acceptance $153° < \theta < 177.5°$ [App97]. It is a *sampling* calorimeter, i.e. different materials are employed for the absorption and detection of particles. For the SpaCal lead is used as absorber material while the active material are scintillating fibres. The incident particles induce a shower of secondary particles in the lead which cause the fibres to scintillate. The amount of light registered by photomultiplier tubes is a measure for the energy of the primary particles. Special photomultipliers have been chosen capable of operating in the strong magnetic field [Jan94].

As can be seen from figure 2.4 the SpaCal is composed of an electromagnetic and a hadronic section. The electromagnetic part consists of 1192 cells with a dimension of $4.05 \times 4.05 \times 25.5 \, \text{cm}^3$. The smallest construction units of the calorimeter are 2-cell modules, called *sub-modules*. Each of these modules contains 52 layers of lead having 90 grooves instrumented with scintillating fibres. The lead-to-fibre ratio is 2.27 : 1 by
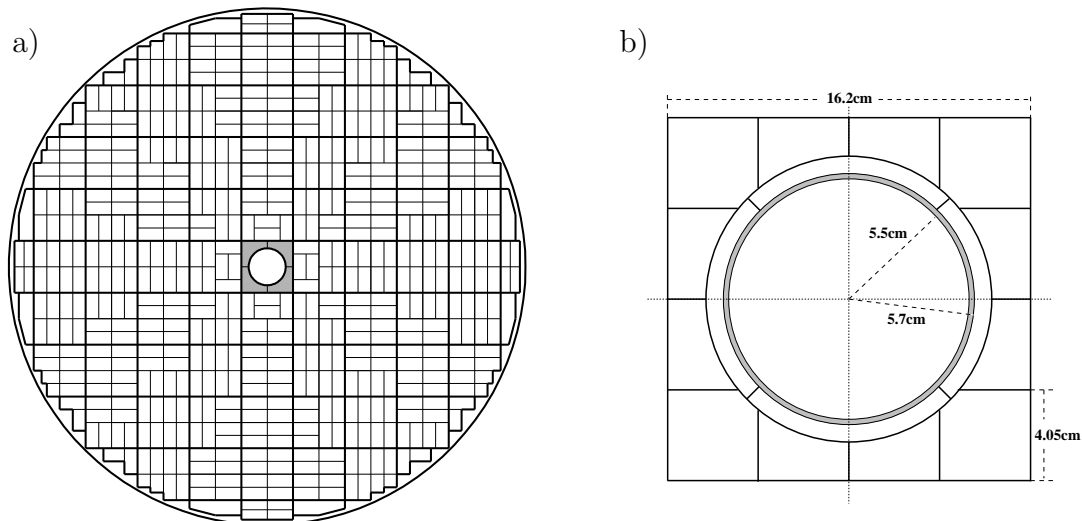
Figure 2.7: *a) Electromagnetic section of the SpaCal calorimeter in the $r\phi$-plane. The thin (thick) solid lines refer to the borders of the sub-modules (super-modules). An magnified view of the highlighted area, the insert module, is depicted in b).*

volume. Sets of eight sub-modules in turn constitute so-called *super-modules* which have a quadratic cross-section and are the main building blocks of the electromagnetic section as shown in figure 2.7 a). The innermost region of the SpaCal (see figure 2.7 b)) is equipped with a special arrangement of cells, called *insert module* [Dir95]. It accounts for the space needed by the beam pipe. The purpose of four inner cells surrounding the beam pipe, called *veto cells*, is to detect energy leakage of neighbouring cells into the beam pipe. A tantalum layer of 2 mm thickness protects the active detector from synchrotron radiation.

The cross-section of the cells is well matched to the Molière radius of 2.55 cm to ensure a good spacial resolution[5] of $\sigma = (6.3 \pm 0.4)\,\mathrm{mm}/\sqrt{E/\mathrm{GeV}} \oplus (1.7 \pm 0.1)\,\mathrm{mm}$ and a reliable electron/hadron separation based on transverse shower profiles. The cell dimension in z-direction of 25.5 cm corresponds to 28 radiation lengths. Test beam measurements have shown that the longitudinal energy leakage is negligible for 30 GeV electrons [Nic96]. In addition the energy resolution of the electromagnetic section has been determined to $(7.1 \pm 0.2)\%/\sqrt{E/\mathrm{GeV}} \oplus (1.0 \pm 0.1)\%$ [Nic96].

Due to the fast response and precise timing information of better than 1 ns reached by the photomultipliers the SpaCal proves to be useful for the online event selection. Apart from suppressing beam induced background events based on the timing information DIS events can be selected by requiring energy depositions above a certain threshold in the calorimeter (see section 2.6).

The hadronic section of the SpaCal consists of 136 cells, each having a dimension of $11.93 \times 11.90 \times 25\,\mathrm{cm}^3$. It adds 1.02 nuclear interaction lengths of material to the electromagnetic section which correspond to 1.0 interaction lengths. Therefore it can only provide a coarse hadronic energy measurement, but it allows to distinguish between electromagnetic and hadronic showers.

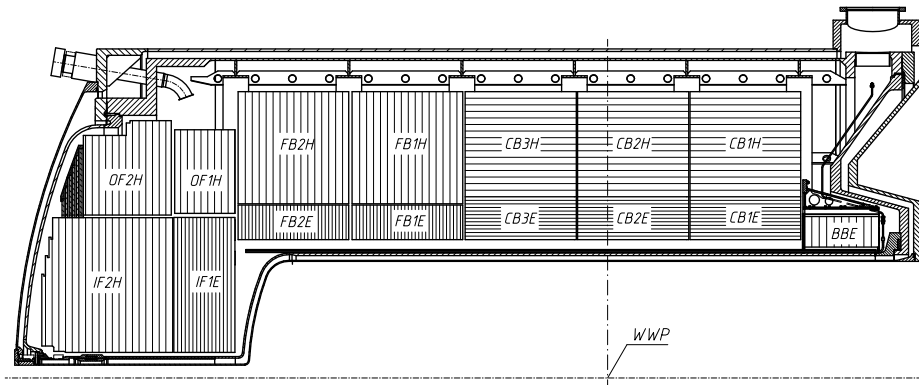[5]$A \oplus B$ is defined as: $A \oplus B \equiv \sqrt{A^2 + B^2}$

Figure 2.8: *View of the LAr calorimeter in the rz-plane with nomenclature for the different wheels: Inner Forward (IF), Outer Forward (OF), Forward Barrel (FB1, FB2), Central Barrel (CB1, CB2, CB3) and Backward Barrel (BBE). The last letter distinguishes electromagnetic (E) and hadronic (H) sections. The nominal interaction point (WWP) is indicated.*

Liquid Argon Calorimeter

The liquid argon calorimeter is responsible for the energy measurement in a large range of the polar angle ($4° < \theta < 154°$). Like the SpaCal it is a sampling calorimeter, but using LAr as active material. Choosing this technique has the advantages of a good stability, a homogeneous response and a fine granularity. The calorimeter is segmented into eight self-supporting wheels in z-direction (see figure 2.8) which are in turn divided into octants in ϕ. Six of the wheels are composed of an electromagnetic and a hadronic section, the BBE has an electromagnetic section only, the OF consists of two hadronic sections.

In the electromagnetic (hadronic) part of the calorimeter lead (steel) plates are used as absorbers. In order to obtain a uniform energy resolution their orientation is chosen such that particles originating from the interaction region cross them with an angle of larger than 45°. The absorption length of the electromagnetic part varies between 20 and 30 radiation lengths in the central and forward direction, respectively. The total amount of absorbing material of the calorimeter sums up to about five to eight nuclear interaction lengths.

The fine granularity of the LAr calorimeter is reflected in a total number of 44532 readout channels. The readout system provides calibrated charges for each readout cell. A first suppression of electronics noise is already performed online by excluding cells from the readout for which the absolute value of the signal after the subtraction of the pedestal does not exceed a certain threshold (for details see section 3.6). The calibrated charges are converted to energies with the help of a complex reconstruction software comprising several steps. Among them the correction for dead material effects, cluster formation as well a several measures to further suppress the noise contribution.

These reconstruction steps provide the correct energy if the incident particle is an electron or a photon. Since the LAr calorimeter is non-compensating the charge output for hadrons is about 30% smaller than for electrons[6]. Hence an additional correction

---

[6]The exact value depends on the incident particle energy.

has to be applied for hadrons to compensate for this deficit. For this purpose special software weighting techniques are employed [Wel94, İşs96]. They rely on the fine segmentation of the LAr calorimeter which allows to identify the electromagnetic components within hadronic showers.

Test beam measurements of calorimeter modules have revealed an energy resolution of $12\%/\sqrt{E/\mathrm{GeV}} \oplus 1\%$ for electrons and $50\%/\sqrt{E/\mathrm{GeV}} \oplus 2\%$ for hadrons [And94, And93].

2.5 Luminosity System

For a collider experiment the *instantaneous luminosity* $\mathcal{L}$ is the factor of proportionality between the observed event rate dN/dt and the cross-section σ for a given process:

$$\frac{dN}{dt} = \mathcal{L}\,\sigma \tag{2.1}$$

The total number of events N is related to the integrated luminosity $L = \int \mathcal{L}dt$ in the same way. Therefore a precise determination of the luminosity is necessary to perform a cross-section measurement based on the observed number of events.

The luminosity is determined via the measurement of the event rate for a process with a precisely known cross-section. H1 utilises the Bethe-Heitler process of small-angle bremsstrahlung $ep \rightarrow e'\gamma p$ for this purpose which has been introduced in section 1.7. Its cross-section is calculable to high precision within QED. Since the angular distributions of the electrons and the radiated photons have a strong peak in the direction of the incoming electron the detectors of the luminosity system have to be placed close to the electron beam line in negative z-direction.

Figure 2.9 shows a typical event in the luminosity system. The main components of the system are two electromagnetic calorimeters: the photon detector (PD) located at $z_{PD} = -102.9\,\mathrm{m}$ and the electron tagger (ET) at $z_{ET} = -33.4\,\mathrm{m}$. Both consist of thallium chloride / thallium bromide crystals serving as Čerenkov counters. The signals in each crystal are registered by a separate photomultiplier.

In total 25 crystals constitute the photon detector corresponding to an active area of $10 \times 10\,\mathrm{cm}^2$ in the xy-plane and a depth of 22 radiation lengths. Photons emitted collinearly with the incoming lepton reach the photon detector by leaving the beam pipe through an exit window at $z = -92.3\,\mathrm{m}$ where the beam pipe bends upwards. The photon detector is shielded from synchrotron radiation by a lead filter (F) of two radiation lengths depth. A water Čerenkov counter (VC) with a depth of one radiation length is used to veto events with photons interacting in the lead absorber to guarantee a precise energy measurement.

The electrons emerging from the bremsstrahlung process have a reduced momentum compared to the beam electrons. Hence they are deflected by the HERA beam magnets and reach the electron tagger after leaving the beam pipe through an exit window at $z = -27.3\,\mathrm{m}$. The electron tagger is assembled of 49 crystals resulting in an active area of $15.4 \times 15.4\,\mathrm{cm}^2$. The tagger acceptance is defined by the field of the magnets and may thus vary significantly if the beam optics changes.

Two methods are used for the luminosity measurement of the H1 experiment [Ahm95, Gog96]: the instantaneous luminosity is determined online by requiring the detection
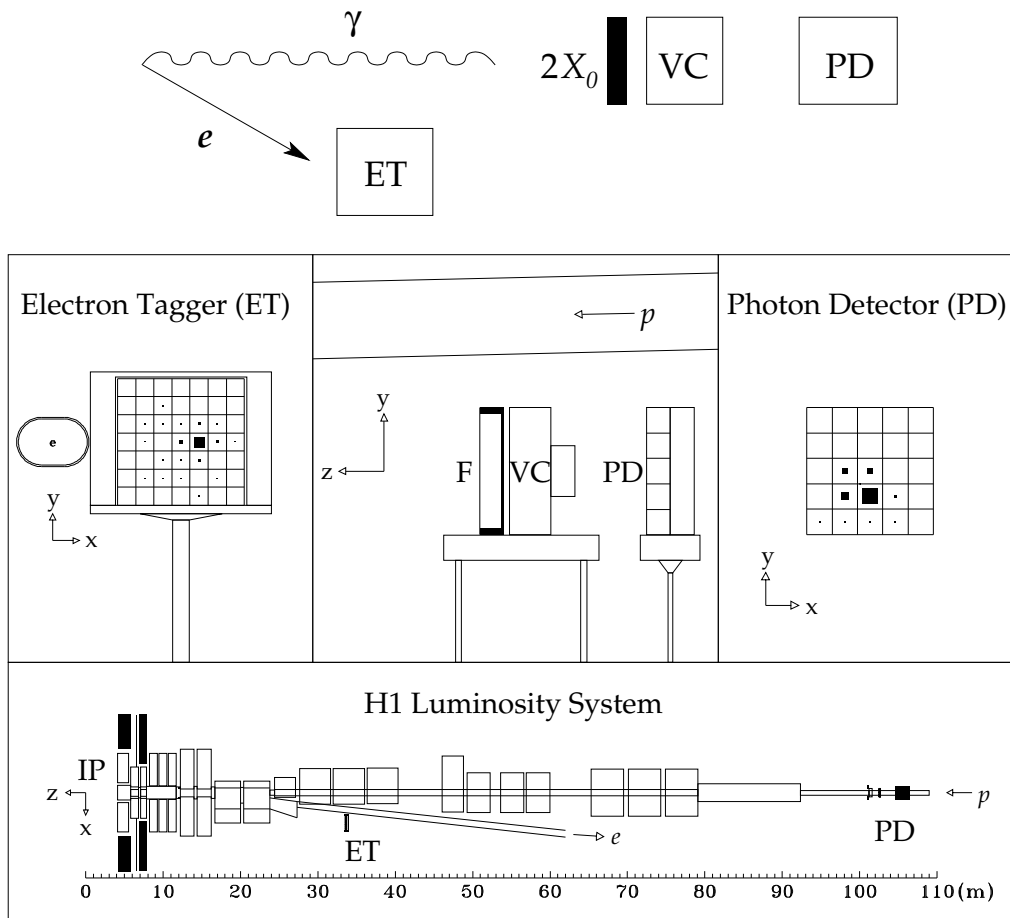
Figure 2.9: *The luminosity system of the H1 experiment. The top part depicts the detection of a Bethe-Heitler event schematically. In addition typical energy depositions in the electron tagger (middle left) and the photon detector (middle right) are shown as well as the positions of both detectors w.r.t. the beam line (middle centre, bottom).*

of both the scattered electron and the radiated photon. This information is used to optimise the beam position during the operation of the HERA accelerator. Since this method utilises the electron tagger the measurement depends strongly on the beam optics. Hence the integrated luminosity used for physics analyses is calculated based on the photon detector information only. This method provides a higher precision, but only after a precise absolute calibration and resolution determination has been performed offline. The main background to the Bethe-Heitler events is caused by interactions of the electrons with residual gas atoms in the beam pipe. Their contribution is estimated with the help of electron pilot bunches, i.e. electron bunches which have no proton partner bunch.

Apart from the luminosity measurement the luminosity system is employed for the identification of photoproduction events (see section 4.9) and initial state radiation events (see section 4.6).
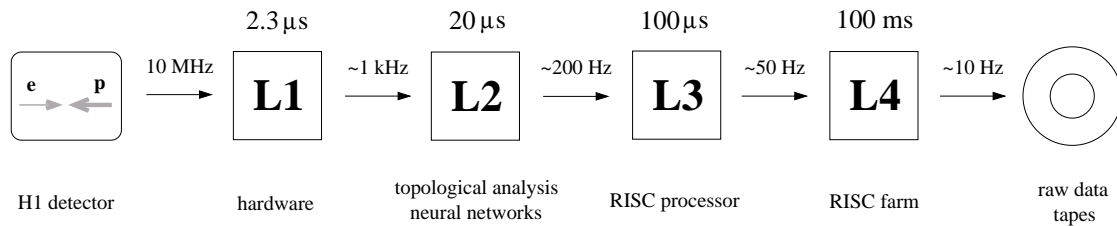
Figure 2.10: *Overview of the H1 trigger system. Decision times and typical input rates are shown at each level.*

2.6 Trigger System

Depending on the beam quality it is possible that the rate at which background events induce a signal in the H1 detector exceeds the one for *ep* interactions by more than a factor of 1000. Apart from synchrotron radiation the main background sources are interactions of the proton or electron beam with residual gas atoms in the beam pipe or atoms of the beam pipe itself. Cosmic muons constitute another important background source.

Rejecting background events while at the same time efficiently selecting *ep* interactions of interest for physics analyses is the task of a trigger system. For the H1 experiment in particular this implies a rate reduction from the bunch crossing rate of $10.4\,\mathrm{MHz}$ to a rate of approximately $10\,\mathrm{Hz}$ at which the data are stored on raw data tapes. This is realised with the help of a multi-level trigger system [Els93]. The decision time increases from level to level while the rate is reduced successively. Figure 2.10 gives an overview.

Basically one has to distinguish between two sets of information: the information that is sent from most of the subdetectors to the trigger system and the data that are finally used for the event reconstruction. While fast availability is of importance for the former, emphasis is placed on precision in the case of the latter. The signal formation in the subdetectors, signal transmission via long cables and processing time on the first trigger level (L1) take significantly longer than the $96\,\mathrm{ns}$ of two consecutive bunch crossings. Hence the subdetector systems feed their data into a ring buffer system in order to keep the first trigger level deadtime free.

Typical criteria to arrive at a trigger decision on L1 are the information of the time-of-flight system, multiplicities and momenta of charged tracks in the drift chambers or localised energy deposition in the calorimeter. They are encoded in Boolean decisions known as trigger elements. Up to 256 trigger elements can be sent from the subsystems to the central trigger where they are combined to 128 subtriggers via logical operations. The L1 decision is taken based on the subtriggers. If one of the subtriggers accepts the event the ring buffers are frozen and the deadtime begins. The latency of L1 is $2.3\,\mu\mathrm{s}$, the rate is reduced to $1\,\mathrm{kHz}$.

The second trigger level (L2) receives all the trigger data from the independent L1 trigger subsystems. They are analysed at a much higher granularity compared to the L1 trigger elements and correlations between them are taken into account. For this purpose two independent systems are available taking a decision within a latency of $20\,\mu\mathrm{s}$ [Nic98]: the topological trigger (L2TT) represents the detector geometry as a 16×16 matrix in the $\theta\phi$-space [Biz92b, Biz92a]. The trigger decision is taken based on

the event topology. For example it is possible to select only events which have at least one energy deposition in the SpaCal outside a predefined radius r (see section 4.3). The second system (L2NN) consists of several neural networks [Köh97, Krä98]. They are trained using previously recorded data samples of background events and events from the physics process of interest. Both systems can send up to 16 L2 trigger elements to the central trigger which are used to validate L1 subtriggers. In the case of a negative trigger decision the ring buffers stopped on L1 are started again and the deadtime ends. If the event is accepted the readout of the ring buffers is started.

The third trigger level (L3) is based on software algorithms implemented on a single RISC[7] processor. In the case of a negative trigger decision the readout is aborted to reduce the deadtime. Due to long decision times this system has not been active during data taking. In the course of the luminosity upgrade the third trigger level has been realised within the Fast Track Trigger project by a modern processor farm [Bai01, Nau02].

The data are transferred to the fourth trigger level (L4). It has the full detector information available and aims for a reduction of the data logging rate and volume. L4 consists of a farm of RISC processors operating asynchronously to the data taking and hence not contributing to the deadtime. Fast algorithms especially designed for the processor farm or parts of the standard offline reconstruction are run at this level. The event processing proceeds in two steps: during the L4 *trigger verification* step the L1 subtrigger decision is checked on the basis of the refined detector information. In the case of a positive verification an event is kept if it fulfils either one of the *hard scales* or if it is recognised by one of the *finders* dedicated to special final state signatures. The hard scale selection aims to identify events in which a hard subprocess is involved. These events are characterised by particles with a high momentum, high energy jets or large values of Q^2. A small fraction of the events rejected by L4 is kept for cross-checks. This technique is referred to as *downscaling*.

The events accepted by L4 are written to raw data tapes with a typical rate of 10 Hz. Finally the raw data are subjected to the full offline event reconstruction.

The input rate of the processor farm on L4 is limited to 50 Hz. This bandwidth has to be divided between the 128 L1 subtriggers. The rate of the various subtriggers differs significantly and also the rate of a single subtrigger changes according to the instantaneous luminosity and background conditions. In order to achieve an optimal distribution of the bandwidth it is therefore possible to downscale each of the 128 individual subtriggers generated at L1 by a pre-settable factor, called *prescale factor*. If a prescale factor d_i is assigned to the subtrigger i only one out of d_i events satisfying the conditions of the subtrigger leads to a positive L1 decision. This is realised by the introduction of *raw* and *actual subtrigger bits*: if an event matches the requirements of the subtrigger i its raw bit is set. But only for one out of d_i events for which the raw bit is set also the actual bit is set. An event is accepted by the first trigger level if the actual bit of at least one of the subtriggers is set.

To react on the changing conditions during data taking in a convenient way an automatic optimisation procedure has been developed and established, known as *auto-prescale* program [SC99]. It analyses the rate of the individual subtriggers, estimates their future trend and calculates an optimal set of prescale factors. The distribution

---

[7]Reduced Instruction Set Computing
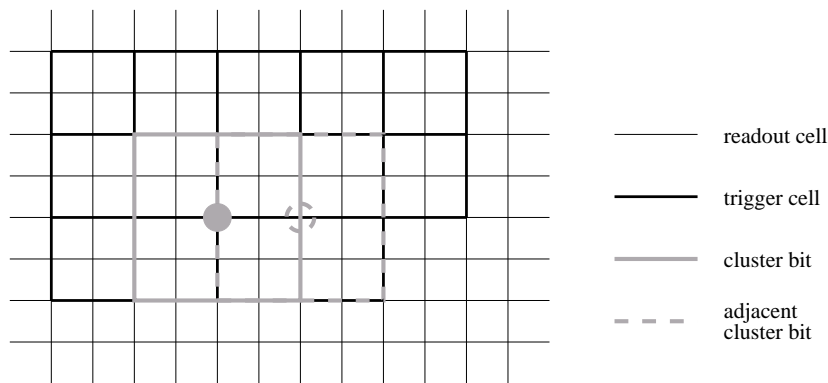
Figure 2.11: *Illustration of the sliding window technique: trigger cells are formed by combinations of four readout cells. Four of these trigger cells are in turn combined to a cluster-bit. To avoid energy losses at the borders of the cluster bits they overlap with each of their neighbours by half the area they cover.*

of the bandwidth can be steered via a complex strategy file.

Inclusive Electron Trigger

Since in the phase space relevant to this analysis the electron is scattered into the acceptance of the SpaCal calorimeter the corresponding trigger subsystem, the inclusive electron trigger (IET), provides the basis for the event selection. It compares local energy depositions in the SpaCal with pre-defined thresholds [Bou95]. All considered subtriggers contain at least one of its trigger elements (see section 4.3). Therefore its operation principle is explained in the following.

For triggering purposes the SpaCal is segmented into groups of 2×2 readout cells, so-called *trigger cells*. The energy attributed to a trigger cells is calculated by summing up the energy depositions in the readout cells belonging to it. Subsequently the energy in 2×2 trigger cells is added. To this combination of trigger cells a *cluster bit* is assigned. The deposited energy attributed to the cluster bit is compared to pre-defined thresholds. To avoid losses at the borders of the cluster bits a sliding window technique is applied: Adjacent cluster bits overlap as depicted in figure 2.11. Their centres of gravity are separated by $8.1\,\text{cm}$, the transverse extension of two readout cells.

Figure 2.12 shows a representation of the SpaCal on trigger level. The information whether an energy threshold is exceeded in a certain cluster bit is encoded in bit patterns. The bits of 4×4 cluster bits are combined with the logical operation OR to a so-called *LIET*[8] *region*. If an energy threshold is exceeded for a cluster bit, the bit of the corresponding LIET region is set. The surface of the SpaCal is covered by 25 LIET regions. The LIET region which contains the intersection with the nominal beam axis is called *central LIET region*.

---

[8]Local Inclusive Electron Trigger

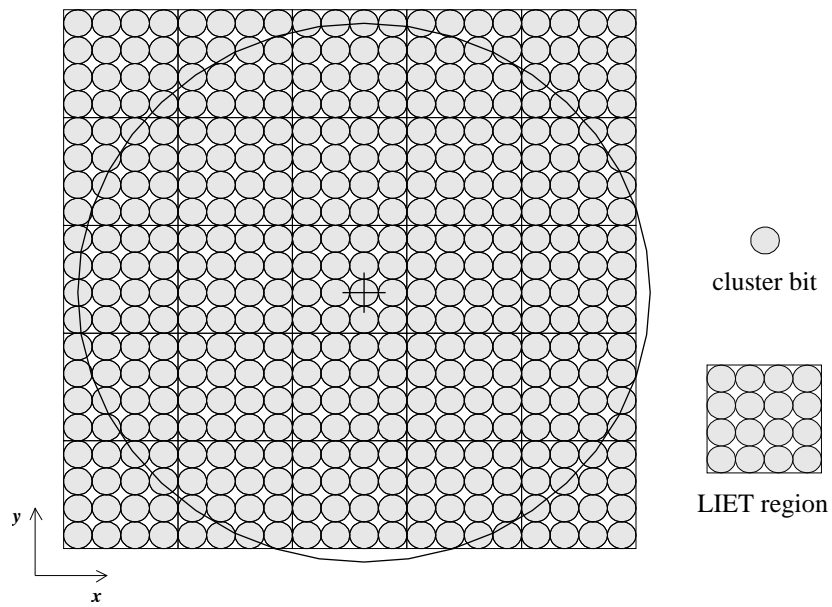Figure 2.12: *Representation of the SpaCal on trigger level. The cross indicates the nominal position of the beam axis..*

3 Basics of the Cross-Section Measurement

The last two chapters have been devoted to the foundations of the theoretical description and experimental observation of deep inelastic scattering. The information of both enters the present chapter which gives a review of the basic concepts of the DIS cross-section measurement. Most of the technical details are explained in the next chapter.

For the present analysis a data sample is employed which has been recorded during a special running period of the HERA collider. To measure the kinematic variables various methods are available utilising the information of different detector components and thus involving several reconstruction algorithms. They are discussed in detail.

In order to model detector acceptances and efficiencies the recorded data are compared to event samples obtained from simulations of the event kinematics and the detector response. The same technique is applied to determine the contribution of background processes mimicking the signature of a DIS event. The underlying Monte Carlo models are introduced.

With these requisites the methods to determine the double differential cross-section and to extract the proton structure function F_2 are presented.

The chapter ends with an overview of the coverage of the kinematic phase space achieved by the present analysis as well as complementary analyses using the same data set.

Emphasis is placed in this chapter on the role of radiative events. Apart from affecting the reconstruction of the event kinematics they allow for a significant extension of the accessible kinematic phase space compared to non-radiative events.

3.1 Data Sample

With the scattered electron being detected in the main detector photon virtualities down to $Q^2 \approx 1.5\,\text{GeV}^2$ can be reached with the H1 experiment for non-radiative events during standard operation conditions of the HERA collider [Aid96, Adl01a]. To access lower values of Q^2 a so-called *shifted vertex run* has been performed during three days in the year 1995. For this special run the interaction vertex has been shifted by 70 cm in the direction of the incoming proton. By this means the acceptance of the existing detector components is extended towards larger polar angles and hence smaller values of the photon virtuality[1]. Values of Q^2 down to $0.35\,\text{GeV}^2$ have been reached in the corresponding analysis [Adl97b].

---

[1] The correlation between the polar angle θ_e of the scattered electron and Q^2 is discussed in section 3.2.

A second data sample with the same special running conditions and approximately the same duration has been collected in August 2000. It constitutes the basis for the present analysis. With an integrated luminosity of approximately $500\,\mathrm{nb}^{-1}$ the statistics of the former shifted vertex run is exceeded by a factor of four corresponding to a reduction of the statistical error by a factor of two.

In figure 3.1 a typical event of this data taking period is depicted: the scattered electron causes a sizeable cluster in the electromagnetic section of the SpaCal as well as hits in the BST and BDC. The hadronic final state occupies the forward region of the H1 detector. Its presence is indicated by energy depositions in the electromagnetic and hadronic part of the LAr calorimeter to which tracks in the Central Tracker can be attributed[2]. In section 3.3 it is explained how the information of the different detector components contributes to the determination of the event kinematics.

As can be seen from the displayed tracks the interaction vertex is sizably shifted in positive z-direction w.r.t. the origin of the H1 coordinate system, i.e. the nominal vertex position for standard running conditions. To illustrate the effect of this shift figure 3.2 compares the region in the xQ^2-plane covered by the SpaCal calorimeter for standard and special running conditions: the two thin solid lines display the upper acceptance limit of the SpaCal calorimeter concerning the polar angle θ_e of the scattered electron for a standard ($177.5°$) and a shifted ($178.3°$) interaction vertex[3]. The dotted line corresponds to a constant energy of the scattered electron of $E_e = 7\,\mathrm{GeV}$ which is the lower energy limit of the analysis (see section 4.6). All events located at larger x than indicated by the line of constant energy and at larger Q^2 than indicated by the lines of constant θ_e can be reconstructed with the help of the SpaCal calorimeter for the corresponding running conditions. Hence the highlighted area shows the region that gets accessible due to the shift of the interaction vertex. The covered phase space is considerably extended towards lower Q^2.

3.2 Determination of the Event Kinematics

A precise measurement of the DIS cross-section requires an accurate reconstruction of the kinematic variables describing the scattering process (see section 1.1). Since the H1 experiment is a collider experiment and the detector covers almost the entire solid angle the most important part of the hadronic final state particles can be detected. Therefore the reconstruction of the event kinematics relies not solely on the scattered electron, i.e. the kinematics is overconstrained and several reconstruction methods are available. This redundancy allows for a flexible choice of the reconstruction method providing the best resolution in each region of the kinematic phase space. Furthermore

---

[2]The tracks in the Forward Tracker pointing to energy depositions in the forward part of the LAr calorimeter have been omitted. They are not considered in the analysis due to general problems with the Forward Tracker reconstruction.

[3]The polar angle values correspond to the geometrical acceptance limit of the SpaCal as given in section 2.4 for the mean z-position of the interaction region. Neither the sizeable spread of the position of the interaction vertex nor the fact that the maximal θ_e reached in the analysis is smaller than the values given are correctly taken into account. Therefore the following considerations are intended to explain the principal effect of a shift of the interaction vertex rather than to give an accurate representation of the kinematic phase space covered by the measurement.
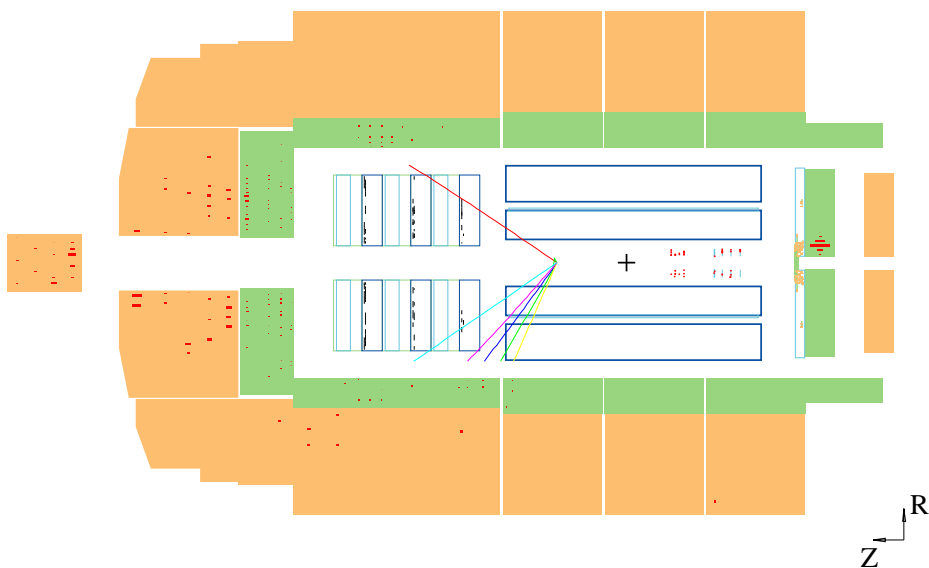
Figure 3.1: *A typical event of the shifted vertex data taking period. Only tracks re-constructed by the Central Tracker are displayed. The cross indicates the origin of the H1 coordinate system. Run and event number are 278977 and 19081, respectively.*
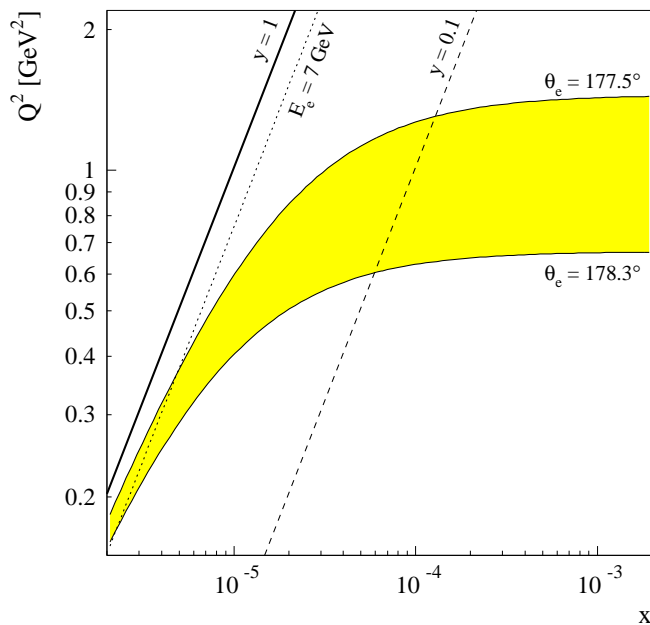
Figure 3.2: *Change of the geometrical acceptance of the SpaCal calorimeter in the xQ^2-plane due to a shift of the interaction vertex in positive z-direction by $70\,\text{cm}$. The thin solid lines depict the acceptance limits for a standard $(177.5°)$ and a shifted $(178.3°)$ interaction vertex. Hence the highlighted area represents the gain in acceptance due to the vertex shift. Lines of constant inelasticity y (dotted) and energy (dashed) of the scattered electron E_e are displayed in addition.*

it allows for an experimental control of the systematic errors of the measurement. The different reconstruction methods are introduced and compared in the following.

In the case of the *electron method* the kinematic variables are expressed in terms of the energy E_e and the polar angle θ_e of the scattered electron:

$$y_e = 1 - \frac{E_e(1 - \cos \theta_e)}{2E_e^0} = 1 - \frac{E_e}{E_e^0} \sin^2 \frac{\theta_e}{2} \tag{3.1}$$

$$Q_e^2 = 2E_e^0 E_e(1 + \cos \theta_e) = \frac{E_e^2 \sin^2 \theta_e}{1 - y_e} \tag{3.2}$$

The variable E_e^0 corresponds to the HERA electron beam energy of 27.6 GeV. To determine the Bjorken variable x one makes use of the relation $x = Q^2/sy$ (see equation 1.4) as for all other reconstruction methods presented in the following.

From the given formulae the following conclusion can be drawn: if the scattered electron is detected in the SpaCal ($\theta_e > 150°$) the inelasticity y is almost solely defined by its energy E_e. The lower the energy the larger values of y are reached. Furthermore the virtuality Q^2 depends predominantly on the polar angle θ_e for low values of y. Large θ_e correspond to small values of Q^2 and vice versa. These dependencies are reflected in figure 3.2: the line of constant energy is parallel to the lines of constant y and the lines of constant θ_e get parallel to the abscissa for low y (high x).

With the scattered electron being identified all other particles are attributed to the hadronic final state. Since it is impossible to build a perfectly hermetic detector particle losses in beam direction are unavoidable. Due to the large energy imbalance between incoming electron and proton the losses along the direction of the incoming proton beam are more important. Variables as insensitive as possible to losses are chosen for the reconstruction of the event kinematics based on the hadronic final state. These are the total transverse momentum

$$p_{t,h} = \sqrt{\left(\sum_i p_{x,i}\right)^2 + \left(\sum_i p_{y,i}\right)^2} \tag{3.3}$$

and the difference of energy and longitudinal momentum

$$\Sigma = \sum_i E_i - p_{z,i} = \sum_i E_i(1 - \cos \theta_i) \tag{3.4}$$

In both equations the summation is performed over all particles of the hadronic final state. The variables E_i, $p_{x,i}$, $p_{y,i}$ and $p_{z,i}$ are the components of the four vector of the hadronic final state particle i. The transverse momentum is rather insensitive to particle losses in the forward and backward direction while Σ is not affected by losses in the forward direction, but is very sensitive to losses in the backward direction. Energy and momentum conservation implies the following relations to hold[4]:

$$p_{t,e} - p_{t,h} = E_e \sin \theta_e - p_{t,h} = 0 \tag{3.5}$$

$$E - p_z \equiv (E_e - p_{z,e}) + \Sigma = E_e(1 - \cos \theta_e) + \Sigma = 2E_e^0 \tag{3.6}$$

---

[4]Neglecting particle masses the longitudinal momentum of the incoming electron and proton is given by $p_{z,p}^0 = E_p^0$ and $p_{z,e}^0 = -E_e^0$, respectively. Furthermore both have only a negligible transverse momentum.

The former conservation rule is employed for the hadronic calibration (see section 4.5), the latter proves to be useful in various aspects, among them the rejection of background processes (see section 3.4).

Finally one defines the so-called *hadron angle*

$$\tan \frac{\theta_h}{2} = \frac{\Sigma}{p_{t,h}} \tag{3.7}$$

which corresponds to the direction of the struck quark in the naive quark parton model.

Using Σ and $p_{t,h}$ the equations 3.1 and 3.2 can be transformed such that the event kinematics is defined based on the hadronic final state only:

$$y_h = \frac{\Sigma}{2E_e^0} \tag{3.8}$$

$$Q_h^2 = \frac{p_{t,h}^2}{1 - y_h} \tag{3.9}$$

This approach to determine the kinematics is denoted as *hadron method* [Jac79]. It is the only method applicable for charged current events as it incorporates no information concerning the scattered lepton.

The energy of the incoming electron E_e^0 enters the calculation of the kinematic variables for both, electron and hadron method (see equations 3.1 and 3.8). It is assumed to be equal to the nominal beam energy of $27.6\,\text{GeV}$. However, for ISR events (see section 1.7) the energy available for the interaction with the proton is lowered due to the photon emission collinear with the incoming electron. Hence both methods fail to reconstruct the kinematics correctly in this case. To overcome this problem E_e^0 is replaced by $(E - p_z)/2$ according to equation 3.6 in the case of the *sigma method* [Bas95b] which makes use of information concerning the scattered electron and the hadronic final state:

$$y_\Sigma = \frac{\Sigma}{\Sigma + E_e(1 - \cos\theta_e)} \tag{3.10}$$

$$Q_\Sigma^2 = \frac{E_e^2 \sin^2\theta_e}{1 - y_\Sigma} \tag{3.11}$$

In this way the energy loss of the incident electron is implicitly corrected for.

A fourth method, the so-called *double angle method* defines the kinematic variables in terms of θ_e and θ_h. It is used for calibration purposes (see section 4.5).

The resolution of the presented methods in different regions of the kinematic phase space has been investigated in detail [Buc91, Bas95b, Gla98a, Var06]. A brief summary of the results follows.

Performing an error propagation for the inelasticity y results in the following equations:

$$\frac{\delta y_e}{y_e} = \frac{1 - y_e}{y_e}\left(\frac{\delta E_e}{E_e} \oplus \frac{\delta\theta_e}{\tan\frac{\theta_e}{2}}\right) \tag{3.12}$$

$$\frac{\delta y_h}{y_h} = \frac{\delta\Sigma}{\Sigma} \tag{3.13}$$

$$\frac{\delta y_\Sigma}{y_\Sigma} = (1 - y_\Sigma)\left(\frac{\delta\Sigma}{\Sigma} \oplus \frac{\delta E_e}{E_e} \oplus \frac{\delta\theta_e}{\tan\frac{\theta_e}{2}}\right) \tag{3.14}$$

At high y the resolution of the electron method is superior to all other methods. Towards lower values of y it degrades as $1/y$. Such a divergence is not present in the case of the hadron and the sigma method. These two methods show the same behaviour at low y since the term $\delta\Sigma/\Sigma$ dominates the resolution of y_Σ. For large values of y the resolution of y_Σ is better than the one of y_h due to the suppression by the factor $(1-y)$. In this region of the phase space the contribution from hadrons to $E - p_z$ becomes comparable to the one of the electron. Thus the fluctuations of the measured hadronic energies partly cancel between numerator and denominator of equation 3.10.

For the present analysis the electron and the sigma method are used. The decision which method to use for a specific region of the kinematic phase space is taken based on the deviation from the reconstructed to the generated variables for a Monte Carlo simulation. As expected the electron method is preferred at high y, the transition to the sigma method takes place at $y \approx 0.1$ (see section 5.1). The corresponding regions in the xQ^2-plane can be inferred from figure 3.2.

3.3 Event Reconstruction

According to the previous section the energy E_e and the polar angle θ_e of the scattered electron as well as the difference of the energy and the longitudinal momentum Σ of the hadronic final state have to be reconstructed to determine the event kinematics with the electron or sigma method.

The energy of the scattered electron is measured with the help of the SpaCal. As the spatial resolution of the BST and BDC is better than the one of the SpaCal (see sections 2.3 and 2.4) either of the two detectors is used for the reconstruction of the polar angle. Due to the worse resolution compared to the BST and the long lever arm for the extrapolation to the interaction region a standalone reconstruction of θ_e is not possible for the BDC. Therefore its hits are combined with the vertex position as determined by the Central Tracker. In both cases the reconstructed position of the scattered electron in the SpaCal is used as a starting point to search for the corresponding hits in the backward tracking detector.

It has to be considered that the identification of the scattered electron is not unambiguous as particles of the hadronic final state can mimic its typical signature (see section 3.4). Therefore the term *electron candidate* is used in the following for the particle most likely being the scattered electron.

For the reconstruction of the hadronic final state energy depositions in the LAr and SpaCal calorimeter as well as tracks in the Central Tracker are considered.

Cluster Reconstruction in the SpaCal

The SpaCal reconstruction starts from the energy depositions in the individual cells of the electromagnetic section. Adjacent cells with an energy deposition above a certain threshold are combined to *clusters* each of them ideally corresponding to a single particle. The cluster algorithm starts from cells showing a local maximum of the energy deposition [Sch96a]. Neighbouring cells are subsequently added to these seeds.

The cluster energy is given by the sum of the energies in the individual cells belonging to it.

As the SpaCal has no segmentation in z-direction apart from the separation in an electromagnetic and a hadronic section only the projection of the shower profile to the surface of the SpaCal can be used for the spatial reconstruction. The centre of gravity $\vec{r}$ of the cluster in the xy-plane is calculated via:

$$\vec{r} = \frac{\sum_i w_i \vec{r}_i}{\sum_i w_i} \qquad (3.15)$$

Both sums contain all cells in the cluster, $\vec{r}_i$ is the position of the centre of cell i with the energy E_i. Different energy dependent weight factors w_i have been considered: linear weighting ($w_i = w_i^{lin} = E_i$) [Dre85], square root weighting ($w_i = \sqrt{E_i}$) and finally a logarithmic weight function [Awe92] given by:

$$w_i = w_i^{log} = \max\left(0, w_0 + \ln\frac{E_i}{\sum_i E_i}\right) \qquad (3.16)$$

For the latter the weights follow the exponential decrease of the deposited energy with the transverse distance from the centre of gravity. The cutoff parameter w_0 effectively excludes cells with an energy below a certain threshold from the calculation of $\vec{r}$. The larger w_0 is the lower energies are considered. Detailed studies in [Pös96] revealed that the best results are obtained with the logarithmic weighting. In addition, the special shape of the cells in the insert module is taken into account for this analysis as proposed in [Dir97].

Electrons produce on average more compact showers than hadrons. Therefore the *cluster radius* which describes the transverse extension of a cluster is a good cluster shape estimator to identify the scattered electron. One distinguishes between the linear cluster radius

$$r_{Cl}^{lin} = \frac{\sum_i w_i^{lin}\sqrt{(\vec{r}_i - \vec{r})^2}}{\sum_i w_i^{lin}} \qquad (3.17)$$

and the logarithmic cluster radius

$$r_{Cl} = \sqrt{\frac{\sum_i w_i^{log}(\vec{r}_i - \vec{r})^2}{\sum_i w_i^{log}}} \qquad (3.18)$$

It has been shown in [Gla98a] that r_{Cl}^{lin} strongly depends on the impact point of the particle. For clusters with a centre of gravity close to the cell edges the reconstruction yields systematically larger radii than for those with a centre of gravity in the middle of the cell. In contrast, the logarithmic cluster radius r_{Cl} is almost independent of the impact point. Therefore the latter is preferred for the analysis. The linear cluster radius is employed for the online event selection on the fourth trigger level (see section 4.3).

With the centre of gravity $\vec{r}$ the x- and y-coordinates of a cluster are known. Since the SpaCal is not segmented in z-direction the z-position of the cluster is derived from a parameterisation [She96]:

$$z_\perp(E_{Cl})\,[\mathrm{cm}] = 0.001956 \cdot E_{Cl}\,[\mathrm{GeV}] + 0.8529 \cdot \ln(2479 \cdot E_{Cl}\,[\mathrm{GeV}]) \qquad (3.19)$$

The variable $z_\perp$ is defined with respect to the SpaCal surface and corresponds to the penetration depth of a particle impinging on the SpaCal rectangular to its surface. It is to first approximation assumed to depend logarithmically on the cluster energy E_{Cl}. From $z_\perp$ the z-coordinate of the cluster in the H1 coordinate system can be easily calculated taking the angle of incidence into account.

Track and Vertex Reconstruction in the Central Tracker

The track reconstruction of the Central Tracker starts from the hits in the Central Jet Chambers [Abt97b]. In the first phase one searches for short track elements, so called track segments, which are combinations of three hits detected by wires belonging to the same angular cell of the CJC (see section 2.3). These are combined to track candidates based on the precise drift time information in the xy-plane. Subsequently the trajectories in the xy-plane are determined by subjecting all hits belonging to a track candidate to a circle fit[5] based on a non-iterative algorithm [Kar91]. Among the free parameters of the fit is the azimuthal angle ϕ at the closest distance of the track to the z-axis in the xy-plane. In the Sz-space, S being the path length in the xy-plane, tracks are straight lines. Thus after the circle fit in the xy-plane a linear fit in the Sz-space is performed allowing to determine the polar angle θ.

For a fixed z-coordinate the position of the interaction vertex in the xy-plane varies by only a few hundred μm for a sequence of runs[6]. Therefore tracks fulfilling certain quality criteria are used during the online reconstruction on the fourth trigger level to determine the mean vertex coordinates $\overline{x_{vtx}}$ and $\overline{y_{vtx}}$ as a function of the z-coordinate z_{vtx} [Kle06].

The average position $(\overline{x_{vtx}}, \overline{y_{vtx}})$ at $z_{vtx} = 0$ is used as a constraint to improve the parameters of tracks compatible with this vertex during the next step of the offline track reconstruction[7]. At this stage corrections for multiple scattering in the detector material and the non-uniformity of the magnetic field are applied. For all tracks assigned to the vertex in the xy-plane a common fit in the Sz-space is performed to determine an initial approximation of the z-position of the vertex and the polar angles. Knowing the actual z-position the procedure is repeated using the corresponding values of $\overline{x_{vtx}}$ and $\overline{y_{vtx}}$ [Kle06].

As the z-information of the Central Jet Chambers is not very precise the resolution of the polar angle and the z-position of the vertex can be significantly improved using the signals of the two drift chambers CIZ and COZ (see section 2.3). In the presence of noise and inefficiencies a stand alone track reconstruction in the z-chambers is rather ineffective given the relatively small number of sense wires planes. Hence the individual hits in CIZ and COZ are linked to the tracks reconstructed in the Central Jet Chambers and new track and vertex parameters are determined. The assignment of hits and tracks and the track-vertex fit are parts of a combined procedure. A simple combinatorial approach for the linking would be very time consuming. Therefore a special technique, known as the *Method of Deformable Templates* is used for this purpose [Ohl92]. A detailed description of its application for the described task can be found in appendix B of [Gla98a]. In the following the basic concept is shortly reviewed as the same technique is applied for the track reconstruction in the BDC and BST.

Since tracks are straight lines in the Sz-space the parameterisation

$$z(S) = a \cdot S + z_0 \tag{3.20}$$

---

[5]In the magnetic field of the H1 detector tracks form helices. Thus their projections in the xy-plane are circles. Small deviations from the ideal helix shape occur due to multiple scattering in the detector material, energy losses due to dE/dx and non-uniformities of the magnetic field.

[6]This holds only for a fixed z-position as the beams are inclined with respect to the z-axis of the H1 coordinate system (see section 3.6).

[7]During the online track reconstruction the corresponding parameters of the previous run are used.

is used to fit the hits in the z-chambers, a denoting the slope of the track and z_0 its z-coordinate at $S = 0$. Hence the problem of simultaneously fitting all z-chamber hits can be formulated as the minimisation of the following functional:

$$\mathcal{L}(a_j, z_0) = \sum_{k,i,j} W_{ij}^k (z_{ij}^k - S_{ij}^k \cdot a_j - z_0) \tag{3.21}$$

The sum extends over all wire planes of the z-chambers (k), z-points (i) and CJC tracks (j). The number of z-points equals two times the number of hits in CIZ and COZ. Each hit is considered twice as one cannot distinguish on which side of a wire a particle has passed the corresponding drift cell. This *left-right ambiguity* has to be resolved. Furthermore z_{ij}^k and S_{ij}^k refer to the z-coordinate of the z-point and the path length to reach it, respectively. The track parameters to be determined are a_j and z_0. For simplicity is assumed that all tracks stem from the same vertex[8].

The assignment of CJC tracks and z-points is governed by the matrices W^k, one for each wire plane k. The matrix elements W_{ij}^k can take values of 0 or 1. A value of 1 indicates that track j and z-point i of wire plane k are assigned to each other, if not the value is 0. If a z-point belongs to no CJC track it is most likely caused by chamber noise, if a track in the acceptance of the z-chambers has no corresponding z-point in a wire plane this is a sign of an inefficiency.

For a given set of weights W_{ij}^k the track parameters a_j and z_0 are determined by solving the system of linear equations belonging to the minimisation of the functional $\mathcal{L}$. As already mentioned, a combinatorial search to determine the optimal set of matrices W_{ij}^k is extremely time consuming. Therefore the given functional is modified according to the Method of Deformable Templates [Ohl92]. This implies that weights W_{ij}^k acquire a dependence on an additional parameter, the temperature T. The combinatorial search among the possible W_{ij}^k is replaced by an iterative minimisation of the new functional gradually decreasing the temperature to 0. For finite temperatures the weights W_{ij}^k are real numbers between 0 and 1. They can be interpreted as the probability that the z-point i belongs to the track j. At $T = 0$ the new weights coincide with the old ones.

One expects the z-points to have a Gaussian distribution around the particle trajectory with a width defined by the resolution $\sigma_{CIZ/COZ}$ of the z-chambers. Accordingly, one assumes the following dependence of the weights on the distance D_{ij}^k of the z-points to the tracks[9]:

$$W_{ij}^k \sim \exp\left(-\frac{(D_{ij}^k)^2}{T\sigma_{CIZ/COZ}^2}\right) \tag{3.22}$$

With decreasing temperature the weights get smaller for a given distance D_{ij}^k, i.e. the corridor around a track from which z-points are assigned to the track gets smaller. Initially the tracks are defined by the Central Jet Chambers only, i.e. the initial temperature T_{ini} should satisfy the condition

$$T_{ini} \approx \left(\frac{\sigma_{z,CJC}}{\sigma_{CIZ/COZ}}\right)^2 \tag{3.23}$$

---

[8]This simplification is only used for the explanation. The real implementation handles secondary vertices correctly as well.

[9]The quoted formula shows the basic dependence of the weights on the distance D_{ij}^k and the temperature T. The precise expression for W_{ij}^k is significantly more complicated to meet the boundary condition that the new weights coincide with the old ones for $T = 0$.

where $\sigma_{z,CJC}$ corresponds to the z-resolution of the Central Jet Chambers.

The weights depend on the distances of the z-points to the tracks and therefore on the track parameters. This leads to a highly non-linear functional $\mathcal{L}$. Therefore a two step minimisation procedure is used for a fixed temperature: at first, given the track parameters from the previous temperature, the weights W_{ij}^k are calculated. Secondly, knowing the weights, new track parameters a_j and z_0 are calculated by solving the system of linear equations implied by minimising $\mathcal{L}$. If the changes of W_{ij}^k, a_j and z_0 exceed certain maximal values the procedure is repeated. Otherwise one continues with a smaller temperature.

For typical background conditions in total 20 iterations[10] are needed for all considered temperatures to perform the link of CJC tracks and z-chamber hits. By this procedure the resolution of the z-coordinate of the vertex is improved by a factor of 10 from about $1\,\mathrm{cm}$ to about $0.1\,\mathrm{cm}$ [Gla98a].

Track Reconstruction in the BDC

To measure the polar angle of the scattered electron with the BDC SpaCal clusters and BDC information have to be combined. Two algorithms to do so are discussed in the following.

The first analyses making use of the BDC [Kat97, Mey97] have started from standalone SpaCal, vertex and BDC reconstructions. The former proceed as described above, for the latter BDC hits are combined to track candidates based on a so-called Kalman-Filter [Sch96b, Bil89]. It turns out that in a single event a large number of BDC tracks is reconstructed close to the cluster of the scattered electron [Kat97]. Only in about 40% of the events less than five BDC tracks are reconstructed within a cylinder of $3\,\mathrm{cm}$, up to 100 tracks are possible. Two effects are responsible for this: for a large fraction of events (60-70%) the scattered electron interacts with the dead material situated between the interaction point and the BDC causing a shower of secondary particles. Secondly, the BDC provides little redundancy to resolve drift direction ambiguities of the hit positions since its eight layers cover a distance on only $6.8\,\mathrm{cm}$ in z-direction. The large number of tracks in the vicinity of the SpaCal cluster makes the selection of the corresponding BDC track difficult. In [Kat97] a generalised χ^2 selection criterion has been introduced. Among the five tracks with the minimal χ^2 the one with the least distance to the SpaCal cluster centre of gravity is selected.

In 1998 a new algorithm (BDCLEV[11]) has been developed to improve the resolution of the polar angle [Gla98b]. This uses the line connecting the Central Tracker vertex and the SpaCal cluster as an initial approximation for the corresponding track. The azimuthal angle ϕ_{Spa} derived from the SpaCal cluster is used to select the octants of the BDC of which hits are considered for the track reconstruction[12]. In addition ϕ_{Spa} is employed to transform the radial information derived from the BDC drift time into a hit position in the xy-plane. This is beneficial as the resolution of ϕ_{Spa} is better than the resolution of the azimuthal angle derived from the stereo information of the BDC.

---

[10]Each iteration comprises one calculation of weights and one minimisation of $\mathcal{L}$.

[11]BDC LEpton Validator

[12]Depending on the distance of the cluster to the octant border, one or two octants are selected in each layer.

Hit selection and track fit are performed in a global minimisation procedure similar to the linking of CJC tracks and z-chamber hits. For the track fit a straight line in the rz-plane is used combining the Central Tracker vertex, the centre of gravity of the SpaCal cluster and all BDC hits (with a twofold drift direction ambiguity). Initially the width Δr of the corridor around the track from which hits are assigned to the track is $5\,\mathrm{cm}$ driven by the spatial resolution of the SpaCal. It is gradually decreased to approximately $5\sigma_{r,BDC}$, with $\sigma_{r,BDC} = 300\,\mu\mathrm{m}$ [Gla06] being the resolution of the BDC for the measurement of the r-coordinate.

For a given SpaCal cluster BDC hits are assigned to a single track only such that combinatorics is much reduced compared to the linking of CJC tracks and z-chamber hits. If more than one electromagnetic SpaCal cluster exists the algorithm is run for each cluster separately.

The conceptual difference between the old and new track reconstruction is that the assignment of the BDC information to the SpaCal and Central Tracker information is done on track level for the former method while on hit level for the latter. This implies that the imprecise SpaCal information influences the track selection in case many tracks are present for the old algorithm. For the new algorithm the SpaCal reconstruction provides the initial approximation while the resolution at the final stage is defined by the BDC. This results in a significantly better performance of the new track reconstruction: the resolution of the polar angle improves from $\sigma_{\theta,BDC} = 0.77\,\mathrm{mrad}$ to $\sigma_{\theta,BDC} = 0.57\,\mathrm{mrad}$ with a simultaneous decrease of the number of outliers [Gla98b].

Track Reconstruction in the BST

To reconstruct the scattered electron with the help of the BST a special track finding algorithm has been developed in [Ark00], thereafter called *BST electron finder*. It provides apart from the polar angle also the z-coordinate of the interaction vertex.

The BST electron finder can be operated in two modes (see appendix A of [Ark00]): the first one makes use of the Central tracker vertex. A corridor around the connecting line between SpaCal cluster and Central Tracker vertex is used for an initial hit selection. The hits closest to the prediction in each plane are subjected to a straight line fit in the rz-plane. The resulting parameters are used to define a more narrow corridor for a second iteration of hit selection and track fit. The alternative operating mode is completely independent of the Central Tracker vertex. The track finding proceeds via successively attributing hits to track candidates based on the position of the SpaCal cluster. The assignment starts from the BST plane closest to the SpaCal. If more than one track candidate is found the one with the maximum number of assigned hits is chosen. Finally, a straight line fit is performed as for the first operating mode.

For the first analysis making use of the BST to measure the DIS cross-section the approach independent of the Central Tracker vertex has been chosen [Ark00]. In [Eck02] and [Laš04b], however, the Central Tracker information is employed if existing. If no Central Tracker vertex exists different hypotheses concerning the z-position are tested.

For both operation modes it turned out that the BST electron finder is rather sensitive to hits caused by electronics noise or secondary particles. This is especially problematic for the shifted vertex period as the flatter electron track leads to larger showering effects compared to standard running conditions of the HERA collider [Laš04a].

The average number of BST hits for the shifted vertex run is approximately 80 while for the minimum bias run in 1999[13] on average only 20 hits are recorded per event [Pet06].

For this reason an improved version of the BST electron finder has been developed [H1]: it starts from the azimuthal angle ϕ_{Spa} of the SpaCal cluster to select three sectors of r-sensors in each BST plane to provide hit candidates for the track fit. Afterwards a small eccentricity correction is applied for the hits to account for the BST not being centred w.r.t. the beam axis. Subsequently the r-coordinate of each hit is projected along the line connecting the hit and the SpaCal cluster to the BST plane closest to the SpaCal and filled into a histogram. The maximum of this histogram is assumed to indicate the group of hits belonging to the SpaCal cluster. Therefore the straight line between the maximum of the histogram and the centre of gravity of the cluster is used as an initial approximation for the track finding. Hit assignment and track fit proceed in exactly the same way as in the case of BDCLEV. The initial width $\Delta r = 1.5$ cm of the corridor is again defined by the SpaCal resolution and stepwise decreased to $\Delta r = 5\sigma_{r,BST}$ where $\sigma_{r,BST} = 50\,\mu$m denotes the resolution of the BST for the measurement of the r-coordinate.

Electron Identification

From the discussion in section 3.2 it can be inferred that a correct identification of the scattered electron is essential to reconstruct the event kinematics since without this also the hadronic final state is not-well defined. As explained above the clusters in the backward calorimeter constitute the starting point for the reconstruction of the scattered electron. For inelasticities $y \gtrsim 0.1$ also hadrons deposit energy in the SpaCal as the hadron angle θ_h enters its acceptance[14] (see figure 3.3). Since these energy depositions can mimic the signature of the scattered electron (see section 3.4) its identification is not unambiguous in this region of the kinematic phase space.

The situation improves if one restricts the search for the electron candidate to those clusters having the properties of an electromagnetic cluster produced by a charged particle. This involves several selection criteria (see table 4.10) including the link to a BDC or BST track. Nevertheless a significant fraction of events remains with more than one cluster passing all the selection criteria. Therefore an additional requirement has to be found.

If the inelasticity satisfies $y < 0.5$ the polar angle θ_e of the scattered electron is always larger than the polar angle θ_h of the current jet (see figure 3.3). The same holds for the energies. Hence the electromagnetic SpaCal cluster with the largest energy can be identified with the scattered electron. The situation is opposite for $y > 0.5$. Nevertheless the maximum cluster energy remains a reliable criterion since backward going hadronic jets are typically broad causing several clusters. Hence the cluster of the scattered electron is likely to remain the one with the highest energy.

The present analysis considers the SpaCal cluster with the highest energy passing all selection criteria to be the electron candidate.

For a cross-check the cluster with the largest transverse momentum is used. This criterion is based on the transverse momentum conservation in the event (see equa-

---

[13]For this data taking period the average z-vertex position is close to $z \approx 0$ cm.

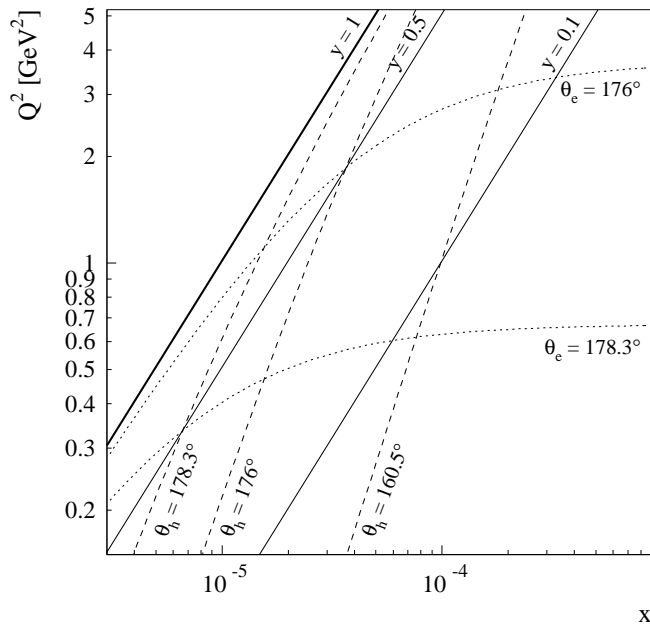[14]The polar angle acceptance of the SpaCal for the shifted vertex period is $160.5° < \theta_e < 178.3°$.

Figure 3.3: *Lines of constant inelasticity y (solid), polar angle of the scattered electron* θ_e *(dotted) and hadron angle* θ_h *(dashed) in the* xQ^2*-plane.*

tion 3.5). The transverse momentum of the scattered electron is balanced by the sum of the transverse momenta of the hadronic final state particles. Hence the particle with the largest transverse momentum is in most of the cases the scattered electron. The resulting DIS cross-sections for the two identification strategies agree well within 0.5%, differences being only visible at large inelasticities. This has been checked individually for using the BST and the BDC to reconstruct the polar angle of the scattered electron.

A detailed investigation of the electron identification in the backward region of the H1 detector can be found in [Gla98a].

Reconstruction of the Hadronic Final State

All particles apart from the electron candidate are attributed to the hadronic final state. The most important detector component for its reconstruction is the LAr calorimeter. The hadronic energy resolution $\sigma_E/E = 50\%/\sqrt{E/\text{GeV}} \oplus 2\%$ (see section 2.4) of the LAr deteriorates with decreasing energy. In contrast, the momentum and thus energy resolution of the central tracking system improves with decreasing momentum: $\sigma_p/p = 0.01\,\text{GeV}^{-1}p$ [Abt97b]. Hence the reconstruction of low energetic particles can be improved by combining the calorimeter information with Central Tracker tracks.

A special algorithm (FSCOMB) has been developed for this purpose [Bas95a, Adl97a]: each track with a momentum $p < 10\,\text{GeV}$ fulfilling certain quality criteria is extrapolated to the surface of the LAr. Subsequently one searches for energy depositions in a cylinder with a radius of 20 cm (40 cm) around the axis defined by the track direction in the electromagnetic (hadronic) section. If the summed energy within these cylinders exceeds the track momentum, the calorimetric information is used for measurement. Otherwise the track information is employed and the corresponding energy in the LAr is masked to avoid double counting, i.e. it is not taken into account for the reconstruc-

tion of the hadronic final state. If a track does not reach the calorimeter surface it is also considered.

Apart from the LAr and the Central Tracker also the hadronic energy measured in the SpaCal enters the reconstruction of the hadronic final state. It comprises all energy depositions in the electromagnetic and hadronic section apart from the ones assigned to the electron candidate. The SpaCal should contribute only at high y where the hadronic final state occupies the backward region of the detector. However, a detailed study in [Gla98a] has shown that its contribution is sizeable even at very low values of the inelasticity. This effect is caused by secondary clusters induced by the scattered electron which are wrongly identified as hadronic final state particles. Secondary clusters can be invoked by the scattered electron due to bremsstrahlung or showering in the material between interaction point and SpaCal. To correct for this effect 10% of the energy of the electron candidate is subtracted from the total hadronic energy measured in the SpaCal. If the resulting energy is negative the contribution of the SpaCal is assumed to be equal to zero.

For the reconstruction of the event kinematics with the sigma method the difference of the energy and longitudinal momentum Σ of the hadronic final state has to be calculated. It has already been mentioned in section 3.2 that it is insensitive to losses in the forward, but very sensitive to losses in the backward region of the H1 detector. The same holds for additional energy depositions in the calorimeters not attributed to the genuine hadronic final state, called 'noise' in the following. It leads to a systematic bias of the event kinematics at low values of y where hadrons are produced in the forward direction and little energy is deposited in the calorimeters.

In events recorded with a random trigger[15] about 1000 of the 45000 cells of the LAr calorimeter pass a $+2\sigma_{noise}$ noise threshold[16] on average [Abt97b]. Adding up this energy for the whole calorimeter yields an average value of 48 GeV. Apart from pure electronics noise energy depositions due to beam-induced secondary particles contribute. For ep events additional energy depositions can be caused by final state particles reaching the calorimeter via secondary scattering, e.g. due to interactions with the beam pipe wall.

Various measures are taken during data acquisition and reconstruction to remove the noise. On top of this FSCOMB performs a topological noise suppression: LAr cells with an energy below 0.4 GeV (0.8 GeV) and separated from other cells by more than 40 cm (20 cm) in the central (forward) region of the LAr calorimeter are classified as noise and excluded from the reconstruction of the event kinematics. This procedure does sometimes exclude isolated clusters from the genuine hadronic final state.

A detailed investigation of the reconstruction of the hadronic final state including the influence of noise can be found in [Var06]. In section 3.6 the incorporation of the noise into the simulation of the detector response is discussed.

---

[15]Among the selected events there should be nearly no ep interactions.

[16]The energy of a LAr cell corresponding to $1\sigma_{noise}$ varies between 15 MeV and 30 MeV depending on the calorimeter region [Abt97b].

3.4 Background Processes

A number of reactions can imitate ep interactions in the Q^2 regime of interest and thus lead to a wrong determination of the DIS cross-section. Two classes of background processes can be distinguished:

The term *non-ep interactions* is used to summarise background events induced by non-colliding beam particles, cosmic muons or beam halo muons. Their contribution can be suppressed by appropriate selection criteria up to a negligible amount.

The only significant remaining background source are so-called *photoproduction* events in which the scattered electron escapes the main detector along the beam pipe and the electron signal is mimicked by a particle of the hadronic final state.

Both classes of processes are discussed in the following.

Non-ep Background

Despite the good vacuum in the beam pipe, interactions of the beam particles with the residual gas molecules or the beam pipe material create a large background to the ep interactions. Most of them are already rejected during data taking by requirements concerning the timing and energy depositions in the SpaCal imposed by the trigger system (see section 4.3). A further reduction of the background rate is achieved by the selection criteria of the final analysis, first of all by the cut on the z-position of the interaction vertex (see section 4.6). The same holds for background events caused by cosmic or beam halo muons.

The remaining non-ep background is estimated making use of special non-colliding, i.e. unpaired particle bunches: proton (electron) *pilot bunches* have an empty electron (proton) partner bunch. Thus they can interact with residual gas molecules or beam line elements only. In the case of *empty bunches* electron and proton bunch carry almost no current. During the time when these bunches cross in the H1 detector signals can be only caused by random background processes such as cosmic or beam halo muons.

One determines the number of events passing all selection criteria (see section 4.6) for p-pilot ($N_{p-pilot}$), e-pilot ($N_{e-pilot}$) and empty bunches (N_{empty}) in a special study. They are used to estimate the residual amount of background events N_{non-ep} among the number of events N_{coll} passing all selection criteria for the colliding bunches, i.e. among the total number of events for the cross-section determination. To account for the different number of colliding (n_{coll}) and unpaired ($n_{p-pilot}$, $n_{e-pilot}$, n_{empty}) bunches the contributions of the different types of unpaired bunches have to be normalised in the following way:

$$N_{non-ep} = \frac{n_{coll}}{n_{p-pilot}}N_{p-pilot} + \frac{n_{coll}}{n_{e-pilot}}N_{e-pilot} + \frac{n_{coll}}{n_{empty}}N_{empty} \qquad (3.24)$$

The assumption behind this way of normalising is that all filled bunches carry almost the same current. Knowing N_{non-ep} the fraction f_{non-ep} of non-ep events in the analysis sample used for the cross-section measurement can be calculated:

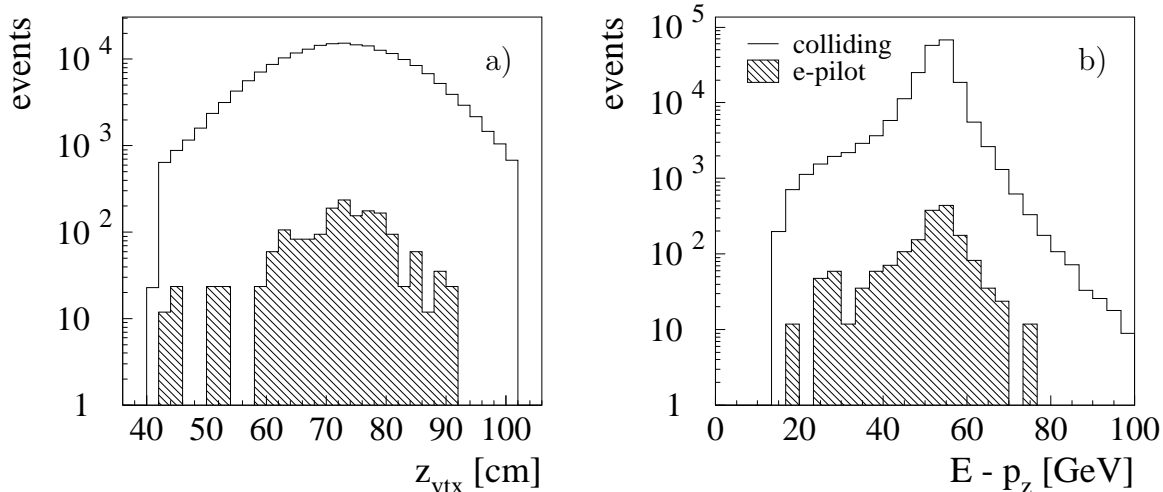$$f_{non-ep} = \frac{N_{non-ep}}{N_{coll}} \qquad (3.25)$$

Figure 3.4: *Number of events for colliding and electron pilot bunches passing all se-
lection criteria of the final cross-section analysis as a function of a) z_{vtx}
and b) $E - p_z$. The distributions of the electron pilot bunches have been
renormalised to account for the different number of colliding and electron
pilot bunches according to equation 3.24.*

Not a single event passes the event selection for the p-pilot and empty bunches
regardless whether the BST or the BDC is used for the polar angle reconstruction of
the scattered electron[17]. Only events from the e-pilot bunches significantly contribute.
This is expected since e-pilot bunches should indicate background events induced by
the electron beam. Particles originating from such events may reach the SpaCal at
the same time as particles from ep interactions. Hence they are not rejected by timing
requirements based on the SpaCal like p-pilot or empty bunch events.

Figure 3.4 shows the estimated contribution of non-ep background to the number of
events in the colliding bunches determined according to equation 3.24[18] as a function of
the z-position of the interaction vertex z_{vtx} and $E - p_z$. The fraction f_{non-ep} amounts
to $0.81 \pm 0.09\%$ and $0.81 \pm 0.07\%$ for the BST and the BDC analysis, respectively. This
is already significant for the desired precision of the analysis.

Since the e-pilot bunches should indicate background events one would neither ex-
pect that the distribution of z_{vtx} for e-pilot events shows a maximum at the nominal
position for ep interactions of approximately $70 \, \text{cm}$ nor that the $E - p_z$ distribution
peaks at $2E_e^0 = 55.2 \, \text{GeV}$, a value expected from conservation of energy and longitu-
dinal momentum for DIS events (see equation 3.6). Hence there seems to be a large
amount of ep events among the contribution of e-pilot bunches.

This is possible if the proton partner bunches of the e-pilot bunches carry a non-
negligible current. This is indeed the case for a fraction of the shifted vertex data taking
period as can be seen in figure 3.5 a) which shows the proton beam current for colliding
and e-pilot bunches as a function of the luminosity run. The dashed lines indicate the

---

[17]For the remaining part of this section the statements hold for both backward tracking detectors.
For the figures shown the reconstruction of θ_e has been performed with the help of the BDC. The
corresponding distributions for the BST look similar.

[18]As the number of bunches for the different bunch types varies with time the time averaged values
over the shifted vertex period are used for n_{coll}, $n_{p-pilot}$, $n_{e-pilot}$ and n_{empty}.
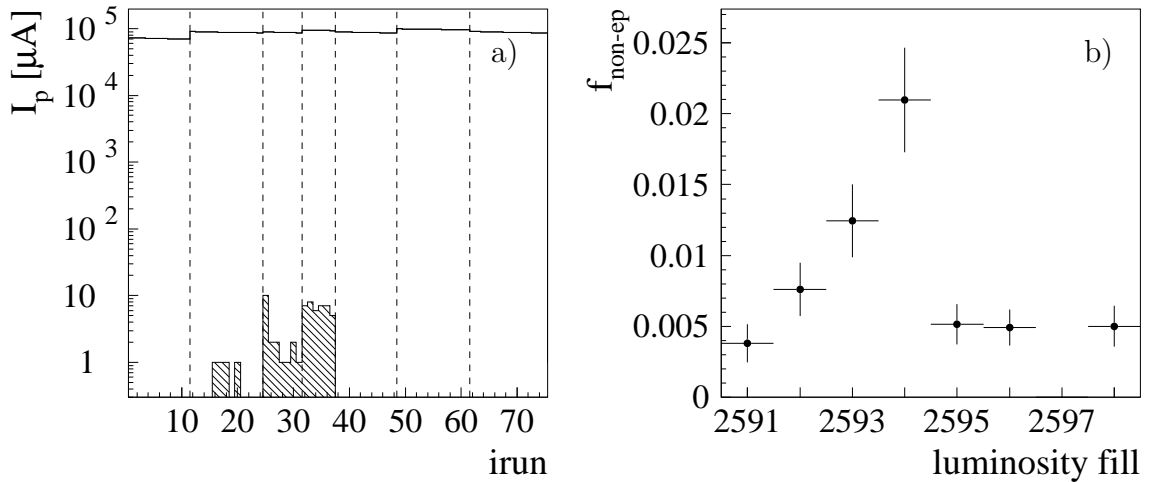
Figure 3.5: a) *Proton current I_p for colliding (open histogram) and e-pilot bunches (hatched histogram) as a function of a continuous run number. The dashed lines separate the different luminosity fills. b) Fraction of non-ep background events f_{non-ep} (see equation 3.25) as a function of the luminosity fill. Fill 2597 has lasted for only one hour, none of its runs has passed the run selection explained in section 4.1. The values of f_{non-ep} shown are overestimated (see text).*

different luminosity fills[19]. For the same luminosity fills in which the proton partner bunches carry a non-negligible current the fraction f_{non-ep} is significantly higher than for the rest of the data taking period (see figure 3.5 b)). Thus a fraction of the e-pilot events cannot be attributed to electron beam induced background, i.e. the fractions f_{non-ep} given above are overestimated.

The problem with the not empty proton partner bunches is known and can be explained in the following way [Pit06]: as can be seen from figure 2.1 electrons and protons are accelerated in DESY and PETRA before they are injected into HERA. DESY has 11 proton bunches while PETRA and HERA store protons in packets of 10 bunches. The superfluous bunch is supposed to be eliminated by a so-called kicker magnet. This however does not work completely reliably such that proton buckets in HERA are filled which are not supposed to be. Hence an electron bunch is already classified as an e-pilot bunch if the current in the proton partner bunch does not exceed $6\,\mu\mathrm{A}$.

To determine the correct fraction of non-ep events the following model is used [Krü06]: N_{coll} and $N_{e-pilot}$ can be split into a fraction of events originating from ep interactions ($N_{ep,coll}$, $N_{ep,e-pilot}$) and a fraction of events stemming from electron beam induced background ($N_{e-bgr,coll}$, $N_{e-bgr,e-pilot}$). The contribution from ep interactions should be proportional to the product of proton ($I_{p,coll}$, $I_{p,e-pilot}$) and electron current ($I_{e,coll}$, $I_{e,e-pilot}$) carried by the corresponding bunch type while the number of beam induced background events should rise linearly with the electron current only. One can therefore

---

[19]Luminosity runs and luminosity fills are well-defined intervals of the data taking period (see section 4.1). In figure 3.5 a) a continuous run number is given which conserves the original sequence of runs.

specify the following equations:

$$N_{coll} = N_{ep,coll} + N_{e-bgr,coll}$$
$$= aI_{p,coll}I_{e,coll} + bI_{e,coll} \tag{3.26}$$
$$N_{e-pilot} = N_{ep,e-pilot} + N_{e-bgr,e-pilot}$$
$$= aI_{p,e-pilot}I_{e,e-pilot} + bI_{e,e-pilot} \tag{3.27}$$

This system of two linear equations with two unknown coefficients a and b can be easily solved to determine $N_{e-bgr,coll}$. The fraction

$$f_{e-bgr} = \frac{N_{e-bgr,coll}}{N_{coll}} \tag{3.28}$$

is the sought-after fraction of electron beam induced background events in the analysis sample. Performing the necessary steps[20] the resulting f_{e-bgr} amounts to $0.78\% \pm 0.08\%$ ($0.78\% \pm 0.07\%$) for the BST (BDC). The quoted errors denote the statistical uncertainty only, no uncertainty on the currents has been considered. The fraction f_{e-bgr} seems to be again overestimated, i.e. the fraction of ep interactions contributing to $N_{e-pilot}$ seems to be underestimated.

Two effects can possibly cause this: at first single bunch currents below $1\,\mu$A are not recorded in the accessible database. This is already a significant amount for the proton partners of the e-pilot bunches. Secondly, the proton partner bunches of e-pilot bunches may be more compact than proton colliding bunches as they contains less protons and therefore the Coulomb repulsion within the bunches is reduced. For the latter explanation to hold one expects the z-vertex distribution for the e-pilot bunches to be narrower than for the colliding ones[21]. As a matter of fact this is the case (see figure 3.6). The z-vertex distribution is sensitive to the longitudinal bunch size. If one assumes that the transverse size of the proton partner bunches is also smaller there should be more ep interactions for a given product of currents than for the colliding bunches. Hence the coefficient a is not the same in equations 3.26 and 3.27 and f_{e-bgr} cannot be calculated as outlined above.

A correct quantitative treatment of the contribution of non-ep background events based on bunch currents and sizes is beyond the scope of this thesis. The upper limit on the fraction of electron beam induced background in the e-pilot events is estimated to be 10% comparing the shape of the $E - p_z$ distribution for e-pilot and colliding bunches. Given the estimates for f_{non-ep} this implies that the amount of non-ep background events in the final analysis sample is at the per mill level and therefore not considered further.

According to [Pit06] the upper limit of 10% is conservative: special runs with electrons in the machine only have been performed to study the background conditions for the running phase II of the HERA collider. In almost none of the events a vertex has been reconstructed, i.e. the events observed in the present study should be almost exclusively caused by ep interactions.

---

[20]For the currents corresponding to the different bunch types time averaged values over the shifted vertex period have been used.

[21]For details concerning the dependence of proton bunch size and width of the z-vertex distribution see section 4.7

Figure 3.6: *z-vertex distribution for colliding and electron pilot bunches. The distribution for the colliding bunches has been renormalised to contain the same number of events as the distribution for the electron pilot bunches.*
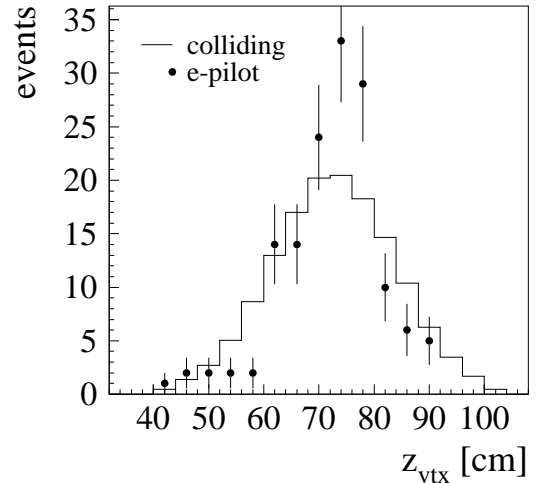
Photoproduction Background

Photoproduction (γp) events are ep interactions with a very small momentum transfer $Q^2 \approx 0$, i.e. the exchanged photon is quasi-real. The polar angle of the scattered electron is so large that it escapes detection in the SpaCal and leaves the main detector through the beam pipe[22]. Nevertheless a photoproduction event can pass the selection criteria of the analysis if it has a large inelasticity y and a particle of the hadronic final state mimics the signature of a scattered electron in the backward detectors. The contribution of this background source is significant as the inclusive cross-section for ep interactions is proportional to $1/Q^4$ (see equation 1.7).

Two classes of hadronic final state particles constitute the dominant sources for spurious electron candidates: neutral π mesons and charged hadrons. The former decay almost exclusively into two photons. For the cluster energies considered in this analysis ($E_e > 7\,\mathrm{GeV}$) the opening angle of the two decay photons is so small that they are most likely reconstructed as a single electromagnetic cluster in the SpaCal. Since photons are neutral particles one would expect no associated hits in the backward tracking detectors. However, they convert with a large probability to e^+e^- pairs while interacting with the detector material on their way from the interaction region to the SpaCal. Such conversions can cause a BST and/or BDC track to be linked to the SpaCal cluster. Furthermore charged hadrons can imitate the scattered electron as the corresponding clusters can be classified as electromagnetic due to fluctuations in the hadronic shower development or an overlap with a final state photon.

Due to the same mechanisms a final state hadron of a DIS signal event can mimic the signature of the scattered electron such that the electron identification is not unambiguous (see section 3.3).

Photoproduction events can be rejected to a large extent by applying selection criteria concerning shower shape, track validation and $E - p_z$ (see section 4.6). The remaining contribution is statistically subtracted from the data based on a Monte Carlo simulation (see sections 3.5 and 3.8).

---

[22]To define photoproduction events experimentally the lower acceptance limit of the SpaCal in Q^2 is used, i.e. for the shifted vertex period events with $Q^2 \lesssim 0.5\,\mathrm{GeV}^2$ are classified as photoproduction events (see figure 3.2).

3.5 Monte Carlo Models

For the measurement of the DIS cross-section the number of selected events has to be corrected for the limited detector efficiencies and acceptances. Furthermore the migration of events due to the finite resolution or photon radiation from the electron line has to be considered. It is very difficult to determine the individual corrections based on the recorded data alone since they are hard to disentangle. For example, the influence of radiative events may not be distinguished from inefficiencies (see section 4.7) or resolution effects. Hence a complicated unfolding procedure would have to be applied to measure the cross-section.

To avoid this Monte Carlo techniques are employed to perform a simulation of the ep interactions in the H1 detector. If detector effects and radiative ep scattering are correctly implemented the unfolding technique can be replaced by a simple comparison of the number of events in recorded data and simulation (see section 3.8). This involves a subtraction of the photoproduction background again performed based on a Monte Carlo simulation. The simulated event samples are employed further to quantify some of the sources for systematic errors of the measurement.

The Monte Carlo calculations are divided into two parts: the simulation of the pure physics process and the simulation of the detector response. The former is realised by using *Monte Carlo generators* having specific underlying theoretical models. Two generators are introduced in the following. The result of the event generation are the four-momenta and identities of all final state particles. They are subjected to the detector simulation which is the topic of section 3.6. The Monte Carlo events are reconstructed in the same way as the recorded data.

The generation of events proceeds in the following way: before the actual event generation the total cross-section σ_{tot} for the ep scattering is calculated via a numerical integration over the kinematical variables. During the generation a point (x, Q^2) of the kinematic phase space is chosen randomly for each event with a probability $(d\sigma/dxdQ^2)/\sigma_{tot}$. First the elementary scattering process for the event is calculated. In a second step additional partons, so-called *parton cascades* are created. Finally, during the *hadronisation* the partons are transformed into observable hadrons.

DJANGO

DIS events are simulated with the generator DJANGO [Sch91] which provides an interface to the programs HERACLES [Kwi92] and LEPTO [Ing91]. For the present analysis the version DJANGOH 1.4 is used.

LEPTO simulates the hadronic final state for the bulk of the kinematic phase space. This includes the calculation of QCD matrix elements to first order in α_s as well as the generation of parton cascades. For the latter the Colour Dipole Model [Gus86, Gus88, And89] as implemented in ARIADNE [Lön92] is chosen. The hadronisation is performed by the JETSET package [Sjö94] making use of the Lund string model [And83a, And83b].

With previous versions of DJANGO used by the H1 collaboration it was not possible to generate events with invariant masses of the hadronic final state W below $5\,\mathrm{GeV}$ due to problems with LEPTO and JETSET in this region of the kinematic phase

space [Len06]. This has led to discrepancies between simulation and recorded data at low transverse momenta of the hadronic final state $p_{t,had}$ for former analyses (see section 4.6). To overcome this problem the SOPHIA model [Müc00] has been included into the present version of DJANGO. It has been developed for astrophysical applications and provides an accurate description of photon-hadron interactions reproducing a large set of available data. Depending on W SOPHIA simulates the production of the major baryon resonances, direct pion production, multiparticle production based on the Dual Parton Model [Cap94] with subsequent Lund string fragmentation as well as the diffractive production of the light vector mesons ρ and ω. For $W < 5\,\text{GeV}$ SOPHIA takes over the simulation of the hadronic final state instead of LEPTO. The Lund string fragmentation is performed by JETSET.

The complete one-loop electroweak radiative corrections as well as radiative scattering to first order in α are taken into account by HERACLES. The influence of radiative events on the cross-section measurement is discussed in detail in section 3.7.

The x and Q^2 dependence of the generated cross-section can be chosen by selecting a set of proton structure functions available in the PDFLIB [PB00]. For the present simulation the parton densities derived in a global QCD analysis by the MRST group [Mar98] are used[23], the longitudinal structure function F_L is set to zero. During the analysis the simulated events are reweighted using the ALLM97 parameterisation [Abr97] for F_2 and a prediction based on the saturation model [GB99a] for the longitudinal structure function[24] (for details on the two models see section 1.6).

If the events were generated strictly according to the inclusive ep cross-section only a rather limited amount of events would be available at large values of Q^2 leading to sizeable statistical fluctuations. Therefore only a fraction of the events is generated below a certain value of Q^2. In order to restore the original cross-section weight factors are calculated which have to be applied during the analysis. This procedure is referred to as Q^2 *weighting*.

Ten million DJANGO events have been produced corresponding to an integrated luminosity of approximately $3\,\text{pb}^{-1}$ which is more than a factor of five larger than for the data sample. Hence the systematic error of the cross-section resulting from the limited Monte Carlo statistics is negligible.

PHOJET

The photoproduction background is simulated with the help of version 1.10 of the generator PHOJET [Eng96]. It aims for a complete description of the total photoproduction cross-section[25] based on the two-component Dual Parton Model [Cap94]. Soft and hard hadronic processes are incorporated. The former are modelled using Regge phenomenology while the latter are calculated in perturbative QCD using leading order matrix elements. Like for DJANGO the hadronisation proceeds according to the Lund String Model as realised in JETSET.

To exclude double-counting of events the kinematic phase space has to be divided

---

[23]The number of the corresponding set of proton structure functions in the PDFLIB is 75.

[24]The MRST parton densities cannot be used for the analysis as they should not be applied below $Q^2_{min} = 1.25\,\text{GeV}^2$ [PB00].

[25]A comprehensive review on photoproduction processes at HERA can be found in [Erd96].

between DJANGO and PHOJET: for $Q^2 > 0.1 \, \text{GeV}^2$ DJANGO is used, for lower virtualities PHOJET.

The normalisation of the DJANGO sample with respect to the data sample can be simply performed based on the luminosities of the two samples. The luminosity for DJANGO can be easily calculated from the number of events and the total inclusive DIS cross-section taking the Q^2 weights into account. For PHOJET the normalisation is more difficult, section 4.9 is devoted to this issue. Like in the case of DJANGO a Q^2 weighting has been applied and the number of generated events amounts to ten million.

3.6 Detector Simulation

Since the Monte Carlo samples shall be used to model various detector effects instead of explicitly correcting the data for them it has to be ensured that they are well described within the simulation. This includes detector acceptances, efficiencies and resolutions as well as the influence of noise and dead material. To achieve an accurate description all generated signal and background events pass a detailed detector simulation and reconstruction comprising the following steps:

1. The passage of the particles through all detector components is simulated by the H1SIM package based on GEANT3 [Bru87]. To save computing time the shower development in the calorimeters is by default not simulated in detail. Instead a fast but accurate shower parameterisation has been developed and implemented into the program H1FAST [Gri90].

2. In the *digitisation* step which is also part of H1SIM the simulated subdetector responses are converted into data of the same form as collected from the real detector components. Basic efficiency and noise corrections are applied at this stage.

3. The fully simulated events are subjected to the same reconstruction procedure as the recorded data. The software package H1REC is responsible for this step.

The version 32800 of H1SIM used for the simulation benefits from the improved description of the dead material in the backward region of the H1 detector achieved in [Len99]. This is especially important for the present analysis as it heavily employs subdetectors in the backward region.

The crossing angle of the final state particles with the detector material of the LAr is different between shifted vertex period and standard running conditions. The shower parameterisation has been derived for the latter. Therefore the level of detail for the geometry description and the particle tracking in the LAr has been set to 'fine' instead of 'coarse' (default) granularity[26]. This implies simulating the full shower development

---

[26]For the fine granularity the calorimeter stacks are implemented layer by layer whereas for the coarse granularity a calorimeter stack is realised as a block of properly mixed homogeneous material without any substructure.

instead of employing the fast parameterisation. The change of the granularity is motivated by the observation of differences in the distribution of y_Σ between data and Monte Carlo for the shifted vertex period [Var06].

Detector simulation and reconstruction are the time consuming part during the production of Monte Carlo samples, the time needed for the event generation is negligible compared to this. The complete Monte Carlo production has been performed on a computer farm at the University of Dortmund using approximately 50 nodes. Each of the computers is equipped with two Intel Xeon processors having a clock rate between 2 GHz and 3 GHz. On average the simulation of one events takes about 5 s. As already mentioned, 20 million Monte Carlo events are used for the cross-section analysis. Dedicated Monte Carlo samples with special settings used for systematic studies concerning the reconstruction of the hadronic final state performed in [Var06] amount to approximately the same number of events. On a single processor of the given type the Monte Carlo production would have required more than five years.

Noise in the LAr Calorimeter

To quantify the importance of the different detector components (LAr, Central Tracker, SpaCal) for the reconstruction of the hadronic final state, their relative contribution to the inelasticity y_h reconstructed with the hadron method (see section 3.2) has been determined in [Var06]. The result can be seen in figure 3.7 as a function of y_h. For the calculation of y_h the LAr noise identified by the FSCOMB algorithm (see section 3.3) is not subtracted, but its contribution is indicated separately. As expected, the SpaCal dominates at high y_h, the Central Tracker contributes at intermediate y_h and at low y_h only the LAr can reconstruct the hadronic final state particles. The identified noise plays an important role for $y \lesssim 0.03$. Since discrepancies between data and Monte Carlo simulation have been observed for $y_\Sigma < 10^{-2}$, the implementation of the noise in the detector simulation has been investigated in detail. The results are presented in the following.

If the event samples generated by DJANGO and PHOJET were passed to the detector simulation without any additional measures only energy depositions originating from ep interactions would be simulated in the LAr calorimeter. No signals due to noise would be present. To include noise into the simulation events selected by random triggers[27] are collected in special runs with no online noise suppression. The total amount of recorded events is referred to as a *noise file*. During the simulation the signals in the LAr cells stored in the noise file are superimposed to the energy depositions caused by the genuine hadronic final state. Noise files contain typically a few thousand events and are recorded every few months. While for the simulation of long running periods several noise files are available, for the shifted vertex period only a single noise file is employed, referred to as default noise file in the following. It has been recorded one day after the shifted vertex run. This implies that at the time the noise events have been collected the average z-position of the interaction vertex has been already back at its standard value of $\overline{z_{vtx}} \approx 0$ cm.

Due to the different running conditions for analysis sample and noise file it is desirable to check that the latter is indeed well-suited to model the noise situation in the LAr

---

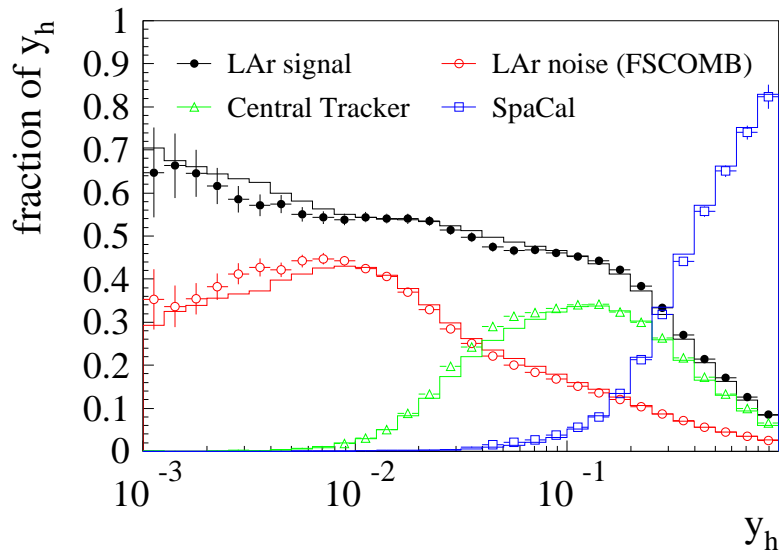[27]Among the selected events there should be nearly no ep interactions.

Figure 3.7: *Relative contribution of LAr, Central Tracker and SpaCal to y_h as a function of y_h. The symbols represent the data while the histograms refer to the Monte Carlo simulation [Var06].*

period	run range	number of events
before SVX run	278412 - 278575	28644
during SVX run	278707 - 278891	29578
after SVX run	279053 - 279338	25062

Table 3.1: *Details about the samples of random events employed for the comparison with the noise files (see table 3.2). The shifted vertex period covers the run numbers 278687 - 278978.*

during the shifted vertex run. This is realised in the following way: also during standard data taking a small fraction of events is selected by random triggers[28]. They are used in the following for comparisons with the default noise file. It has to be considered that for the random events recorded during standard data taking an online noise suppression is performed while for the noise file not.

Three samples of random events recorded before, during and after the shifted vertex run are investigated. Apart from the default noise file two additional ones are analysed: one collected roughly two months before the shifted vertex period and the other during the running phase II of HERA without any beams in the machine. The latter should allow to estimate the contribution of beam induced noise. Details about all samples of random events and noise files can be found in tables 3.1 and 3.2.

The comparison is realised by subjecting all samples to the module ASCALE which is the first one in the LAr reconstruction chain [Küs91]. It converts the calibrated charges in the individual cells which are read out during data taking to energies at a so-called *ideal electromagnetic scale*. These would correspond to energies of the incident particles if they were all electrons or photons and no detector imperfections such as dead material would be present. Cluster formation, correction for dead material and

---

[28]The random trigger rate is typically 0.2 Hz.

name	run	number of events	running conditions
alternative noise file	274095	3002	luminosity
default noise file	279046	3003	luminosity
noise file w/o beams	348720	15745	no beams, HERA II

Table 3.2: *Details about the noise files used for the comparison with the samples of random events (see table 3.1). The shifted vertex period covers the run numbers 278687 - 278978.*

calorimeter wheels	f
CB	2.0
FB	2.5
IF, OF	3.0

Table 3.3: *Multiplication factor f used for the cell-wise noise cut in ASCALE for the different wheels of the LAr calorimeter. For their notation see figure 2.8.*

the reconstruction of energies for hadrons (see section 2.4) are the task of the later modules of the reconstruction software.

The energies registered in each calorimeter cell due to pure electronics noise form a Gaussian distribution [Bor92]. Its mean value is called pedestal, the corresponding standard deviation is referred to as σ_{noise}. After subtraction of the pedestal which is done online the distribution of the noise signals is symmetric around zero. Hence the pure physics signal is increased or decreased depending on the sign of the registered energy.

ASCALE performs a noise suppression on top of the online noise suppression: first it applies a symmetric cut $f \cdot \sigma_{noise}$ similar to the online noise suppression, i.e. only LAr cells are taken into account during the further reconstruction for which the absolute value of the deposited energy after subtraction of the pedestal exceeds $f \cdot \sigma_{noise}$. This implies that also cells with negative energies pass the selection which is important since they partly compensate the positive noise contribution to the measured signal. The value of the multiplication factor f depends on the calorimeter wheel (see table 3.3), σ_{noise} is determined for each LAr cell individually during special calibration runs. Depending on the calorimeter region the values of σ_{noise} vary between $15\,\mathrm{MeV}$ and $30\,\mathrm{MeV}$ [Abt97b]. This holds also for the year 2000 [Gay06].

In the course of the further reconstruction within ASCALE a topological noise cut is applied in addition. Cells are only kept for the reconstruction if their signal or the signal of one of their neighbouring cells exceeds $+4\sigma_{noise}$ or if their signal undershoots $-4\sigma_{noise}$. The cells below $-4\sigma_{noise}$ are kept in order to compensate for the noise contribution to the seed cells above $+4\sigma_{noise}$, but no neighbours are collected around them since they are purely noise.

Since the cuts against noise applied by ASCALE are at least as restrictive as the online noise suppression the noise files and samples of random events can be compared after this reconstruction step though for the random event samples in contrast to the noise files an online noise suppression is performed. For the comparison four quantities

are chosen. At first two quantities to investigate the energy dispersion within the LAr calorimeter for the different samples: the distribution of the energy E_i^{em} reconstructed in the individual LAr cells and the reconstructed energy per interval of the polar angle θ which is calculated with respect to $z = 0\,\mathrm{cm}$. To estimate the influence of the noise on the reconstruction of the hadronic final state two additional kinematic variables are constructed following equations 3.3 and 3.4:

$$p_{t,LAr}^{em} = \sqrt{(\sum_i E_i^{em} \sin\theta_i \cos\phi_i)^2 + (\sum_i E_i^{em} \sin\theta_i \sin\phi_i)^2} \tag{3.29}$$

$$\Sigma_{LAr}^{em} = \sum_i E_i^{em}(1 - \cos\theta_i) \tag{3.30}$$

In both equations the summation is performed over all LAr cells. Correspondingly, θ_i and ϕ_i represent the polar and azimuthal angle of the LAr cell i, respectively. The former is calculated w.r.t. the average z-position of the vertex $\overline{z_{vtx}} = 71.9\,\mathrm{cm}$ for the shifted vertex period.

The noise files and the random event samples are compared among each other and the default noise file for the simulation of the shifted vertex period is compared to the corresponding random event sample. The results are presented in figures 3.8 and 3.9.

The following conclusions can be drawn: the distribution of the individual cell energies E_i^{em} shows almost no entries in the interval $-50\,\mathrm{MeV} < E_i^{em} < 50\,\mathrm{MeV}$. This gap is expected given the typical values for σ_{noise} and the values of f used by ASCALE (see table 3.3).

The different noise files show differences for the distributions of the basic quantities as well as the kinematic variables. The distribution of E_i^{em} is symmetric around zero for the noise file without beams in the machine as one would expect from pure electronics noise (see figure 3.8 a)). For the two noise files with beams there is a clear excess at positive energies. In addition they show a significant rise of the reconstructed energies towards small θ in contrast to the noise file without beams (see figure 3.8 b)). Hence one can conclude that the majority of the noise is beam-induced. This can be also clearly seen in figure 3.10 which shows an rz-view of the average reconstructed energy per event in the LAr calorimeter for the default noise file and the noise file without beams. For the default noise file the forward region is occupied by large positive energy depositions while there are no such depositions in the case of the noise file without beams. The differences for Σ_{LAr}^{em} and $p_{t,LAr}^{em}$ (see figure 3.9 a) and b)) are less significant than for the basic quantities as both quantities are rather insensitive to losses or additional energy depositions in the forward region as already explained in section 3.2.

As far as the different random event samples are concerned the sample recorded before the shifted vertex period shows a difference in the kinematic distributions compared to the other two (see figure 3.9 c) and d)).

The comparison of the default noise file with the random event sample recorded during the shifted vertex run reveals that the default noise file is well-suited for the simulation of LAr noise in the shifted vertex run.

A general outcome of this study is the realisation that the random events continously recorded during standard data taking are not only useful to judge the suitability of a noise file, but may be used instead of the dedicated noise files as an input for the
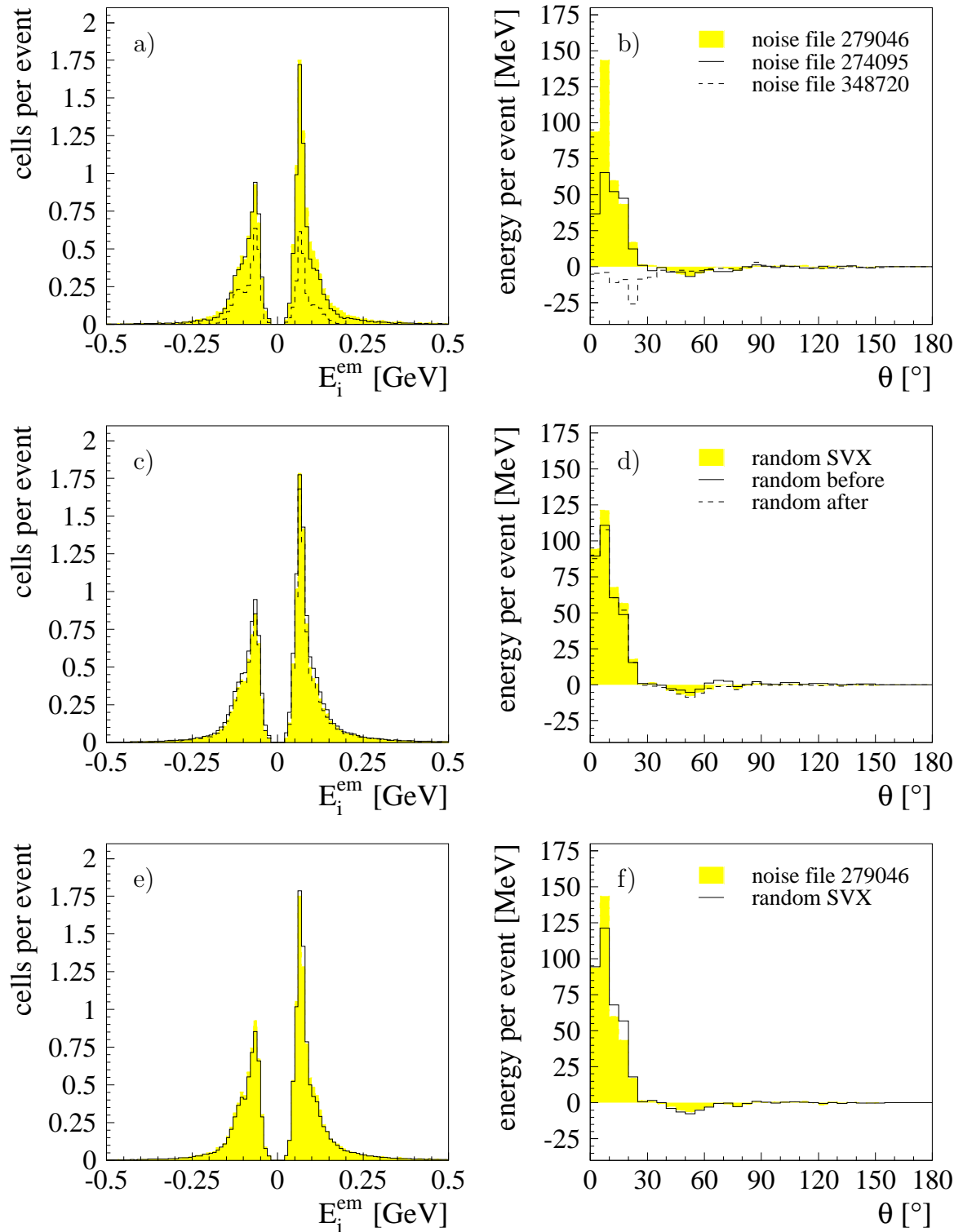
Figure 3.8: *Left column: distribution of the energy E_i^{em} reconstructed in the individual cells of the LAr calorimeter. Right column: distribution of the energy in the LAr as a function of the polar angle θ. Each distribution is shown for various random event samples (see table 3.1) and noise files (see table 3.2). Each row corresponds to one set of samples.*
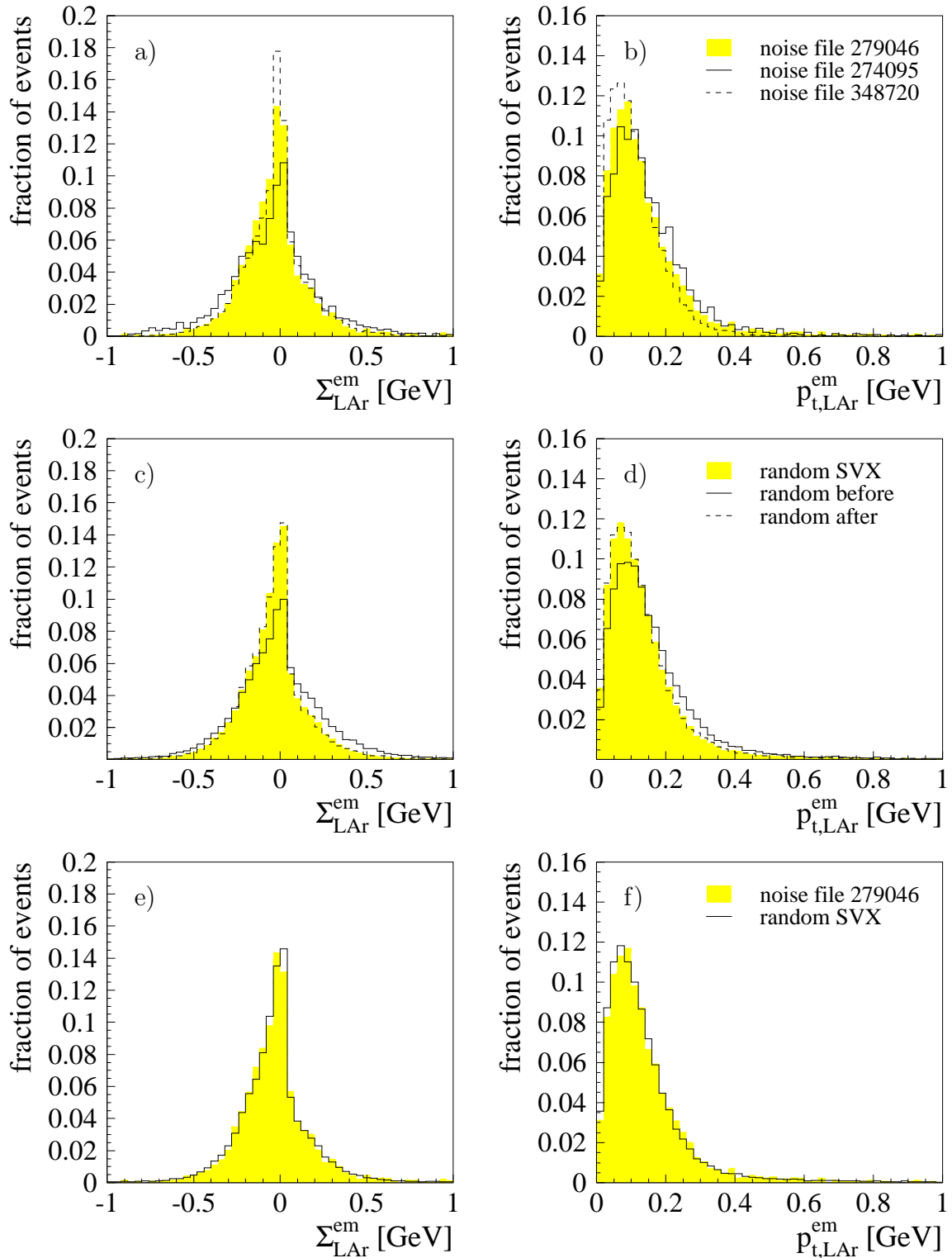
Figure 3.9: *Left column: distribution of Σ_{LAr}^{em} (see equation 3.30). Right column: distribution of $p_{t,LAr}^{em}$ (see equation 3.29). Each distribution is shown for various random event samples (see table 3.1) and noise files (see table 3.2). Each row corresponds to one set of samples.*
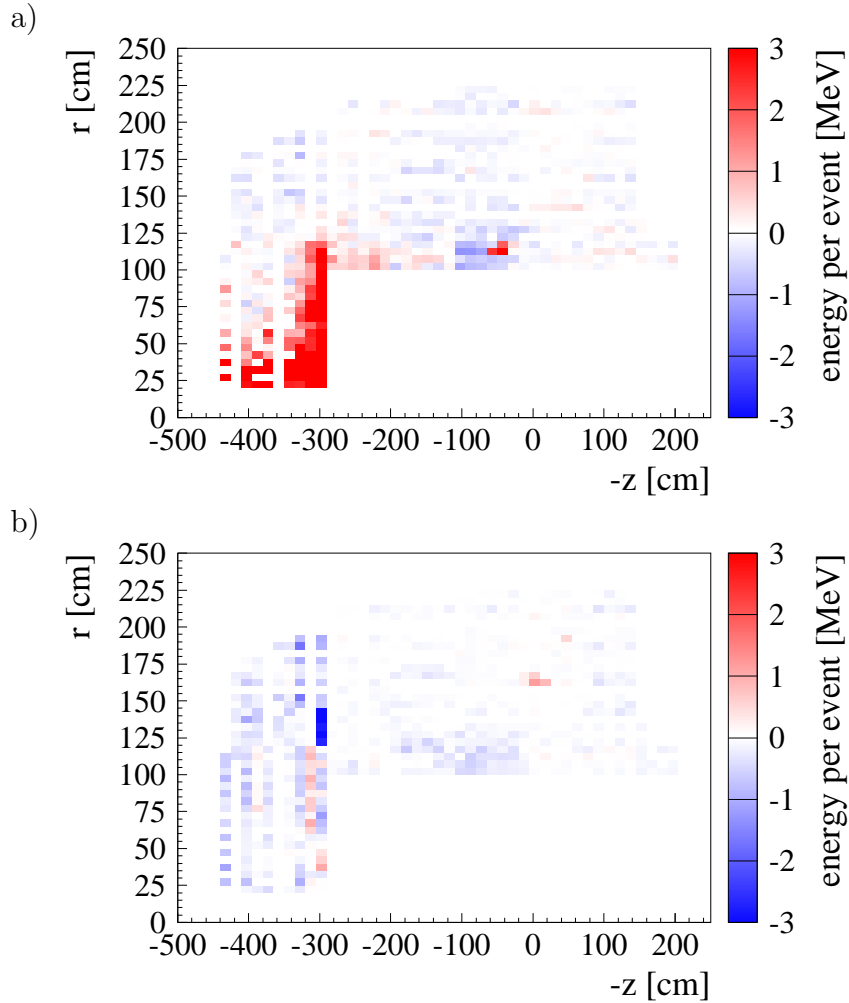
Figure 3.10: *Average energy per event reconstructed in the LAr calorimeter at the ideal electromagnetic scale for the noise files a) 279046 and b) 348720 (see table 3.2) depicted in the rz-plane.*

simulation. Their great advantage is that they are permanently recorded and hence allow to react on changing running conditions on short time scales. This option is discussed within the H1 collaboration. Additional studies are necessary to quantify the influence of the online noise suppression on physics analyses.

To estimate the influence of the LAr noise on the discrepancy between data and Monte Carlo simulation in the y_Σ-distribution for $y_\Sigma < 10^{-2}$ a number of dedicated Monte Carlo samples has been produced: for one sample the alternative noise file has been employed, for a second one a special noise file containing only half of the events of the default noise file is considered[29]. Finally, one Monte Carlo simulation has been performed without adding any LAr noise at all. Detailed investigations in [Var06] have shown that none of the samples leads to a significant improvement or worsening of the discrepancy. With the help of the simulation without noise it has been demonstrated

---

[29]As the noise files contain only three thousand events the same noise pattern is overlayed to the physics signal quite often during the simulation. This may create large fluctuations. If they are the reason for the discrepancy it should be enhanced when using the special noise file.

Figure 3.11: a) *Schematic of the beam tilt and the variables used for its parameterisation in the yz-plane. The points indicate primary vertices. b) Difference of the polar angle of the scattered electron measured in the H1 coordinate system (θ_e^{H1}) and the one describing the ep interaction (θ_e) illustrated for a cluster in the SpaCal.*

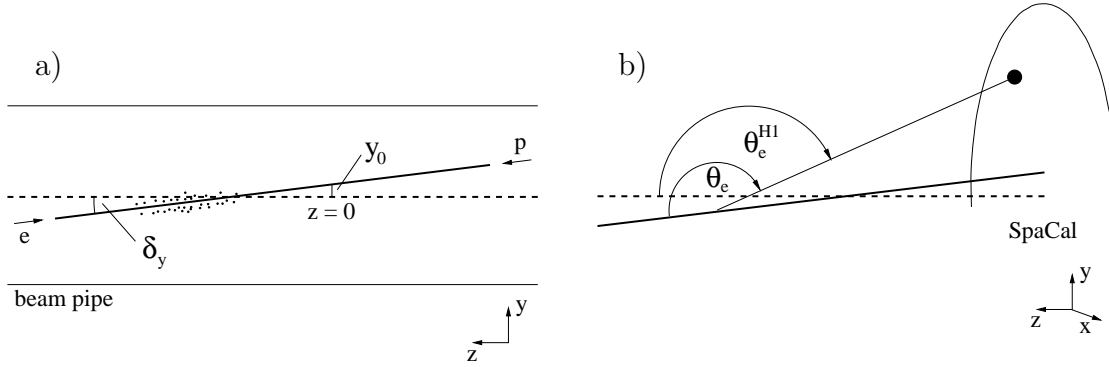| x_0 [cm]	y_0 [cm]	δ_x [mrad]	δ_y [mrad]
-0.27	0.20	0.2	1.0

Table 3.4: *Average beam tilts and offsets for the shifted vertex period as defined in equations 3.31 and 3.32.*

that a large fraction of the noise identified by FSCOMB are in fact energy depositions caused by isolated particles of the genuine hadronic final state.

Beam Tilt

Due to the changing beam conditions the H1 coordinate system is not ideally aligned with respect to the beam axis. Correspondingly, the beams are inclined w.r.t. to the z-axis, an effect called *beam tilt*. It is reflected in the distribution of the primary vertices as schematically depicted in figure 3.11 a).

Because of the beam tilt the polar angles of all final state particles measured in the H1 coordinate system are not identical to the polar angles describing the scattering process, i.e. all reconstructed polar angles have to be corrected for the effect of the beam tilt. This holds especially for the scattered electron as shown in figure 3.11 b).

To determine the beam tilt the primary vertices reconstructed by the Central Tracker are subjected to straight line fits in the xz- and yz-plane, i.e. the average vertex position $(\overline{x_{vtx}}, \overline{y_{vtx}})$ is parameterised in the following way:

$$\overline{x_{vtx}}(z_{vtx}) = x_0 + z_{vtx} \tan \delta_x \tag{3.31}$$

$$\overline{y_{vtx}}(z_{vtx}) = y_0 + z_{vtx} \tan \delta_y \tag{3.32}$$

The free parameters of the fit are the offsets x_0 and y_0 at $z_{vtx} = 0$ cm as well as the tilts δ_x and δ_y of the beam. Figure 3.11 a) illustrates them in the yz-plane, their values for the shifted vertex period as obtained from the data are listed in table 3.4.

Since the beam tilt affects θ_e it influences the mapping of the detector acceptance to the xQ^2-plane (see figure 3.3). Thus the accurate implementation of the beam tilt in
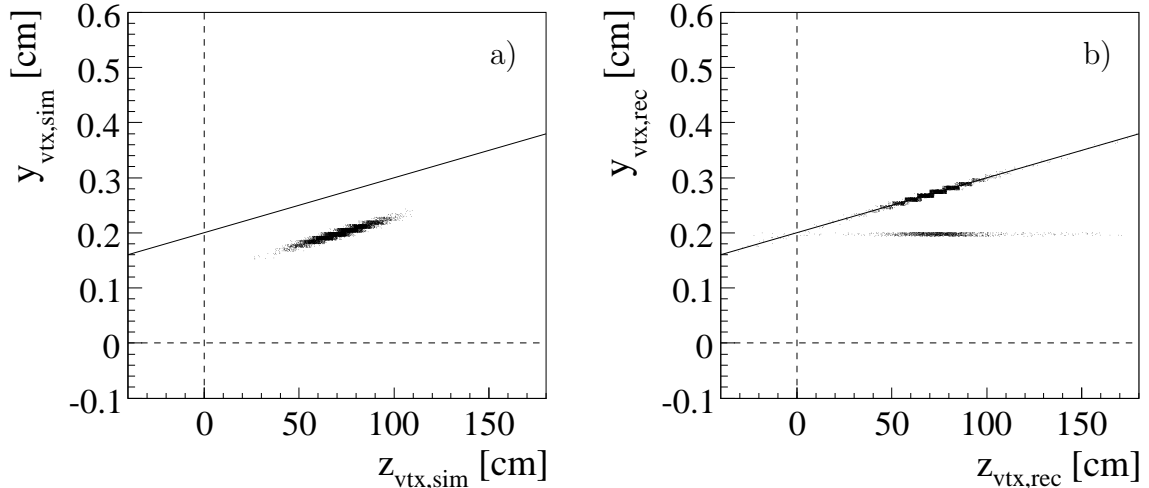
Figure 3.12: *Distribution of primary vertices in the yz-plane after a) detector simulation and b) reconstruction before correction (see text). The solid line indicates $\overline{y_{vtx}}(z_{vtx})$ as observed in the data (according to equation 3.32 and the values from table 3.4).*

the detector simulation is essential for the method of the cross-section determination to be valid. Like the simulation of the finite spread of the z-vertex distribution the realisation of the beam tilt is the task of H1SIM. The beam offsets and tilts determined from the data sample are used as input parameters for the simulation.

Figure 3.12 shows the distribution of the reconstructed primary vertices in the yz-plane for the Monte Carlo sample after the detector simulation and after the complete event reconstruction, respectively. Though only Central Tracker vertices are used for the analysis Forward Tracker vertices are also contained in the distributions[30]. The solid lines indicate the average vertex position $\overline{y_{vtx}}$ observed for the data calculated from equation 3.32 based on the values listed in table 3.4. Two problems with the Monte Carlo samples can be identified: firstly no beam tilt has been taken into account for parts of the reconstructed vertices. Furthermore the simulated and reconstructed vertex positions deviate systematically. However, a significant fraction of the reconstructed vertices agrees with the findings in the data.

Though the observations seem to be contradictory they can be traced back to an inconsistency concerning the treatment of the vertex offsets in H1SIM and H1REC: the beam offset x_0 and y_0 given in table 3.4 refer to $z_{vtx} = 0$ cm. They are directly used as an input for the simulation. H1SIM however interprets them as if they would correspond to the mean z-vertex position used for the simulation, i.e. $z_{vtx} \approx 70$ cm. Finally, within H1REC they are treated as if they would correspond to $z_{vtx} = 0$ cm again. As a consequence the majority of the events seems to be reconstructed at the correct position though all particles of the event have the wrong origin in the simulation. The resulting shift of 1 mm in the y-direction is already significant for the desired precision of the analysis. In contrast, the effect of the inconsistency in x-direction is almost negligible as the tilt of the beam in the xz-plane is a factor of five

---

[30]If no primary vertex reconstructed by the Central Tracker is present for a given event a primary vertex of the Forward Tracker is searched for.
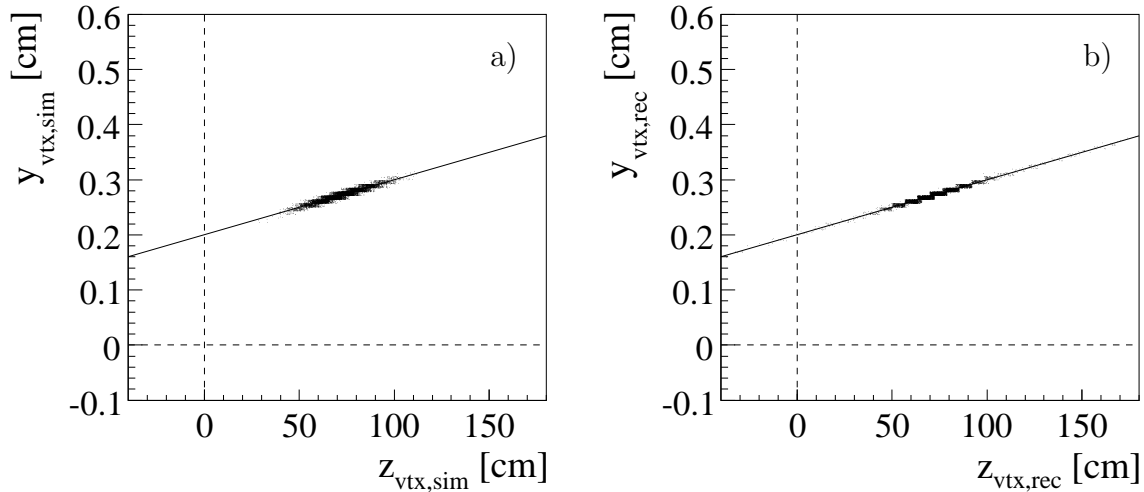
Figure 3.13: *Distribution of primary vertices in the yz-plane after a) detector simulation and b) reconstruction after correction (see text). The solid line indicates $\overline{y_{vtx}}(z_{vtx})$ as observed in the data (according to equation 3.32 and the values from table 3.4).*

smaller than in the yz-plane. For standard running conditions of the HERA collider the problem is almost not recognisable as the average z-position of the vertex is close to $0\,\mathrm{cm}$.

The vertices which do not show the effect of the tilted beams are all forward vertices. As they are not used the problem is not relevant for the present analysis, but has nevertheless been identified: at the time when the beam tilt has been included into the simulation it has been forgotten to change the corresponding routine of the Forward Tracker reconstruction accordingly.

The mentioned problems have been fixed in the following way: the beam offsets of table 3.4 have been converted to the mean z-position of the simulation before using them in the steering for H1SIM. The routines of H1REC have been changed accordingly. Finally, the beam tilt has been implemented for the Forward Tracker. The result of the changes can bee seen in figure 3.13 which shows that simulated and reconstructed vertices are in agreement between themselves and with the data.

All simulations employed for the present analysis have been performed with a corrected version of the software. All changes have been communicated to the authors of H1SIM and H1REC and are available in the new versions of the packages.

3.7 Radiative Corrections

The structure functions F_2 and F_L are defined with respect to the Born cross-section which describes the interaction of electron and proton in the single photon approximation to the lowest order in the electromagnetic coupling constant α (see section 1.2). The measured cross-section however contains contributions from various radiative processes. Apart from a change of the cross-section they can cause a wrong determination of the event kinematics depending on the reconstruction method. Their influence can be sizeable.

Hence the pure Born cross-section needed for the extraction of the structure functions has to be calculated from the measured cross-section by applying a correction factor:

$$\frac{d^2\sigma}{dxdQ^2} = \frac{1}{1 + \delta_{RC}(x, Q^2)} \left.\frac{d^2\sigma}{dxdQ^2}\right|_{meas} \tag{3.33}$$

The variable $\delta_{RC}(x, Q^2)$ quantifies the radiative corrections and can be estimated from Monte Carlo simulations or analytical programs. Since radiative processes are included in the DJANGO generator as already mentioned in the previous section no explicit correction is needed for the present analysis. It is performed implicitly by comparing data and Monte Carlo (see section 3.8). The remaining part of this chapter deals with the relevant radiative processes, their influence on the measurement and their implementation in DJANGO.

A detailed description of radiative corrections can be found in [Spi91]. Different contributions are distinguished therein: *leptonic corrections* are described by diagrams containing an additional photon attached to the lepton line, i.e. photon radiation from the lepton line and photonic lepton vertex corrections. The corresponding processes for the quark line are referred to as *quarkonic corrections*. In addition the interference of the two as well as purely weak corrections have to be considered. For the Q^2 values considered in this analysis the dominant contribution stems from the leptonic corrections. Among these the most important ones are the experimental configurations introduced in section 1.7, i.e. ISR, FSR and QEDC events[31].

Neglecting detector effects all reconstruction methods introduced in section 3.2 should give the same results for non-radiative events. For radiative events this statement does not longer hold, depending on the method the kinematics is reconstructed wrongly. This has been already shortly addressed for the case of ISR events.

While in ISR events the radiated photon escapes from the detector, final state radiated photons typically end up in the same cluster as the scattered electron. For only about 0.5% of the FSR events two cluster can be resolved [Mey97]. Hence FSR events are experimentally almost indistinguishable from non-radiative events and do not affect the reconstruction of the event kinematics.

In contrast to this the event reconstruction becomes incorrect for ISR and QEDC events if the electron method is used[32]: the energy of either the incoming or the outgoing electron is lowered due to the radiation. Hence the energy of the incoming electron at the leptonic vertex is overestimated or the one of the outgoing underestimated when using equations 3.1 and 3.2. Consequently, the reconstructed y_e is larger than the true inelasticity as calculated at the hadronic vertex. For QEDC events final state electron and photon have a sizeable transverse momentum. Thus the polar angle of the final state electron is smaller than the polar angle corresponding to the scattering process, i.e. the true Q^2 is smaller than Q_e^2.

The sigma method reconstructs ISR events correctly as no information concerning the incoming electron enters the calculation (see equations 3.10 and 3.11). For QEDC events the reconstructed variables deviate from the true ones as the photon is not explicitly identified but dealt with as a particle of the hadronic final state.

---

[31]Bethe-Heitler events do not enter the analysis sample as final state electron and photon disappear through the beam pipe.

[32]Reference is made at this point to section 3.2 where it has been explained that y_e depends predominantly on E_e and Q_e^2 on θ_e.

Given the explanations above one expects that the radiative corrections for the electron method are significantly larger than for the sigma method. This has been shown in various studies (see e.g. [Bas95b]).

DJANGO comprises all radiative processes mentioned above by interfacing HERACLES apart from elastic QEDC events. Therefore they are excluded from the data sample (see section 4.6). For the simulation at hand photon radiations from the quark line have not been included as they are estimated to be small for low x.

HERACLES allows for a separate treatment of the Born term and several parts of the QED corrections, i.e. in the present case ISR, FSR and QEDC processes. The contribution of each subprocess is integrated first at the initialisation stage and then events are generated according to the estimated fractions. During the analysis of the minimum bias run of the year 1999 it has been observed that the subprocess fractions for the generated events do not agree with the fractions reported at the initialisation stage [Gla05a]. Deviations of up to 5% occur.

Checking the subprocess fractions for the present analysis revealed the same problem. While doing so it has been realised that the problem is connected to the Q^2 weighting. This has been confirmed by producing and analysing a sample of generated events without making use of the Q^2 weighting. Indeed, the problem does not occur. Since no Q^2 dependence of the difference in the subprocess fractions has been found the problem can be easily compensated: global weight factors are derived to be applied during the analysis which allow the restore the original subprocess fractions from the initialisation step. The problem has been communicated to the author of DJANGO.

To derive an uncertainty on the simulation of the radiative corrections it has been checked using semi-analytical calculations implemented in the HECTOR [Arb96] package. An agreement better than 0.5% is observed in the kinematic phase space relevant for this analysis [Gla05b].

3.8 Extraction of the Structure Function F_2

The measurement of the double differential cross-section is performed in bins of x and Q^2 or y and Q^2 depending on the region in the kinematic phase space (for details see section 5.1). For the following explanations a bin in x and Q^2 denoted by $\square$ is considered[33].

The uncorrected bin-integrated cross-section $\tilde{\sigma}^{\square}$ is obtained from the number of events in the bin for the data sample $N_{Data}^{\square}$ that have passed the DIS selection criteria (see section 4.6) and the integrated luminosity $\mathcal{L}_{Data}$ for the selected runs:

$$\tilde{\sigma}^{\square} = \frac{N_{Data}^{\square}}{\mathcal{L}_{Data}} \tag{3.34}$$

To determine the bin integrated Born cross-section

$$\sigma_{Born}^{\square} = \int_{\square} \frac{d^2\sigma}{dxdQ^2}\, dxdQ^2 \tag{3.35}$$

$$= \frac{N_{Data}^{\square} - N_{\gamma p}^{\square} - N_{non-ep}^{\square}}{A\,\mathcal{L}_{Data}} \frac{1}{c_{\epsilon}} \frac{1}{1+\delta_{RC}} \tag{3.36}$$

---

[33]This is no restriction as each bin in y and Q^2 can be mapped to the xQ^2-plane.

several corrections have to be applied:

- $N_{\gamma p}^{\square}$ is the number of photoproduction background events accumulated in the analysis bin which fulfil the DIS selection criteria. It is estimated using the PHOJET Monte Carlo sample (see section 4.9).

- $N_{non-ep}^{\square}$ is the number of non-ep background events passing the DIS selection criteria. According to section 3.4 their contribution is negligible.

- The detector acceptance A is determined from the Monte Carlo simulation. It is defined as the ratio of the number of reconstructed to the number of generated events in the analysis bin: $A = N_{MC}^{\square}/N_{MC,gen}^{\square}$.

- c_ϵ are corrections for efficiencies not included or not properly described in the Monte Carlo simulation.

- δ_{RC} denotes the radiative corrections. They are obtained from Monte Carlo simulations or analytic programs and given by $\delta_{RC} = \sigma_{rad,MC}^{\square}/\sigma_{Born,MC}^{\square} - 1$. Here $\sigma_{rad,MC}^{\square}$ and $\sigma_{Born,MC}^{\square}$ refer to the full and Born bin-integrated cross-section, respectively (see section 3.7).

To derive the differential cross-section at the chosen central values (x_c, Q_c^2) of the bin from $\sigma_{Born}^{\square}$ the bin size and the cross-section behaviour inside the bin have to be taken into account. The bin size correction transforms the integrated cross-section into a bin averaged differential cross-section. The so-called *bin centre correction* converts the latter to the desired cross-section at (x_c, Q_c^2). Both corrections are contained in a single factor c_{BC} which is determined from the Monte Carlo simulation:

$$c_{BC} = \frac{\left.\frac{d^2\sigma}{dxdQ^2}\right|_{x=x_c,Q^2=Q_c^2}^{MC}}{\sigma_{Born,MC}^{\square}} = \frac{\left.\frac{d^2\sigma}{dxdQ^2}\right|_{x=x_c,Q^2=Q_c^2}^{MC}}{\int_{\square} \left.\frac{d^2\sigma}{dxdQ^2}\right|^{MC} dxdQ^2} \tag{3.37}$$

The differential cross-section in the numerator is calculated with the help of equation 1.7 using the predictions for the structure functions to which the simulated events are reweighted during the analysis (see below).

Hence the desired differential cross-section is given by:

$$\left.\frac{d^2\sigma}{dxdQ^2}\right|_{x=x_c,Q^2=Q_c^2} = \frac{N_{Data}^{\square} - N_{\gamma p}^{\square} - N_{non-ep}^{\square}}{A\,\mathcal{L}_{Data}} \frac{1}{c_\epsilon} \frac{c_{BC}}{1+\delta_{RC}} \tag{3.38}$$

The cross-section determination can be simplified significantly if the Monte Carlo model employed to simulate DIS events includes radiative corrections which is the case for DJANGO (see sections 3.5 and 3.7). This can be seen in the following way: if radiative corrections are incorporated in the simulation the relation

$$N_{MC,gen}^{\square} = \mathcal{L}_{MC}\,\sigma_{rad,MC}^{\square} \tag{3.39}$$

holds, $\mathcal{L}_{MC}$ denoting the luminosity corresponding to the DJANGO sample. Considering this and inserting the definitions of A, δ_{RC} and c_{BC} into equation 3.38 one

obtains:

$$\left.\frac{d^2\sigma}{dxdQ^2}\right|_{x=x_c,Q^2=Q_c^2} = \frac{N_{Data}^\square - N_{\gamma p}^\square - N_{non-ep}^\square}{N_{MC}^\square}\; \frac{\mathcal{L}_{MC}}{\mathcal{L}_{Data}}\; \frac{1}{c_\epsilon}\; \left.\frac{d^2\sigma}{dxdQ^2}\right|_{x=x_c,Q^2=Q_c^2}^{MC} \qquad (3.40)$$

To determine the differential cross-section following equation 3.40 is referred to as the *Monte Carlo method.* A similar relation to equation 3.40 is valid for the reduced cross-section. From the latter the structure function F_2 can be extracted (see equation 1.8):

$$\left.F_2(x,Q^2)\right|_{x=x_c,Q^2=Q_c^2} = \left.\frac{d^2\sigma_r}{dxdQ^2}\right|_{x=x_c,Q^2=Q_c^2} + \frac{y^2}{Y^+}\; \left.F_L(x,Q^2)\right|_{x=x_c,Q^2=Q_c^2} \qquad (3.41)$$

This implies employing external information on the longitudinal structure function F_L. For the present analysis a prediction based on the saturation model is used [GB99a]. It has been found to be in agreement with the results on F_L extracted from the data of the shifted vertex run and other data in the low Q^2 regime [Łob03]. The inelasticity y is calculated from x_c and Q_c^2 via equation 1.4 using the nominal centre of mass energy $\sqrt{s}$. This should not lead to a wrong estimation of the contribution from F_L since at high y and thus low x the fraction of ISR events should be negligible.

The use of the Monte Carlo method is only justified if all relevant aspects of the experiment, like subdetector acceptances and efficiencies, are correctly described in the Monte Carlo simulation. Therefore the next chapter is devoted to a large extent to a thorough comparison between data and Monte Carlo simulation. Remaining differences are absorbed into the extra correction factor c_ϵ or considered as systematic errors of the measurement. This is necessary for the vertex reconstruction with the Central Tracker (see section 4.7) and the polar angle reconstruction with the BDC (see section 4.8).

To calculate the differential cross-section at (x_c,Q_c^2) for the Monte Carlo requires an assumption concerning F_2 and F_L. The chosen parameterisation has to be the same as for the generation of the events. To first order the resulting cross-section should be independent of the input parameterisations for F_2 and F_L. However, they influence the result via smearing effects. Therefore the cross-section is determined in an iterative procedure: for the first iteration arbitrary parameterisations for F_2 and F_L can be used. The choice of a realistic behaviour is preferable but not necessary. If the prediction for the cross-section is too different from the result obtained from equation 3.40 new parameterisations are derived from model fits and the cross-section determination is repeated. To avoid a repetition of the time consuming simulation for each iteration the Monte Carlo events are reweighted to the parameterisation obtained from the previous step.

With the ALLM97 parameterisation [Abr97] for F_2 and the saturation model [GB99a] for F_L predictions for the proton structure functions are available which describe the data reasonably well (see [Łob03] and section 5.5). Therefore the differential cross-section can be determined in a single step.

3.9 Coverage of the Kinematic Phase Space

Two options exist to reconstruct the polar angle θ_e of the scattered electron as has been discussed in section 3.3: Either to use the BDC in combination with the Central Tracker

or the BST alone. This already allows for two independent cross-section determinations for the shifted vertex period. Furthermore it has been shown in [Laš04b] that the accessible kinematic phase space can be considerably extended towards larger values of x at low Q^2 by employing initial state radiation events in the analysis in addition to the standard non-radiative events.

The present section is intended to explain how the different detector components and event types can be utilised to allow for a maximum possible coverage of the kinematic phase space in the low Q^2 regime. Special emphasis is placed on the reconstruction of the event kinematics for ISR events as the reconstruction methods can provide wrong results for radiative events (see section 3.7). Since many people have been involved in the analysis of the shifted vertex data the aim of the last part of this section is to distinguish the contributions stemming from the thesis at hand and other people.

Figure 3.14 shows the accessible regions in the xQ^2-plane defined by the selection criteria explained in detail in section 4.6. At first only non-radiative events are considered: the cut $E_e > 7\,\text{GeV}$ on the energy of the electron candidate defines the lowest accessible value of x for a given value of Q^2. The minimum value of Q^2 for a given x is determined by the maximum polar angle θ_e allowed for the analysis. For the event selection a cut is placed instead on the distance R_e of the electron track to the beam axis in the plane[34] $z = -160.5\,\text{cm}$. It has to be larger than than $10\,\text{cm}$ and $9\,\text{cm}$ for the BST and BDC, respectively[35]. For the BST the acceptance at $R_e = 10\,\text{cm}$ has already decreased to approximately 50% [H1] while even at $R_e = 9\,\text{cm}$ the BDC acceptance is still close to 100% (see figure 4.27). Thus the BDC should provide a larger amount of events at low Q^2. In return the BDC analysis is restricted towards large x by the cut $y_\Sigma > 0.03$ ensuring the vertex reconstruction efficiency for the Central Tracker to be larger than 50%.

Typical inclusive analyses concentrate on non-radiative events. Since ISR events can lead to a wrong determination of the event kinematics they are excluded by placing a cut on $E - p_z$ (see equation 3.6). This is effective since the photon escapes through the beam pipe undetected such that $E - p_z$ is smaller than $2E_e^0$.

Due to the photon radiation an ISR event can be interpreted as a usual ep scattering event at a lower electron beam energy E_e^0 resulting in a lower centre of mass energy $s = 4E_e^0 E_p^0$. Hence according to equation 1.4 lower values of Q^2 for a given x or larger values of x for a given Q^2 can be reached compared to non-radiative events. ISR events allow to cover a region of the kinematic phase space at high x and very low Q^2 which is inaccessible for non-radiative events. It is schematically indicated in figure 3.14.

Previous analyses performed by the H1 and ZEUS Collaborations have explicitly detected the radiated photon in the photon arm of the luminosity system [Ahm95, Der96, ZEU03, İşs00]. Assuming a collinear radiation of the photon the incoming electron energy $E_{e,ISR}^0$ can be calculated in this case from the photon energy E_γ measured in the photon detector:

$$E_{e,ISR}^0 = E_e^0 - E_\gamma \tag{3.42}$$

---

[34]The value $z = -160.5\,\text{cm}$ corresponds to the average z-position of the clusters in the electromagnetic section of the SpaCal.

[35]The lines of constant R_e in figure 3.14 indicate the acceptance limit for the average z-vertex position of the shifted vertex run $\overline{z_{vtx}}$. For larger values of z_{vtx} even lower values of Q^2 can be accessed.
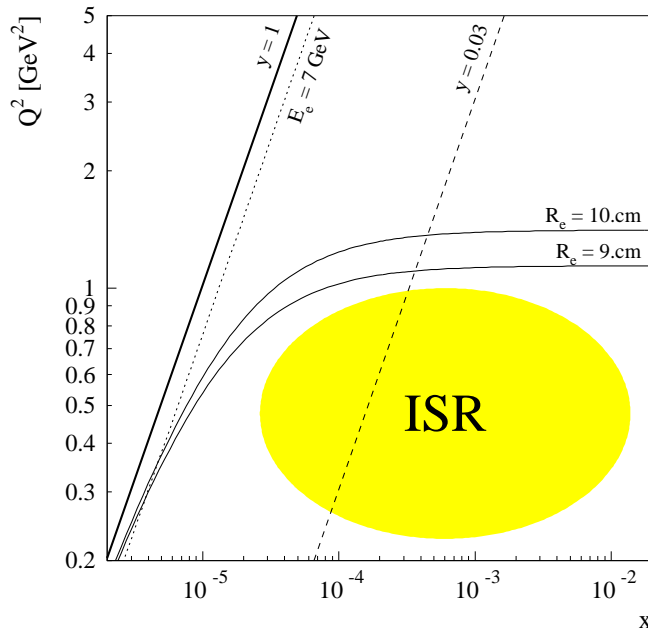
Figure 3.14: *Comparison of the coverage in the xQ^2-plane reached by the BST and the BDC, non-radiative and radiative events. Apart from the kinematic limit $y = 1$ (thick solid) lines of constant electron energy E_e (dotted), distance R_e (thin solid) and y (dashed) for non-radiative events are shown. The lowest values of R_e accepted for the analysis are $10\,\mathrm{cm}$ and $9\,\mathrm{cm}$ for the BST and BDC, respectively. The region of the phase space exclusively accessed by ISR events is schematically highlighted.*

Replacing E_e^0 by $E_{e,ISR}^0$ in equations 3.1 and 3.2 also the electron method yields correct results for ISR events.

The disadvantage of explicitly detecting the radiated photon is the contribution of coincidences of photoproduction/DIS and Bethe-Heitler events to the analysis. They constitute the dominant background source. While the photoproduction or DIS event causes an electron signature in the SpaCal the photon of the overlapping Bethe-Heitler event deposits energy in the photon detector. This source of background events is significant due to the large rate of Bethe-Heitler events.

For this reason it has been proposed in [Laš04b] to incorporate ISR events into the shifted vertex analysis without explicitly detecting the radiated photon. Apart from the absence of the mentioned background source this has the advantage of an increased acceptance for ISR events. The sigma method correctly reconstructs the kinematic variables y and Q^2 (see equations 3.10 and 3.11). However, for the determination of x via equation 1.4 one has to take into account that the centre of mass energy s is lowered in ISR events. This is done by replacing $s = 4E_e^0 E_p^0$ by a so-called *reduced centre of mass energy* s_r employing equation 3.6:

$$x_\Sigma = \frac{Q_\Sigma^2}{s_r\, y_\Sigma}, \; s_r = 2(E - p_z)E_p^0 \tag{3.43}$$

The value of s_r is close to s for non-radiative events while smaller for ISR events. Hence the presence of an ISR event is inferred from energy and longitudinal momentum

conservation. In contrast to [Laš04b] no separation between non-radiative and ISR events is performed for the present analysis. Equation 3.43 is consistently applied throughout the entire phase space allowing for an optimal coverage of the transition region between the parts of the phase space which are dominated by non-radiative or ISR events.

In case the electron method is used to reconstruct the kinematic variables a cut on $E - p_z$ is applied to avoid a wrong reconstruction of the kinematics (see section 4.6). This implies that for the region in the xQ^2-plane with a significant contribution of ISR events the sigma method is employed by definition.

A first preliminary measurement of the inclusive DIS cross-section for the shifted vertex data concentrating on non-radiative events was already presented on conferences in the year 2002 [Laš02a]. An independent cross-check was considered to be vital for such a precision analysis. The preliminary results have been derived based on the BST. It was decided that the cross-check is to be performed using the BST on the one hand and the combination of BDC and Central Tracker on the other. The latter should provide a higher level of independence w.r.t. the preliminary results. Accordingly, two analyses have been started, referred to as *BST analysis* and *BDC analysis*. Their results are the topic of two theses, [Var06] and the one at hand. Apart from providing independent measurements the main focus of the analyses is the identification and accurate quantification of the systematic errors affecting the cross-section determination.

Also the first preliminary measurement of the inclusive DIS cross-section based on ISR events in the shifted vertex data sample [Pet04] was presented on conferences in the course of the work on the two new analyses. Hence the results are cross-checked as well.

The two analyses have been performed in close collaboration, the work has been split in the following way: the focus of [Var06] is the BST analysis. The calibrations of the SpaCal and LAr calorimeters developed therein are applied for the present thesis which concentrates on the BDC analysis. The BDC analysis also incorporates ISR events, but covers only a small part of the kinematic phase space in principle being accessible by ISR events due to the cut on y_Σ (see figure 3.14). Therefore details on this topic beyond the explanations within this chapter can only be found in [Var06]. All results presented in the following refer to the BDC analysis if not explicitly stated differently. The selection criteria for the BST analysis are also shortly explained as a comparison between the two analyses will be presented in the last chapter of this thesis.

The final outcome of the two new analysis is the proton structure function F_2. A first preliminary extraction of the longitudinal structure function F_L already exists [Lob03]. More details about the underlying analyses of the preliminary results can be found in [Laš04b].

The data obtained from the shifted vertex run are complemented at larger values of Q^2 by the analysis of another data taking period dedicated to the low Q^2 regime in 1999, referred to as *minimum bias run* [Eck01, Laš04b]. The running conditions of the HERA accelerator have been standard, but the same special trigger setup for the online event selection has been used as for the shifted vertex run (see section 4.3). A combination of the results of the shifted vertex and minimum bias run is anticipated (see section 5.5).

4 Data Selection and Treatment

As discussed in the previous chapter, the determination of the deep inelastic scattering cross-section relies on a comparison of the number of events for data and a signal Monte Carlo sample in each analysis bin. For data the background contribution has to be subtracted beforehand. It is estimated based on a dedicated Monte Carlo sample. To keep the fraction of background events small an adequate set of selection criteria is applied.

Employing the described method is only justified if the efficiencies for the event selection and reconstruction as well as the uncertainties on the reconstruction are well described by the Monte Carlo simulation. Investigating and ensuring this is the topic of the present chapter.

At first problematic periods of the data taking as well as inefficiencies of the online event selection are identified and excluded from the analysis. To allow for a precise event reconstruction the relevant detector components are aligned and calibrated subsequently. Afterwards the selection criteria used for the analyses are introduced and it is checked whether their efficiency agrees between data and Monte Carlo. The remaining part of the chapter is devoted to corrections for the Monte Carlo samples in order to ensure a good description of the data. For each step the uncertainty relevant for the cross-section determination is discussed.

4.1 Run Selection

The operation cycle of the HERA accelerator divides the data acquisition of the H1 experiment into so-called *luminosity fills*. A luminosity fill starts as soon as collisions between electrons and protons have been established and ends if one of the beams is dumped or lost. To identify periods with nearly constant experimental conditions the stream of recorded events is further split into *luminosity runs*. A typical luminosity run lasts for one hour and contains 100000 events. For each run characteristic parameters like beam offsets and tilts (see section 3.6) are recorded in the H1 database. The integrated luminosity is stored in the same way.

Before carrying out a detailed selection of DIS events for the final cross-section measurement a preselection of the data is performed on a run-by-run basis to ensure stable detector and background conditions. It is based on the following quality criteria:

1. **Trigger Phase.** Two trigger phases can be distinguished in the data taking period relevant for this analysis: at the beginning of the luminosity run the beam currents are high and the beam parameters are still optimised by the HERA shift crew. To account for the resulting large beam induced background the H1 trigger system is operated in phase 1 which is characterised by large prescale factors (see section 2.6) especially for the calorimeter triggers. At this time the tracking

detectors have still not reached their nominal high voltage settings. Once these are achieved trigger phase 2 is selected and a new run is started. The autoprescale procedure (see section 2.6) is used regularly to calculate new prescale factors to make optimal use of the available bandwidth of the data acquisition system. Only runs in trigger phase 2 are considered in this analysis.

2. **Run Quality.** After the complete offline reconstruction the luminosity runs are classified as *good*, *medium* or *poor* based on data quality checks. In runs to which the quality flag poor has been assigned an important detector component (e.g. CJC, luminosity system or one of the calorimeters) is not operating. Such runs are excluded from the analysis.

3. **High Voltage and Readout Status.** The high voltage and readout status of the different H1 detector components is continuously monitored during data taking. If the high voltage of the detector components is below its nominal value for a significant amount of time this could indicate detector instabilities, usually due to a large rate of background events. Therefore runs are not taken into account for which the fraction of time with all relevant detector components being at nominal high voltage is less than 70%. The same is done for runs in which one of the important readout branches has not been operating. The high voltage and readout status is checked for the subdetectors SpaCal, BDC, BST, LAr, CJC, CIP, COP, CIZ and the luminosity system. The readout status is verified in addition for the Central Trigger and the calorimeter trigger system. Within accepted runs events are rejected in which one of the relevant detector components is not supplied with the nominal high voltage. The integrated run luminosity is corrected accordingly.

4. **Trigger Prescale.** To keep the overall trigger rate at a reasonable level for the data acquisition prescale factors can be applied to individual subtriggers during data taking (see section 2.6). In the course of the analysis the prescale factors of the relevant subtriggers are used as weights w_i for the events of the data sample in order to obtain the original number of events (for details see section 4.3). The weights enter the statistical error of the measurement quadratically: $\sigma_{stat} = \sqrt{\sum_i w_i^2}$. To reduce the statistical error of the measurement runs in which one of the considered subtriggers has a prescale factor larger than 3 are excluded from the analysis.

5. **Stability.** The stability studies presented in the next section have shown that the event rate of the luminosity run 278804 is significantly lower than of all the other runs. The shift crew comment to the consequent run indicates a loss of the proton beam. It is likely that the beam conditions have been already unstable in run 278804. Therefore it is not considered for the analysis.

4.2 Stability Studies

The stability of the measurement as a function of time is an important criteria for the quality of the data used for the cross-section measurement. Therefore the number of
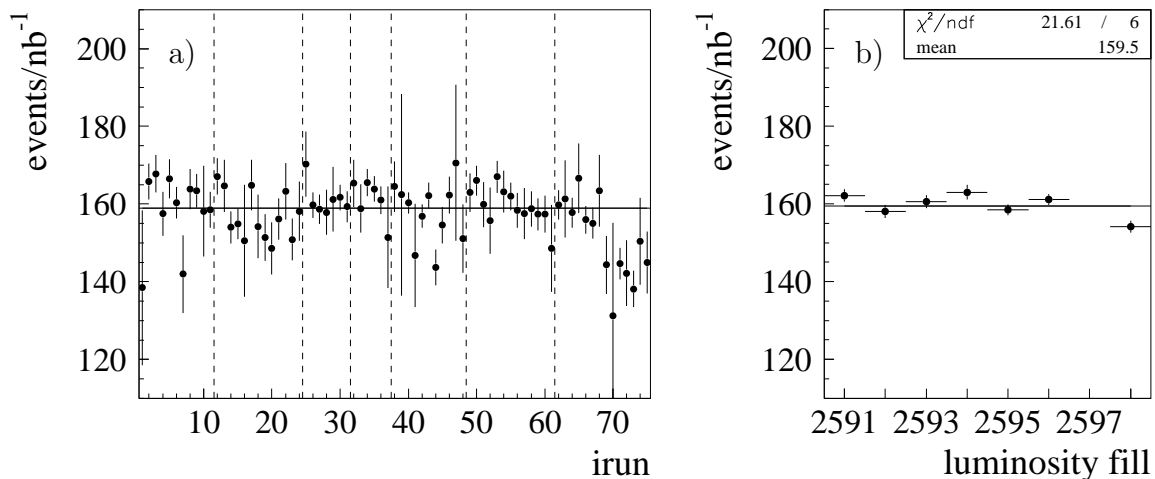
Figure 4.1: *Event yield per a) continuous run number and b) luminosity fill. The solid lines indicate the average event yield determined by fitting a constant to the data points. The dashed lines in a) separate the different luminosity fills. Fill 2597 has lasted for only one hour, none of its runs has passed the run selection of section 4.1. The luminosity entering the calculation of the event yield depicted here is based on the wrong estimation of the satellite correction, the corrected event yield is shown in figure 4.3 (for details see text).*

events per nb^{-1} of integrated luminosity (*event yield*) is investigated per luminosity run and fill. The former allows to identify problems occurring on short time scales while the latter provides a substantially larger statistical significance.

For the stability study the run selection discussed in the last section is already applied. The events under consideration have passed all selection criteria of the final cross-section analysis (see section 4.6). In addition a special selection is performed to equalise the detector acceptance for different runs: the mean and spread of the z-coordinate of the interaction vertex changes from run to run (see figure 4.25). As the detector acceptance depends on the vertex position this would result in a varying event yield. Therefore the polar angle of the electron candidate is restricted to $165.5° < \theta_e < 175.5°$ ensuring a backward detector acceptance of 100% independent of the vertex position (see section 4.7).

Figure 4.1 shows the obtained event yield as a function of a continuous run number[1] and the luminosity fill number. For the last luminosity fill a significant deviation from the mean event yield is observed. This deviation inspired a complete redetermination of the luminosity for the shifted vertex run by the luminosity working group. It revealed that the fraction of the luminosity attributed to the proton satellite bunches has been wrongly determined beforehand as is explained in detail in the remaining part of this section.

From figure 4.25 it can be seen that the spread of the z-position of the vertex for the last luminosity fill is significantly larger than for the others. Figure 4.2 compares the z-vertex distribution of the first and the last luminosity fill of the shifted vertex

---

[1] The original sequence of the runs is conserved.

Figure 4.2: *z-vertex distributions of the first and last luminosity fill of the shifted vertex run normalised w.r.t. each other based on the number of events. The vertical dashed lines indicate the z-vertex interval entering the final cross-section analysis. The vertical dashed lines indicate an interval of* 30 cm *around the nominal vertex position.*
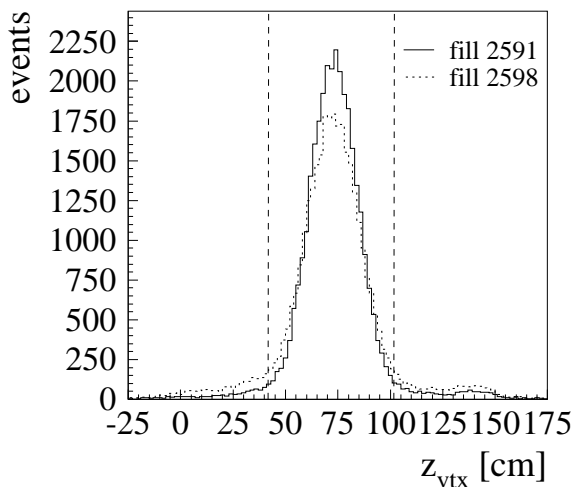
run. As expected both distributions have their main maximum at the nominal z-vertex position of approximately 70 cm. A second maximum is seen at about 140 cm. The last luminosity fill has a broader main maximum and more pronounced tails including a larger second maximum.

The additional maximum is caused by the complicated longitudinal structure of the HERA proton beam: 52 MHz and 208 MHz radiofrequency systems are installed in the proton ring for the acceleration. The protons are transferred from the PETRA pre-accelerator into the 52 MHz buckets and gradually compressed into the 208 MHz buckets during the acceleration to decrease the longitudinal size of the bunches to $\sigma_b \approx 20$ cm [Mon00]. This corresponds to a length of the luminous region of $\sigma_l \approx 10$ cm since the longitudinal size of the electron bunches is a factor of 10 smaller and therefore negligible. As the potential wells created by the radiofrequency systems are not sufficiently deep a small fraction of the proton current escapes from the main bunches and forms so-called *satellite bunches*. The satellite bunches are separated by $\Delta t = \pm \tau_{sat} = \pm 19.2$ ns and $\Delta t = \pm \tau_{sat} = \pm 4.8$ ns from the main bunch for the 52 MHz and 208 MHz system, respectively. Most relevant for the analysis are the satellites closest to the main bunch in the 208 MHz buckets. They cause additional maxima of the z-vertex distribution separated by $\Delta z = \mp c\tau_{sat}/2 = \pm 72$ cm from the main one. The maximum separated by $\Delta z = +72$ cm corresponding to the *forward* (or *early*) satellite is most pronounced since it provides access to the lowest values of Q^2 and thus the largest event rates. It is well visible in figure 4.2.

As indicated by the vertical dashed lines only events having a z-vertex position within 30 cm of the nominal one are accepted for the cross-section analysis (see section 4.6). The luminosity system (see section 2.5) however cannot distinguish Bethe-Heitler events originating from the main and satellite bunches and thus measures the luminosity in the entire z_{vtx} range. Therefore a procedure has been developed to subtract the satellite fraction of the luminosity based on the information of other sub-detectors [Lev95, Gog96].

As has been already mentioned the problematic last luminosity fill has a more clearly developed contribution of the forward satellite to the z-vertex distribution compared
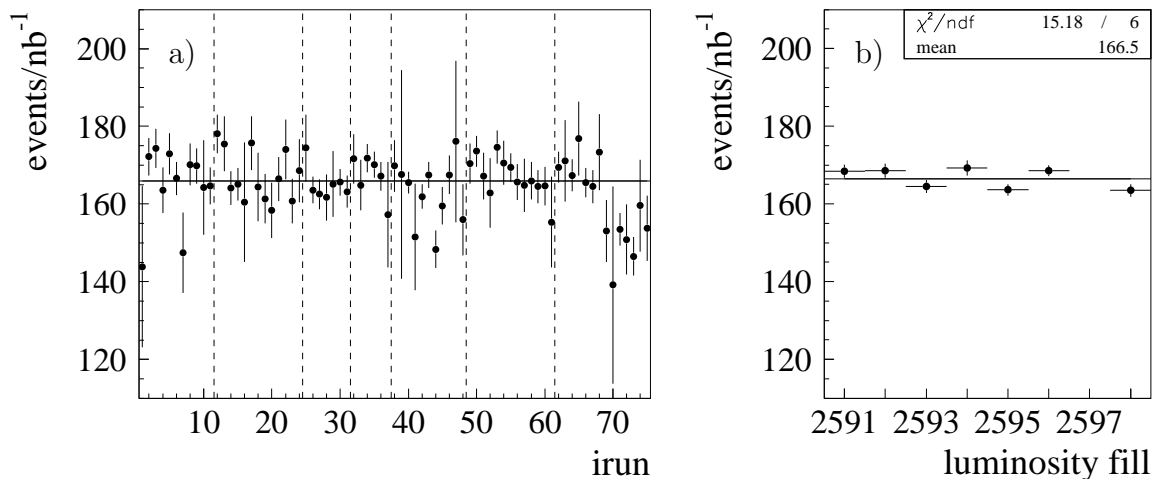
Figure 4.3: *Corrected event yield per a) continuous run number and b) luminosity fill. The solid lines indicate the average event yield determined by fitting a constant to the data points. The dashed lines in a) separate the different luminosity fills.*

to the first fill. Therefore it has been checked by the luminosity working group whether the satellite correction has been determined correctly. To derive this correction data from the proton pickup unit (PPU) located at $z \approx 3\,\mathrm{m}$ are used [Kar96, Wis98]. It measures the voltage induced by the electrically charged protons in a conductor coil allowing to extract the longitudinal beam profile. The correction is determined per luminosity fill.

In order to reach a high luminosity HERA focuses the beams in transverse direction at the interaction regions of H1 and ZEUS. This leads to a variation of the transverse beam size with z that has to be considered when calculating the luminosity corresponding to the main and satellite bunches from the longitudinal beam profile. The common measure of the transverse beam size is the β-function which is available from the HERA database. While revising the satellite correction it has been realised that the wrong β-function has been applied for the existing correction [Lev06]: it has been assumed that the β-function for the shifted vertex run is different from the one for standard running conditions to enhance the interaction rate at $70\,\mathrm{cm}$. Actually, the β-function is the same and the shift of the interaction vertex has been reached by changing the timing of the beams. In this way the satellite fraction of the luminosity has been underestimated by approximately a factor of two.

The new determination of the satellite corrections leads to a decrease of the total integrated luminosity by 4%, the measured cross-section thus increases by the same amount. For the last fill the change is most significant since it has the largest satellite bunches. Figure 4.3 shows the corrected event yield. The agreement of the yield of the last fill with the average yield has improved. Of course the run-wise deviations within this fill are still present as the satellite correction can only be determined as one global factor per luminosity fill.

The uncertainty on the luminosity determination has been estimated to be 2.2% by the luminosity working group [Lev06].

subtrigger	definition	L2 validation
S0	SPCLe_IET > 1 ‖ SPCLe_IET_Cen_2	SPCL_R10
S3	SPCLe_IET > 2 ‖ SPCLe_IET_Cen_3	-
S9	SPCLe_IET > 0	-

Table 4.1: *L1 subtriggers relevant for this analysis and their validation on L2. Additional veto conditions against beam background are omitted.*

4.3 Online Event Selection

In the region of the kinematic phase space covered by this analysis the scattered electron is detected in the backward region of the H1 detector. Therefore the online event selection is based on energy depositions releasing the Inclusive Electron Trigger (IET) of the SpaCal calorimeter (see section 2.6).

To benefit from the shifted vertex run as much as possible for the cross-section measurement at low Q^2 a special *minimum bias* trigger setup has been used: in comparison to the standard trigger conditions most of the subtriggers dedicated to high Q^2 and exclusive final state analyses have been disabled. Hence a larger bandwidth of the data acquisition system is available for the remaining subtriggers allowing them to run with lower prescale factors and thus reducing the statistical error of the measurement as much as possible. For the standard trigger setup the central LIET region of the Inclusive Electron Trigger is usually not taken into account since it causes a large subtrigger rate. However, in the case of the minimum bias setup one can allow to include it for some of the subtriggers giving access to larger polar angles θ and thus lower values of Q^2 than for the standard subtrigger definition. The resulting increased trigger rate is partly compensated by larger energy thresholds.

As described in section 2.6 the online event selection of the H1 experiment comprises the trigger levels L1, L2 and L4. The definition of the L1 subtriggers relevant for the analysis and their validation on L2 is covered in detail in the following with a subsequent determination of their efficiency. After a discussion of the event selection on L4 the section closes with an explanation how to retrieve the original number of events in the data sample by using event weights to account for the prescale factors applied during data taking.

Subtrigger Definition

The L1 subtriggers used for the analysis and their validation on L2 are listed in table 4.1. Apart from so-called global options[2] the used subtriggers are solely built from trigger elements of the Inclusive Electron Trigger (see section 2.6). The trigger elements SPCLe_IET > m (m = 0, 1, 2) and SPCLe_IET_Cen_n (n = 1, 2, 3) require that the energy deposition belonging to one cluster bit exceeds a certain threshold in the outer LIET regions and the central LIET region, respectively (see table 4.2).

To keep the trigger rate at a reasonable level the L2TT trigger element SPCL_R10 validating subtrigger S0 excludes the innermost region of the SpaCal [Biz98]. To be more

---

[2]Global options are additional veto conditions to reject beam induced background.

| trigger element | | threshold |
central LIET region	outer LIET regions	
SPCLe_IET_Cen_1	SPCLe_IET > 0	2 GeV
SPCLe_IET_Cen_2	SPCLe_IET > 1	5 GeV
SPCLe_IET_Cen_3	SPCLe_IET > 2	10 GeV

Table 4.2: *Energy thresholds of the Inclusive Electron Trigger. For the standard trigger setup the corresponding thresholds are 0.5 GeV, 2 GeV and 6 GeV, respectively.*

precise, the 9 cluster bits of the Inclusive Electron Trigger surrounding the beam pipe do not contribute to the trigger decision leaving a square of $8.1 \times 8.1 \, \text{cm}^2$ uncovered. This exactly corresponds to the insert module of the SpaCal.

The subtrigger definition reveals the following trigger strategy for the shifted vertex analysis: the bulk of the events are selected by subtrigger S0 as it has a lower energy threshold than S3 and its L2 condition excludes only the innermost region of the SpaCal. The latter is covered by subtrigger S3 enhancing the statistics for the lowest Q^2 values[3].

The subtrigger S9 has been defined to access the high y region of the kinematic phase space with the objective to measure F_L. However, it turned out that one of its global options based on the signals of the proportional chambers CIP and COP and the Forward Proportional Chambers has a low efficiency, because it has not been optimised for the shifted interaction vertex. Therefore subtrigger S9 is not employed for the cross-section measurement, but it proves to be useful for the determination of the trigger efficiency.

Trigger Efficiency

Inefficiencies of the Inclusive Electron Trigger are caused by individual SpaCal cells. The majority of the cells has an efficiency close to 100%, whereas only a few cells show problems. It is difficult to model the behaviour of the problematic cells in the Monte Carlo simulation. Therefore the analysis is restricted to regions of the phase space where the subtrigger efficiency is close 100%. To be more precise, the aim is to determine the fiducial volume and the energy range in which the subtriggers are fully efficient. This incorporates the identification of problematic SpaCal cells such that they can be excluded from the subsequent analysis.

The efficency of a specific subtrigger is typically determined by considering each trigger element separately. The standard procedure to do so is to use an event sample selected by independent *reference subtriggers*, i.e. subtriggers which do not contain any trigger element of the trigger subsystem under investigation [Urb05]. For the IET trigger elements these are typically subtriggers based on the trigger subsystems of tracking detectors or the LAr calorimeter. Due to the reduced number of active subtriggers in the minimum bias setup however the number of events selected by the

---

[3]As the innermost SpaCal region excluded by subtrigger S0 is anyhow not covered by the BST acceptance the BST analysis utilises S0 only.

reference subtriggers is not sufficient to determine the trigger efficiency separately for each SpaCal cell. Therefore the described method is used as a final cross-check whereas the detailed studies are performed based on a different approach as outlined below.

Different parts of the Inclusive Electron Trigger electronics cover the central LIET region and the outer LIET regions. Hence the groups of trigger elements `SPCLe_IET > m` and `SPCLe_IET_Cen_n` are independent of each other. Therefore they can be used for a mutual efficiency determination. This proceeds in the following way: one starts from an ensemble of events which have been selected by subtriggers containing trigger elements independent of the trigger element under investigation. From this sample events are selected which have exactly one cluster in the SpaCal region covered by the trigger element to be investigated. These events constitute the so-called *reference sample*. The fraction of events which are accepted by the trigger element of interest is the trigger efficiency. The requirement of exactly one cluster in the region attributed to the trigger element to be investigated is necessary in order not to overestimate the efficiency due to the presence of events in which a different SpaCal cluster has fired the trigger element than has been selected in the reference sample.

To reject background events several selection criteria have been applied: the z-position of the vertex as determined by the Central Tracker is to be reconstructed within an interval of 30 cm around the nominal position $\overline{z_{vtx}} = 71.9$ cm: $|z_{vtx} - \overline{z_{vtx}}| < 30$ cm. The SpaCal cluster has to match the requirements $r_{Cl} < 4$ cm and $f_{had} < 0.15$, r_{Cl} being the logarithmic cluster radius and f_{had} the fraction of the cluster energy deposited in the hadronic section of the SpaCal. This ensures that the cluster is most likely induced by the scattered electron[4].

At first the efficiency of the trigger elements `SPCLe_IET_Cen_2` and `SPCLe_IET_Cen_3` is studied by using a sample of events that have been selected by the subtrigger S9 which covers only the outer LIET regions. Subsequently the trigger element `SPCLe_IET > 0` is checked based on a reference sample selected by the subtriggers S0 and S3 explicitly requiring the trigger elements `SPCLe_IET_Cen_2` and `SPCLe_IET_Cen_3` to have fired, respectively. To avoid a possible bias it is ensured that the SpaCal cluster with the highest energy fulfils the requirements of the reference sample while a different cluster is used to check the efficiency of the trigger elements to be investigated. Since the second cluster is most likely caused by a hadron no cuts on r_{Cl} and f_{had} are placed. Its energy is so small that it is not sufficient to study the trigger elements `SPCLe_IET > 1` and `SPCLe_IET > 2`. The study of `SPCLe_IET > 0` solely serves to identify cells with general problems while the trigger element itself is not relevant for the subtriggers S0 and S3[5]. Having identified such cells it is sufficient to restrict the investigation of the trigger elements `SPCLe_IET > 1` and `SPCLe_IET > 2` to their threshold behaviour. The latter is analysed by again employing the subtrigger S9 to select the reference sample as its trigger element `SPCLe_IET > 0` has a lower threshold than the ones to be investigated.

The SpaCal cells with the numbers 7, 8, 13, 14, 32 and 33 (see appendix B) have been excluded from the Inclusive Electron Trigger already during data taking. They are located close to the beam pipe and exhibit an abnormally high trigger rate presumably induced by synchrotron radiation. In addition the cells 30, 62, 250, 253, 306 and 763 have been identified to show a low trigger efficiency. All listed cells are excluded from

---

[4]The selection criteria are explained in detail in section 4.6.

[5]Therefore it should be fine that no cuts concerning the electron identification are applied.

Figure 4.4: *Efficiency of the L1 trigger elements of the subtriggers S0 and S3 as a function of the energy of the SpaCal cluster. A Fermi function according to equation 4.1 is fitted to the data (solid line). The dashed line displays the energy cut to be applied for the corresponding trigger element in the final analysis. A deviation of 0.5% from an efficiency of 100% is indicated by the horizontal band.*

the analysis.

The resulting efficiencies of the L1 trigger elements contributing to the subtriggers S0 and S3 are depicted in figure 4.4 as a function of the energy E_e of the SpaCal cluster. A Fermi function is fitted to the data points given by

$$\epsilon(E_e) = \frac{\epsilon_{max}}{e^{\frac{E_t - E_e}{\Delta E}} + 1} \tag{4.1}$$

Here ϵ_{max} denotes the efficiency at the plateau, E_t the threshold energy and ΔE the width of the threshold. The threshold of each trigger element is at its designated position as specified in table 4.2. The plateau of the efficiency is reached a few GeV above the threshold as indicated by the dashed lines. The cuts for the final analysis are placed at the corresponding energies.

Apart from the efficiency of the IET trigger elements the phase space covered by the

Figure 4.5: *Efficiency of the L2 condition* `SPCL_R10` *of the subtrigger S0 as a function of $R_{box} = \max(|x_{Spa}|, |y_{Spa}|)$. The cut to be applied for the final analysis is represented by the dashed line. A deviation of 0.5% from an efficiency of 100% is indicated by the horizontal band.*

subtrigger S0 is determined by the L2 condition `SPCL_R10`. Its efficiency is analysed using a sample of events selected by the subtrigger S9 asking for the trigger element `SPCLe_IET_Cen_2` to have fired in addition. The fraction of these events being accepted by the L2 condition corresponds to the efficiency. It is depicted in figure 4.5 as a function of the quantity $R_{box} = \max(|x_{Spa}|, |y_{Spa}|)$ where x_{Spa} and y_{Spa} are the x- and y-position of the SpaCal cluster, respectively. A cut $R_{box} > 10$ cm ensures an efficiency of almost 100% for the L2 condition of S0.

For a final cross-check the efficiencies of the subtriggers S0 and S3 are determined based on independent reference subtriggers as mentioned at the beginning of this section: the starting point is a sample of events accepted by subtriggers which do not contain any IET trigger elements. From this sample events are selected which have a SpaCal cluster. The fraction of these events for which the raw bit of the subtrigger to be investigated is set corresponds to the trigger efficiency.

To reject background events the requirements introduced above for z_{vtx}, r_{Cl} and f_{had} have to be matched. In addition the time of flight information of the SpaCal has been employed to reject events which have a SpaCal time t_{Spa} not compatible with an ep interaction. A cut $t_{Spa} > -20$ ns is applied. To ensure that this requirement really rejects background events and not signal events which are hampered by individual SpaCal cells providing bad timing information the following cross-checks have been performed: it has been checked that the events rejected by the timing cut are uniformly distributed over the SpaCal surface within the limited statistics. In addition it has been verified that the time measurement of the Central Jet Chambers indicates the presence of a background interaction for these events[6].

Figure 4.6 shows the resulting trigger efficiencies as a function of the cluster energy.

---

[6]For the efficiency studies presented above no cut has been placed on the timing. This is not necessary, because the subtriggers used to select the reference sample contain IET trigger elements which can only be released during a time interval compatible with an ep interaction, i.e. a timing cut is implicitly present.
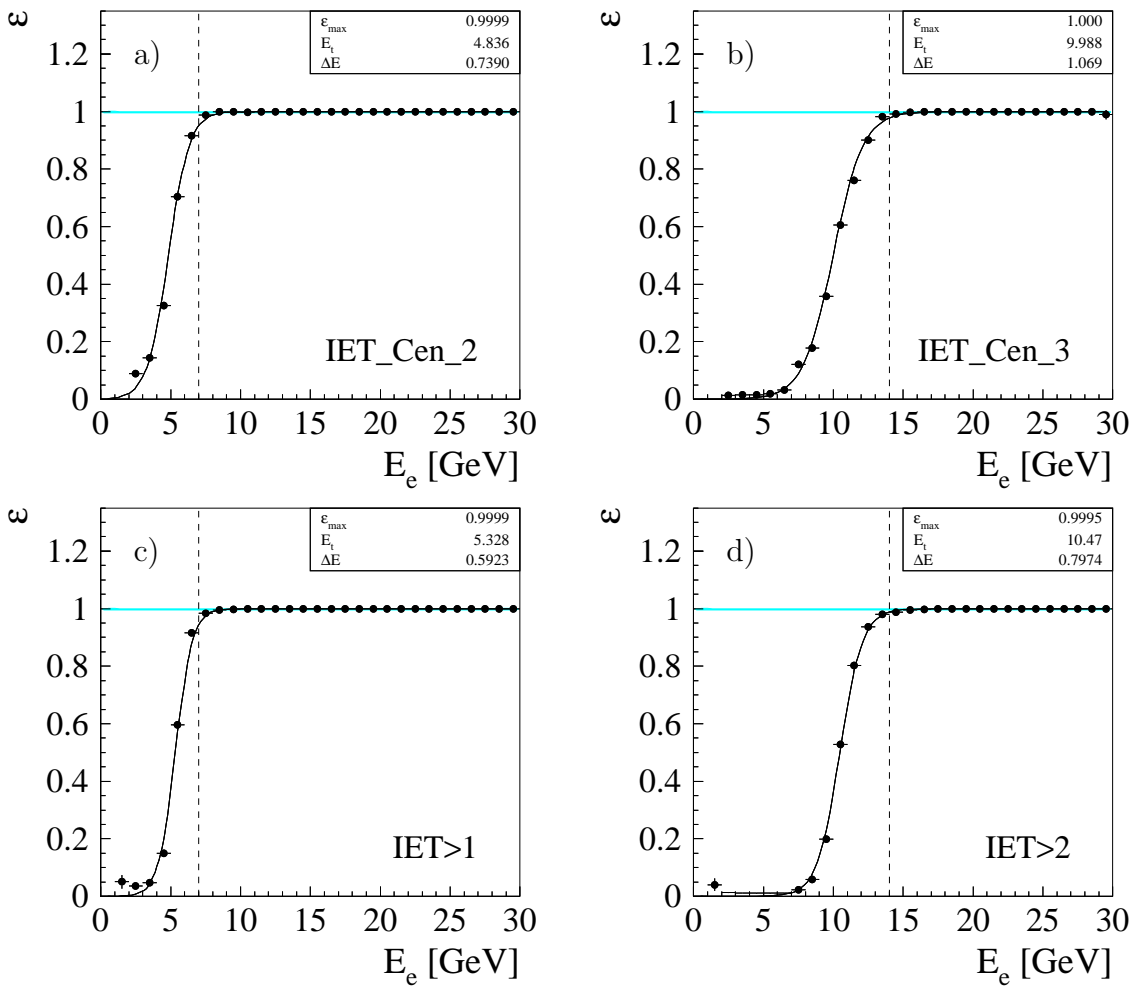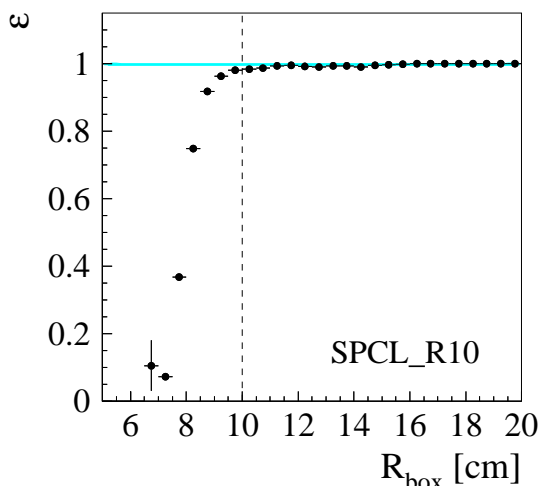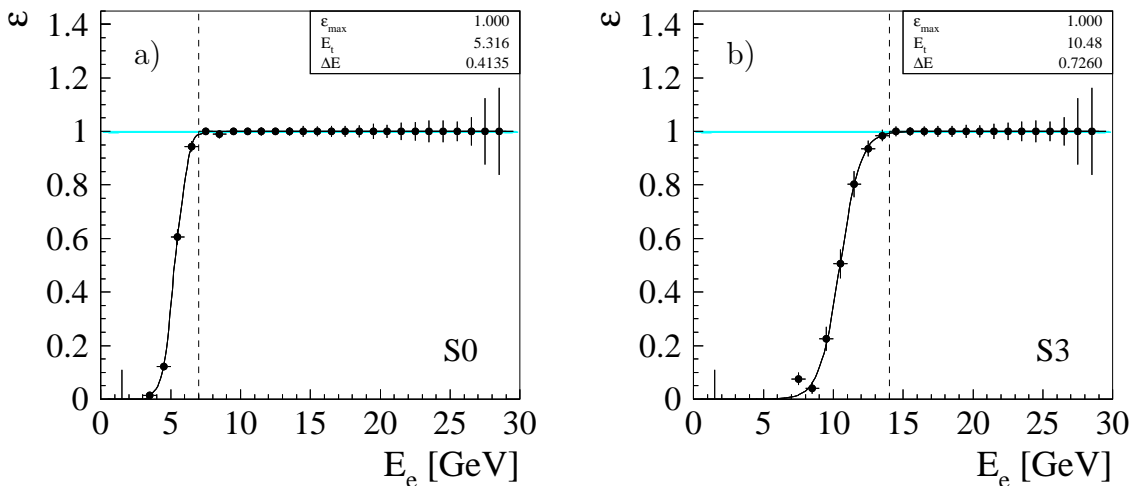
Figure 4.6: *Efficiency of the subtriggers a) S0 and b) S3 as a function of the energy of the SpaCal cluster. A Fermi function according to equation 4.1 is fitted to the data (solid line). The dashed line displays the energy cut to be applied for the corresponding subtrigger in the final analysis. A deviation of 0.5% from an efficiency of 100% is indicated by the horizontal band.*

analysis	energy range	fiducial volume
BST	$E_e > 7\,\mathrm{GeV}$	$R_{box} > 10\,\mathrm{cm}$
BDC	$E_e > 14\,\mathrm{GeV}$ $7 < E_e < 14\,\mathrm{GeV}$	entire SpaCal $R_{box} > 10\,\mathrm{cm}$

Table 4.3: *Selection criteria for the BST and BDC analyses resulting from the trigger efficiency study.*

They show the same threshold behaviour as the corresponding trigger elements. For the subtrigger S0 only events satisfying $R_{box} > 10\,\mathrm{cm}$ have been used in order not to mix inefficiencies because of the threshold behaviour and the L2 condition SPCL_R10. Especially at large energies one can see that the statistics for this method is rather limited.

From the trigger efficiency study different selection criteria arise for the BST and BDC analyses: since the BST analysis relies solely on subtrigger S0 only electron candidates fulfilling the requirements $E_e > 7\,\mathrm{GeV}$ and $R_{box} > 10\,\mathrm{cm}$ are used. The BDC analysis accepts events selected by S3 in addition and therefore no cut on R_{box} is necessary for energies above 14 GeV. For the selection criteria summarised in table 4.3 the subtrigger efficiency is 100% within an uncertainty of 0.5% (indicated by the horizontal band in figures 4.4 - 4.6).

Event Selection on L4

For the selection of the low Q^2 events on the fourth trigger level the L4 finder 18 is responsible. It imposes different selection criteria on the subtriggers S0/S3 and S9 as specified in table 4.4.

ST	L4 condition	explanation
S0 S3	R_SPAC_ECRA $< 4\,\mathrm{cm}$	r_{Cl}^{lin} of cluster with max. E_{Cl}
	R_SPAC_Q2MAX $> 0.2\,\mathrm{GeV}^2$	max. Q_{Cl}^2 of clusters with $E_{Cl} > 4.0\,\mathrm{GeV}$ and $r_{Cl}^{lin} < 4\,\mathrm{cm}$
	R_SPAC_EMAXCLUSTER $> 4\,\mathrm{GeV}$	max. E_{Cl}
S9	R_SPAC_ECRAMIN $< 5\,\mathrm{cm}$	min. r_{Cl}^{lin} of clusters with $E_{Cl} > 3.5\,\mathrm{GeV}$
	R_SPAC_RCLUSTERMAX $> 15\,\mathrm{cm}$	max. R_{Cl} of clusters with $E_{Cl} > 2\,\mathrm{GeV}$
	R_SPAC_EMAXCLUSTER $> 2\,\mathrm{GeV}$	max. E_{Cl}

Table 4.4: *Selection criteria on L4. E_{Cl} denotes the cluster energy, r_{Cl}^{lin} the linear cluster radius, R_{Cl} the distance of the cluster to the origin of the SpaCal in the $r\phi$-plane and Q_{Cl}^2 the photon virtuality as calculated from the cluster properties.*

analysis	fraction of L4 rejected events
BST	$0.80\% \pm 0.18\%$
BDC	$0.48\% \pm 0.18\%$

Table 4.5: *Fraction of events rejected by the L4 filter farm for the BST and BDC analyses.*

To determine the efficiency of the L4 filter farm events are searched for which have not been selected by the L4 finder 18, but fulfil all selection criteria of the final analyses. Events not selected by finder 18 can pass the online event selection if they are selected by one of the hard scales, a different finder or if they are among the fraction of rejected events which are kept for cross-checks (see section 2.6). Indeed a few events of the last type have been found for both analyses. A detailed investigation of the record of the L4 decision for each of these events has revealed that they have been classified as non-ep background events, because their vertex position as reconstructed on L4 is not compatible with an ep scattering event originating from the interaction region around 70 cm. They pass the final analysis selection as the offline vertex reconstruction gives a different result than the fast vertex reconstruction on the L4 filter farm. The fraction of rejected events taking into account the downscale factor is listed in table 4.5 for the two analyses. The downscaled events are excluded from the analysis and considered in the uncertainty on the online event selection. Consequently the latter contains the fraction of rejected events and the uncertainty on the subtrigger efficiency added in quadrature. It amounts to 0.9% for the BST and 0.7% for the BDC analysis, respectively.

Event Weights

As prescaling has been employed to account for the changing interaction rate during a luminosity fill weights have to be applied to the events of the data sample to obtain the original number of events.

In the case of the BST analysis only events are accepted which have been selected

by subtrigger S0, i.e. for which the actual bit of subtrigger S0 is set. Its run-dependent prescale factor is used as a weight for each event.

The BDC analysis uses the subtrigger S3 in addition. Therefore a more complicated strategy is necessary to avoid double counting: all events for which the actual bit of the subtrigger with the lower prescale for the given run is set are accepted. In addition events are kept if the actual bit of the subtrigger with the higher prescale is set, but not the raw bit of the subtrigger with the lower prescale. All remaining events are rejected. The prescale factor of the subtrigger responsible for the selection of an event is applied as a weight for this event. In this way the phase space of the cross-section measurement is divided into two non-overlapping regions with one subtrigger being uniquely assigned to each of them. Priority is given to the subtrigger with the lower prescale factor.

4.4 Alignment

A precise determination of the polar angle of the scattered electron is crucial for the reconstruction of the event kinematics as well as the definition of the fiducial volume covered by the analysis. This demands for an accurate knowledge of the position of the backward detectors SpaCal, BST and BDC. Therefore the alignment of the SpaCal and the BDC with respect to the H1 coordinate system is the topic of the present section, the alignment of the BST is discussed in [Laš04b]. Offsets in all three dimensions with respect to the nominal detector position are derived by comparing the angle measurement of the backward detectors and the Central Tracker with different methods. The resulting alignment constants for the SpaCal are cross-checked with QED Compton events.

Alignment with respect to the Central Tracker

The track reconstruction in the Central Tracker relies on the Central Jet Chambers CJC1 and CJC2 and the two z-chambers CIZ and COZ as mentioned in section 2.3. They define the H1 coordinate system and are already aligned with respect to each other in the data sample used for the analysis. Thus they are well suited to serve as a reference for the alignment of the SpaCal and the BDC.

A dedicated event sample has been used for the alignment being defined by the following selection criteria: only events are taken into account which have one electron candidate and one associated track in the Central Tracker[7]. In addition the same selection criteria are applied as for the trigger efficiency study in the previous section. For a further suppression of background events only electron candidates are considered with an energy $E_e > 20\,\text{GeV}$. To ensure a precise angle measurement in the Central Tracker cuts on the estimated error of the z-position of the vertex ($\sigma_{z_{vtx}} < 1\,\text{cm}$) and of the polar angle of the track ($\sigma_{\theta_{CT}} < 2\,\text{mrad}$) are placed. The former is more strict than the cut of $8\,\text{cm}$ to be used for the final analysis (see section 4.6), the latter ensures that

---

[7]To assign electron candidates and Central Tracker tracks the distance in the $r\phi$-plane between the position of the SpaCal cluster and the track extrapolated to the z-coordinate of the cluster is determined. If this does not exceed $10\,\text{cm}$ electron candidate and track are attributed to each other.
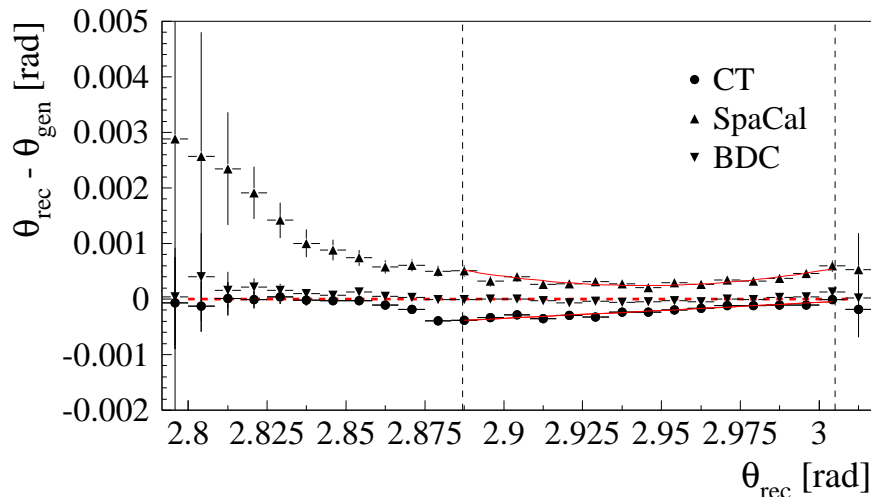
Figure 4.7: *Difference of the reconstructed and generated polar angle for Central Tracker, SpaCal and BDC. In the interval $2.887 < \theta < 3.005$ (indicated by the vertical dashed lines) a second order polynomial (solid lines) is fitted to the points for the Central Tracker and the SpaCal which is used as a correction function for the alignment (for details see text). The horizontal dashed line indicates the base line.*

the track has been linked to at least one of the z-chambers. For alignment methods which use the polar angle of the Central Tracker at least three of maximal eight linked hits in the z-chambers are required.

The polar and azimuthal angle as reconstructed by the SpaCal and the BDC are derived from the position of the cluster or track segment and the Central Tracker vertex assuming that the trajectory of the electron is a straight line. This is a good approximation for energies above 20 GeV. Nevertheless, the azimuthal angle is corrected for the influence of the magnetic field while its effect on the polar angle can be neglected [Mer05].

As a preparatory study for the alignment the reconstructed polar angles of Central Tracker, SpaCal and BDC are compared to the generated angle of the scattered electron for the Monte Carlo sample. This provides an important check as for the Monte Carlo the detector components are perfectly aligned by definition. Figure 4.7 shows the difference of the reconstructed and generated polar angle as a function of the reconstructed angle.

The polar angles as reconstructed by the SpaCal are systematically too large. The region of large discrepancies at low polar angles corresponds to the outer acceptance edge of the SpaCal. Here energy leakage beyond the active detector volume leads to a systematic shift of the cluster position towards the centre of the SpaCal. Furthermore the SpaCal possesses no segmentation in the z-direction such that the z-coordinate of the cluster is not measured, but calculated from a parameterisation (see section 3.3). In the case of the Central Tracker the polar angles are smaller than the generated ones. The situation improves for $\theta_{CT} < 2.88$ rad, because the electron enters the acceptance of the COZ. For larger values of θ the CJC track is only linked to hits of the CIZ. The BDC reconstruction shows no significant deviation from the generated quantities.

During the alignment systematic deviations of the polar angle reconstruction cannot

be distinguished from a misalignment of the detector components. Hence the polar angle range used for the alignment is restricted to the interval $2.887 < \theta < 3.005$ for which the differences between reconstructed and generated values are not too large. Furthermore correction functions are derived for the Central Tracker and the SpaCal by fitting a second order polynomial to the points in figure 4.7 for the specified interval. Both, the restriction of the polar angle range and the correction function are only applied for alignment methods which make use of the θ information.

The selected event sample together with the derived corrections is used in the following to determine the alignment constants Δx, Δy and Δz for the SpaCal and the BDC. The sign convention is the following: the alignment constants specify the shift of the detector component in the corresponding direction with respect to its nominal position, i.e. they have to be added to the cluster or track segment coordinates resulting from the reconstruction to calculate the position in the H1 coordinate system. Three different methods are employed for their determination:

- One possibility to derive alignment constants in x- and y-direction is to measure $R_{Spa/BDC}\Delta\phi_{Spa/BDC} = R_{Spa/BDC}(\phi_{Spa/BDC} - \phi_{CT})$ as a function of ϕ_{CT} where $R_{Spa/BDC}$ denotes the distance of the cluster or track segment from the origin of the SpaCal or BDC in the $r\phi$-plane [Mer05]. A sinusoidal shape of this distribution indicates a shift of the corresponding detector in the $r\phi$-plane. To quantify this shift one calculates the mean of $R\Delta\phi$ in slices of ϕ_{CT} with the help of a robust mean estimator [Yui90] and fits the following function to the resulting data points:

$$R\Delta\phi = P_1^{\Delta\phi}\sin(\phi_{CT} - P_2^{\Delta\phi}) + P_3^{\Delta\phi} \tag{4.2}$$

The alignment constants are finally obtained from the parameters $P_i^{\Delta\phi}$ of the fit in the following way:

$$\Delta x = P_1^{\Delta\phi}\cos P_2^{\Delta\phi}$$
$$\Delta y = P_1^{\Delta\phi}\sin P_2^{\Delta\phi}$$

The described alignment method is only used for the SpaCal as the BDC electron finder BDCLEV uses the R and z measurement of the BDC while ϕ stems from the SpaCal, i.e. the values of ϕ for SpaCal and BDC are the same (for details see section 3.3).

- An alternative approach to determine the alignment constants in x- and y-direction is to plot $\Delta R_{Spa/BDC} = R_{Spa/BDC} - R_{CT}$ as a function of ϕ_{CT}. The distance in the $r\phi$-plane R_{CT} of the Central Tracker track to the origin of the H1 coordinate system is calculated at the z-position of the SpaCal cluster or the BDC track segment. The resulting distribution is parameterised by the following function:

$$\Delta R = P_1^{\Delta R}\cos(\phi_{CT} - P_2^{\Delta R}) + P_3^{\Delta R} \tag{4.3}$$

The alignment constants are calculated with the help of:

$$\Delta x = -P_1^{\Delta R}\cos P_2^{\Delta R}$$
$$\Delta y = -P_1^{\Delta R}\sin P_2^{\Delta R}$$

Figure 4.8: *Distribution to derive alignment constants in x- and y-direction for the SpaCal using the Central Tracker as a reference. The accuracy of the Central Tracker information for this alignment method is mainly driven by the hits in the CJCs. To extract the alignment constants a sinus function according to equation 4.2 is fitted to the data (solid line).*

The two methods used to extract Δx and Δy are complementary: the difference in the azimuthal angle $\Delta\phi$ is mainly determined by the CJC as this has a better ϕ-resolution, whereas ΔR is driven by the accurate z-measurement of CIZ and COZ. Comparing the results of both methods constitutes an important consistency check for the alignment.

• To obtain the z-position of SpaCal and BDC a method proposed in [Mer05] is used: $F_{Spa/BDC}\Delta\theta_{Spa/BDC} = F_{Spa/BDC}(\theta_{Spa/BDC} - \theta_{CT})$ is measured as a function of ϕ_{CT}, $F_{Spa/BDC}$ being defined as:

$$F = \frac{z^2}{R} \cdot \frac{1}{(\frac{R}{z})^2 - (\frac{R}{z})^4 + (\frac{R}{z})^6 - 1}$$

The subscript Spa/BDC has been omitted for all variables, $z_{Spa/BDC}$ is the z-coordinate of the SpaCal cluster or BDC track segment. A fit is performed using the function:

$$F\Delta\theta = P_1^{\Delta\theta}\sin(\phi_{CT} - P_2^{\Delta\theta}) + P_3^{\Delta\theta} \tag{4.4}$$

The negative of $P_3^{\Delta\theta}$ is the sought-after alignment constant in z-direction.

The underlying distributions for the different methods are shown in figures 4.8 - 4.10, table 4.6 summarises the alignment constants. The results are discussed at the end of this section.

Alignment with QED Compton Events

QED Compton events have been introduced in section 1.7. They are characterised by an electron and a photon in the final state which have sizeable transverse momenta and are
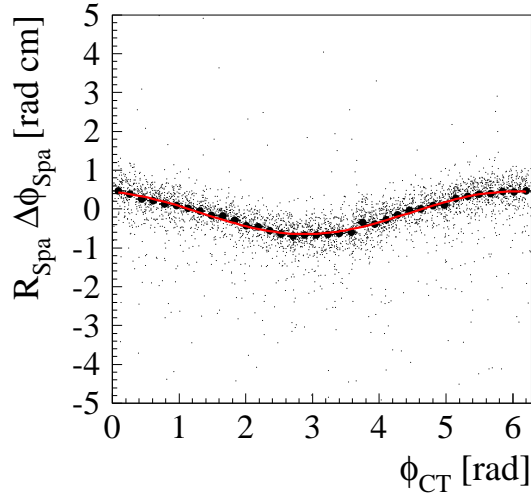
Figure 4.9: *Distributions to derive alignment constants in x- and y-direction for a) the SpaCal and b) the BDC using the Central Tracker as a reference. The accuracy of the Central Tracker information for this alignment method is mainly driven by the hits in the z-chambers. To extract the alignment constants a cosinus function according to equation 4.3 is fitted to the data (solid lines).*
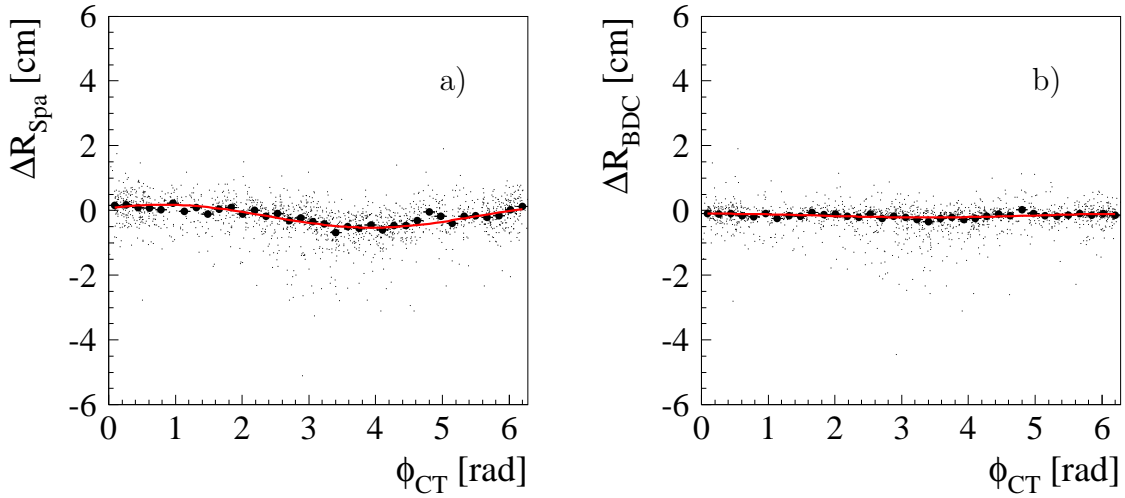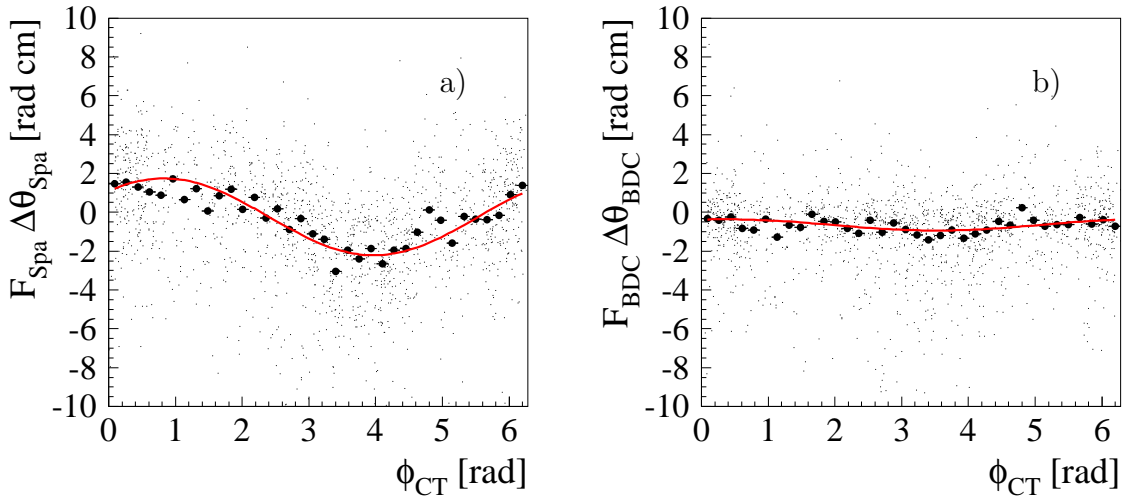

Figure 4.10: *Distributions to derive alignment constants in z-direction for a) the SpaCal and b) the BDC using the Central Tracker as a reference. To extract the alignment constants a sinus function according to equation 4.4 is fitted to the data (solid lines).*

method	SpaCal			BDC		
	Δx [cm]	Δy [cm]	Δz [cm]	Δx [cm]	Δy [cm]	Δz [cm]
$R\Delta\phi$	-0.14	-0.53	-	-	-	-
ΔR	-0.25	-0.26	-	-0.06	-0.01	-
$F\Delta\theta$	-	-	0.23	-	-	0.65
QEDC	-0.08	-0.34	-	-	-	-

Table 4.6: *Summary of the alignment constants for the SpaCal and the BDC derived from different methods using the Central Tracker as a reference or QEDC events.*

back-to-back in the azimuthal plane. Thus they can be detected as two electromagnetic clusters in the SpaCal with a difference in the azimuthal angle $\Delta\phi = |\phi_1 - \phi_2|$ close to 180°. A useful variable to select QEDC events is the *acoplanarity A* being defined as

$$A = |\Delta\phi - 180°|$$

To derive alignment constants with the help of QEDC events, as proposed in [Sta98], one defines the actual position of the SpaCal in the H1 coordinate as the position for which the summed acoplanarity of all QEDC events is minimal. Technically this is done by performing a χ^2 minimisation of the expression

$$\chi^2 = \sum_{\text{events}} \frac{A^2}{\sigma_A^2}$$

with

$$\sigma_A^2 = \frac{y_1^2\sigma_x^2 + x_1^2\sigma_y^2}{(x_1^2 + y_1^2)^2} + \frac{y_2^2\sigma_x^2 + x_2^2\sigma_y^2}{(x_2^2 + y_2^2)^2}$$

Here x_1, y_1 and x_2, y_2 are the coordinates of the electron and the photon cluster, respectively, corrected for the effects of beam offset and tilt. The average spatial resolution parameters σ_x and σ_y are set to 0.3 cm. For the alignment with QEDC events the x- and y-coordinates are measured w.r.t. the origin of the SpaCal which does not coincide with the origin of the H1 coordinate system in the xy-plane due to the misalignment.

For the alignment elastic QEDC events are used as they are characterised by a smaller acoplanarity than inelastic ones. The applied selection criteria follow a detailed investigation in [Len01]:

- acoplanarity
$$A < 10°$$

- energies E_1 and E_2 of the cluster with the highest and second highest energy in the SpaCal
$$E_1 > 10 \,\text{GeV} \qquad E_2 > 4 \,\text{GeV} \qquad 20 \,\text{GeV} < E_1 + E_2 < 32 \,\text{GeV}$$

- residual energy in the electromagnetic section of the SpaCal

$$E_{res} = E_{tot} - E_1 - E_2 < 1 \, \text{GeV}$$

where E_{tot} denotes the total energy in the electromagnetic SpaCal

- logarithmic cluster radius of the two SpaCal clusters

$$r_{Cl,1} < 4.5 \, \text{cm} \qquad r_{Cl,2} < 4.5 \, \text{cm}$$

- rejection of events with a Central Tracker vertex fulfilling

$$|z_{vtx} - \overline{z_{vtx}}| > 30 \, \text{cm}$$

if the vertex accuracy $\sigma_{z_{vtx}}$ is better than $8 \, \text{cm}$

The z-vertex cut ensures that events most likely being caused by beam induced background are excluded from the analysis. Events having no reconstructed vertex are accepted. This has no negative influence on the χ^2 minimisation as no z-information is needed.

Performing the minimisation for the selected QEDC sample leads to the alignment constants given in table 4.6. To check the result one visualises the QEDC events in the following way: the cluster positions of electron and photon in the SpaCal are connected by a line in the $r\phi$-plane for all events and the line density is plotted. The maximum indicates the intersection point of the beam with the surface of the SpaCal. For a perfectly aligned SpaCal its x- and y-coordinates should be $(0,0)$. Figure 4.11 shows the line density before and after the alignment. Indeed the maximum of the line density indicates a good alignment of the SpaCal.

In principle a similar study can be performed for the BDC as a track can be reconstructed for QEDC photons with a probability of approximately 60% [Len01]. The main reason for this are photon conversions into electron-positron pairs while passing the material of the beam pipe or the chamber walls. However, such a study does not make sense as the ϕ-information stems from the SpaCal anyhow.

Discussion and Combination of the Results

If one considers the alignment constants in table 4.6 obtained from the different methods the following conclusions can be drawn: the results for the alignment constants Δx and Δy for the SpaCal do not agree with each other, the disagreement being larger for the y-direction. The errors resulting from the fits in the case of the comparison to the Central Tracker and the χ^2 minimisation for the QEDC events are negligible compared to the differences between the approaches. Similar discrepancies have been reported before and have been investigated in detail in [Mer05], unfortunately without a decisive explanation. The difference of the two Central Tracker results may point to a problem concerning the internal alignment of the Central Tracker. For the minimum bias run in 1999 a difference of $2 \, \text{mm}$ for Δy is observed between the $R\Delta\phi$ and the ΔR method [Gla06] which is in agreement with the present analysis. The alignment with QEDC events provides a value of Δy in between the two Central Tracker results as well.

A number of cross-checks has been performed to test the alignment procedure:
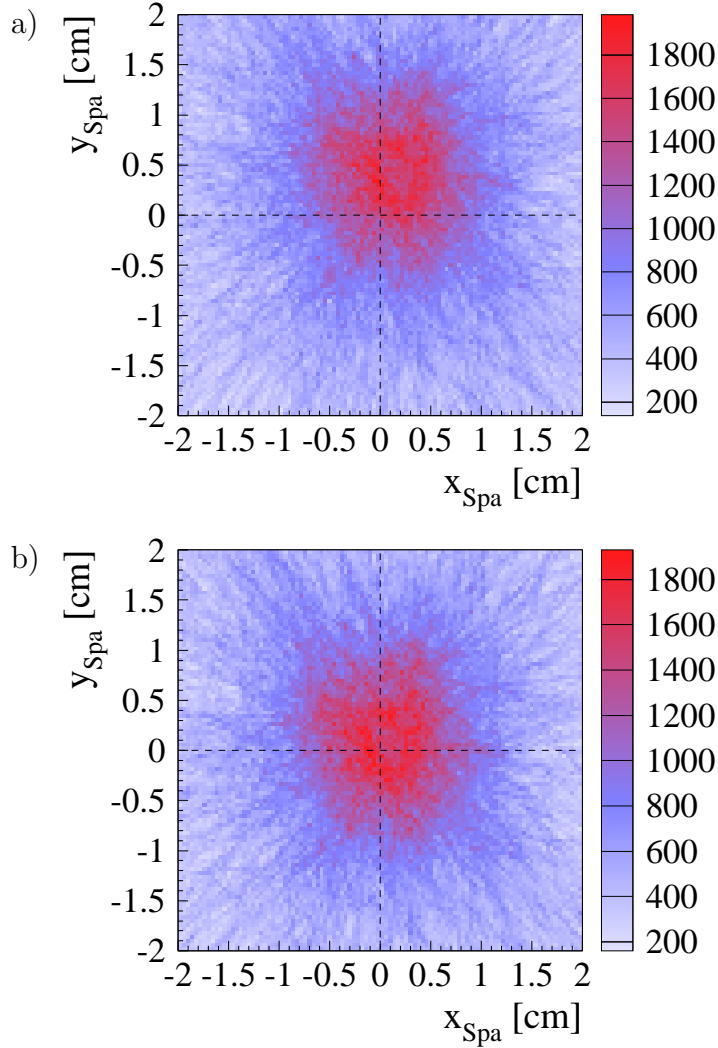
Figure 4.11: *Density of lines connecting the electron and the photon cluster of QED Compton events in the SpaCal a) before and b) after the alignment with QED Compton events.*

- The results of the different approaches for the Monte Carlo sample have been checked. They are consistent with 0, only the $F\Delta\theta$ method yields $\Delta z = 0.1\,\mathrm{cm}$ and the QEDC method $\Delta y = -0.1\,\mathrm{cm}$ for the SpaCal.

- A misalignment has been introduced for the Monte Carlo sample. All methods determine this with high precision apart from the χ^2 minimisation for QED Compton events which gives $\Delta y = -0.2\,\mathrm{cm}$ though a $0.4\,\mathrm{cm}$ shift has been applied. However, the density line plot indicates a shift of $0.4\,\mathrm{cm}$.

- To test the stability of the methods the alignment constants have been applied and the analysis has been repeated. All methods provide results consistent with zero as expected, only the QEDC method claims $\Delta y = -0.1\,\mathrm{cm}$.

The χ^2 minimisation for the QEDC events seems not to find the global minimum. Therefore the QEDC alignment is not considered further.

detector	Δx [cm]	Δy [cm]	Δz [cm]
SpaCal	-0.19 ± 0.06	-0.39 ± 0.14	0.23 ± 0.36
BDC	-	-	0.65 ± 0.15

Table 4.7: *Alignment constants to be applied to the final analysis obtained by combining the different alignment methods (for details see text).*

Figure 4.12: *Comparison of the polar angle reconstruction of the Central Tracker and the BDC after the alignment. The solid line represents the fit of a Gaussian to the distribution.*

The alignment constants to be applied to the final analysis are derived in the following way: in the case of the SpaCal the average of the $R\Delta\phi$ and the ΔR method is taken for Δx and Δy, half of the difference is used as the error. The results of the ΔR method for the BDC are compati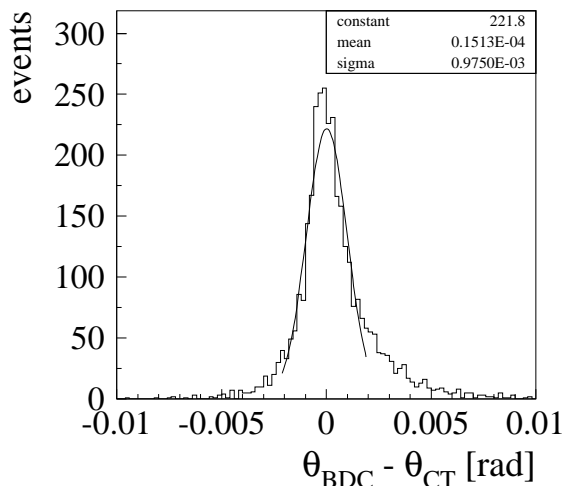ble with 0. Thus no alignment in the $r\phi$-plane is needed to improve the θ measurement of the BDC. To obtain an error for Δz the alignment is repeated without applying correction functions for θ as reconstructed by the Central Tracker and the SpaCal. Half of the difference to the nominal alignment is used as the error. The alignment constants to be used for the final analysis are collected in table 4.7.

The uncertainty on the polar angle reconstruction of the BDC is the figure of merit to be derived from the alignment study for the final analysis. Therefore the polar angles as reconstructed by the BDC and the Central Tracker are compared with the alignment constants being applied. To have a sample of events as close as possible to the one which is used for the final analysis the cut on the energy of the scattered electron is relaxed to $7\,\text{GeV}$. Figure 4.12 shows the distribution of $\Delta\theta = \theta_{BDC} - \theta_{CT}$. No residual systematic shift between the Central Tracker and the BDC is observed. The tail towards larger values of $\Delta\theta$ is caused by electrons showering in the dead material behind the Central Tracker. This can be concluded from comparing the distribution of $\Delta\theta$ for events with small and large hit multiplicities in the BDC. A similar effect has been observed in [Kel98] when comparing the polar angle measurement of the BDC and the BST. The Monte Carlo sample shows an analogous behaviour. With the error of the alignment constant Δy for the SpaCal (see table 4.7) being the dominant uncertainty on θ as reconstructed by the BDC the latter has been determined to be $\sigma_\theta = 0.5\,\text{mrad}$.

4.5 Calibration

Both the energy of the scattered electron and the hadronic final state affect the reconstruction of the event kinematics. The former directly enters the formulas necessary to calculate y and Q^2 based on the electron method, the latter affects the quantity Σ essential for the sigma method (see section 3.2). Therefore a precise calibration of both energies is necessary. In the case of the electron energy this implies a calibration of the electromagnetic section of the SpaCal. For a precise measurement of the energy of the hadronic final state the hadronic section of the SpaCal as well as the electromagnetic and hadronic part of the LAr calorimeter have to be accurately calibrated in addition. This complex task has been fulfilled in [Var06], a short overview of which is given in the chapter at hand[8].

Scattered Electron

As explained in section 3.3 the energy of the scattered electron is reconstructed in the electromagnetic section of the SpaCal. The largest challenge for the calibration of the latter is the control of the fluctuations of its 1192 photomultipliers. This starts already during data taking. A special LED system sending well-defined light pulses to each photomultiplier monitors potential time-dependent instabilities such that they can be corrected for [Jan96, Mey96]. Subsequently the inner cells of the SpaCal are pre-calibrated with the help of the so-called *kinematic peak* method [Jan95]. It makes use of the fact that the energy distribution of the scattered electron for low Q^2 DIS events shows a prominent maximum close to the electron beam energy. Since the method requires large statistics, the outer part of the SpaCal ($R_e \gtrsim 50\,\mathrm{cm}$) has instead been pre-calibrated with the help of muons originating from cosmic rays [Dir96] or proton beam halo events [Arn95].

A precise calibration on analysis level is provided by a method originally proposed in [Gla98a]. It uses the energy of the scattered electron reconstructed with the help of the so-called *double angle method* as a reference. This reconstruction method expresses the kinematic variables y and Q^2 in terms of the polar angle θ_e of the scattered electron, the hadron angle θ_h and the electron beam energy E_e^0:

$$y_{DA} = \frac{\tan(\theta_h/2)}{\tan(\theta_e/2) + \tan(\theta_h/2)} \tag{4.5}$$

$$Q_{DA}^2 = 4(E_e^0)^2 \frac{\cot(\theta_e/2)}{\tan(\theta_e/2) + \tan(\theta_h/2)} \tag{4.6}$$

Based on these equations the energy of the scattered electron is calculated to

$$E_{DA} = E_e^0 \frac{1 - y_{DA}}{\sin^2(\theta_e/2)} \tag{4.7}$$

With the double angle energy E_{DA} a reference energy for the calibration is available which is to first order insensitive to the energy measurement in the SpaCal and LAr calorimeters. The double angle method reveals a good resolution for medium values

---

[8]Unless stated differently all results presented in this chapter are taken from [Var06].

of y ($0.05 < y < 0.2$) [Bas95b]. Therefore events are selected for the calibration which fulfil the requirement $15° < \theta_h < 80°$. The lower limit suppresses energy losses in the forward region of the LAr calorimeter, the upper limit restricts y to maximum values of approximately 0.15. Only events with a single electron candidate matching the cuts $20\,\mathrm{GeV} < E_e < 32\,\mathrm{GeV}$ and $r_{Cl} < 4\,\mathrm{cm}$ are accepted, i.e. the calibration sample should contain almost no photoproduction events. The polar angle of the scattered electron is reconstructed with the BST or the BDC. If both backward trackers validate the SpaCal cluster the BST information is preferred. The z-position of the interaction vertex is restricted to an interval of 30 cm around the nominal position $\overline{z_{vtx}}$.

The energy of the cluster E_{Spa} as reconstructed by the SpaCal is the sum of the energies E_i in the individual cells belonging to it:

$$E_{Spa} = \sum_i E_i \tag{4.8}$$

Based on this the so-called event pull δ_{ev} is calculated

$$\delta_{ev} = \frac{E_{DA}}{E_{Spa}} \tag{4.9}$$

which is investigated as a function of various variables to derive a sequence of corrections to be applied for a precise energy measurement.

In a first step calibration constants are derived for each cell of the SpaCal calorimeter. The event pull δ_{ev} cannot be attributed to a single cell since SpaCal clusters typically extend over several cells. Therefore the following procedure is used: for each SpaCal cell a histogram is booked capable of storing a distribution of δ_{ev}. In each event δ_{ev} is filled to the histograms of all cells belonging to the cluster with a weight E_i/E_{Spa}. The distribution of δ_{ev} for each SpaCal cell should have a mean value of one for a perfectly calibrated calorimeter. Hence the mean pull δ_i is determined for each SpaCal cell and used as a correction factor. For this purpose the same robust mean estimator [Yui90] is employed as for the alignment.

During the filling of the histograms the same event pull δ_{ev} is attributed to each cell. In order to separate the influence of the individual cells several iterations are necessary applying in each iteration step the results from the previous ones. After eight iterations the changes are below 0.1% and the final cell-wise calibration constants are derived. They correct the energy measurement by $2 - 3\%$.

Three additional corrections are derived afterwards having a significantly smaller influence on the energy measurement: to account for energy losses at the cell and super-module borders of the SpaCal δ_{ev} is investigated as a function of the cluster position relative to the centre of the cell with the largest energy deposition (inbox correction) and as a function of $R_{box} = \max(|x_{Spa}|, |y_{Spa}|)$ (crack correction)[9]. Finally losses in the dead material in front of the calorimeter are compensated by deriving a correction as a function of R_e (radial correction).

The same calibration procedure is carried out for data and Monte Carlo simulation. It turned out that the resolution for the Monte Carlo sample is better than for the data sample. Therefore the reconstructed energy of the Monte Carlo is smeared by 0.2%

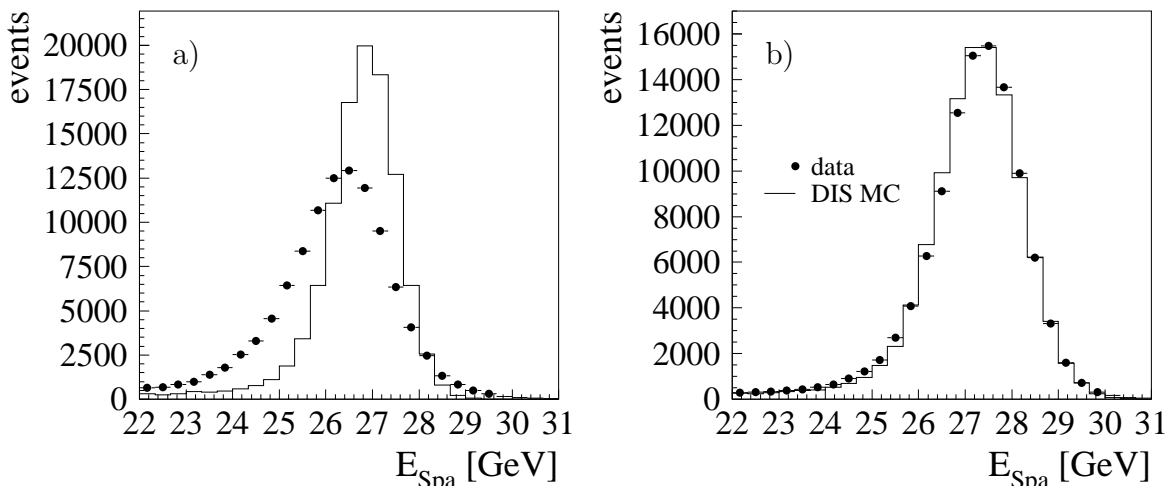[9]The variable R_{box} has been introduced in section 4.3

Figure 4.13: *Energy distribution of the scattered electron as reconstructed by the SpaCal a) before and b) after the calibration [Var06]. In the case of b) the energy of the Monte Carlo is additionally smeared by 0.2%.*

to ensure good agreement with the data. Figure 4.13 shows the energy distribution of the scattered electron for the calibration sample a) before the calibration and b) after applying all derived corrections and smearing the Monte Carlo. It can be seen that the calibration improves the agreement between data and Monte Carlo significantly. The uncertainty on the energy scale of the scattered electron is estimated by comparing δ_{ev} as a function of R_e between data and Monte Carlo after applying all corrections. The differences are well compatible with a systematic uncertainty of 0.2%.

The event sample used for the calibration with the double angle method is restricted to large energies. To check the applicability of the calibration at low energies, i.e. the linearity of the SpaCal response, the invariant mass of π^0 mesons decaying into two photons is studied[10]. Comparing the mass spectrum between data and Monte Carlo shows that the energy response of the SpaCal in the Monte Carlo has to be reduced by 2.5% to achieve a good agreement. The uncertainty on this correction is determined to 1% by studying the dependence of the energy scale on the energy of the photon with the higher and lower energy, respectively as well as on the distance of the two photon clusters. These values are attributed to an energy of $2\,\text{GeV}$ since this is the average energy of the decay photons.

From figure 4.13 b) it can be seen that no additional correction to the energy scale on top of the double angle calibration is necessary at larger energies. The uncertainty on the energy scale of 0.2% already identified in the study of δ_{ev} is attributed to an energy of $27.6\,\text{GeV}$ since the energy distribution should have its maximum close to the electron beam energy as explained at the beginning of this section.

Hence the corrections for the energy scale of the scattered electron and the corre-

---

[10]In contrast to the standard cross-section analysis the required cluster energy for this study is so small that for a considerable fraction of the events the opening angle between the two photons is sufficiently large to detect them as two separate clusters in the SpaCal.

electromagnetic section	hadronic section	reference
1.1	1.3	[Zho95]
1.5	1.5	[Mey97, Gla98a]
1.07	1.07	[Mey97]

Table 4.8: *Corrections factors to the hadronic energy scale of the SpaCal calorimeter.*

sponding uncertainties can be summarised as follows:

$$2.5\% \pm 1.0\% \qquad \text{at } E_e = 2\,\text{GeV} \qquad\qquad (4.10)$$

$$0.0\% \pm 0.2\% \qquad \text{at } E_e = 27.6\,\text{GeV} \qquad\quad (4.11)$$

For correction and uncertainty a linear interpolation is used for intermediate energies.

Hadronic Final State

The calibration procedure to ensure a precise reconstruction of the hadronic final state starts with an investigation of the hadronic energy scale of the SpaCal. This comprises both the electromagnetic and the hadronic section of the SpaCal since hadron showers occupy both of them. Several correction factors to the hadronic energy scale have been derived prior to [Var06] and provide the starting point for the study to be presented in the following. They are listed in table 4.8 separately for the electromagnetic and hadronic section. The corresponding references are listed in addition, an overview can be also found in [Ark00]. The product of the correction factors is applied for both data and Monte Carlo to each cell which does not belong to the electron candidate.

A final correction is derived using the already calibrated energy of the scattered electron as a reference. For this purpose events with $y_e > 0.5$ are selected. In this region of the phase space y_h is almost exclusively determined by the hadrons reconstructed in the SpaCal (see figure 3.7). Therefore a comparison of the ratio y_h/y_e reveals differences of the hadronic energy scale between data and Monte Carlo. Since the amount of photoproduction background events is large at high y only events with $E - p_z > 35\,\text{GeV}$ are accepted. This cut suppresses the photoproduction contribution as is explained in the next section. Indeed a shift in the distribution of y_h/y_e between data and simulation is observed. This is accounted for by applying a correction factor of 0.97 to the Monte Carlo. This corresponds to a shift of 700 MeV. Half of the shift, i.e. 350 MeV is assumed to be the uncertainty on the hadronic energy scale of the SpaCal.

The hadronic energy flow in the LAr is distributed over large areas and thus it is impossible to select individual hadrons for the calibration. Therefore global quantities have to be employed. An elegant method to make use of transverse momentum conservation (see equation 3.5) for the calibration is the *Lagrangian method* developed in [Ark00]. The method utilises the compensation of the transverse momenta of the scattered electron and the hadronic final state via the minimisation of the following functional:

$$\mathcal{L} = \sum_{i=1}^{N} \left(p_{t,e}^i - \left(p_{t,CT}^i + p_{t,Spa}^i - p_{t,noise}^i \right) - \sum_{j=1}^{M} \alpha_j p_{t,LAr}^{ji} \right)^2 \qquad (4.12)$$

source	uncertainty
hadronic SpaCal	350 MeV
hadronic energy scale LAr and CT	10% at $y = 10^{-3}$
	2% at $y = 10^{-2}$
LAr noise	10%

Table 4.9: *Uncertainties on the reconstruction of the hadronic final state.*

The outer summation is performed over all events, the index i is omitted for the following discussion. The transverse momentum $p_{t,e}$ of the scattered electron constitutes the reference. All other transverse momenta are projected on the electron direction such that the minimisation can be performed in one dimension. To the transverse momentum of the hadronic final state $p_{t,h}$ several subdetectors contribute according to the explanations at the end of section 3.3. These are the SpaCal ($p_{t,Spa}$), the Central Tracker ($p_{t,CT}$) and the LAr calorimeter. Since the latter is to be calibrated the corresponding transverse momentum is split to the level of the individual modules. The variable $p_{t,LAr}^{j}$ denotes the transverse momentum of the module j and α_j its calibration constant to be determined by the minimisation of $\mathcal{L}$. The transverse momentum $p_{t,noise}$ corresponding to the noise in the LAr calorimeter is subtracted. For the combination of the LAr and Central Tracker information as well as the noise identification the FSCOMB algorithm (see section 3.3) is employed.

The LAr calorimeter is build of eight wheels with eight octants each. One of the wheels (BBE) has only one section, all others have two sections (see figure 2.8). Hence $M = 120$ calibration constants α_j have to be determined. The minimisation requirement

$$\frac{\partial \mathcal{L}}{\partial \alpha_j} = 0 \tag{4.13}$$

defines a set of M linear equations to be solved using matrix techniques.

Figure 4.14 shows a comparison of the distribution of the quantity $p_{t,bal} = p_{t,had}/p_{t,e}$ between data and Monte Carlo for two intervals in y_Σ. All calibration constants derived in this section are applied. For medium values of y_Σ the agreement is perfect and the maximum of the distribution is located at one as expected. At low y_Σ the distribution is significantly shifted towards lower values of $p_{t,bal}$ since hadrons escape detection in the forward region of the LAr calorimeter. In addition a discrepancy between data and Monte Carlo occurs. This behaviour is reflected in the uncertainty on the hadronic energy scale of the LAr calorimeter. It amounts to 10% at $y = 10^{-3}$ and is linearly interpolated in $\ln y$ to 2% at $y = 10^{-2}$. For values above $y = 10^{-2}$ it stays at 2%. The same uncertainty is assumed for the Central Tracker. It has been derived by varying the contribution of LAr and Central Tracker and investigating the agreement between data and Monte Carlo in figure 3.7. In the same way the uncertainty on the noise contribution in the LAr calorimeter has been determined to be 10%. Table 4.9 summarises all uncertainties attributed to the reconstruction of the hadronic final state.
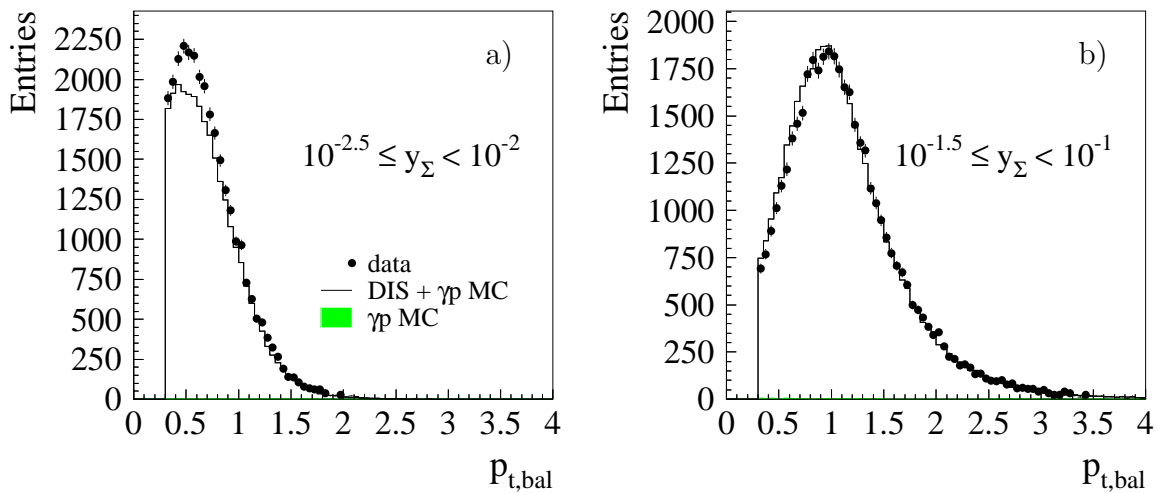
Figure 4.14: *Distribution of $p_{t,bal} = p_{t,had}/p_{t,e}$ for two intervals of y_Σ after application of all correction constants [Var06].*

4.6 DIS Event Selection

The aim of the event selection is to provide a sample of events for the cross-section determination which contains only a small fraction of background events while keeping the number of selection criteria as small as possible. The latter requirement should minimise the loss of signal events and the influence of Monte Carlo reconstruction efficiencies.

Background contributions to the cross-section measurement arise from photoproduction events and interactions of the proton or electron beam particles with the residual gas molecules or the beam pipe walls (see section 3.4). Most of the latter are already rejected during the online event selection due to the requirements concerning the timing and energy depositions in the SpaCal.

The selection criteria applied for the BST and BDC analyses (see table 4.10) are well established as they have been used in various previous analyses. Therefore the values of the cuts are not investigated in detail, but their selection and rejection power is compared between data and Monte Carlo samples for signal and background events, respectively. Here only the BDC analysis in covered, a similar study for the BST analysis can be found in [Var06]. An agreement between data and simulation is essential for the cross-section measurement as explained in the introduction to this chapter.

Explanation of the Selection Criteria

Restricting the z-coordinate of the interaction vertex to an interval of $30\,\text{cm}$ around the nominal vertex position $\overline{z_{vtx}} = 71.9\,\text{cm}$ (see section 4.7) rejects beam-induced background events. Contributions from the satellite bunches being separated by $\pm 72\,\text{cm}$ from the main bunch are removed in addition. This is of importance as the satellite bunches are not considered in the Monte Carlo simulations. The uncertainty on the z-position is required to be smaller than $8\,\text{cm}$ and thus the maximal allowed value is significantly larger than the resolution of $1\,\text{cm}$ quoted in section 3.3. This is appropriate since according to [Gla06] a resolution of $1\,\text{cm}$ can only be reached for events with

selection criterion		BST analysis	BDC analysis
vertex	position	$\|z_{vtx} - \overline{z_{vtx}}\| < 30\,\mathrm{cm}$	
	precision	-	$\sigma_{z_{vtx}} < 8\,\mathrm{cm}$
	type	BST	Central Tracker
cluster properties	energy	$E_e > 7\,\mathrm{GeV}$	
	radius	$r_{Cl} < 4\,\mathrm{cm}, \quad r_{Cl}^{lin} < 3.8\,\mathrm{cm}$	
	hadronic fraction	$f_{had} < 0.15$	
	veto cell energy	$E_{veto} < 1\,\mathrm{GeV}$	
track validation	number of linked hits	$N_{hits} \geq 3$	$N_{hits} \geq 4$
	total number of hits	$N_{hits}^{total} < 200$	-
	track - cluster match	$\Delta R < 1.5\,\mathrm{cm}$	
	type	BST	BDC
kinematics		$E - p_z > 35\,\mathrm{GeV}$ (electron method only)	
		$p_{t,bal} > 0.3$	$y_\Sigma > 0.03$
rejection of elastic QEDC events		✓	✓
fiducial cuts	acceptance	$R_e > 10\,\mathrm{cm}$	$R_e > 9\,\mathrm{cm}$
	trigger	$R_{box} > 10\,\mathrm{cm}$ (BDC: only for $E_e < 14\,\mathrm{GeV}$)	
		excl. cells: 7,8,13,14,30,32,33,62,250,253,306,763	
	hot spot	$R_e > 11.5\,\mathrm{cm}$ for $-6.5\,\mathrm{cm} < y < 7.5\,\mathrm{cm}$	
		excl. cells: 4,5,6,11,12	
	energy spectrum	excl. cell: 29	

Table 4.10: *Selection criteria for the BST and BDC analyses (for details see text). The position of the individual SpaCal cells is shown in appendix B.*

a large number of tracks reconstructed in the Central Tracker. Hence a harsher cut would reject a significant fraction of events at low y for which only a few particles per event enter the acceptance of the Central Tracker.

From the clusters validated by the BDC or BST electron finder the one with the largest energy fulfilling the selection criteria concerning the cluster properties and track validation is chosen to be the electron candidate (see section 3.3).

Photoproduction events can be misinterpreted as signal events if a particle of the hadronic final state mimics the scattered electron (see section 3.4). Significant contributions stem from neutral π mesons and charged hadrons. The former predominantly decay into two photons and thus induce electromagnetic showers in the SpaCal. Moreover, a large fraction of the decay photons converts into e^+e^- pairs while interacting with the detector material and causes signals in the backward trackers. Also purely hadronic showers can be classified as electromagnetic due to statistical fluctuations in the shower development. In general, hadron induced clusters are less compact than electron or photon induced ones.

Thus the contribution of charged hadrons can be reduced by selection criteria based on the transverse and longitudinal shower shape. Detailed studies in [Gla98a] and [Eck02] have shown that a cut on the logarithmic cluster radius $r_{Cl} < 4\,\mathrm{cm}$ rejects a significant fraction of the photoproduction events while accepting electron induced clusters. The rejection comprises π^0 mesons as for cluster energies considered in this analysis the opening angle is too small for the two decay photons to be detected as separate clusters in the SpaCal. Thus both photons are reconstructed as a single broad cluster.

The SpaCal is designed such that electron induced showers with an energy up to $30\,\mathrm{GeV}$ are fully contained in the electromagnetic section. However, for hadrons the electromagnetic section constitutes only one nuclear interaction length such that their showers reach the hadronic section of the SpaCal. Therefore clusters are considered to be hadron induced if the energy fraction f_{had} deposited in the hadronic section of the SpaCal within a cylindrical volume of $15\,\mathrm{cm}$ radius behind the cluster identified in the electromagnetic section exceeds 15% of the total cluster energy.

A further suppression of photoproduction events is achieved by placing a cut on the track cluster matching ΔR which is the distance of the SpaCal cluster in the $r\phi$-plane to the track of the BST or BDC extrapolated to the z-position of the cluster. Photons not converted before the BST or BDC cannot fulfil the selection criterion as they do not produce a track. As photon conversions in the dead material behind the Central Tracker do only lead to a signal in the BDC but not in the BST, the cut is more efficient for the BST analysis in this respect. Charged hadrons may also fail to match the requirement on ΔR since the fluctuations of the energy deposited by them in the electromagnetic section of the SpaCal is large which may lead to a significantly misreconstructed cluster position.

At least three (four) hits have to be linked to the track of the electron candidate for the BST (BDC) analysis. This requirement ensures a good track resolution and suppresses accidental validations of SpaCal clusters due to noise hits. The cut $N_{hits}^{total} < 200$ keeps the overall level of noise in the BST at a reasonable level.

The quantity $E - p_z = \Sigma + E_e(1 - \cos\theta_e)$ should be equal to $2E_e^0 = 55.2\,\mathrm{GeV}$ due to energy and momentum conservation (see section 3.2). For photoproduction events it is

likely to be smaller than $2E_e^0$ as the electron is scattered below the SpaCal acceptance and the SpaCal cluster is a misidentified hadron. However, also in initial state radiation events $E - p_z$ has lower values as the photon escapes through the beam pipe undetected decreasing $E - p_z$ by twice its energy. Therefore the cut $E - p_z > 35\,\text{GeV}$ is applied if the event kinematics is reconstructed with the help of the electron method but not if the sigma method is used. This is due the fact that ISR events are reconstructed correctly by the sigma method and allow for a significant extension of the accessible kinematic phase space while they are reconstructed wrongly by the electron method (see detailed discussion in the previous chapter).

In earlier analyses a significant discrepancy between data and Monte Carlo simulation at low values of the ratio $p_{t,bal} = p_{t,had}/p_{t,e}$ of the transverse momenta of the hadronic final state $p_{t,had}$ and the scattered electron $p_{t,e}$ has been observed [Laš04b, Ark00]. Low values of $p_{t,bal}$ characterise events in which particles of the hadronic final state are scattered outside the acceptance limits of the H1 detector leading to energy losses and thus low values of $p_{t,had}$. In the low Q^2 regime the losses become especially pronounced at low values of y (large values of x) where the hadronic final state particles are partially scattered below the forward modules of the LAr calorimeter. In this region of the phase space the squared centre of mass energy W^2 of the photon-proton system becomes very small indicating that the resonance region is reached. The latter has not been included in previous versions of the DJANGO generator. Thus the fraction of events at low values of $p_{t,bal}$ is significantly too small in the Monte Carlo sample. A cut $p_{t,bal} > 0.3$ has been applied to exclude the problematic region of the kinematic phase space. For the present analysis a new version of DJANGO has been used to overcome the problem, it includes the SOPHIA model allowing to generate nuclear resonances (see section 3.5). The agreement between data and Monte Carlo has indeed improved, but is still not sufficient. Hence the cut has to be sustained [Var06].

However, for the BDC analysis there is no need for a rejection of events based on $p_{t,bal}$ as the low y region is avoided by the y_Σ cut. The latter guarantees a vertex reconstruction efficiency above 50% as discussed in the forthcoming section. Another missing contribution of the DJANGO generator are elastic QEDC events as already mentioned in section 3.5. Therefore elastic QEDC events are rejected using similar cuts as for the SpaCal alignment based on QEDC events described in the previous section.

Several analysis cuts result from the investigation of the online event selection in section 4.3: for the BST analysis only events selected by subtrigger S0 are accepted, the BDC analysis makes use of subtrigger S3 in addition. The energy threshold and the L2 condition of S0 motivate the rejection of electron candidates with energies below $7\,\text{GeV}$ and the exclusion of a square with a side length of $10\,\text{cm}$ from the inner SpaCal. In the case of the BDC analysis the latter is only excluded for energies below $14\,\text{GeV}$ as subtrigger S3 is used in addition. The cells indicated in table 4.10 are not considered in the analysis either because they have been a priori excluded from the trigger or reveal bad efficiencies[11]. The cut on the linear cluster radius $r_{Cl}^{lin} < 3.8\,\text{cm}$ accounts for the corresponding selection criterion on trigger level L4 (see table 4.4). The additional rejection of events compared to the cut on the logarithmic cluster radius is negligible.

---

[11]The cells 30 and 62 exhibit a lower efficiency as their threshold is slightly higher than the nominal one. As they contribute significantly to the statistics of the measurement they have been only excluded for energies below the threshold.

Only events are accepted for which the distance of the electron track to the beam axis R_e in the plane $z = -160.5\,\text{cm}$ is larger than $10\,\text{cm}$ and $9\,\text{cm}$ for the BST and BDC analysis, respectively[12]. In the case of the BST the acceptance gets lower than 50% for larger polar angles [H1]. For the BDC analysis the cut excludes the region very close to the beam pipe which exhibits energy leakage effects and a deterioration of the spatial resolution of BDC and SpaCal. A cut of $8.7\,\text{cm}$ has been used in previous analyses [Kat97, Mey97]. The contribution of events affected by leakage effects is suppressed further by restricting the energy deposition E_{veto} in the veto cells of the SpaCal to $1\,\text{GeV}$.

In section 4.3 it has been mentioned that the SpaCal cells 7, 8, 13, 14, 32 and 33 (see appendix B) have been excluded from the Inclusive Electron Trigger since they cause an abnormally high trigger rate. This is presumably caused by synchrotron radiation, the corresponding region in the SpaCal is referred to as hot spot. In some of the neighbouring cells a significant excess of the data over the Monte Carlo prediction has been observed in the course of the analysis. Therefore the region $R_e > 11.5\,\text{cm}$ and $-6.5\,\text{cm} < y < 7.5\,\text{cm}$ is not considered and the cells 4, 5, 6, 11 and 12 are excluded in addition. Finally, cell 29 is excluded since it shows a suspicious energy distribution for data. The BST analysis excludes some additional cells [Var06].

All selection criteria concerning the fiducial volume of the analysis are applied such that Data and Monte Carlo samples are treated consistently concerning the kinematic acceptance, i.e. it is assured that they are identical in the beam coordinate system.

Selection Efficiency

To verify that the different selection criteria affect data and simulated events in the same way one defines the fraction ϵ_i of events accepted by a certain cut i:

$$\epsilon^i = \frac{N_{all}}{N_{all\setminus i}}$$

The variable N_{all} ($N_{all\setminus i}$) denotes the number of events accepted by all cuts including (excluding) cut i. For the selection criteria aiming for a reduction of the photoproduction background one expects ϵ^i to rise with the electron energy: for large energies the sample is almost background free and ϵ^i corresponds to the selection efficiency for signal events, whereas for lower energies more and more background events get rejected. To obtain a pure signal selection efficiency one determines the following quantity:

$$\epsilon_s^i = \frac{N_{all}^{DIS}}{N_{all\setminus i}^{DIS}} \tag{4.14}$$

Here N_{all}^{DIS} ($N_{all\setminus i}^{DIS}$) denotes the number of DIS events accepted by all cuts including (excluding) cut i. To test the agreement of data and simulation one compares ϵ_s^i between data and the DJANGO sample. For the DJANGO sample the number of selected events for the particular cut scenario directly corresponds to N_{all}^{DIS} and $N_{all\setminus i}^{DIS}$ as the DJANGO sample contains only signal events. In the case of the data sample the

---

[12]The value $z = -160.5\,\text{cm}$ corresponds to the average z-position of the clusters in the electromagnetic section of the SpaCal.

name	definition
cluster radius	$r_{Cl} < 4\,\text{cm}, \quad r_{Cl}^{lin} < 3.8\,\text{cm}$
hadronic energy fraction	$f_{had} < 0.15$
veto cell energy	$E_{veto} < 1\,\text{GeV}$
BDC validation	$N_{hits} \geq 4, \quad \Delta R < 1.5\,\text{cm}$
$E - p_z$	$E - p_z > 35\,\text{GeV}$
y_Σ	$y_\Sigma > 0.03$
elastic QEDC rejection	see QEDC alignment (section 4.4)

Table 4.11: *Combinations of cuts for which the selection efficiency according to equation 4.14 is studied.*

photoproduction background has to be subtracted beforehand, i.e. one determines the quantities $N_{all}^{DIS} = N_{all} - N_{all}^{\gamma p}$ and $N_{all\backslash i}^{DIS} = N_{all\backslash i} - N_{all\backslash i}^{\gamma p}$. $N_{all}^{\gamma p}$ and $N_{all\backslash i}^{\gamma p}$ are estimated from the PHOJET sample.

The selection efficiency is determined for all combinations of cuts listed in table 4.11. These are all selection criteria for the BDC analysis listed in table 4.10 apart from the cuts concerning the z-vertex and the fiducial volume. The latter are excluded as the simulation contains neither satellite bunches nor are the SpaCal cells excluded from the trigger or the L4 cut implemented correctly. The z-vertex is the topic of a separate study in the next section.

For the determination of the selection efficiency all necessary corrections to the Monte Carlo simulation which are explained in the forthcoming sections are already applied. The normalisation of the PHOJET sample is needed as well. Its determination is the topic of the last section of this chapter.

The figures 4.15 and 4.16 show the selection efficiencies for data and Monte Carlo as a function of the energy E_e and the distance R_e, respectively. Compared to table 4.11 the cut on the energy deposition in the veto cells is not considered as it has turned out that this selection criterion rejects almost no events. Thus its efficiency is $\epsilon_s^i \approx 1$ resulting in data and Monte Carlo agreeing perfectly by definition. The dominant systematic error for the comparison between data and Monte Carlo arises from the uncertainty on the PHOJET normalisation. The shaded band shows this error assuming an uncertainty on the PHOJET normalisation of 15% (see section 4.9). The individual combinations of cuts are discussed in the following.

For the selection criteria concerning the electron identification (cluster radius, hadronic energy fraction, BDC validation) the efficiency drops for lower electron energies. This is due to the fact that for low energies, i.e. large values of y, particles of the hadronic final state reach the SpaCal such that the probability increases that a cluster of the hadronic final state overlaps with the cluster of the scattered electron. The radial dependent efficiency of the BDC validation shows a significant drop around $R_e \approx 25\,\text{cm}$. This is an effect resulting from the changing cell geometry of the BDC as explained in section 4.8. For energies above 17.5 GeV the cut on $E - p_z = \Sigma + E_e(1 - \cos\theta_e)$ does not reject any events as it is fulfilled by the energy of the scattered electron alone. The efficiency of the cut against elastic QED Compton events exhibits a dip having its minimum at $E_e \approx 15\,\text{GeV}$. This is in agreement with the energy distributions for electron and photon clusters of QEDC events shown in [Len01] having their maxima

Figure 4.15: *Selection efficiency (see equation 4.14) as a function of the electron energy E_e for the combinations of cuts listed in table 4.11 apart from the cut concerning the veto cell energy. The shaded band indicates the uncertainty on the PHOJET normalisation.*
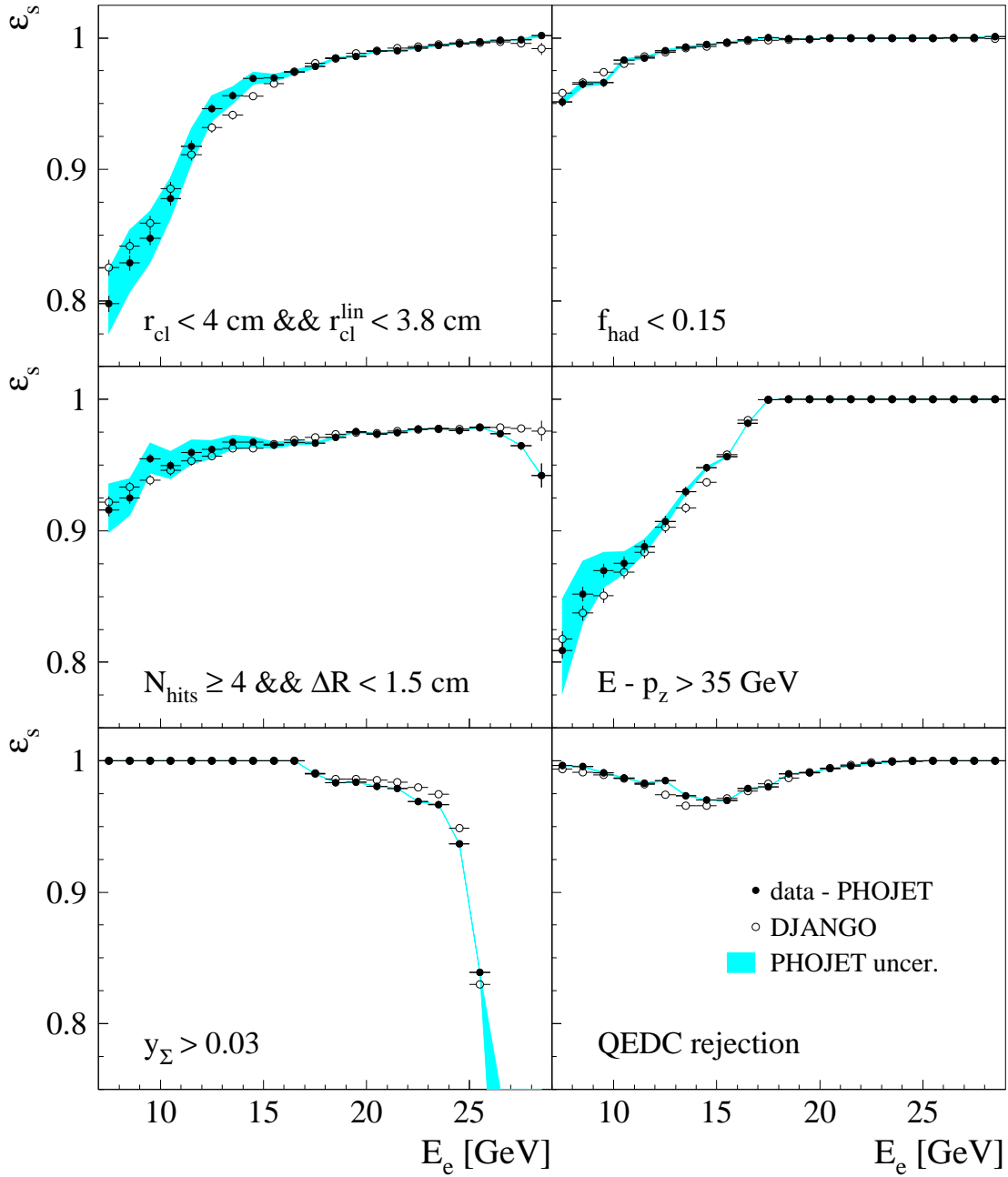
Figure 4.16: *Selection efficiency (see equation 4.14) as a function of the distance R_e for the combinations of cuts listed in table 4.11 apart from the cut concerning the veto cell energy. The shaded band indicates the uncertainty on the PHOJET normalisation.*
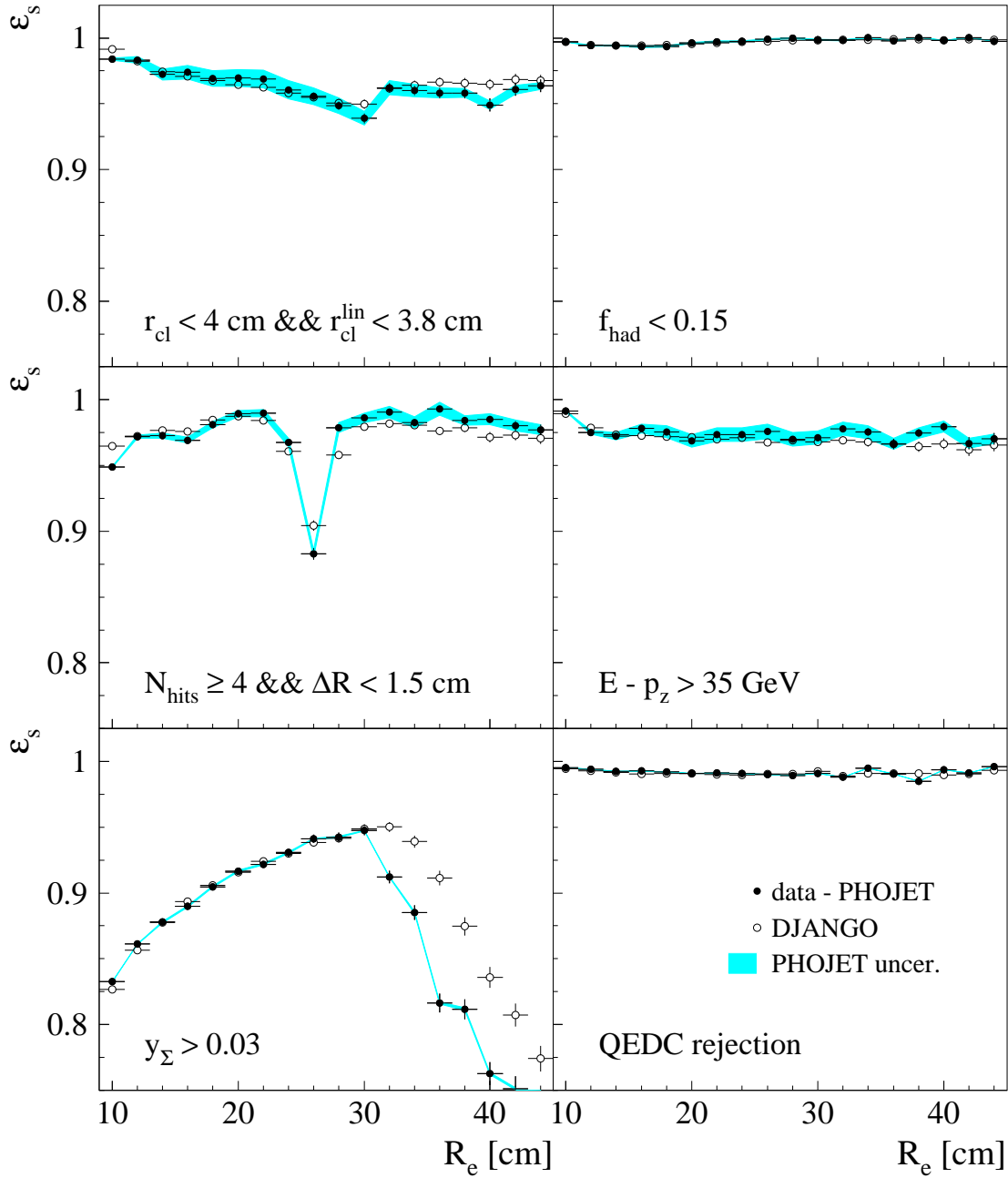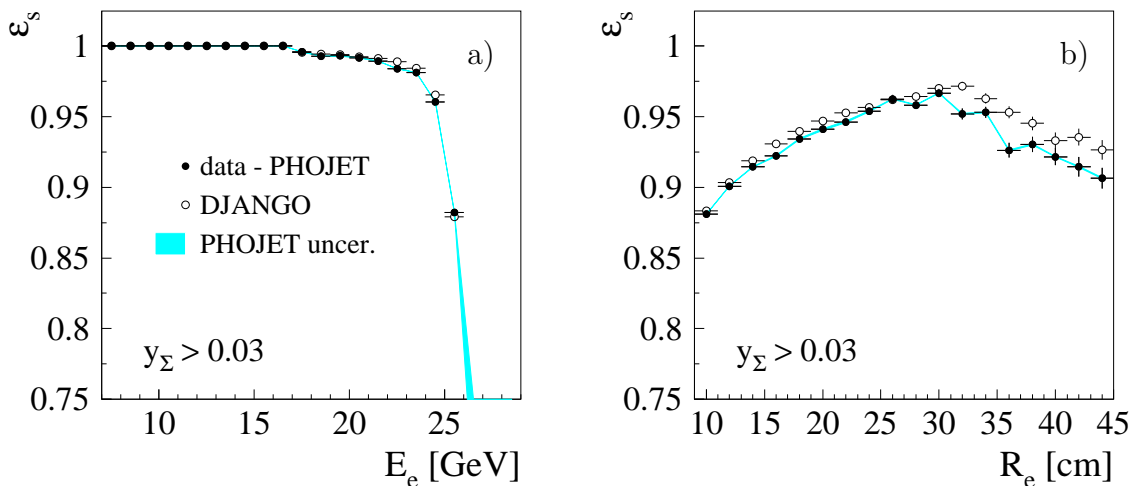
Figure 4.17: *Selection efficiency (see equation 4.14) for the cut $y_\Sigma > 0.03$ as a function of a) the electron energy E_e and b) the distance R_e for events containing at least two tracks in the Central Tracker. The shaded band indicates the uncertainty on the PHOJET normalisation.*

at half the initial electron energy.

A large discrepancy between data and Monte Carlo is observed for the radial dependence of the efficiency of the y_Σ cut from 30 cm onwards. In this region the polar angle of the scattered electron becomes large enough to enter the acceptance of the Central Jet Chamber CJC1 which has the following implications: for distances below 30 cm the presence of a reconstructed vertex implies that the hadronic final state reaches the acceptance of the Central Tracker and thus that y_Σ is sufficiently large. In contrast, for distances exceeding 30 cm a Central Tracker vertex can be reconstructed regardless of the hadronic final state due to the track of the scattered electron. This transition may not be well-described in the Monte Carlo simulation. To verify this explanation the selection efficiency y_Σ requirement has been determined again for events containing at least two tracks in the Central Tracker, i.e. at least one track in addition to the track corresponding to the scattered electron. Indeed the discrepancy becomes significantly smaller for this restricted sample as displayed in figure 4.17. The discrepancy has almost no relevance for the present analysis as it significant only for distances R_e larger than 32 cm. The contribution of events from this region to the chosen analysis bins is negligible even for the largest values of Q^2 considered. Thus the discrepancy is not considered further.

At low energies the significance of the comparison of the selection efficiency is limited by the uncertainty on the PHOJET contribution which has been statistically subtracted. Therefore it would be desirable to perform a similar study with a sample of events containing scattered electrons down to low energies with almost no background contribution. This is achieved by selecting Initial State Radiation events with the radiated photon being detected in the photon arm of the luminosity system, so-called *tagged* ISR events. For the cross-section determination the detection of the radiated photon is not required. This extends the accessible phase space significantly while at the same time increasing the number of photoproduction background events. As the

latter is to be avoided here a signal in the photon detector is explicitely required for the selection of the event sample which proceeds as follows:

- energy of the electron candidate

$$E_e < 25 \, \text{GeV}$$

- inelasticity y as reconstructed by the hadron method

$$y_h < 0.1$$

- energy deposition in the photon detector, i.e. energy of the radiated photon

$$E_\gamma > 1 \, \text{GeV}$$

- energy deposition in the electron tagger

$$E_{ET} = 0 \, \text{GeV}$$

- sum of electron and photon energy

$$22 \, \text{GeV} < E_e + E_\gamma < 32 \, \text{GeV}$$

The cut $E_e < 25 \, \text{GeV}$ allows for the radiation of an ISR photon. By accepting only events with $y_h < 0.1$ one selects a region of the phase space where ISR events are present (see section 3.9). The hadron method is used to measure the inelasticity as it reconstructs the event kinematics correctly regardless of photon radiation from the lepton line. As explained in section 3.9 Bethe-Heitler events overlapping with DIS events or photoproduction events constitute the dominant background sources to the tagged ISR events. A non-negligible fraction of these events can be identified by detecting the scattered electron of the Bethe-Heitler or the photoproduction event in the electron tagger of the luminosity system. Hence restricting the energy deposition in the electron tagger allows to reduce the influence of this background source [İşs00]. Apart from resolution effects the sum of the energies of the scattered electron and the radiated photon cannot be larger than the initial electron energy in the considered region of the kinematic phase space. This motivates the upper limit of $32 \, \text{GeV}$. Energies $E_e + E_\gamma < 22 \, \text{GeV}$ are not consistent with inelasticities $y_h < 0.1$. In addition to these selection criteria for tagged ISR events the standard selection cuts for the BDC analysis are applied. Only the y_Σ cut is relaxed to $y_\Sigma > 0.01$ in order to increase the statistics since the requirements imposed by the ISR selection and the vertex reconstruction efficiency leave only a small interval of allowed inelasticities.

The comparison of the selection efficiencies for tagged ISR events between data and Monte Carlo simulation (DJANGO) is shown in figures 4.18 and 4.19 for the cuts concerning the electron identification and BDC validation. The statistical errors are significantly larger than the ones obtained for the standard event selection statistically subtracting the photoproduction background (compare to figures 4.15 and 4.16). Nevertheless, the striking difference is the energy dependence. The decrease of the

efficiency towards lower energies is by far less developed if not absent for the tagged ISR sample. This is due the fact that no events with large values of y are present such that overlaps between the clusters of the scattered electron and a particle of the hadronic final state are not possible.

At low energies the selection efficiency of the cluster radius cut for the data is systematically smaller than for the DJANGO sample. A similar observation has been made using the same method to determine the selection efficiency for the minimum bias run in 1999. A detailed investigation has revealed the following explanation [Gla05c]: the DJANGO generator does not include radiative effects beyond leading order, i.e. for ISR events no additional photons are radiated from the lepton line. Concerning the event kinematics this should not lead to a discrepancy between data and simulation since an additional ISR photon should not modify the event kinematics, because the sigma method resums over multiple emissions. FSR radiation is also effectively resummed as electron and FSR photon mostly end up in a single cluster. The contribution of QEDC radiation is negligible. However, for FSR radiation one expects a larger cluster radius. Since such events are not present in the DJANGO sample one expects that more events are rejected by the cluster radius cut in data than in the simulation, i.e. the selection efficiency should be smaller for the data sample which is exactly the observed trend. In [Gla05c] the efficiency change due to photon radiation beyond leading order has been estimated[13] to be 1% which is in agreement with figure 4.18.

In general both comparisons of the cut efficiencies between data and Monte Carlo simulation have shown good agreement apart from the y_Σ cut which has been discussed in detail. The remaining differences are covered by an uncertainty. For its determination the distance of the DJANGO prediction to the PHOJET uncertainty band depicted in figures 4.15 and 4.16 is summed up quadratically for each combination of cuts. If the DJANGO prediction lies inside the band a distance of zero is taken. The accumulated difference as a function of E_e and R_e is well described by a global uncertainty of 1.5%. In the case of R_e this holds of course only for the region relevant for the analysis. Accordingly, a global systematic error of 1.5% is taken into account for the cross-section determination.

For the selection efficiencies derived by subtracting the photoproduction background statistically the $E - p_z$ cut has been included. The study has been repeated excluding it to obtain the selection efficiencies for the region of the phase space where the events are reconstructed with the help of the sigma method. The agreement between data and Monte Carlo is of the same quality.

4.7 Vertex Reconstruction

A detailed comparison of the vertex reconstruction in data and Monte Carlo simulation is performed in the following: at first the fraction of ep events which should enter the analysis, but are lost due to the vertex requirement is investigated by determining the *vertex efficiency*. A difference between data and Monte Carlo simulation would be

---

[13]The estimation proceeds in the following way: the efficiency of the cluster radius cut is compared between non-radiative and FSR events for the DJANGO sample. Determining the fraction of FSR and non-radiative events in addition the expected change can be calculated.
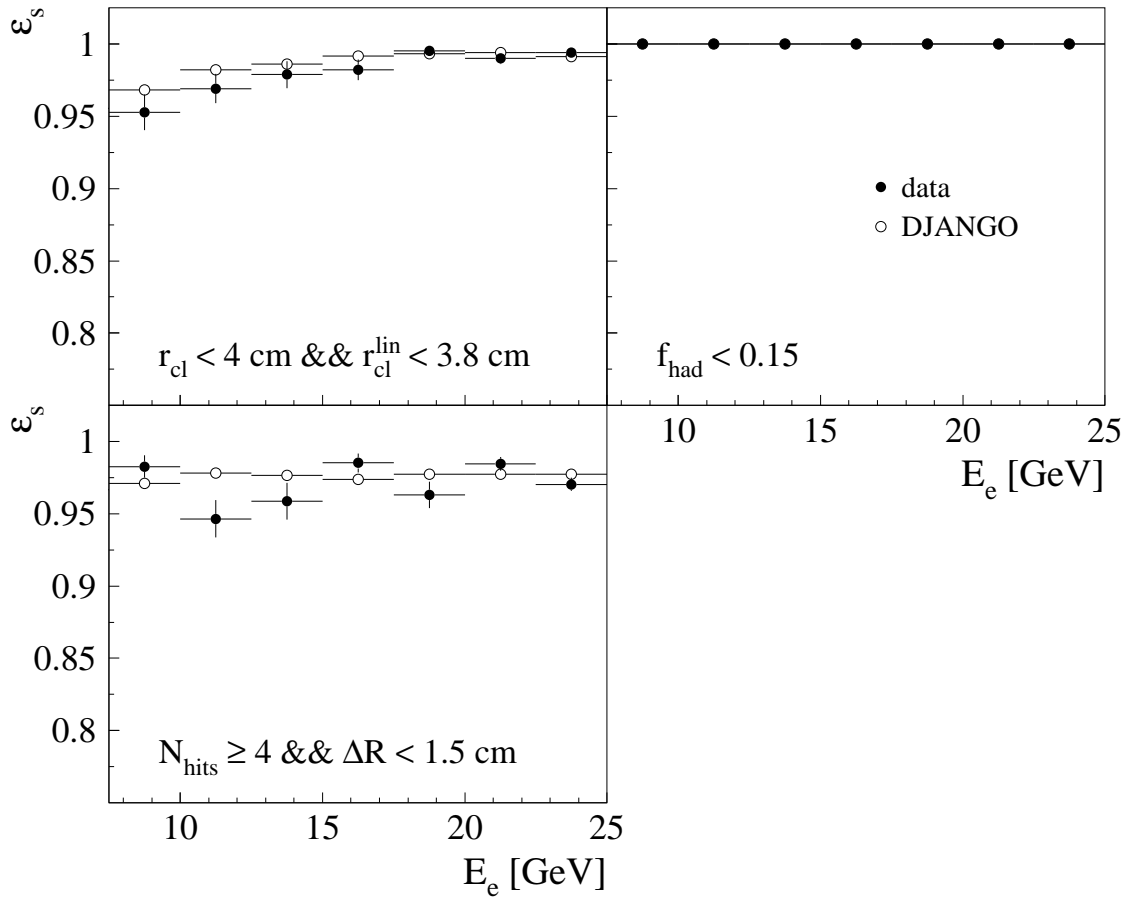
Figure 4.18: *Selection efficiency as a function of the electron energy E_e as determined in tagged ISR events for some of the cut combinations listed in table 4.11.*

reflected directly in a wrong cross-section determination[14]. Secondly, the acceptance of the detector components depends on the vertex position. Consequently, also the region of the kinematic phase space corresponding to the fiducial volume of the analysis depends on the vertex position. Hence the influence of the limited detector acceptance and the fiducial cuts can be only modelled correctly in the Monte Carlo simulation if the spatial distribution of the vertices is the same as for the data sample. To ensure this the z-vertex distribution of the Monte Carlo simulation has to be reweighted to agree with the one observed in the data.

Vertex Reconstruction Efficiency

To determine the efficiency of the vertex requirement one selects a reference sample of events being classified as *ep* events which should enter the analysis whereby the vertex is reconstructed independently of the Central Tracker. The fraction of events for which

---

[14]The selection efficiency cannot be determined, like for most of the other selection criteria, by just relaxing the vertex requirement as has been explained in the previous section.
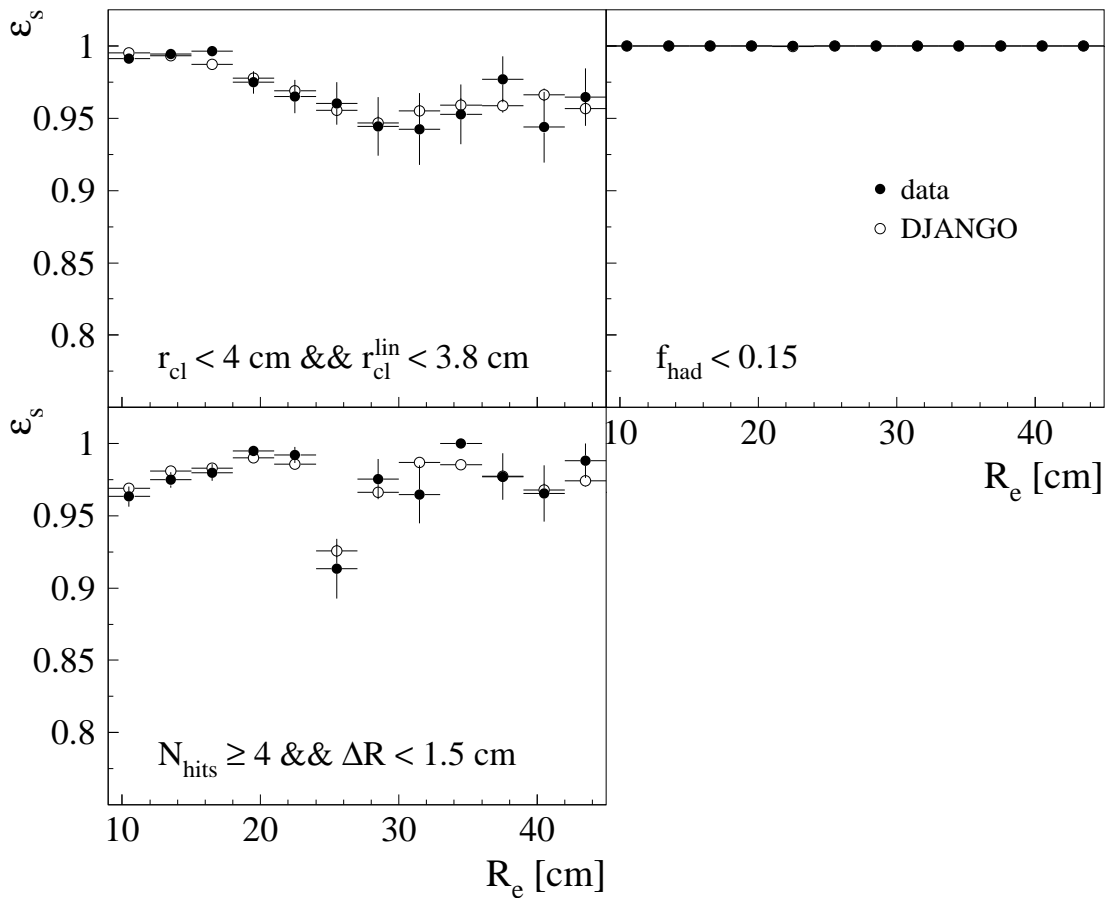
Figure 4.19: *Selection efficiency as a function of the distance R_e as determined in tagged ISR events for some of the cut combinations listed in table 4.11.*

a Central Tracker vertex exists is the vertex efficiency:

$$\epsilon_{vtx} = \frac{N_{BST/CIP\,\text{val. }\&\&\,\Delta z_{BST/CIP}<25\,\text{cm }\&\&\,\Delta z_{CT}<30\,\text{cm }\&\&\,\sigma_{z_{CT}}<8\,\text{cm}}}{N_{BST/CIP\,\text{val. }\&\&\,\Delta z_{BST/CIP}<25\,\text{cm}}} \tag{4.15}$$

For the reference sample the vertex is determined with the help of the BST or the CIP for which the vertex reconstruction solely relies on the scattered electron. The event is accepted if the electron candidate is validated by the BST[15] or the CIP and if the z-vertex position fulfils the condition $\Delta z = |z_{vtx} - \overline{z_{vtx}}\,\text{cm}| < 25\,\text{cm}$. BST and CIP are used in parallel as the BDC analysis extends into a region of small polar angles of the scattered electron which exceeds the acceptance of the BST. In this region the CIP is able to reconstruct the event vertex. The BST vertex is preferred, only in case it does not exist the CIP vertex is considered. To enter the reference sample the event has to pass the selection criteria concerning cluster properties, QED Compton events and fiducial cuts in addition (see table 4.10).

The Central Tracker vertex requirement comprises the z-coordinate to lie within $30\,\text{cm}$ of the nominal position and the error of the z-coordinate not to exceed $8\,\text{cm}$ (see table 4.10). The allowed interval of the z-position for the BST and CIP is smaller than the one for the Central Tracker to avoid accounting resolution effects as inefficiency.

---

[15]The validation by the BST implies meeting the track validation criteria as given in table 4.10.
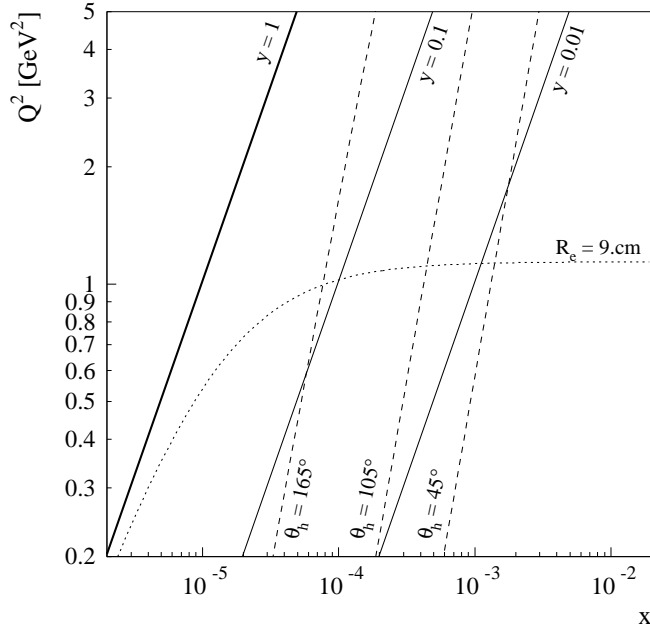
Figure 4.20: *Lines of constant hadron angle θ_h (dashed), inelasticity y (solid) and distance R_e (dotted) in the xQ^2-plane. Hadron angles of $45°$ and $165°$ roughly correspond to the lower and upper polar angle acceptance limit of the Central Tracker.*

The Central Tracker vertex reconstruction is predominantly based on tracks caused by hadronic final state particles. Only at sufficiently small polar angles the scattered electron enters the acceptance of the CJC. The lower limit of $25°$ for the polar angle acceptance of the Central Tracker (see section 2.2) during standard running conditions corresponds to roughly $45°$ for the shifted vertex period. Therefore one expects Central Tracker vertices to exist for events with hadron angles larger than this value. Accordingly, the vertex efficiency should rise steeply as a function of y starting at $y \approx 0.01$ (see figure 4.20). Hence the vertex efficiency is investigated as a function of y in intervals of Q^2.

The kinematic variables are determined with the help of the sigma method. If the electron method was used, y would be reconstructed systematically too large for ISR events (see section 3.7). Events at low y would be misinterpreted as events at high y, such that artificial inefficiencies would emerge at large inelasticities.

Figure 4.21 shows the vertex reconstruction efficiency for data and Monte Carlo simulation. The intervals in Q^2_Σ have been chosen such that they contain almost the same number of events. In the case of the Monte Carlo simulation the contributions of the DJANGO and PHOJET sample have been added according to their luminosity and normalisation[16], respectively. Data and Monte Carlo simulation show the expected steep rise of ϵ_{vtx} with y_Σ. At $y_\Sigma = 0.03$ the efficiency exceeds 50% for all Q^2 bins. This is the lower limit of y_Σ for events to be accepted for the final analysis as already mentioned in the previous section (see table 4.10). However, at large values of y_Σ the efficiency decreases again, the drop being more pronounced for the data sample. The difference

---

[16]The PHOJET normalisation is discussed in the last section of this chapter.

between data and Monte Carlo gets smaller with increasing Q^2_Σ. The efficiency drop is unexpected since for typical DIS events the region between the current jet and the proton remnant is filled with particles resulting from colour forces and gluon radiation, i.e. even if the hadron angle exceeds the upper acceptance limit[17] of the Central Tracker of 165° a vertex should be present.

ISR events should not be the reason for the drop of ϵ_{vtx} at large values of y as discussed above. The same holds for elasti QEDC events since they are excluded from the analysis due to the corresponding cut. In principle they can cause artificial inefficiencies in this regime: though being characterised by $y \approx 0$, their reconstructed y_Σ can be large if the photon is treated as a particle of the hadronic final state. The reason for this is that the photon is scattered into the backward region of the H1 detector causing a large Σ and consequently a large y_Σ (see equation 3.10).

A typical event with a large inelasticity but no reconstructed Central Tracker Vertex is depicted in figure 4.22. It has passed all selection criteria of the reference sample. Apart from the scattered electron a hadronic cluster can be identified in the SpaCal. No activity is observed in the central and forward part of the detector. Thus the event is characterised by a gap in the polar angle distribution, or equivalently the pseudorapidity η of the final state particles[18]. Such events can be interpreted as being diffractively produced. Early measurements of H1 and ZEUS have shown that *diffractive events* constitute about 10% of all DIS events [Der93b, Ahm94]. The rapidity gap causes the event to have no reconstructed Central Tracker vertex while at the same time a large y_Σ due to the hadron in the SpaCal.

A difference in the event reconstruction efficiency between data and Monte Carlo simulation at large values of y has been already reported in [Adl97b]. The reason for this is the absence of events with large rapidity gaps in the DJANGO Monte Carlo model. Dedicated simulation studies using generators for diffractive events have been performed to derive corrections to the predictions of DJANGO. The most important contribution to this corrections is the elastic production of low mass vector mesons (ρ, ω, ϕ). The corrections for the analysis of the previous shifted vertex run in 1995 covering the Q^2-range $0.35\,\mathrm{GeV}^2 < Q^2 < 3.5\,\mathrm{GeV}^2$ can be found in appendix B of [Kat97]. They reach up to 7% increasing with y and decreasing with Q^2 and thus are in agreement with the difference in the vertex efficiency between data and Monte Carlo observed here. The decrease of the correction with Q^2 is due to the fact that the cross-section for the elastic ρ meson production falls off significantly more rapidly with Q^2 than the inclusive DIS cross-section.

To check that the fraction of events with large rapidity gaps is indeed too small in the DJANGO sample one determines the distribution of the maximum pseudorapidity η_{max} being defined as

$$\eta_{max} = \max_i(-\ln\tan\frac{\theta_i}{2}) \qquad (4.16)$$

The variable η_{max} is the pseudorapidity of the cluster in the LAr or SpaCal with the largest pseudorapidity, not considering the scattered electron. For non-diffractive events it is expected to lie near the forward acceptance limit $\eta_{max} \approx 3$ of the LAr

---

[17]For standard running conditions the upper acceptance limit is 155° (see section 2.3).

[18]The pseudorapidity is defined as $\eta = -\ln\tan\frac{\theta}{2}$, positive (negative) values of η correspond to small (large) values of θ, i.e. the forward (backward) region of the detector.
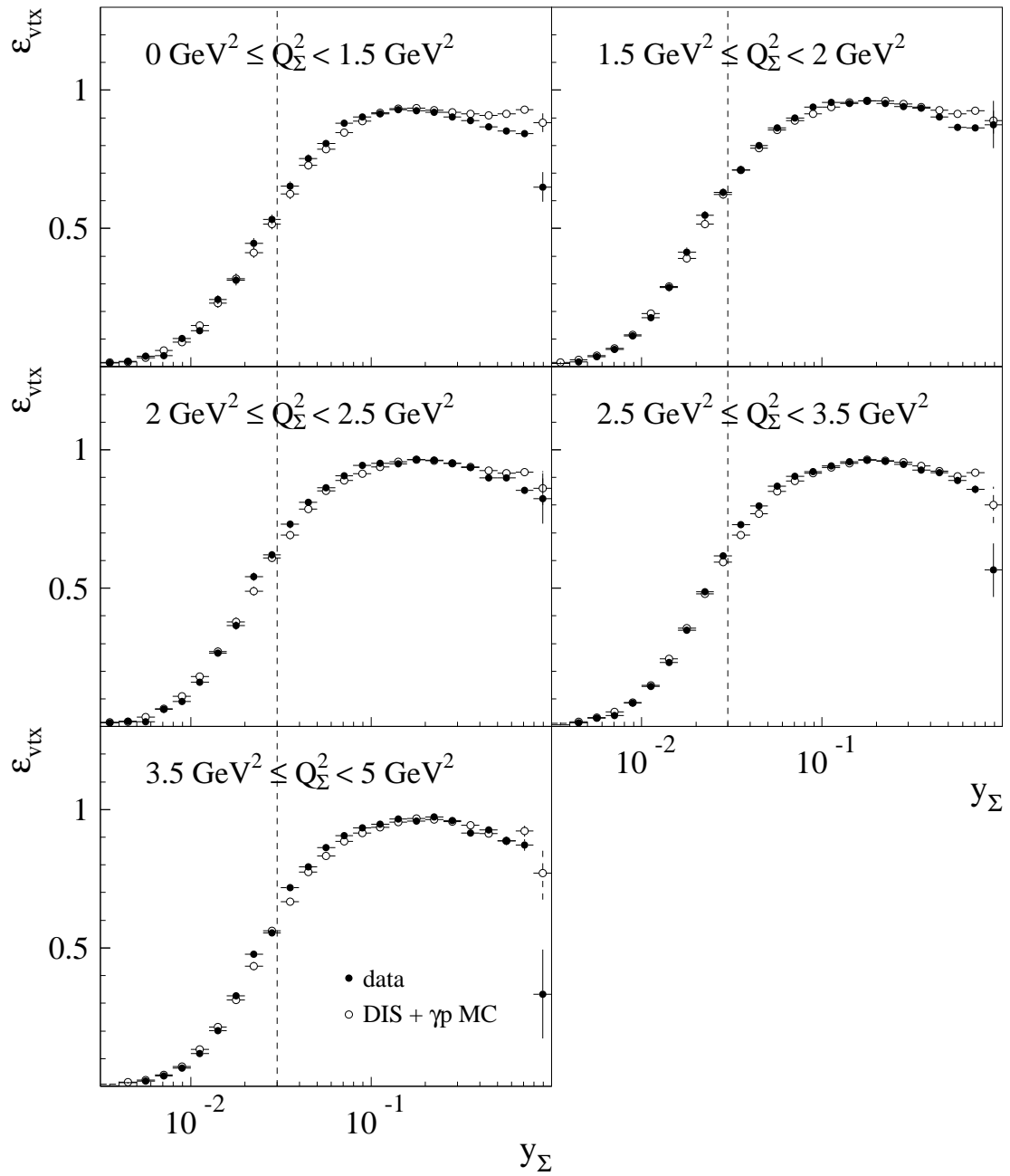
Figure 4.21: *Vertex reconstruction efficiency according to equation 4.15 as a function of y_Σ in intervals of Q_Σ^2. The dashed lines correspond to $y_\Sigma = 0.03$.*
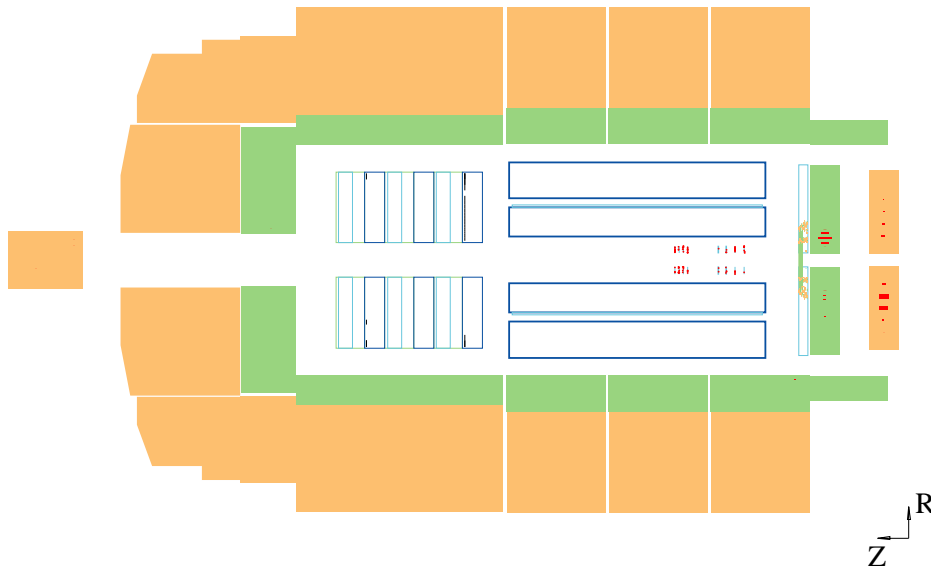
Figure 4.22: *A typical event with $y_\Sigma > 0.5$ which has no reconstructed Central Tracker vertex. Run and event number are 278698 and 47605, respectively.*
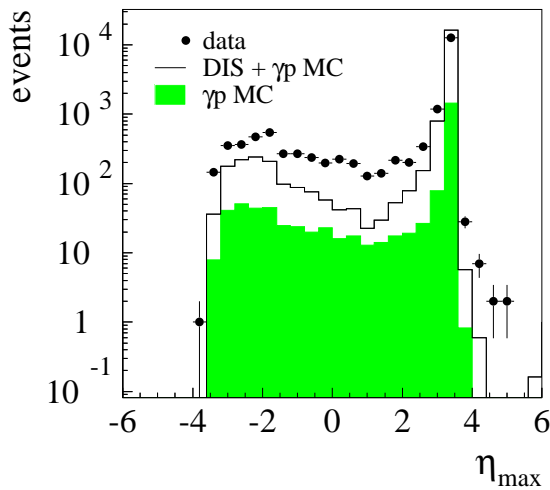
Figure 4.23: *Distribution of η_{max} (see equation 4.16) for events with $y_\Sigma > 0.5$.*

calorimeter as the region between the current jet and the proton remnant is filled with particles. In the case of diffractive events η_{max} can be lower, for the elastic production of vector mesons it reaches the acceptance region $\eta_{max} < -1.8$ of the SpaCal. Figure 4.23 compares the η_{max} distributions of data and Monte Carlo simulation for $y_\Sigma > 0.5$, the contribution of PHOJET is indicated separately. The majority of the events is caused by non-diffractive processes. The fraction of diffractive events in the Monte Carlo sample is in fact too small to describe the data, supporting the explanation of the inefficiencies in the previous paragraphs.

To achieve a correct cross-section determination the Monte Carlo sample has to be corrected for the differences in the vertex reconstruction efficiency. Therefore the ratio

$$c_{vtx} = \frac{\epsilon_{vtx}^{Data}}{\epsilon_{vtx}^{MC}} \tag{4.17}$$

of the efficiencies of data and Monte Carlo sample is calculated as a function of y_Σ in

Figure 4.24: *Ratio c_{vtx} of the vertex reconstruction efficiency of data and Monte Carlo (see equation 4.17) as a function of y_Σ for events with $1.5\,\mathrm{GeV}^2 < Q_\Sigma^2 < 2\,\mathrm{GeV}^2$. The solid line represents a second order polynomial fitted to the data points for $y_\Sigma > 0.03$, the dashed line the projection of the 2-dimensional correction function $c_{vtx}(Q_\Sigma^2, y_\Sigma)$ (for details see text).*

the same Q_Σ^2 intervals as for figure 4.21. Afterwards the obtained data points in each interval are parameterised 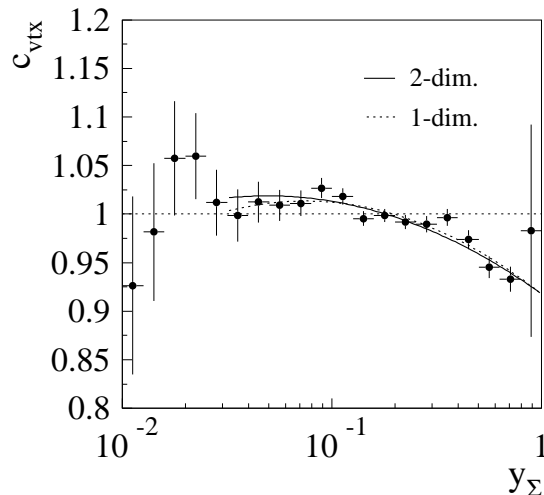with a second order polynomial for the y_Σ-range relevant for the measurement ($y_\Sigma > 0.03$). The resulting values for each of the three parameters are in turn plotted as a function of the average Q_Σ^2 in the corresponding interval and also fitted by a second order polynomial. Thus one ends up up with a continuous correction function $c_{vtx}(Q_\Sigma^2, y_\Sigma)$ which has 9 parameters and is applied as an additional weight to each Monte Carlo event. This is equivalent to the application of an appropriate correction c_ϵ in equation 3.40. Using a function for the reweighting instead of the data points for c_{vtx} directly has the advantage to extrapolate into regions with low statistics rather than to create statistical fluctuations.

Figure 4.24 depicts c_{vtx} as a function of y_Σ in the interval $1.5\,\mathrm{GeV}^2 < Q_\Sigma^2 < 2\,\mathrm{GeV}^2$. Apart from the data points the original fit to this interval is shown as well as the projection of the 2-dimensional function $c_{vtx}(Q_\Sigma^2, y_\Sigma)$, i.e. $c_{vtx}(Q_\Sigma^2, y_\Sigma)$ for the average Q_Σ^2 of the interval. Original fit and extrapolation agree to better than 1% apart from the lowest values of y_Σ where the errors are large. Of all Q_Σ^2 intervals the chosen one shows the largest deviation.

To estimate the systematic error of the cross-section emerging from the uncertainty on the vertex efficiency correction the latter is applied as a function of E_e. Again intervals in Q_Σ^2 are used to take the Q^2 dependence into account, but no fit is performed. Instead, the data points for c_{vtx} are used directly for the reweighting of the Monte Carlo samples. When deriving these corrections the y_Σ cut of the final analysis has been applied. The resulting cross-section is compared to the one obtained for the default correction procedure in each final analysis bin. The differences depend on Q^2 and are considered as systematic errors for the cross-section determination as listed in table 4.12.

Q^2 range	systematic error
$Q^2 \leq 0.35\,\mathrm{GeV}^2$	10%
$0.5\,\mathrm{GeV}^2 \leq Q^2 \leq 0.85\,\mathrm{GeV}^2$	5%
$Q^2 \geq 1.2\,\mathrm{GeV}^2$	2%

Table 4.12: *Systematic error of the cross-section emerging from the uncertainty on the vertex efficiency correction. The Q^2 values given refer to the central values of the analysis bins for which the cross-section is quoted.*

Vertex Position

The spatial distribution of the vertices is studied using the standard selection criteria for the BDC analysis (see table 4.10) apart from the requirements concerning the vertex position and the BDC track validation. The track validation is omitted to avoid a possible bias since the BDC electron finder uses the vertex position as an input. Therefore the SpaCal is used to determine the position of the scattered electron. Additional cuts are applied as explained in the following:

- For large z-coordinates of the event vertex lower values of Q^2 can be accessed than for smaller ones which may lead to a bias of the vertex distribution. The latter can be diminished by restricting the polar angle of the electron candidate to $165.5° < \theta_e < 175.5°$. For all events fulfilling $\Delta z = |z_{vtx} - \overline{z_{vtx}}\,\mathrm{cm}| < 40\,\mathrm{cm}$ this cut ensures a SpaCal acceptance of 100% for the scattered electron[19].

- The requirement $E_e > 15\,\mathrm{GeV}$ excludes the part of the energy spectrum for which the photoproduction background is large.

- It has been shown in section 4.6 that the Monte Carlo simulation has problems to describe the vertex reconstruction at large polar angles where the scattered electron defines the Central Tracker vertex. In order not to be influenced by this effect only events are accepted which have at least two reconstructed tracks in the Central Tracker.

The vertex efficiency correction which has been determined above are applied for this study.

At first the time dependence of the mean $m(z_{vtx})$ and the spread $s(z_{vtx})$ of the z-position of the event vertices for the data sample is investigated. For this purpose the z-vertex distribution for each luminosity run is parameterised by a Gaussian. Figure 4.25 displays the extracted fit parameters as a function of a continuous run number[20]. The dashed lines separate the different luminosity fills. Mean and spread vary by about 4 cm between the different runs and show a systematic development within a luminosity fill. For the last luminosity fill a particularly large spread $s(z_{vtx})$ is observed.

---

[19]To be more precise, the restriction of the polar angle implies that all scattered electrons satisfy $15\,\mathrm{cm} < R_e < 70\,\mathrm{cm}$. The upper limit is motivated by the SpaCal acceptance limit, the lower one covers all fiducial cuts.

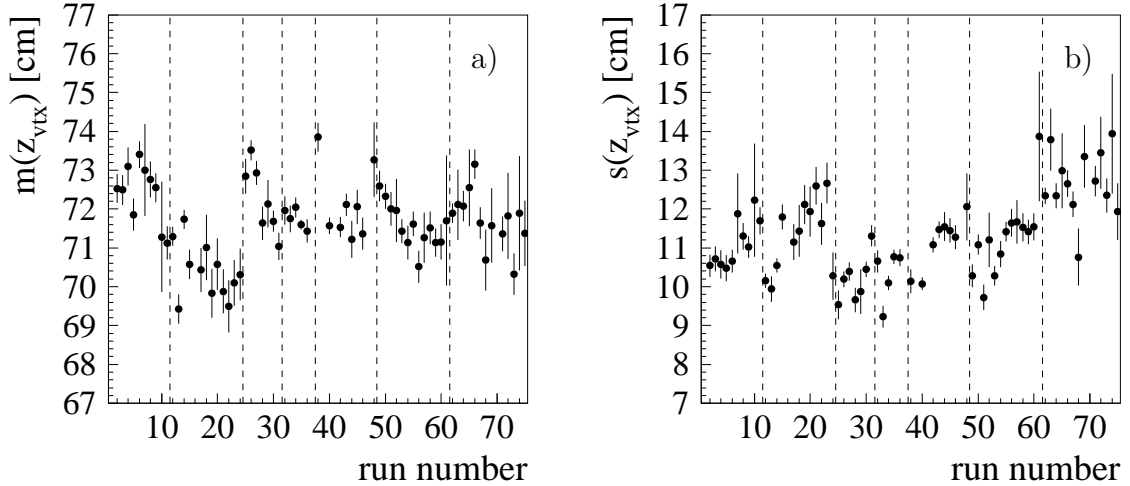[20]The original sequence of the runs is conserved.

Figure 4.25: *a) Mean $m(z_{vtx})$ and b) spread $s(z_{vtx})$ of the z-position of the Central Tracker vertices as a function of a continuous run number. The dashed lines separate the different luminosity fills.*

The spread $s(z_{vtx})$ is compatible with the longitudinal size of the luminous region of approximately 10 cm (see section 4.2). It increases in the course of each fill as the proton bunches get larger due to intrabeam scattering and noise of the radiofrequency being responsible for the acceleration. A measurement of the evolution of the proton bunch length with time during a typical HERA operation cycle is presented in [Mon00].

Despite the variations of mean position and spread the z-vertex distribution of the entire data sample can be well parameterised by the sum of a Gaussian and a first order polynomial (see figure 4.26 a)). The fit shows that the contribution of the polynomial is almost negligible and provides a mean z-position $\overline{z_{vtx}} = 71.9$ cm of the Central Tracker vertices.

For the cross-section determination it would be ideal to perform the Monte Carlo simulation with the z-vertex distribution obtained from data. However, in practise this is difficult to achieve. For example, the final run selection for the data sample is usually fixed only after the Monte Carlo samples have already been produced. Therefore the Monte Carlo events are reweighted to bring the distributions to agreement. For this purpose the z-vertex distribution of the DJANGO sample is subjected to the same fit as the data (see figure 4.26 a)). The weight w_{vtx} to be applied to each Monte Carlo event is given by:

$$w_{vtx}(z_{vtx}) = a_0 \frac{N^{data}(z_{vtx})}{N^{MC}(z_{vtx})} \tag{4.18}$$

Here N^{data} (N^{MC}) denotes the number of events at a certain z-vertex position as given by the fit to the data (Monte Carlo) distribution. Since cuts for a clean electron identification are applied only the DJANGO sample can be used for the extraction of the reweighting function. For the final analysis also the PHOJET sample has to be considered. As this has been simulated with the same vertex parameters as the DJANGO sample the same reweighting is applied. Introducing a suitable constant a_0 ensures that the total number of events for the DJANGO sample is conserved under the reweighting. For the PHOJET sample no special care is necessary in this respect,
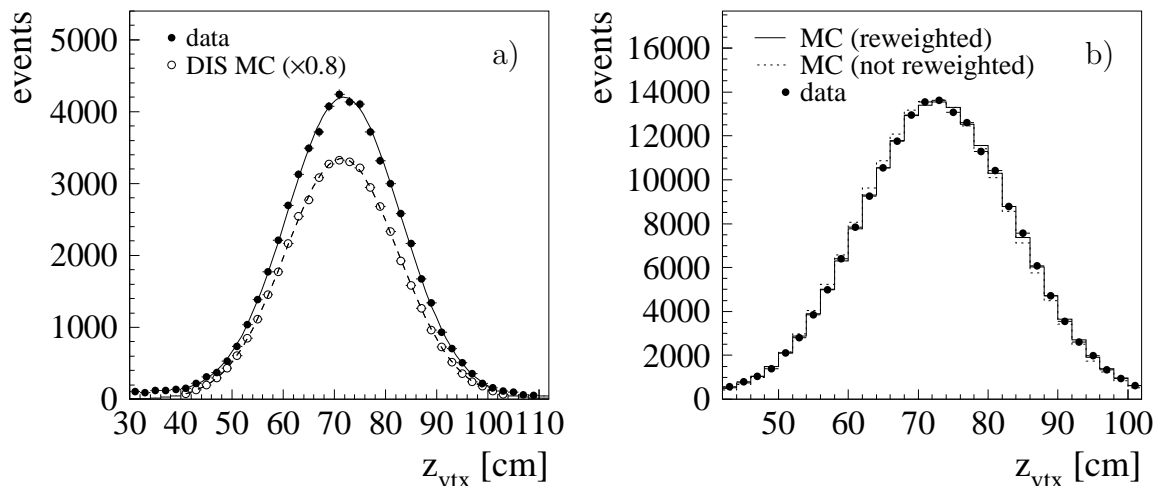
Figure 4.26: a) *z-vertex distribution for data and DJANGO along with a parameter-*
isation by the sum of a Gaussian and a first order polynomial indicated
by the solid and dashed line, respectively. The Monte Carlo prediction is
scaled by a factor of 0.8 for better visibility. b) Comparison of the z-vertex
distribution in data and Monte Carlo (DJANGO + PHOJET) with and
without applying the weight w_{vtx} (see equation 4.18) to the Monte Carlo
events.

because the normalisation is performed with the z-vertex reweighting function already
applied.

Figure 4.26 b) shows a comparison of the z-vertex distribution of the Monte Carlo
simulation with and without reweighting to the distribution obtained for data for all
events passing the cuts of the final analysis. For both Monte Carlo distributions the
contributions of the DJANGO and PHOJET samples have been added according to
their luminosity and normalisation[21], respectively. Since the agreement of the distribu-
tions in shape is the figure of merit for this comparison the Monte Carlo distributions
have been renormalised to contain the same number of events as the distribution for
the data sample. As expected, the agreement between data and Monte Carlo is almost
perfect if the reweighting function is applied. It is important that the difference to the
distribution without reweighting is small. Otherwise large weights would have to be
applied implying larger statistical errors for the Monte Carlo samples.

In the course of the investigations concerning the beam tilt implementation in the
Monte Carlo simulation (see section 3.6) it has been checked that the x- and y-positions
of the vertices for the data sample are well reproduced by the Monte Carlo simulation.

4.8 BDC Efficiency

The matching of the SpaCal cluster with hits in the BDC has two important functions
for the analysis: on the one hand it improves the precision of the polar angle measure-
ment θ_e of the scattered electron. On the other hand it rejects photoproduction events:
Non-showering neutral particles have no associated track. Furthermore hadron induced

---

[21]The PHOJET normalisation is discussed in the last section of this chapter.

Figure 4.27: *BDC efficiency as a function of the distance R_e. The dashed lines denote the region affected by the transition cells.*
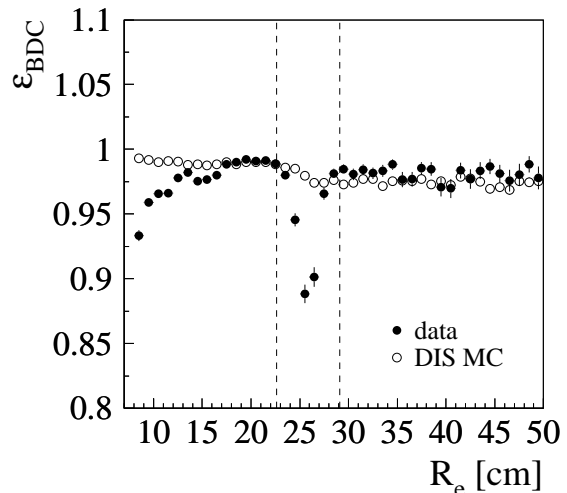
showers exhibit larger fluctuations of the deposited energy than electron induced ones. Therefore the cut on the track cluster matching $\Delta R < 1.5\,\text{cm}$ should reduce the probability for a hadronic final state particle to be misidentified as the scattered electron (see section 4.6).

Consequently, two aspects of the linking of SpaCal clusters and BDC tracks have to be studied: the efficiency with which the BDC validates the scattered electron and the rejection power for background events. The former is called *BDC efficiency* in the following as it should directly reflect the operational state of the chamber.

To determine the BDC efficiency a sample of events is selected for which a misidentification of the scattered electron is almost impossible: only electron candidates with energies above 20 GeV are accepted. In addition the standard selection criteria (see table 4.10) are applied omitting the BDC validation. This implies that the scattered electron is reconstructed based on the SpaCal alone. The fraction of events for which the BDC requirements $N_{hits} \geq 4$ and $\Delta R < 1.5\,\text{cm}$ are fulfilled corresponds to the BDC efficiency ϵ_{BDC}. Vertex efficiency correction and z-vertex reweighting as derived in the last section are applied for this study.

Figure 4.27 shows ϵ_{BDC} as a function of the distance R_e of the electron cluster to the beam axis in the SpaCal plane for data and Monte Carlo simulation. Only the DJANGO sample is considered as there is no contribution from photoproduction events for $E_e > 20\,\text{GeV}$. Three essential differences between data and Monte Carlo are observed which is discussed in the following: The efficiency of the data sample decreases to 90% at $R_e \approx 25\,\text{cm}$. This dip is not reproduced in the simulation. For small R_e the efficiency is significantly overestimated by the simulation, while for $R_e > 30\,\text{cm}$ is slightly underestimated.

An efficiency drop or/and a discrepancy between data and Monte Carlo simulation in the region around $R_e \approx 25\,\text{cm}$ has been reported before [Sch96b, Kat97, Mey97]. In summary two possible explanations have been discussed: An insufficient description of the dead material in front of the BDC in the simulation or problems with the track reconstruction in the region where the BDC cell size changes. For a comparison with the present study it has to be taken into account that a different track reconstruction algorithm has been used for the previous analyses and that the description of the dead material in the backward region of the H1 detector has meanwhile significantly

improved [Len99].

For the bulk of the events without a BDC validation in the problematic region there are less than the required four hits associated to the electron candidate whereas the requirement concerning ΔR is fulfilled. Therefore resolution effects due to interactions of the scattered electron with dead material seem to be less likely the reason for the inefficiency.

As mentioned in section 2.3 the radial cell size of the BDC changes from $1\,\text{cm}$ in the inner region to $3\,\text{cm}$ in the outer region. The intermediate region in each sector is covered by a *transition cell* of $2\,\text{cm}$ size. Taking the chamber geometry into account it can be derived from figure 2.5 that the transition cells of all sectors affect the interval $21\,\text{cm} < R_{BDC} < 27\,\text{cm}$. The variable R_{BDC} denotes the distance from the origin of the BDC in the xy-plane at $z = -145\,\text{cm}$, i.e. at the mean z-position of the BDC. A projection to the SpaCal in consideration of the possible z-positions of the vertex leads to $23\,\text{cm} < R_e < 29\,\text{cm}$. This region is indicated by dashed lines in figure 4.27. A clear coincidence with the efficiency drop is observed.

The transition cells are asymmetric, i.e. the wire is not centred w.r.t. to the cell in the radial direction (see figure 2.5). Furthermore the electric drift field of the transition cells is simultaneously influenced by the high voltage supplies of the inner and the outer half-sectors. Hence the transition cells have a special field configuration. It has been observed that the drift time spectra after the calibration are of worse quality than the ones for the standard cells [Kat06]. If the reconstruction algorithm is not optimised to account for these effects they may lead to inefficiencies which are difficult to model in the Monte Carlo simulation.

The simulation predicts lower efficiencies for the outer half-sectors than for the inner ones. A similar feature for the data has been observed in [Kat97]. Obviously the Monte Carlo simulation has been optimised for the reconstruction algorithm used therein while the BDC electron finder BDCLEV does not show such a behaviour.

It is evident that the Monte Carlo events have to be reweighted for the BDC efficiency of the data sample to be described adequately. Similar to the vertex reconstruction efficiency the correction

$$c_{BDC} = \frac{\epsilon_{BDC}^{Data}}{\epsilon_{BDC}^{MC}} \tag{4.19}$$

is determined for this purpose. The design of the chamber in sectors suggests to investigate also the azimuthal variation of the efficiency in addition to the radial one. Thus the correction c_{BDC} is determined as a function of R_e in four different ϕ-sectors as depicted in figure 4.28. For $R_e < 30\,\text{cm}$ the corrections are derived in intervals of $1\,\text{cm}$, in particular to model the strongly changing efficiency in the region of the transition cell. Above $30\,\text{cm}$ larger intervals are used not to be dominated by statistical fluctuations.

All quadrants show the same general trend of the corrections, but there are significant differences. The most striking one is quadrant II showing almost no correction at low radii while revealing a particularly large correction in the region of the transition cell compared to the other quadrants. As the efficiency ϵ_{BDC}^{MC} looks almost the same for all quadrants the differences can be attributed to the data sample. Therefore it has been checked whether a correlation to the operational conditions of the chamber can be found. Figure 4.29 gives an overview of the detector status in the year 2000. The
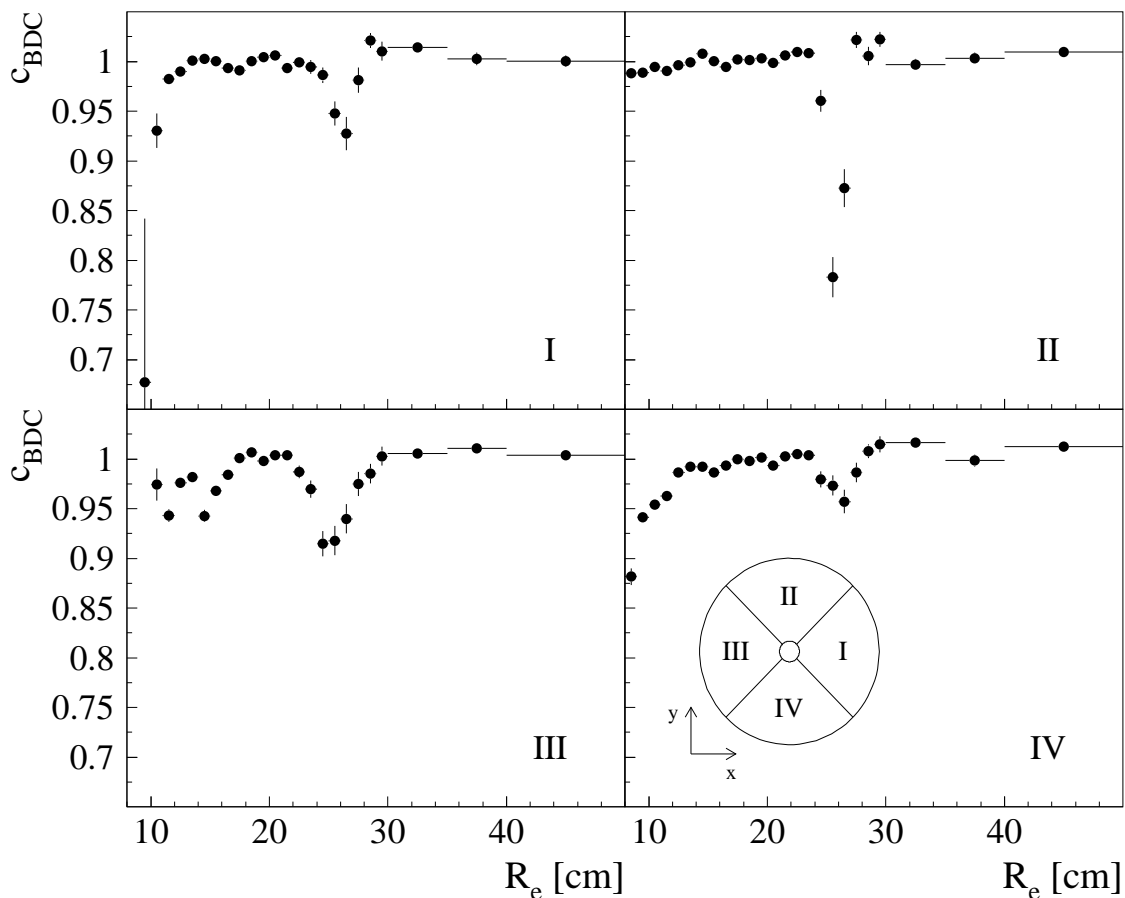
Figure 4.28: *Ratio c_{BDC} of the BDC efficiency of data and Monte Carlo (see equation 4.19) as a function of the distance R_e in quadrants as indicated.*

highlighted sectors have not been operated for various reasons [BDC00].

A clear correlation between the detector status and c_{BDC} can be observed if one assumes that the dead sectors are not considered during the Monte Carlo simulation: in contrast to all others quadrant II is not affected by a single dead inner sector such that it is expected to show the smallest correction at lower radii. The efficiency in the region of the transition cell seems to be most affected by the status of the outer sectors. Quadrant II is influenced by two dead outer sectors, quadrants I and III by one each and quadrant IV by none. Accordingly, quadrant II shows the largest and quadrant IV the smallest correction in the region of the transition cell.

Using c_{BDC} in quadrants as an additional weight for the Monte Carlo events ensures that the BDC efficiency is correctly modelled. This is equivalent to the application of an appropriate correction c_ϵ in equation 3.40.

In a second step it has to be checked that the background rejection power of the BDC selection criteria agrees sufficiently between data and Monte Carlo simulation for the whole energy range of the final analysis. This has been done when determining the efficiency of the selection criteria in section 4.6. The BDC efficiency correction has been already applied for that study. Correspondingly, the uncertainty on the BDC efficiency is already contained in the uncertainty of the selection efficiency determined to 1.5%.
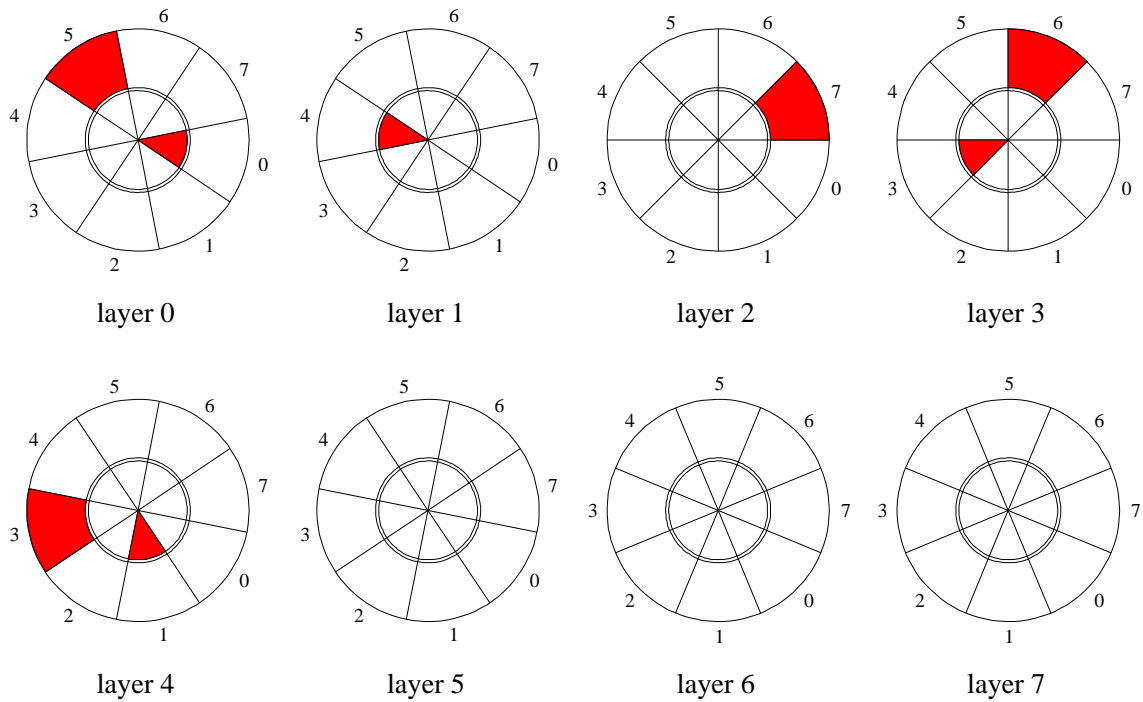
Figure 4.29: *Operational status of the BDC in the year 2000 [BDC00]. Sectors not operated are highlighted.*

4.9 PHOJET Normalisation

If the DIS event selection criteria are applied photoproduction events are the dominant source of the remaining background. Though their virtuality Q^2 is so small that the scattered electron escapes detection in the backward beam pipe they enter the final event sample as a particle of the hadronic final state can mimic the scattered electron (see section 3.4).

To determine the DIS cross-section the photoproduction background is statistically subtracted from the total number of events observed in the data sample using the PHOJET Monte Carlo model (see section 3.8). For the quantity $N_{\gamma p}^{\square}$ in equation 3.40 simply to be the number of PHOJET events passing the selection criteria in table 4.10 the PHOJET sample has to be normalised w.r.t. the data sample. The straightforward approach for the normalisation would be to calculate the luminosity of the PHOJET sample from the photoproduction cross-section and the number of PHOJET events and to compare it to the luminosity of the data sample. It requires all event properties on which cuts are placed to be perfectly described in the simulation which is not the case. This can be seen from figure 4.15 which shows that the discrepancy between data and Monte Carlo simulation for the selection efficiency is largest at low energies where the PHOJET contribution is sizeable.

Therefore one performs the normalisation by selecting events of the data sample which can be unambiguously identified as stemming from a photoproduction process and comparing them to the corresponding events in the PHOJET sample. In order to reduce the sensitivity of the normalisation on the selection criteria they are chosen to be as close as possible to the ones for the final analysis. Two approaches to identify

Figure 4.30: *a) Electron tagger acceptance A_{ET} as a function of the inelasticity y. b) Energy spectrum of the scattered electrons reconstructed in the electron tagger. The PHOJET distribution has been renormalised to contain the same number of events as the distribution for data.*
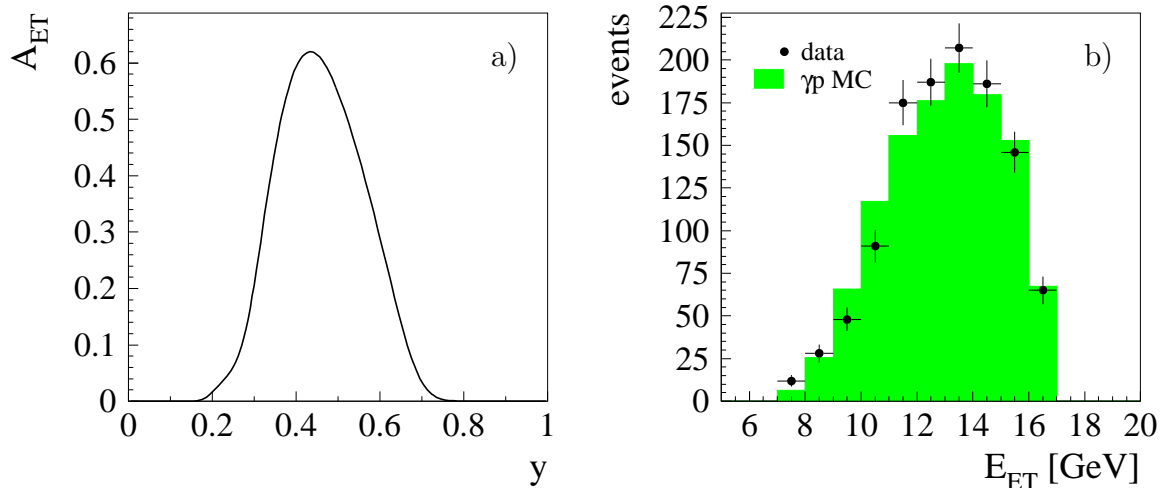
photoproduction events are discussed: one employs the electron tagger of the luminosity system, the other the charge of the electron candidate.

Tagged Photoproduction Events

As the scattered electron in photoproduction events leaves the main detector through the backward beam pipe it can be identified with a certain probability in the electron tagger of the luminosity system (see section 2.5). Events for which this is the case are called *tagged events* in the following. On the way from the interaction region to the electron tagger at $z = -33.4$ m the beam guiding magnets bend the trajectory of the electrons. This leads to a strong dependence of the tagger acceptance A_{ET} on the electron energy and thus the inelasticity y. The tagger acceptance has been determined separately for the shifted vertex period with the help of Bethe-Heitler events (see section 1.7) in which the scattered electron and the emitted photon are detected in the electron tagger and the photon detector of the luminosity system, respectively [And96][22]. From the result shown in figure 4.30 a) it can be inferred that the scattered electron can be identified only in a narrow inelasticity band $0.3 < y < 0.6$ with a reasonable probability. This is the reason why a comparison to a Monte Carlo model is necessary: a direct estimation of the photoproduction background from tagged events in the data sample would involve large extrapolation errors due to the limited tagger acceptance.

The following selection criteria have to be fulfilled for tagged events: to ensure a reasonable acceptance the reconstructed energy in the electron tagger is required to lie within an interval of $7\,\text{GeV} < E_{ET} < 16.5\,\text{GeV}$. All DIS selection criteria as listed in table 4.10 are imposed apart from the $E - p_z$ cut. The latter has to be omitted for a

---

[22]The citation [And96] refers to the old electron tagger of the luminosity system locates at $z = -44$ m. However, the principle of the acceptance determination is still the same.

suitable amount of events to remain in the sample of tagged events given the limited acceptance. Instead cuts are placed on the quantity

$$(E - p_z)_{tot} = E - p_z + 2E_{ET} + 2E_{PD} \tag{4.20}$$

taking apart from the particles in the main detector $(E - p_z)$ also the energy depositions in the electron tagger (E_{ET}) and the photon detector (E_{PD}) into account. If no losses occur $(E - p_z)_{tot}$ should be equal to $2E_e^0 = 55.2\,\mathrm{GeV}$ for photoproduction events due to energy and momentum conservation. Therefore only events with $(E - p_z)_{tot} > 45\,\mathrm{GeV}$ are accepted for this study.

Also coincidences of DIS and Bethe-Heitler events pass the selection criteria mentioned so far and would constitute a sizeable background contribution for the tagged photoproduction sample due to the large rate of Bethe-Heitler interactions. As the quantity $(E - p_z)_{tot}$ for overlapping events can reach up to twice the nominal value they can be efficiently rejected by applying the cut $(E - p_z)_{tot} < 70\,\mathrm{GeV}$ (for details see [Mey97]). Requiring a maximum energy deposition of $2\,\mathrm{GeV}$ in the photon detector further suppresses these events.

To avoid energy leakage over the detector boundaries a cut is placed on the x-coordinate of the electron impact point w.r.t. the centre of the electron tagger for the data sample: $|x_{ET}| < 6.5\,\mathrm{cm}$. Furthermore one asks for the trigger element 115 to be set which requires an energy deposition in the electron tagger within a certain range. The same cuts have been applied during the determination of the tagger acceptance.

In the software package H1SIM responsible for the simulation of the H1 detector the electron tagger is not included. This implies that the latter two selection criteria cannot be applied to the PHOJET sample. To describe the tagger response the acceptance function A_{ET} determined from data as depicted in figure 4.30 a) is used to reweight the Monte Carlo events according to the generated inelasticity.

If one applies all mentioned selection criteria as well as the acceptance reweighting one observes that for about 10% of the PHOJET events in the final analysis the scattered electron can be identified in the electron tagger[23]. Figure 4.30 shows the energy distribution of the scattered electron for data and simulation. The PHOJET distribution has been renormalised to contain the same number of events as the distribution for data. Both distributions agree reasonably well.

Thus tagged events seem to be well-suited to normalise the number of PHOJET events entering the cross-section determination w.r.t. the data sample. To be more precise, the quantity $N_{\gamma p}^{\square}$ in equation 3.40 is calculated for each analysis bin $\square$ in x and Q^2 or y and Q^2 according to[24]:

$$N_{\gamma p}^{\square} = \frac{N_{Data,tag}}{N_{PHOJET,tag}} N_{PHOJET}^{\square} \tag{4.21}$$

The quantity $N_{PHOJET}^{\square}$ denotes the number of PHOJET events passing the DIS selection criteria as given in table 4.10 for the analysis bin $\square$, whereas $N_{Data,tag}$ and $N_{PHOJET,tag}$ correspond to total the number of tagged events in the data and PHOJET sample, respectively. As outlined above the latter have passed the same selection

---

[23]Vertex efficiency correction, z-vertex reweighting and BCD efficiency correction as derived in the previous sections are applied for this study as well.

[24]Details concerning the definition of the analysis bins can be found in section 5.1.
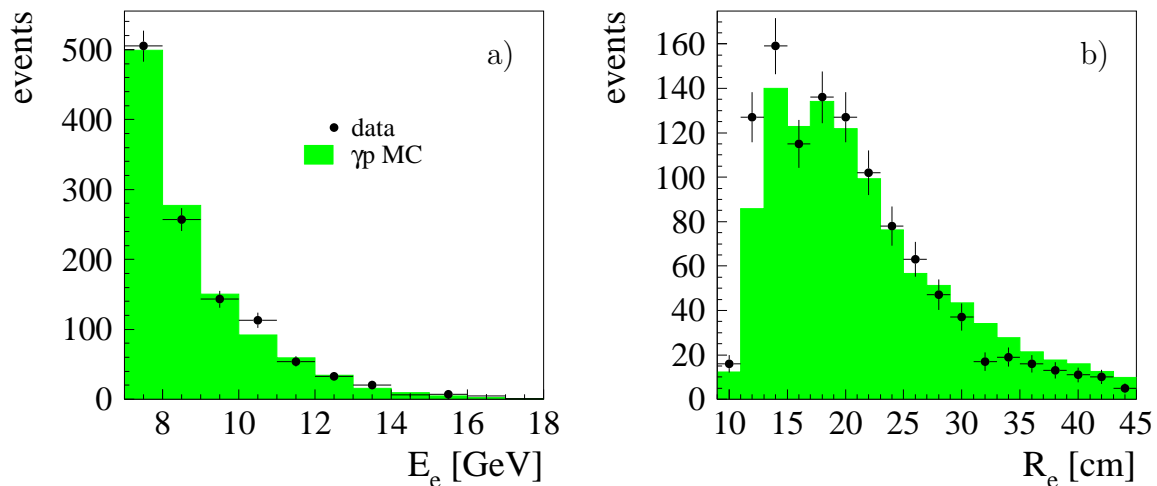
Figure 4.31: *Distributions of a) the energy E_e and b) the distance R_e for the hadrons misidentified as scattered electrons in tagged events. The PHOJET distributions have been renormalised to contain the same number of events as the distributions for data.*

criteria as $N_{PHOJET}^{\square}$ apart from omitting the $E - p_z$ cut and applying additional cuts to identify them as tagged. Therefore the normalisation should be almost insensitive to differences in the distributions of variables on which cuts are placed (e.g. cluster radius) between data and PHOJET.

Using $N_{\gamma p}^{\square}$ to statistically subtract the photoproduction background in the described way works correctly only if the PHOJET sample reproduces the kinematics of photoproduction events in data reasonably well. This can be checked with the help of tagged events. Figure 4.31 shows the distributions of the energy E_e and the distance from the beam axis R_e of the hadronic final state particle being misidentified as the scattered electron. While the simulation almost perfectly describes the energy distribution it underestimates the number of photoproduction events at low R_e and overestimates it at large R_e. The discrepancy is especially large at $R_e \approx 12$ cm. This behaviour is reflected in the distributions of the virtuality Q^2 and Bjorken x and would thus lead to a wrong estimation of the photoproduction background.

Therefore the PHOJET normalisation is performed in each analysis bin separately, i.e. the number of tagged events is counted for each bin and equation 4.21 is changed to

$$N_{\gamma p}^{\square} = \frac{N_{Data,tag}^{\square}}{N_{PHOJET,tag}^{\square}} N_{PHOJET}^{\square} \tag{4.22}$$

In this way the local differences between PHOJET and data are corrected at the price of an increased statistical error compared to the global normalisation. If an analysis bin contains less than three tagged events for the data sample the global normalisation factor is used instead. This imposes no consistency problems on the analysis as the photoproduction background in these bins is anyhow negligible.

The bin-wise PHOJET normalisation is used only for the final cross-section measurement. For the determination of the vertex efficiency correction and the cut efficiencies the global one has been used for simplicity which should be sufficient.

The global normalisation factor $N_{Data,tag}/N_{PHOJET,tag}$ for the BST analysis is approximately 8% larger than for the BDC analysis. One possible explanation for this is the following: before being detected in the BDC particles have passed significantly more dead material than in the case of the BST. If this additional material including CIP, CIZ and CJC readout electronics and cables is not correctly modelled in the Monte Carlo simulation the conversion rate of the decay photons from π^0 mesons is different between data and Monte Carlo sample. This difference which is absorbed and thus corrected for in the normalisation factor affects the BDC but not the BST analysis.

The distribution of R_e for the BST analysis shows a better agreement between data and simulation than the one in figure 4.31 for the BDC analysis [Var06]. This justifies a global normalisation of the PHOJET sample. Nevertheless, for consistency reasons the bin-wise normalisation is used for the comparison of the results of the BST and BDC analyses.

Normalisation Uncertainty

For the standard BST analysis only the signals in the r-sensors are employed which allow to measure the distance of the hits from the z-axis in the $r\phi$-plane and finally the polar angle θ_e of the scattered electron. One of the 16 BST ϕ-sectors is equipped with u-sensors in addition (see section 2.3). By combining the information of both sensor types it is possible to reconstruct the 3-dimensional coordinates of the hits. From these momentum and charge of the corresponding tracks can be derived.

Knowing the charge of the BST tracks corresponding to the electron candidates allows to determine the number of photoproduction background events: in the shifted vertex period positrons have been accelerated in the HERA ring. Hence, tracks belonging to a scattered electron should indicate a particle with a positive charge (*right charge tracks*). Tracks indicating a particle with a negative charge (*wrong charge tracks*) point to the presence of a background event. Moreover, assuming a charge symmetry of the background events the number of events with a wrong charge track gives an estimate of the remaining background in the correct charge sample. If a charge asymmetry is present, this has to be taken into account.

Using this method it is in principle possible to extract the number of photoproduction events $N_{\gamma p}^{\square}$ for each analysis bin from the data sample alone. However, this would result in a large statistical uncertainty on $N_{\gamma p}^{\square}$ as u-sensors have been installed in only one of the 16 ϕ-sectors of the BST and thus their acceptance is rather small. Instead the charge measurement is used to cross-check the PHOJET normalisation for the BST analysis determined with the help of tagged events and to estimate its uncertainty.

Such a cross-check has been performed first in [Eck02] for the minimum bias run in 1999. It has been repeated for the same data set in [H1]. The results of the latter are summarised shortly in the following: all events n_{acc} in the acceptance of the u-sensors passing the nominal analysis cuts are classified as events with right charge (n_+), wrong charge (n_-) or events without a linked track from the u-sensors (n_0). The difference of n_{acc} and the number of signal events n_{sig} is equal to the total amount of background

events $n_{\gamma p}$ in the u-sensor acceptance:

$$n_{\gamma p} = n_{acc} - n_{sig} = n_{acc} - \frac{n_+ - A_{ch}n_-}{\epsilon_u} \qquad (4.23)$$

In this equation A_{ch} corresponds to the charge asymmetry and ϵ_u to the efficiency to link a track defined by the u-sensors to the standard track of the BST electron finder using the information of the r-sensors. The charge asymmetry is defined as $A_{ch} = N_{+,\gamma p}/N_{-,\gamma p}$, i.e. the fraction of the number of background events with a right and wrong charge track. It has been determined to $A_{ch} = 0.90 \pm 0.10$ [H1]. The different amount of events with positively and negatively charged tracks is caused by the fact that the cross-section and released energy for antiproton interactions exceeds that for proton interactions. Hence the antiproton annihilation leads to larger energy depositions in the SpaCal than proton interactions resulting in an asymmetry if the number of events above a certain threshold is counted [Adl01a].

In order to verify the PHOJET normalisation obtained from the tagged events the quantity $n_{\gamma p}$ as given by equation 4.23 is compared between the data and the PHOJET sample applying the global normalisation factor $N_{Data,tag}/N_{PHOJET,tag}$ to the PHOJET prediction. The resulting ratio amounts to $R = 1.004 \pm 0.145_{stat} \pm 0.05_{asym}$, where the first error denotes the statistical uncertainty while the latter corresponds to the uncertainty of the charge asymmetry. Hence the ratio indicates an almost perfect agreement, but is afflicted with a large uncertainty of approximately 15% dominated the statistical error of $n_{\gamma p}$. Therefore an uncertainty of 15% on the PHOJET normalisation is assumed for the cross-section determination based on the BST. The same uncertainty is used for the BDC analysis.

5 Results of the Measurement

After defining the analysis bins the present chapter shows that the corrections derived in the last two chapters lead to a level of agreement between data and simulation in the analysed region of the phase space that allows for a cross-section determination using the Monte Carlo method (see section 3.8). Subsequently, all identified uncertainties on the measurement are summarised and their influence on the cross-section is quantified. The final outcome of the BDC analysis for the shifted vertex data is then presented: the double differential inclusive DIS cross-section and the structure function F_2. The results are compared to the BST analysis [Var06], preliminary results [Laš02a, Pet04], various published measurements and theoretical predictions.

5.1 Definition of the Analysis Bins

For the analysis at hand data and simulated events are binned in the same way as for the H1 publication [Adl01a] to simplify comparisons. In parts of the phase space the binning is also similar to that used for the measurement based on the shifted vertex run from 1995 [Adl97b]. It is a combination of bins in x and Q^2 and in y and Q^2 (see figure 5.1 or 5.2). In the bulk of the phase space bins with a rectangular shape in the xQ^2-plane are used. The basic grid has five bins per decade in x and eight bins per decade in Q^2. Several bins of the basic grid in x are combined to one final analysis bin where necessary, according to the criteria given below. The contribution of the longitudinal structure function F_L to the cross-section is proportional to y^2. Hence a fine binning in y is preferable at high y to isolate bins with a higher sensitivity to F_L. At $y = 0.6$ the transition between the two binning schemes takes place. Bins with a special shape are used in this region to avoid double counting and losses. The choice of the bin size is determined by the following considerations:

- The bins should be small enough in order to permit a measurement of the double differential cross-section at as many points as possible and large enough to accumulate reasonable statistics. The statistical error in each bin should be smaller than the systematic one.

- The bin size has to be adjusted to the resolution of the kinematic variables. A grid that is too small can lead to large bin-to-bin migrations which can influence the results of the measurement.

To control the migration effects two quantities are determined in each bin for the DJANGO Monte Carlo sample, the *stability S* and the *purity P*. They are defined as the ratio of the number of events generated and reconstructed[1] in a bin to the total

---

[1] An event is considered as reconstructed if it passes all selection criteria listed in table 4.10.
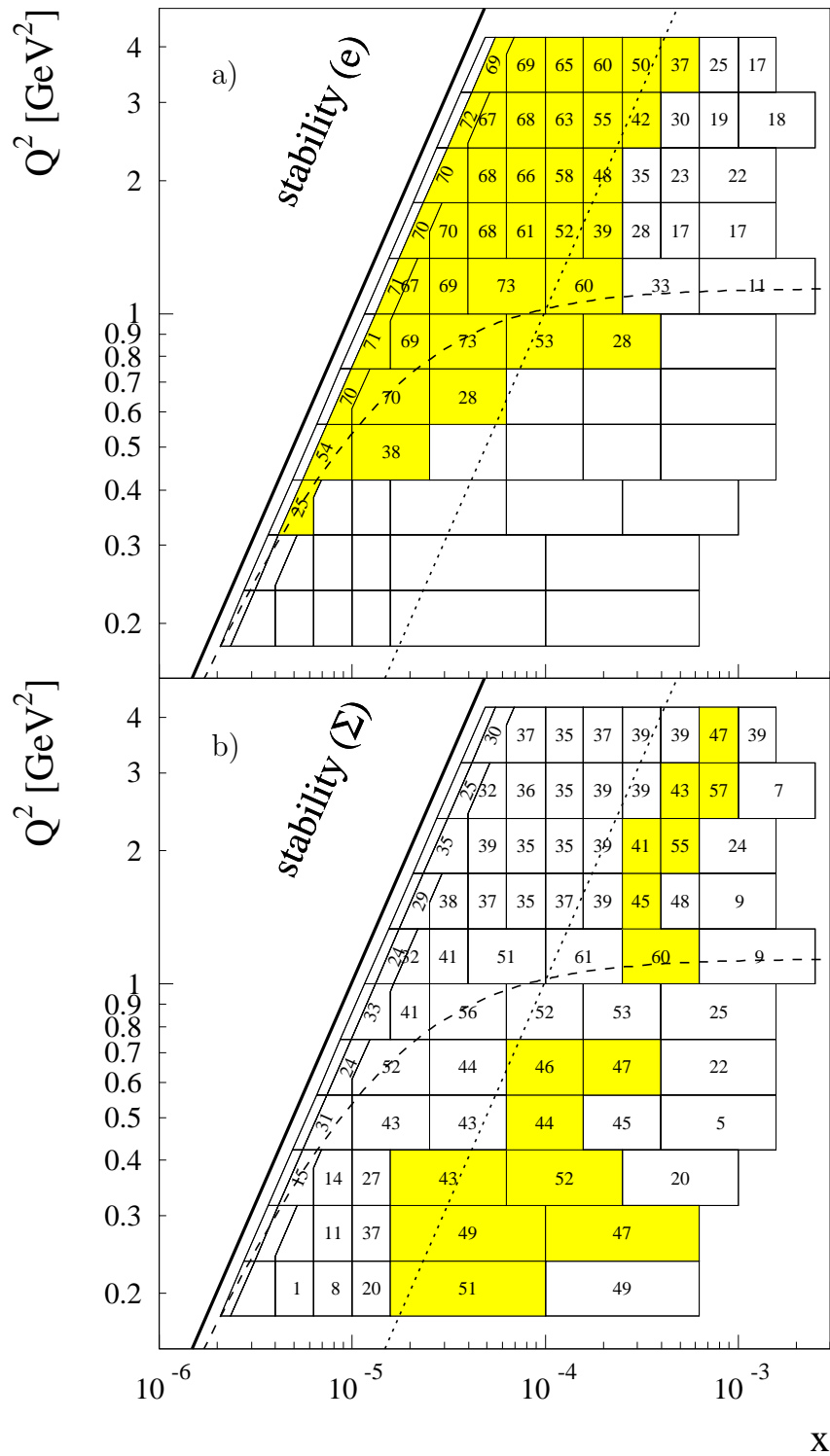
Figure 5.1: *Stability S (according to equation 5.1) in per cent for each analysis bin in the xQ^2-plane for a) the electron and b) the sigma method. Apart from the kinematic limit $y = 1$ (thick solid lines) the line corresponding to $y = 0.1$ (dotted lines) and the acceptance limit imposed by the cut $R_e > 9\,\mathrm{cm}$ (dashed lines) are indicated for non-radiative events. For each reconstruction method the bins contributing to the cross-section measurement are highlighted.*
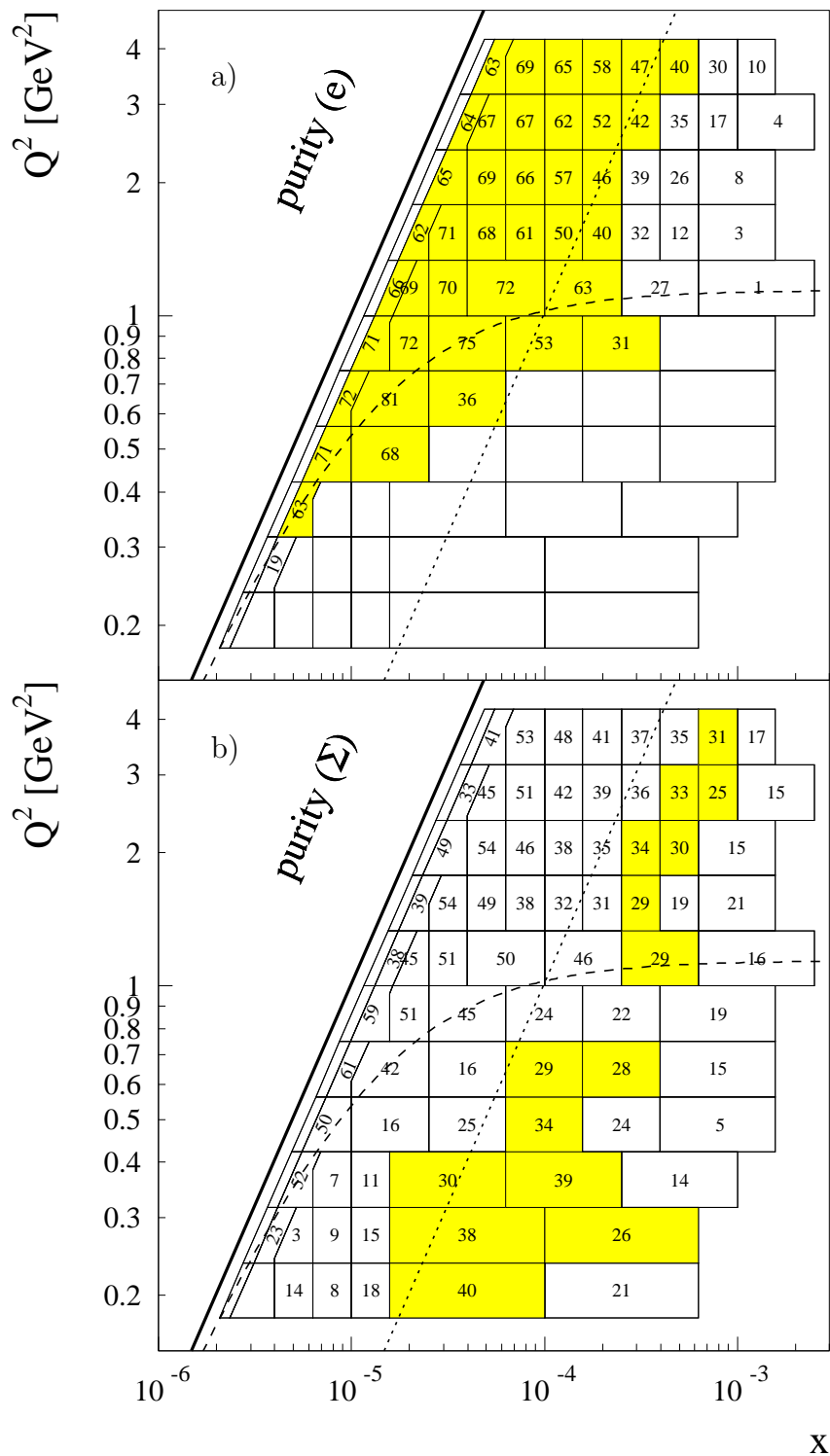
Figure 5.2: *Purity P (according to equation 5.2) in per cent for each analysis bin in the xQ²-plane for a) the electron and b) the sigma method. Apart from the kinematic limit y = 1 (thick solid lines) the line corresponding to y = 0.1 (dotted lines) and the acceptance limit imposed by the cut R_e > 9 cm (dashed lines) are indicated for non-radiative events. For each reconstruction method the bins contributing to the cross-section measurement are highlighted.*

number of events generated (reconstructed) in that bin:

$$S = \frac{N_{MC,gen \ \&\& \ rec}^{\square}}{N_{MC,gen}^{\square}} \tag{5.1}$$

$$P = \frac{N_{MC,gen \ \&\& \ rec}^{\square}}{N_{MC,rec}^{\square}} \tag{5.2}$$

The stability specifies the probability that an event generated in a given bin is also reconstructed in that bin, the purity the probability that an event reconstructed in a given bin has been generated in the same one. Hence the stability expresses the migration out of the given bin while the purity quantifies the migration of events from adjacent bins into that bin. Both variables can only take values between 0 and 1 by definition.

Figures 5.1 and 5.2 show the stability and purity for the electron and sigma methods in the xQ^2 plane. As expected from the discussion of the resolution of the different reconstruction methods in section 3.2 the electron method yields better results at large values of y. Values of S and P above 50% are typically reached for $y > 0.1$. At lower values of y the sigma method provides larger values of stability and purity since the resolution of the electron method degrades as $1/y$ towards low y.

Only the sigma method covers the region of the phase space dominated by ISR events, which are located at lower Q^2 and larger x than the acceptance limit of the BDC analysis for non-radiative events imposed by the requirement $R_e > 9 \, \text{cm}$ (dashed lines). In the case of the electron method ISR events are strongly suppressed by the cut $E - p_z > 35 \, \text{GeV}$. However, some of the bins beyond the acceptance limit are also covered by the electron method. This is due to the fact that the dashed line corresponds to the acceptance limit for the average z-vertex position of the shifted vertex run of $\overline{z_{vtx}} = 71.9 \, \text{cm}$. As z-positions of the interaction vertex of up to $\overline{z_{vtx}} + 30 \, \text{cm}$ are accepted for the analysis, slightly lower values of Q^2 can also be reached for non-radiative events.

Bins are only considered for the cross-section measurement if they have stability and purity larger than 25%. For bins in which both reconstruction methods fulfil this requirement the method yielding the maximum value of

$$W_i = \frac{S_i}{S_e + S_\Sigma} + \frac{P_i}{P_e + P_\Sigma} \tag{5.3}$$

is used for the cross-section determination. Here i corresponds either to the electron or the sigma method. The bins contributing to the cross-section measurement for each reconstruction method are highlighted in figures 5.1 and 5.2. The transition from the usage of the electron method to the sigma method takes place at $y \approx 0.1$.

5.2 Comparison of Data and Monte Carlo Simulation

Figures 5.3 to 5.5 demonstrate the agreement between data and Monte Carlo simulation by showing control distributions for the basic quantities reconstructed in the analysis. The sum of the predictions of DJANGO for the DIS signal and PHOJET for the photoproduction background is compared to the data. The contribution of the former
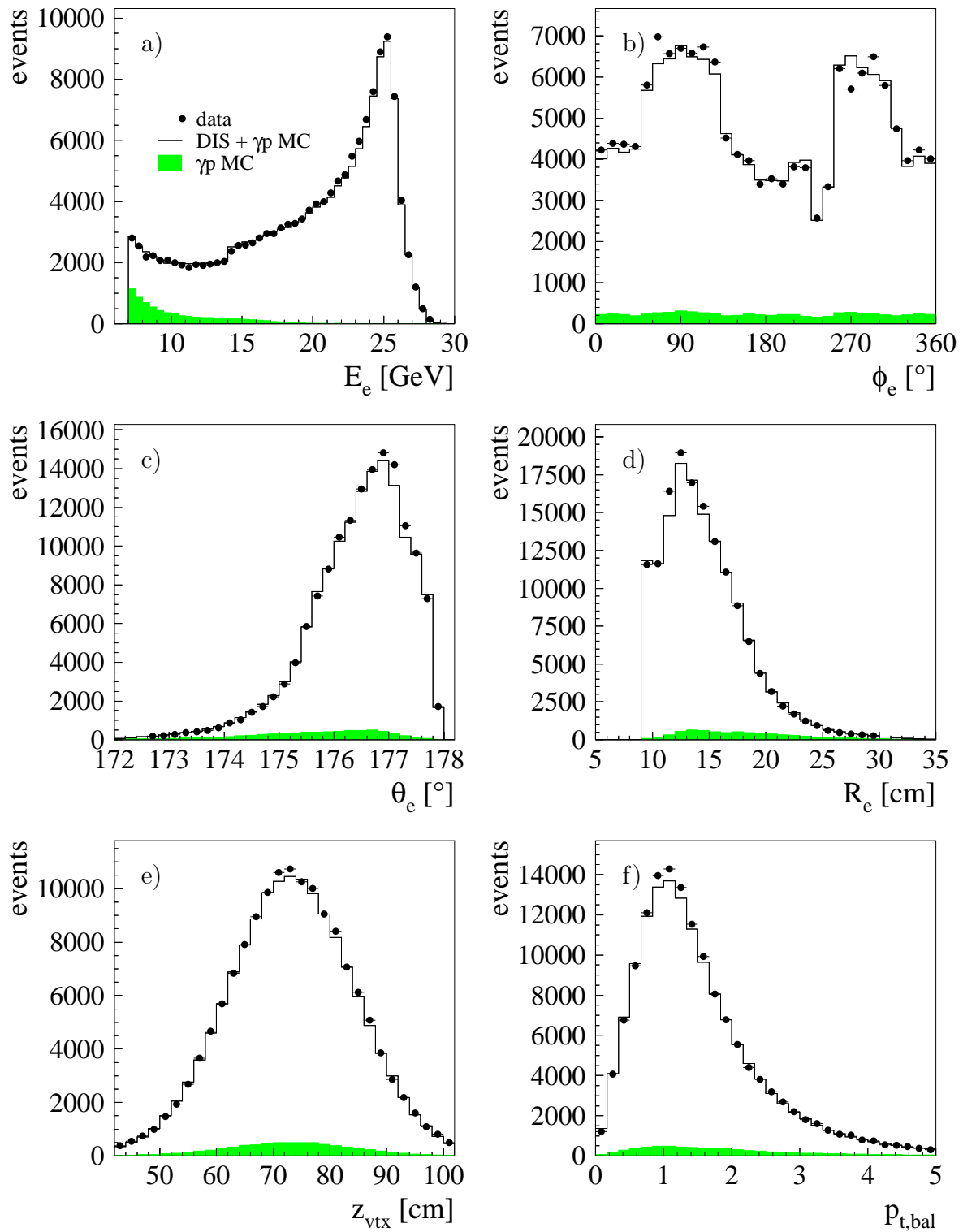
Figure 5.3: *Control distributions of basic observables: a) - d) energy E_e, azimuthal angle ϕ_e, polar angle θ_e and distance R_e of the electron candidate, e) z-position of the interaction vertex z_{vtx}, f) ratio $p_{t,bal}$ of the transverse momenta of the hadronic final state and the scattered electron. Only events from bins contributing to the cross-section determination (see figures 5.1 and 5.2) are considered.*
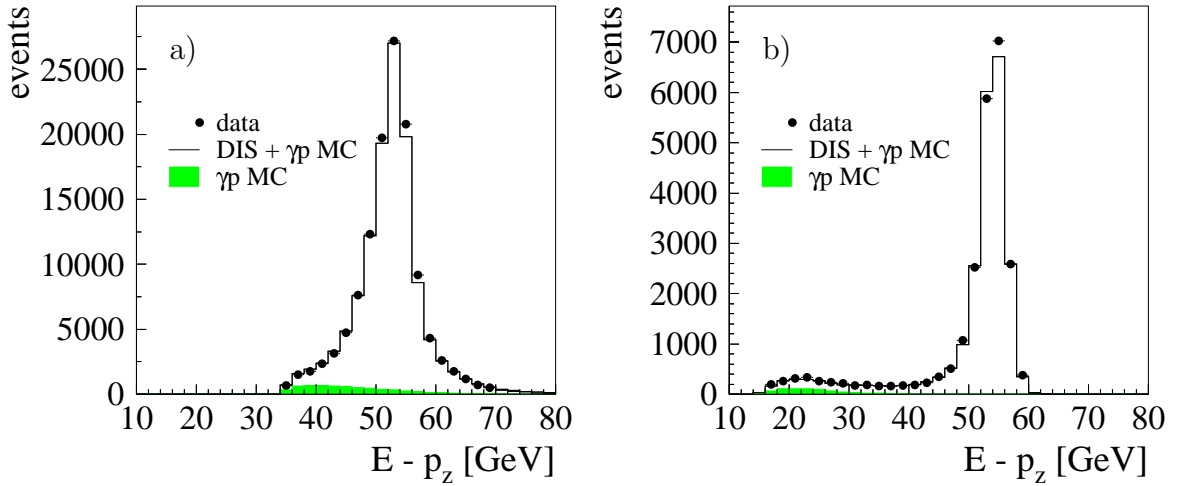
Figure 5.4: *Distribution of $E - p_z$ for events from bins contributing to the cross-section determination covered by a) the electron method and b) the sigma method (see figures 5.1 and 5.2).*

is normalised to the data according to the luminosities of the DJANGO sample and the data sample. The normalisation of PHOJET proceeds as described in section 4.9. The control distributions for the basic observables are depicted in figures 5.3 and 5.4. From these the kinematic variables used for the cross-section determination are derived (see figure 5.5). The distributions in figure 5.3 contain contributions from all analysis bins used for the cross-section determination (see figure 5.1 or 5.2). Figure 5.4 shows the $E - p_z$ spectrum separately for bins covered a) by the electron method and b) by the sigma method. The distributions of figure 5.5 comprise only analysis bins to which events have been assigned by the same method that has been used to reconstruct the displayed variable.

For the basic observables (see figure 5.3) data and Monte Carlo simulation in general agree well. The distribution of the azimuthal angle ϕ_e reflects the complicated fiducial volume of the analysis. Two bins at $\phi_e \approx 60°$ and $\phi_e \approx 270°$ show an excess and deficit of data compared to the Monte Carlo prediction, respectively. Single SpaCal cells being responsible for this could not be identified. The same holds for the excess of data observed at $R_e \approx 12\,\text{cm}$ corresponding to $\theta_e \approx 177.2°$. The latter does not occur at the acceptance edge and is reflected in a rather wide-spread excess of the data over the simulation in the distribution of Q_e^2 around $1.5\,\text{GeV}^2$. Hence it is likely to be caused by a slightly different behaviour of the structure functions from that assumed in the simulation and not by a detector effect.

Figure 5.3 f) depicts the distribution of the ratio $p_{t,bal}$ of the transverse momenta of the hadronic final state and the electron candidate. The maximum is located near one, which one would expect from energy and momentum conservation. The large width is due to the fact that the analysis focuses on events with low values of Q^2. Hence the transverse momenta are typically small and small fluctuations of the measured energies can have large effects on the ratio. The good agreement between data and Monte Carlo simulation indicates that the calibrations of the electromagnetic and hadronic energies are consistent. This is particularly important for the use of the sigma method.
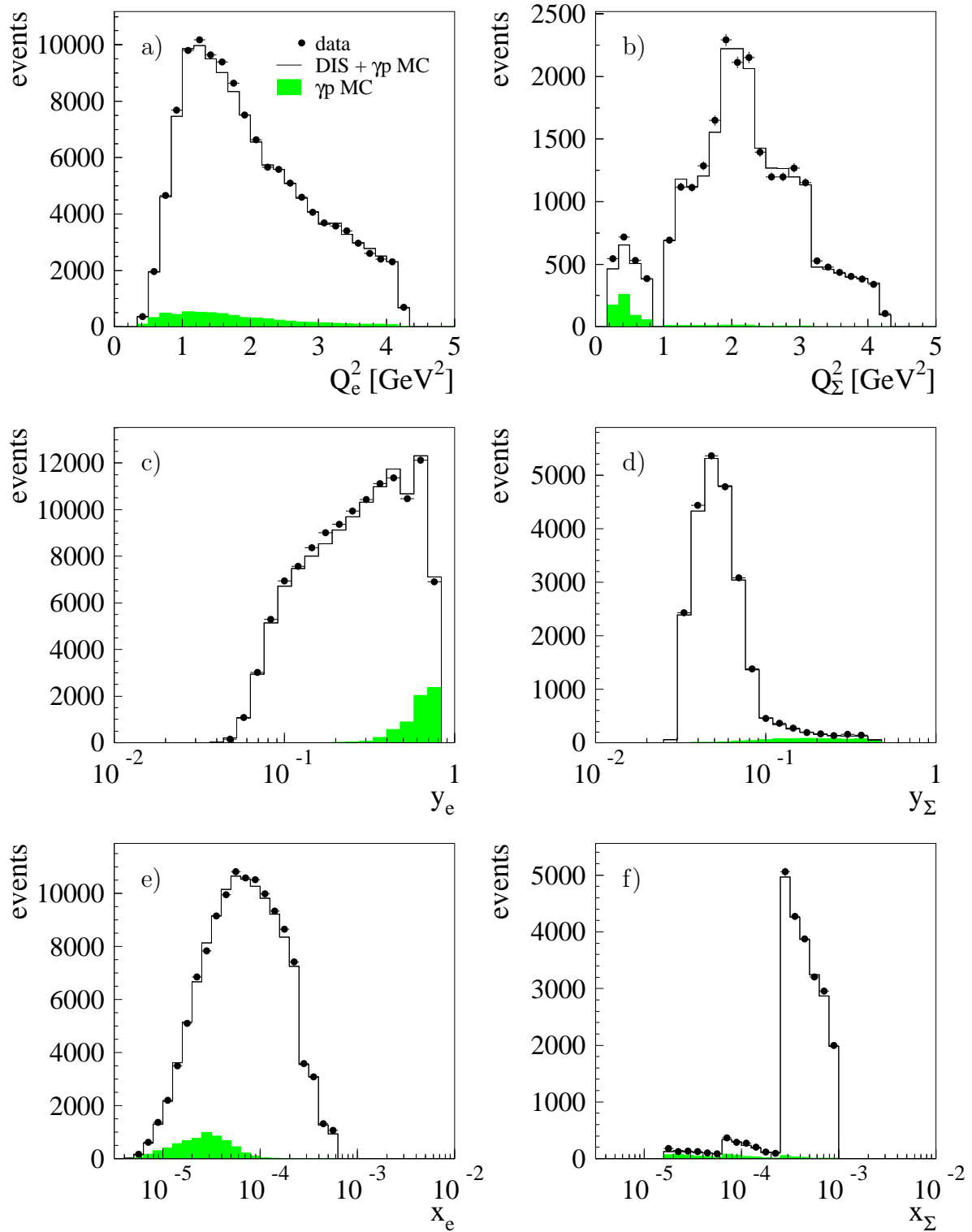
Figure 5.5: *Control distributions of the kinematic variables x, y and Q^2. In the left (right) column the variables have been reconstructed with the electron (sigma) method and only events are considered from bins which contribute to the cross-section determination and are covered by the electron (sigma) method (see figures 5.1 and 5.2).*

The spectrum of $E - p_z$ for the analysis bins which use the sigma method extends below the lower limit of $35\,\text{GeV}$ required in the case of the electron method (see figure 5.4). The ISR events are concentrated in this region of the distribution. They are accompanied by a large fraction of photoproduction events since the latter are also characterised by values of $E - p_z$ well below the nominal value of $2E_e^0 = 55.2\,\text{GeV}$.

For all kinematic variables the Monte Carlo simulation nicely describes the data as can be seen from figure 5.5. Only non-radiative events contribute to the distributions of Q_e^2, y_e and x_e while the spectra of Q_Σ^2, y_Σ and x_Σ contain ISR events in addition (see figures 5.1 and 5.2). This explains why two separate parts can be distinguished in figures 5.5 b), d) and f). The ISR events are located at low Q_Σ^2, high y_Σ and low x_Σ.

5.3 Systematic Uncertainties

All uncertainties associated with the various aspects of the measurement which have been identified in the last two chapters are listed in table 5.1. For comparison the corresponding uncertainties of the BST analysis are specified in addition. The references indicate where the uncertainties have been derived or where additional information about them can be found. Each uncertainty is the source of a systematic error to be quoted for the cross-section determination. The calculation of these errors is the topic of the present section.

The systematic uncertainties are classified in three different categories as proposed in [Adl01a]: *correlated systematic errors*, *uncorrelated systematic errors* and global *normalisation uncertainties* (see table 5.1). Together with the statistical uncertainty of the data sample they constitute the total error of the measurement.

Sources of systematic errors classified as correlated affect the cross-section measurement in different analysis bins in a correlated way. The different sources are considered to be uncorrelated among one another. The distinction of the different error types is important for fits to the data and comparisons with other measurements. For some errors the classification is straightforward: the statistical uncertainty of the Monte Carlo samples is a typical uncorrelated error, the energy scale of the scattered electron is a typical source of a correlated error since the latter affects different bins in a similar way. In contrast, it is rather arbitrary to treat the uncertainty on the radiative corrections as a source of an uncorrelated systematic error.

To estimate the correlated systematic errors one proceeds in the following way: for each of the sources the relevant quantities are varied by the uncertainty, separately in positive and negative directions. The reduced cross-sections for the former (σ_r^+) and latter case (σ_r^-) are redetermined and the relative systematic error δ resulting from the source under consideration is calculated as

$$\delta = \frac{\sigma_r^- - \sigma_r^+}{2\,\sigma_r^0} \tag{5.4}$$

where σ_r^0 denotes the reduced cross-section at the central value. This implies that the whole analysis chain is executed twice for each correlated error source.

The treatment of the uncorrelated and normalisation uncertainties is less complex: the errors resulting from the limited DJANGO and PHOJET statistics are calculated analytically. The quoted uncertainty for the radiative corrections already corresponds

type	source	BST analysis	BDC analysis	reference
correlated	scattered electron energy scale	1% at $E_e = 2\,\mathrm{GeV}$ 0.2% at $E_e = 27.6\,\mathrm{GeV}$		section 4.5, [Var06]
	scattered electron polar angle	0.2 mrad	0.5 mrad	[H1], section 4.4
	hadronic energy scale LAr and CT	10% at $y = 10^{-3}$ 2% at $y = 10^{-2}$		section 4.5, [Var06]
	LAr noise	10%		section 4.5, [Var06]
	hadronic energy scale SpaCal	350 MeV		section 4.5, [Var06]
	PHOJET normalisation	15%		section 4.9, [H1]
uncorrelated	DJANGO statistics			
	PHOJET statistics			
	radiative corrections	0.5%		section 3.7, [Gla05b]
normalisation	luminosity		2.2%	[Lev06]
	online event selection	0.9%	0.7%	section 4.3
	BST efficiency	2%	-	[H1]
	selection efficiency	-	1.5%	section 4.6
	vertex efficiency correction	-	see table 4.12	section 4.7

Table 5.1: *Sources of systematic errors for the BST and BDC analyses.*

to the systematic error on the cross-section without further manipulation. The same holds for all normalisation uncertainties.

The table in appendix A provides a detailed overview of the measurement errors in each analysis bin. All quoted errors are relative errors. The correlated systematic uncertainties are listed individually, adopting the sign convention of equation 5.4, and are added in quadrature to calculate their cumulated contribution δ_{cor}. The quantity δ_{unc} contains all uncorrelated systematic errors as well as the normalisation uncertainties. Adding δ_{cor}, δ_{unc} and the statistical error of the data δ_{stat} in quadrature yields the total error δ_{tot}.

The error on the cross-section determination is clearly dominated by the systematic errors. Only for very few bins at low Q^2 the statistical error exceeds the systematic one. This is the reason why so much emphasis has been placed on an accurate determination of the measurement uncertainties. Among the systematic errors the uncorrelated and normalisation errors typically exceed the correlated ones.

For bins with central values of Q^2 larger than $0.85\,\text{GeV}^2$ the total errors vary in general between 4% and 5%. Only in the bins at lowest x the errors are larger due to the correlated error $\delta_{\gamma p}$ resulting from the uncertainty on the PHOJET normalisation. This is expected since small values of x correspond to large values of y and thus low energies E_e, where the PHOJET contribution is large (see figure 5.3). The largest correlated error in the bins at higher x is caused by the uncertainty on the polar angle measurement. At lower values of $Q^2 < 0.85\,\text{GeV}^2$ the total errors reach 20%, dominated either by the statistical error or the uncertainty on the vertex efficiency correction.

The uncertainties of the measurement affect the cross-section obtained with the electron and the sigma method differently. In order to judge to which extent the uncertainties are controlled the results of the two methods are compared before combining them. Figure 5.6 shows the reduced cross-section σ_r for the electron and the sigma method as a function of x for various values of Q^2. It has been determined at the central values in x and Q^2 for each bin according to equation 3.40. The result is only displayed if stability and purity exceed 25% for the respective method. Statistical and systematic errors are indicated separately. The good agreement between the two methods shows that the uncertainties of the measurement are well controlled.

5.4 Cross-section Determination

In order to derive the final cross-section to be quoted for the BDC analysis the values obtained with the electron and the sigma method are combined based on stabilities and purities as explained in section 5.1. The result is depicted in figure 5.7 as a function of x in different bins of Q^2 between $0.2\,\text{GeV}^2$ and $3.5\,\text{GeV}^2$. Statistical and total errors are indicated separately. The values of the reduced cross-section are also listed in the table of appendix A.

The experimental results are compared to a phenomenological prediction of σ_r based on the ALLM97 parameterisation [Abr97] for F_2 and the saturation model prediction [GB99a] for F_L. In addition the expectation for the reduced cross-section from the ALLM97 parameterisation is displayed for the case that the longitudinal structure function F_L is zero.

As can be seen from the turn-over of the cross-section close to the kinematic limit
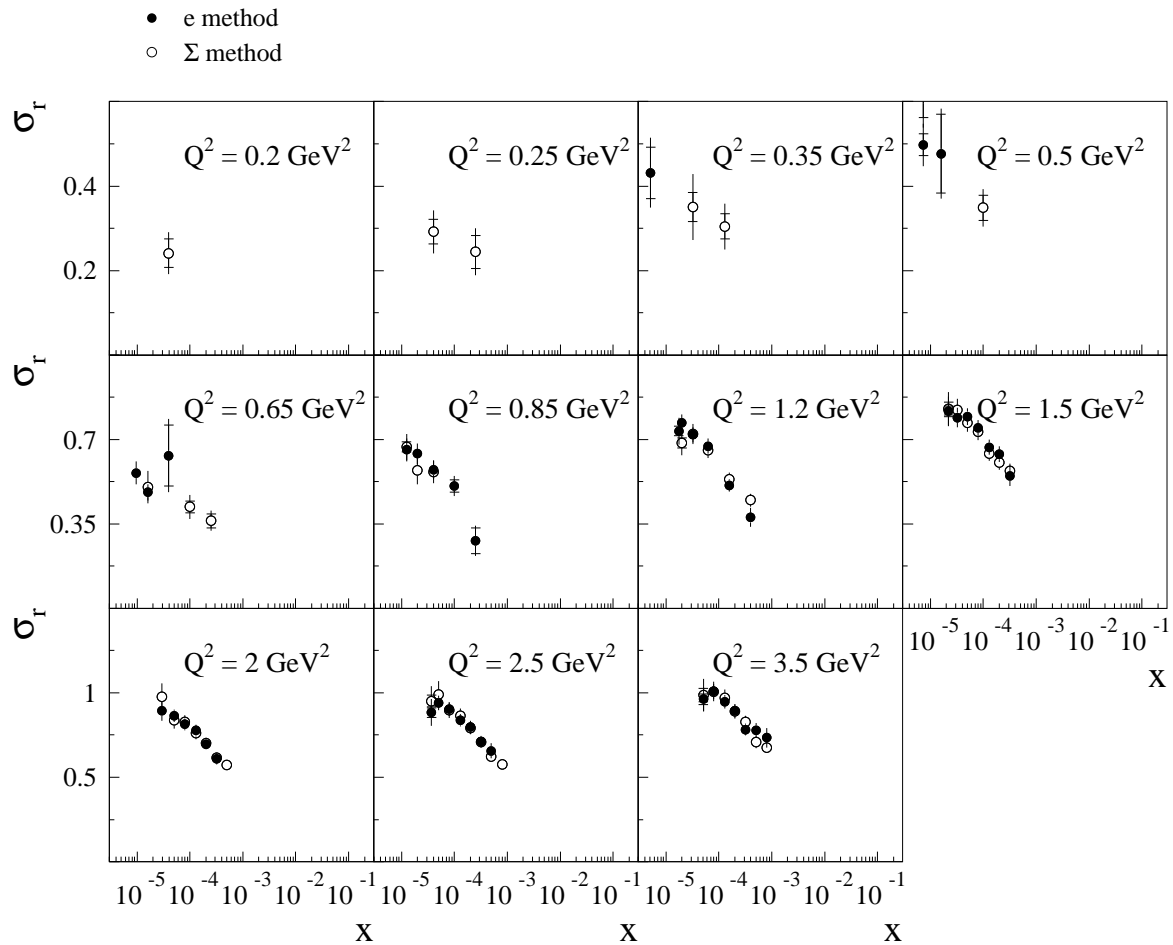
Figure 5.6: *Comparison of the reduced cross-section σ_r as a function of x for vari-ous values of Q^2 measured with the electron (full points) and the sigma (open points) method. The inner error bars represent the statistical errors, the outer error bars indicate the statistical and systematic errors added in quadrature.*

$(y = 1)$ at large values of Q^2 the data provide sensitivity to the longitudinal structure function F_L. This effect is more pronounced in the data than is predicted by the saturation model, i.e. there is an indication that the predicted F_L is too small. Apart from this measurement and prediction agree very well. For the bins with the lowest Q^2 values the measured cross-section is systematically larger than is predicted, but the experimental errors are very large in these bins.

Figure 5.8 compares σ_r for the present analysis and the BST analysis [Var06]. The PHOJET normalisation (see section 4.9) is treated differently from the case of [Var06]. For the comparison the bin-wise normalisation is consistently used for both analyses while in [Var06] the global normalisation is applied. For both analyses statistical and systematic errors are displayed separately.

The BST analysis extends to larger x in the whole Q^2 range as expected due to the cut $y_\Sigma > 0.03$ for the BDC analysis, necessary to ensure a good vertex reconstruction efficiency (see figure 3.14). In contrast, the BDC analysis provides some additional
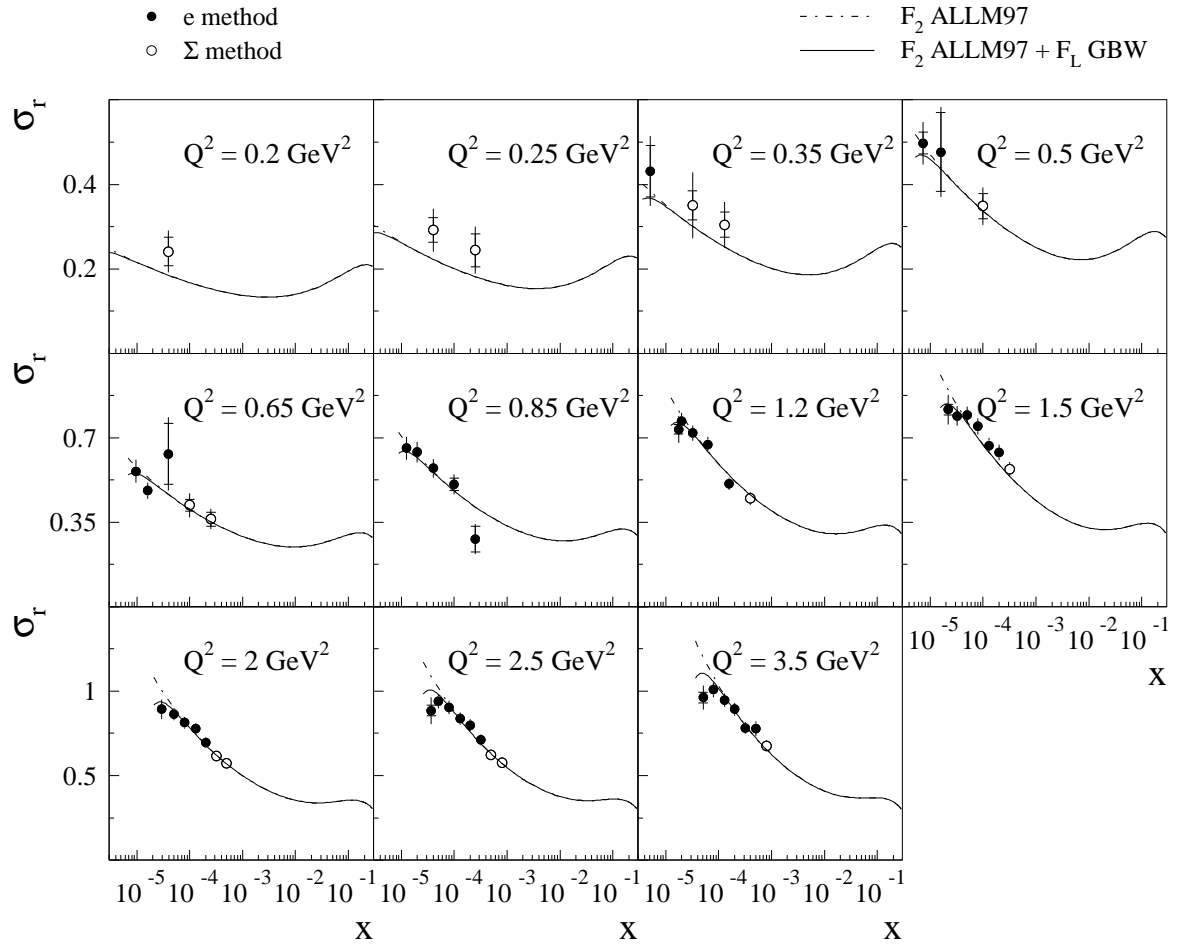
Figure 5.7: *Measurement of the reduced cross-section σ_r as a function of x for various values of Q^2. The inner error bars represent the statistical errors, the outer error bars indicate the statistical and systematic errors added in quadrature. The data are compared with a phenomenological prediction for σ_r based on the ALLM97 parameterisation [Abr97] for F_2 and the saturation model prediction [GB99a] for F_L (solid line). The dashed line shows the ALLM97 parameterisation for F_2 separately.*
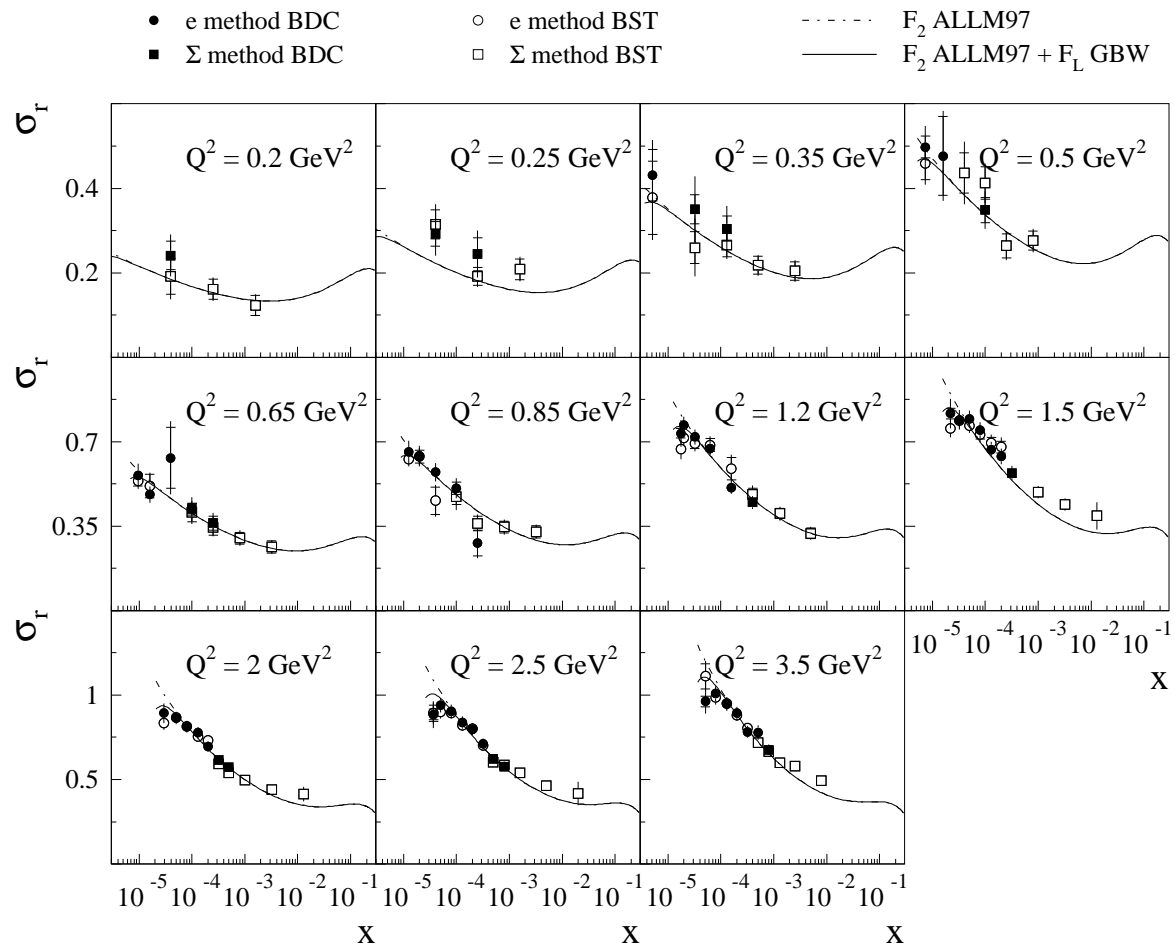
Figure 5.8: *Comparison of the reduced cross-section σ_r as a function of x for various values of Q^2 between the BDC (full symbols) and the BST (open symbols) analysis. The inner error bars represent the statistical errors, the outer error bars indicate the statistical and systematic errors added in quadrature.*

data points or data points with a higher precision in the transition region between the non-radiative and radiative events at intermediate Q^2. This follows from the larger polar angle acceptance of the BDC allowing access to larger values of x at fixed Q^2 for non-radiative events compared to the BST (see figure 3.14). At low Q^2 the transition region between non-radiative events and radiative events is not entirely covered by the cross-section measurement for either of the two analyses. The reason for this is the finite resolution of $E - p_z$ which causes large bin-to-bin migrations and hence values of stability and purity below the required 25% in this part of the kinematic phase space [Var06].

To quantify the consistency of the two analyses is a very difficult task since the statistical as well as the systematic errors are highly correlated. The correlation of the former is due to the fact that the same data set is used and therefore the events passing the DIS selection criteria in each analysis bin are to a large extent the same. Table 5.1 illustrates the correlation of the systematic errors. Only the uncertainties on θ_e and the efficiencies are different. To account for these difficulties the comparison proceeds in the following way. First the ratio r of the reduced cross-section of the BDC and the BST analysis is calculated and its statistical error is determined with the help of a special method explained in the following. Subsequently it is investigated whether the statistically significant deviations of the ratio from one can be explained by systematic errors not correlated between the two analyses.

To estimate the statistical error of r a special technique is employed which is applicable for quantities derived from correlated samples [LM05]: the DJANGO sample is split into 40 sub-samples with 25000 events each. For every sub-sample the ratio of the number of events per analysis bin for the BDC and the BST analysis is calculated. The relative standard deviation of the mean finally yields the expected statistical uncertainty on r if it is properly scaled, taking the luminosities of the data and DJANGO sample as well a the number of sub-samples into account. The validity of the method is verified in the following way: the event sample of the BDC analysis is split in half and the ratio of the cross-sections obtained from each half is calculated. As the two ensembles are statistically totally uncorrelated the statistical error of the ratio can be calculated from the statistical error of each sample. The estimation of the multiple Monte Carlo sample approach reproduces the result almost perfectly.

Figure 5.9 shows the ratio r and its statistical uncertainty in the same bins as in the case of the reduced cross-section in figure 5.8. For technical reasons the statistical uncertainty on r could only be calculated properly for bins in which both analyses use the same reconstruction method. Accordingly, the ratio is only displayed for these bins. This requirement excludes only three of the approximately 50 bins available for the comparison. For each bin in Q^2 the χ^2 per degree of freedom is indicated for the hypothesis $r = 1$, i.e. a perfect agreement of the two analyses. The dashed lines indicate a deviation of 5% from this hypothesis.

For bins with central values of Q^2 below $1.2\,\text{GeV}^2$ it is almost impossible to draw any statistically significant conclusion about the agreement of the two analyses since the statistical uncertainties on r are extremely large. For Q^2 larger than $2\,\text{GeV}^2$ the agreement is reasonably good. For the three intermediate bins the quoted values of χ^2 clearly indicate a disagreement of the two analyses. However, one has to keep in mind that so far only the statistical uncertainty on r estimated from the 40 DJANGO

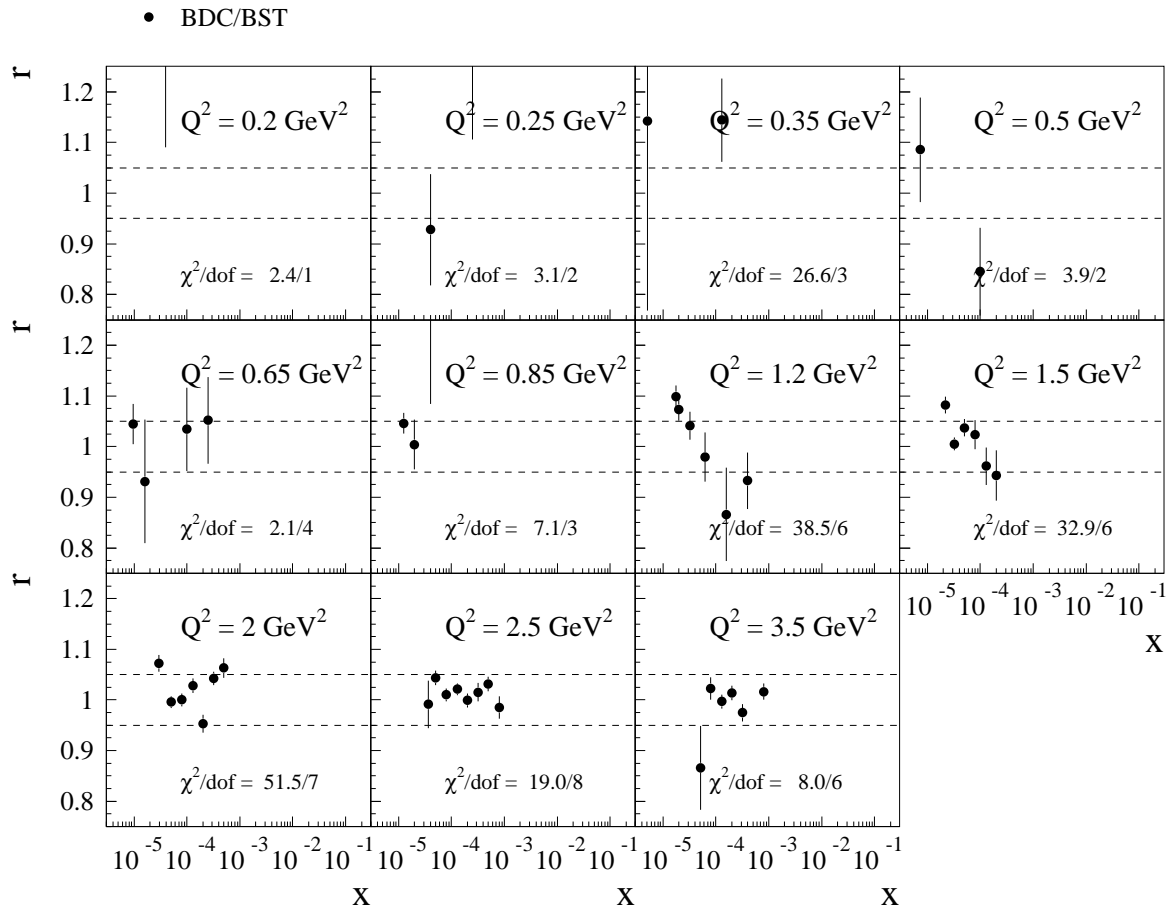Figure 5.9: *Ratio r of the reduced cross-section for the BDC and BST analysis. The dashed lines indicate a deviation of 5% from $r = 1$. The given values of χ^2 per degree of freedom (dof) quantify the level of agreement with $r = 1$. The errors displayed and assumed for the calculation of χ^2 are the statistical errors of r only, determined with the help of a special method (for details see text).*

sub-samples has been taken into account.

The following systematic errors, being uncorrelated between the BST and the BDC analysis, contribute to the uncertainty on r: due to the reduced amount of dead material affecting the track measurement with the BST compared to the BDC the BST is more efficient in rejecting photoproduction events (see section 4.6), i.e. their contribution to the ensemble of events passing all DIS selection criteria is significantly smaller. This is reflected in the systematic error resulting from the uncertainty on the PHOJET normalisation. In the three intermediate Q^2 bins it is a factor of two larger for the BDC than for the BST analysis (compare appendices A of [Var06] and the present thesis). In addition the different uncertainties on θ_e lead to systematic errors which are on average roughly a factor of five larger for the BDC than for the BST analysis. For each of the two sources the difference of the systematic errors between the two analyses is added quadratically to the statistical uncertainty on r and the χ^2 is recalculated. This reduces the χ^2 by 50%, 60% and 30% for the Q^2 bins $1.2\,\text{GeV}^2$, $1.5\,\text{GeV}^2$ and $2\,\text{GeV}^2$, respectively. This is a clear improvement, but not sufficient to claim agreement between the two analyses in these bins.

A possible explanation why the discrepancy is largest in the three intermediate bins may be that they are most highly affected by the lower acceptance limit of the BST analysis for R_e as illustrated in figure 5.10. The thin solid line shows the acceptance limit $R_e = 10\,\text{cm}$ for the BST analysis for the average z-position of the interaction vertex $\overline{z_{vtx}}$. For larger (smaller) actual z-vertex positions it is located at lower (higher) values of Q^2. The dashed lines indicate the change in the acceptance limit in the xQ^2-plane for a z-vertex position varying by $11\,\text{cm}$ in the positive and negative directions which approximately corresponds to the spread of the z-vertex distribution (see figure 4.25). For the analysis, vertices deviating by up to $30\,\text{cm}$ from $\overline{z_{vtx}}$ are accepted. In the region close to the cut the BST acceptance drops rather quickly with decreasing R_e, at $R_e = 10\,\text{cm}$ it already reaches 50% [H1]. For the BDC analysis the situation is different since the requirement $R_e > 9\,\text{cm}$ prevents large migration effects, while the acceptance at $R_e = 9\,\text{cm}$ is still close to 100% (see figure 4.27). Since the lines of constant R_e saturate at large values of x a significant number of bins in x is affected by the BST acceptance limit in the case of the intermediate bins. It is possible that the assumed uncertainties for θ_e and the BST efficiency do not fully account for such effects in this region of the kinematic phase space.

5.5 Extraction of the Structure Function F_2

Having measured the reduced cross-section σ_r the structure function F_2 can be determined by correcting σ_r for the contribution of F_L according to equation 3.41. For this purpose the prediction of the saturation model [GB99a] for F_L is employed. As has been discussed in the previous section the sensitivity of σ_r to F_L at high y (low x) is significant and the prediction of the saturation model yields too small values for F_L. Hence to reduce the dependence of the measurement on F_L the F_2 extraction is limited to $y < 0.6$. This strategy has been followed already in [Adl01a]. Consequently, in almost all Q^2 bins no F_2 extraction is performed for the bin with the lowest x for which a measured reduced cross-section is available.

The result of the F_2 determination is depicted in figure 5.11, the values are listed
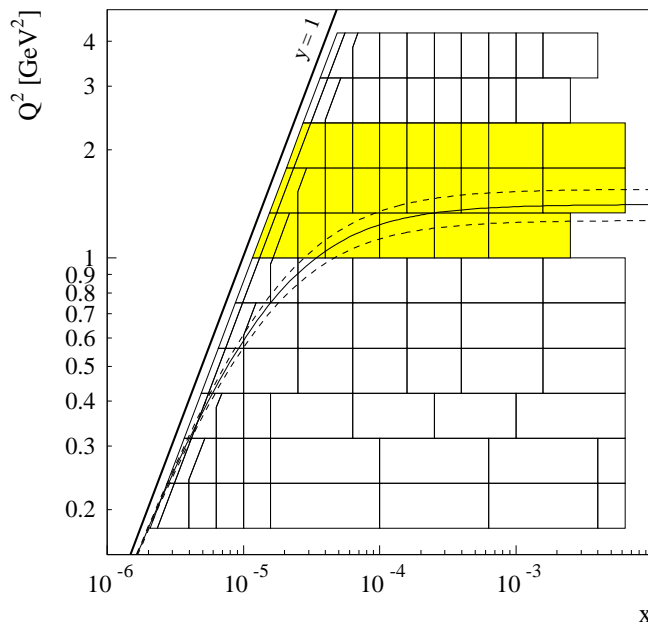
Figure 5.10: *Illustration of the influence of the lower acceptance limit of the BST analysis for R_e on the bins used for the cross-section determination in the xQ^2-plane. Apart from the kinematic limit $y = 1$ (thick solid line) lines representing the acceptance limit $R_e = 10\,\mathrm{cm}$ for z-vertex positions $z_{vtx} = \overline{z_{vtx}}$ (thin solid line) and $z_{vtx} = \overline{z_{vtx}} \pm 11\,\mathrm{cm}$ (dashed lines) are depicted. The bins with central values of Q^2 of $1.2\,\mathrm{GeV}^2$, $1.5\,\mathrm{GeV}^2$ and $2\,\mathrm{GeV}^2$ are highlighted.*

in the table of appendix A. The table also contains the values of F_L predicted by the saturation model and assumed for the extraction.

The data are compared to the phenomenological predictions of the ALLM97 parameterisation [Abr97] and the fractal fit [Laš02b]. As expected from figure 5.7 the ALLM97 parameterisation nicely describes the data. It undershoots the data only in the lowest Q^2 bins, where the experimental errors are large. The fractal fit underestimates the measured F_2 in all Q^2 bins.

As one of the motivations for performing the analysis at hand is to provide an independent cross-check of the preliminary results on F_2 for the shifted vertex period figure 5.12 compares the different analyses. It has already been explained in section 3.9 that the preliminary results have been obtained analysing non-radiative [Laš02a] and ISR [Pet04] events separately while no separation has been performed for the present analysis. Since the BST has been employed for the H1 preliminary results the corresponding data reach larger values of x. The present analysis extends the accessible phase space towards lower Q^2 values[2]. In the common region of the phase space, the smaller values of F_2 for the H1 preliminary analyses compared to the present one constitute the main difference. This arises due to the fact that for the preliminary results the wrong satellite corrections have been used for the luminosity determination (see section 4.2). This causes the luminosity to be too large by 4% and thus the measured

---

[2]The same holds for the BST analysis presented in [Var06].
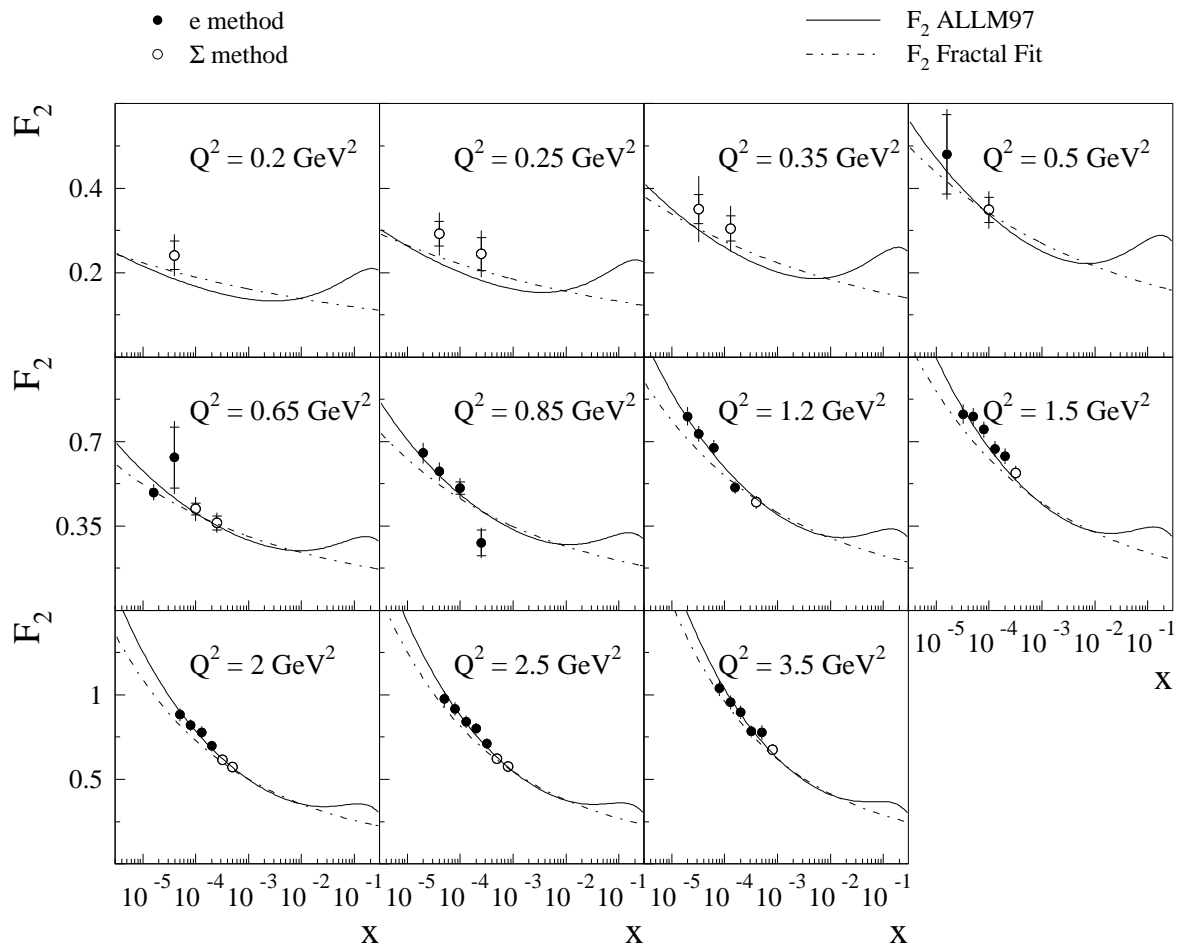
Figure 5.11: *Measurement of the proton structure function F_2, plotted as a function of x in bins of Q^2. The inner error bars represent the statistical errors, the outer error bars indicate the statistical and systematic errors added in quadrature. The data are compared to two phenomenological predictions: the ALLM97 parameterisation [Abr97] and the fractal fit [Laš02b].*
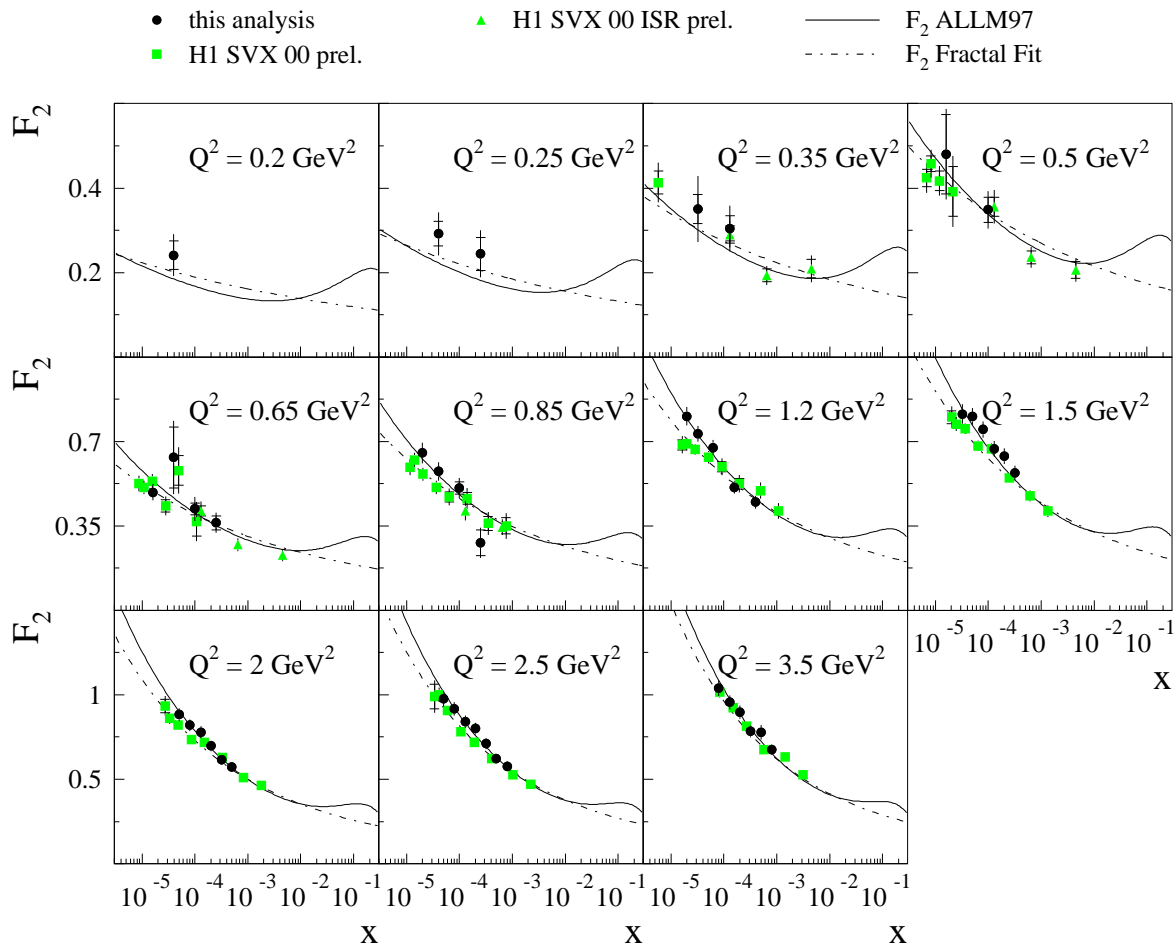
Figure 5.12: *Comparison of the structure function F_2 for the present analysis with the preliminary analyses of non-radiative (squares, [Laš02a]) and ISR (triangles, [Pet04]) events using the BST for the same data taking period. The inner error bars represent the statistical errors, the outer error bars indicate the statistical and systematic errors added in quadrature.*

F_2 to be too small by the same amount. Apart from this the new analysis of the shifted vertex data benefits from various refinements achieved in [Var06] and the present thesis. Among them are the new calibration [Var06] (section 4.5), the new alignment (section 4.4), the correction of the implementation of the beam tilt in the Monte Carlo simulation (section 3.6) and the adjustment of the subprocess fractions in DJANGO (section 3.5).

Finally the structure function F_2 of the present analysis is compared to various published HERA measurements relevant in the phase space covered. These include two analyses performed by the H1 collaboration based on data recorded during the previous shifted vertex run in 1995 [Adl97b] and during the years 1996 and 1997 [Adl01a] with standard running conditions of the HERA collider. In addition a measurement of the ZEUS collaboration using data from the year 1997 is shown. It employs a combination of an electromagnetic calorimeter (Beam Pipe Calorimeter, BPC) and a silicon tracker (Beam Pipe Tracker, BPT) mounted close to the beam pipe in the backward region of
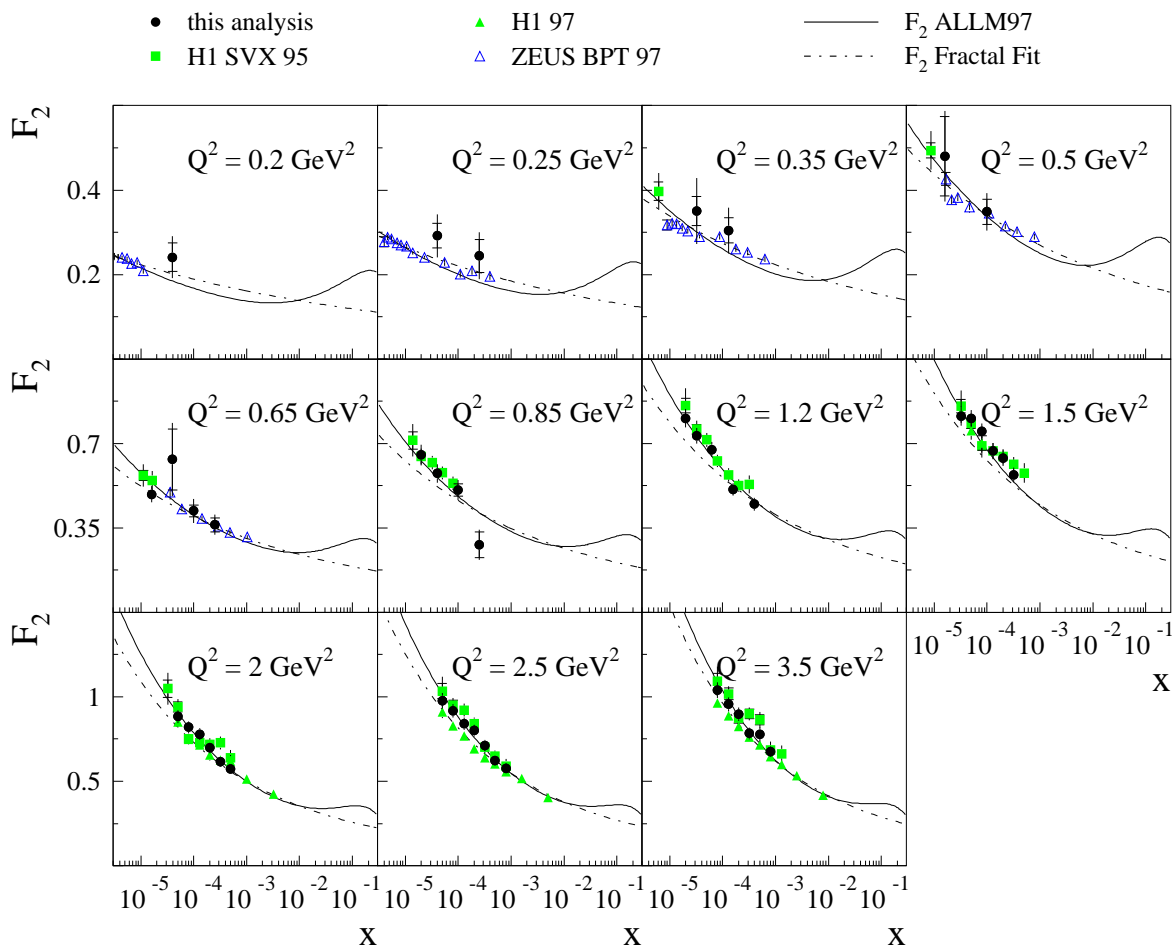
Figure 5.13: *Comparison of the structure function F_2 for the present analysis with various published HERA measurements (closed squares [Adl97b], closed triangles [Adl01a], open triangles [Bre00]). The inner error bars represent the statistical errors, the outer error bars indicate the statistical and systematic errors added in quadrature. The data of [Bre00] are shifted to the Q^2 values of the present analysis using the ALLM97 parameterisation.*

the ZEUS experiment, designed to reconstruct the scattered electron at very large large polar angles and thus to access very low values of Q^2. For all published measurements the proton energy of the HERA collider was $E_p^0 = 820\,\text{GeV}$. The ZEUS collaboration has used a different binning in Q^2 compared to H1. Hence for each Q^2 bin of the present analysis having a central value Q_{H1}^2 the bin of the ZEUS measurement closest in Q^2 is searched for and the corresponding values of F_2 are shifted to Q_{H1}^2. For this purpose the Q^2 dependence of the ALLM97 parameterisation at the central x values of the ZEUS bins is used.

The values of F_2 for the present analysis are slightly larger than for the H1 analysis of the years 1996 and 1997 and slightly smaller than those obtained from the previous shifted vertex run (see figure 5.13). In the lowest Q^2 bins they clearly overshoot the findings in the ZEUS analysis, however with large errors.

The total error of the analysis at hand is typically $30 - 50\%$ smaller than for the

analysis of the previous shifted vertex run. The statistical error is reduced by almost a factor of two as expected due to the roughly fourfold increase in luminosity. The most prominent improvement among the systematic errors is the reduction of the uncertainty on the PHOJET normalisation from 30% to 15%.

To make optimal use of the available precision data for the reduced cross-section σ_r and the structure function F_2 obtained in this thesis the following steps are in preparation: the results are going to be combined with those derived for the BST analysis [Var06]. In addition they are complemented by the data on σ_r and F_2 obtained from the minimum bias run in 1999 covering the Q^2 range $0.5\,\text{GeV}^2 < Q^2 < 12\,\text{GeV}^2$ [Eck01, Laš04b]. Also this analysis has undergone a major revision in the meantime. Based on the resulting large data set one aims for an extraction of the longitudinal structure function F_L as well as the exponent λ characterising the rise of F_2 towards low x. Finally new fits to the fractal and saturation model are foreseen. A comprehensive publication of all results is anticipated for which a draft already exists [H1].

Summary

During a special data taking period of the HERA collider in the year 2000, called shifted vertex run, the interaction region of electrons and protons has been shifted into the direction of the incoming proton. This allows to study the proton structure at virtualities of the exchanged photon $Q^2 \approx 1 \, \mathrm{GeV}^2$ where the transition takes place from a region of the phase space where perturbative calculations based on Quantum Chromodynamics, the theory of the strong interaction, can be performed to a domain where only phenomenological models are able to describe the data.

The topic of the present thesis is a measurement of the inclusive DIS cross-section based on the data recorded with the H1 detector during the shifted vertex run. This requires an accurate reconstruction of the scattered electron. Its polar angle is determined with the help of the Backward Drift Chamber (BDC) and the interaction vertex reconstructed by the Central Tracker, its energy is measured in the backward calorimeter SpaCal. Hence the alignment of BDC and SpaCal w.r.t. the Central Tracker has been studied in detail. The calibration of the SpaCal has been performed in [Var06].

The cross-section determination relies on a comparison of the number of observed events between the data and a Monte Carlo simulation of the scattering process and the detector response. After imperfections in the implementation of the simulation have been identified and overcome a detailed comparison of the detector response between data and Monte Carlo has been carried out. The remaining differences are taken into account by correction factors to the Monte Carlo sample.

The dominant background contribution to this analysis are photoproduction events $(Q^2 \approx 0 \, \mathrm{GeV}^2)$ in which a particle of the hadronic final state mimics the scattered electron. Their contribution is subtracted statistically from the data, again based on a Monte Carlo model. All other background sources are found to be negligible.

With x being the fraction of the proton's momentum carried by the struck quark the data allow to measure the cross-section in the kinematic range $0.2 < Q^2 < 3.5 \, \mathrm{GeV}^2$ and $3 \cdot 10^{-5} < x < 8 \cdot 10^{-4}$. Based on this the structure function F_2, parameterising the quark composition of the proton, can be extracted. For all investigations carried out in this analysis uncertainties have been derived and the resulting systematic errors on F_2 have been determined. The total errors vary between 4% and 5% for $Q^2 > 0.85 \, \mathrm{GeV}^2$, only at the smallest values of x they are larger due to the uncertainty on the contribution of the photoproduction events. At lower virtualities, $Q^2 < 0.85 \, \mathrm{GeV}^2$, the total errors reach 20%, dominated either by the statistical error or the uncertainty on the reconstruction efficiency for the interaction vertex. The errors are typically $30-50\%$ smaller than for the analysis of a previous shifted vertex run performed in 1995. Furthermore the results are in agreement with a second analysis using the same data but employing the Backward Silicon Tracker for the reconstruction of the polar angle of the scattered electron [Var06]. A combined publication of both analyses is anticipated.

A Table of Results

The table in this appendix summarises the results of the analysis presented in the thesis at hand, i.e. the reduced cross-section and the structure function F_2 together with all uncertainties in each analysis bin. The columns of the table contain (from left to right):

- the kinematic variables Q^2, x and y at the bin centres,

- the measured reduced cross-section σ_r, the prediction for the longitudinal structure function F_L of the saturation model [GB99a] used for the extraction of F_2, the structure function F_2 itself,

- the total uncertainty of the measurement δ_{tot} and its components, i.e. the statistical error δ_{stat}, the cumulated uncorrelated systematic and normalisation uncertainties δ_{unc} and the cumulated correlated systematic uncertainties δ_{cor} (for details see table 5.1),

- the individual components of the total correlated systematic error arising from the uncertainty on the energy scale (δ_{E_e}) and polar angle (δ_{θ_e}) of the scattered electron, on the hadronic energy scale of LAr calorimeter and Central Tracker (δ_{LAr}), on the noise in the LAr (δ_{noise}), on the hadronic energy scale of the SpaCal calorimeter (δ_{Spa}) and on the PHOJET normalisation $(\delta_{\gamma p})$ and finally

- the reconstruction method (e: electron method, Σ: sigma method) employed for the measurement in the actual bin.

All quoted errors are relative uncertainties in per cent. To reduce the sensitivity of F_2 on the model assumption for F_L the measurement of the former is limited to $y < 0.6$ (for details see section 5.5).

Q^2 [GeV^2]	x	y	σ_r	F_L	F_2	δ_{tot} [%]	δ_{stat} [%]	δ_{unc} [%]	δ_{cor} [%]	δ_{E_e} [%]	δ_{θ_e} [%]	δ_{LAr} [%]	δ_{noise} [%]	δ_{Spa} [%]	$\delta_{\gamma p}$ [%]	method
0.20	0.0000398	0.049	0.241	0.019	0.241	20.59	14.09	12.32	8.59	-0.33	-1.59	5.11	-0.21	-0.59	-6.68	Σ
0.25	0.0000398	0.062	0.292	0.025	0.292	17.47	9.81	11.57	8.66	-0.16	-2.21	2.40	-1.30	-2.62	-7.46	Σ
0.25	0.0002510	0.010	0.244	0.021	0.244	22.86	15.93	12.39	10.74	4.99	-4.00	-5.13	2.86	-5.84	-2.42	Σ
0.35	0.0000051	0.673	0.432	-	-	19.19	14.12	12.40	3.88	-1.84	0.75	0.82	-0.13	0.75	-3.15	e
0.35	0.0000320	0.108	0.350	0.037	0.350	22.29	9.88	11.42	16.39	-0.91	0.14	-1.39	0.65	-6.81	-14.80	Σ
0.35	0.0001300	0.027	0.304	0.033	0.304	17.79	9.76	11.13	9.87	-0.39	-2.14	-6.18	1.70	-6.17	-3.66	Σ
0.50	0.0000073	0.673	0.498	-	-	10.09	5.25	6.16	6.02	-1.00	1.90	2.09	-0.18	2.11	-4.78	e
0.50	0.0000158	0.312	0.477	0.056	0.480	22.39	19.60	10.23	3.53	-2.16	-2.73	0.10	0.03	0.54	-0.21	e
0.50	0.0001000	0.049	0.348	0.050	0.348	12.71	8.60	6.73	6.51	-3.11	1.37	-0.09	0.32	-1.95	-5.19	Σ
0.65	0.0000095	0.673	0.561	-	-	8.48	3.19	5.88	5.21	-0.19	-1.26	2.30	-0.19	1.41	-4.27	e
0.65	0.0000158	0.405	0.481	0.073	0.490	7.00	3.10	5.87	2.22	-0.74	-1.80	0.41	-0.08	0.26	-0.93	e
0.65	0.0000398	0.161	0.633	0.068	0.634	23.95	19.87	11.77	6.34	-5.84	2.46	-0.04	0.04	-0.12	0.00	e
0.65	0.0001000	0.064	0.420	0.063	0.420	11.92	5.59	6.27	8.46	-1.35	-2.38	-1.47	0.56	-7.16	-3.20	Σ
0.65	0.0002510	0.025	0.363	0.057	0.363	11.58	7.99	6.61	5.15	-1.75	-2.62	-0.71	2.29	-2.97	-1.43	Σ
0.85	0.0000124	0.673	0.657	-	-	7.25	2.22	5.81	3.73	-0.86	-1.29	1.23	-0.22	1.11	-2.95	e
0.85	0.0000200	0.418	0.641	0.092	0.652	6.61	1.95	5.79	2.51	-1.04	-2.22	0.19	-0.10	0.23	-0.44	e
0.85	0.0000398	0.210	0.574	0.086	0.576	6.60	2.04	5.80	2.39	-0.96	-2.19	-0.02	-0.07	0.00	-0.05	e
0.85	0.0001000	0.084	0.507	0.079	0.507	8.06	5.05	6.19	1.11	-0.45	-0.44	0.16	-0.78	0.45	0.00	e
0.85	0.0002510	0.033	0.280	0.071	0.280	22.48	19.40	9.30	6.51	4.49	-4.14	1.45	-1.71	0.00	0.00	e
1.20	0.0000176	0.673	0.735	-	-	7.53	2.73	3.61	6.01	-1.30	-0.80	2.02	-0.31	1.69	-5.18	e
1.20	0.0000200	0.591	0.768	0.123	0.805	4.66	2.06	3.55	2.20	-0.59	-1.62	0.98	-0.12	0.41	-0.87	e
1.20	0.0000320	0.369	0.720	0.118	0.731	4.36	1.66	3.51	2.00	-0.21	-1.69	0.84	-0.09	0.09	-0.59	e
1.20	0.0000631	0.187	0.672	0.110	0.674	4.63	1.38	3.49	2.70	-1.09	-2.46	0.08	-0.21	0.16	-0.02	e
1.20	0.0001580	0.075	0.510	0.098	0.510	4.90	2.07	3.55	2.67	0.75	-2.01	0.68	-1.40	0.25	0.00	e
1.20	0.0003980	0.030	0.448	0.088	0.448	6.18	2.63	3.61	4.27	-1.25	-2.76	-1.93	1.68	-1.56	-0.20	Σ
1.50	0.0000220	0.673	0.817	-	-	7.59	2.59	3.59	6.17	-0.36	-1.69	2.80	-0.30	1.78	-4.89	e
1.50	0.0000320	0.462	0.791	0.140	0.814	5.03	1.71	3.50	3.18	-1.74	-2.10	-0.07	-0.14	0.49	-1.56	e
1.50	0.0000500	0.295	0.795	0.133	0.803	4.40	1.47	3.49	2.23	-0.90	-2.03	0.03	-0.08	-0.04	-0.13	e
1.50	0.0000800	0.185	0.747	0.126	0.750	4.51	1.58	3.50	2.36	-0.78	-2.22	0.03	-0.17	0.11	-0.02	e

| Q^2 [GeV²]	x	y	σ_r	F_L	F_2	δ_{tot} [%]	δ_{stat} [%]	δ_{unc} [%]	δ_{cor} [%]	δ_{E_e} [%]	δ_{θ_e} [%]	δ_{LAr} [%]	δ_{noise} [%]	δ_{Spa} [%]	$\delta_{\gamma p}$ [%]	method
1.50	0.0001300	0.114	0.668	0.118	0.669	4.80	1.78	3.52	2.74	-0.86	-2.53	0.18	-0.53	0.21	-0.01	e
1.50	0.0002000	0.074	0.639	0.111	0.639	5.15	2.12	3.56	3.06	0.30	-2.57	0.78	-1.43	0.13	0.00	e
1.50	0.0003200	0.046	0.569	0.104	0.570	5.13	1.91	3.53	3.19	-0.49	-2.43	-1.18	0.19	-1.61	-0.14	Σ
2.00	0.0000293	0.673	0.894	-	-	6.50	2.16	3.54	5.00	-0.52	-0.64	2.33	-0.30	1.52	-4.07	e
2.00	0.0000500	0.394	0.865	0.164	0.883	4.30	1.62	3.49	1.92	-0.94	-1.44	0.34	-0.09	0.11	-0.78	e
2.00	0.0000800	0.246	0.814	0.154	0.820	4.30	1.51	3.49	2.02	-1.00	-1.75	-0.01	-0.06	0.01	-0.07	e
2.00	0.0001300	0.151	0.777	0.143	0.779	4.41	1.52	3.49	2.23	-0.90	-2.03	0.07	-0.19	0.12	-0.01	e
2.00	0.0002000	0.098	0.697	0.134	0.698	4.50	1.66	3.50	2.29	-0.33	-2.11	0.31	-0.74	0.13	0.00	e
2.00	0.0003200	0.062	0.617	0.125	0.617	4.81	1.68	3.50	2.85	0.09	-2.18	-1.08	-0.30	-1.45	-0.14	Σ
2.00	0.0005000	0.039	0.573	0.117	0.573	4.80	1.89	3.51	2.68	-0.08	-2.03	-1.45	0.53	-0.81	-0.07	Σ
2.50	0.0000366	0.673	0.885	-	-	9.10	3.51	3.69	7.54	-0.80	-1.67	3.11	-0.33	2.19	-6.23	e
2.50	0.0000500	0.492	0.940	0.190	0.977	4.66	2.20	3.54	2.08	-1.24	-0.76	0.58	-0.14	0.58	-1.24	e
2.50	0.0000800	0.308	0.904	0.177	0.916	4.31	1.66	3.50	1.88	-0.36	-1.82	0.05	-0.05	0.01	-0.30	e
2.50	0.0001300	0.189	0.837	0.164	0.841	4.34	1.61	3.49	2.01	-0.95	-1.77	0.02	-0.08	0.04	-0.03	e
2.50	0.0002000	0.123	0.799	0.153	0.800	4.37	1.63	3.50	2.04	-0.98	-1.76	0.11	-0.33	0.09	-0.01	e
2.50	0.0003200	0.077	0.713	0.141	0.713	4.67	1.85	3.51	2.45	0.31	-2.00	0.58	-1.25	0.09	0.00	e
2.50	0.0005000	0.049	0.621	0.130	0.621	4.63	1.83	3.51	2.40	0.36	-1.89	-0.96	-0.35	-1.01	-0.07	Σ
2.50	0.0008000	0.031	0.576	0.121	0.576	5.14	2.29	3.55	2.92	-0.24	-2.28	-1.52	0.67	-0.72	-0.05	Σ
3.50	0.0000512	0.673	0.962	-	-	7.45	3.29	3.68	5.59	-0.14	-1.31	2.62	-0.40	1.84	-4.36	e
3.50	0.0000800	0.431	1.009	0.215	1.039	4.49	2.05	3.52	1.88	-0.95	-1.20	0.45	-0.12	0.34	-0.93	e
3.50	0.0001300	0.265	0.948	0.198	0.957	4.30	1.82	3.51	1.68	-0.77	-1.49	0.05	-0.08	0.01	-0.13	e
3.50	0.0002000	0.172	0.894	0.183	0.897	4.26	1.79	3.51	1.63	-1.04	-1.24	0.02	-0.14	0.04	-0.02	e
3.50	0.0003200	0.108	0.783	0.168	0.784	4.52	1.90	3.51	2.11	-0.54	-1.96	0.24	-0.53	0.05	-0.01	e
3.50	0.0005000	0.069	0.778	0.154	0.779	5.46	2.23	3.55	3.50	1.99	-2.12	0.92	-1.71	0.04	-0.01	e
3.50	0.0008000	0.043	0.676	0.140	0.676	4.66	2.10	3.53	2.20	0.55	-1.74	-1.03	-0.04	-0.66	-0.04	Σ

B SpaCal Cell Numbers
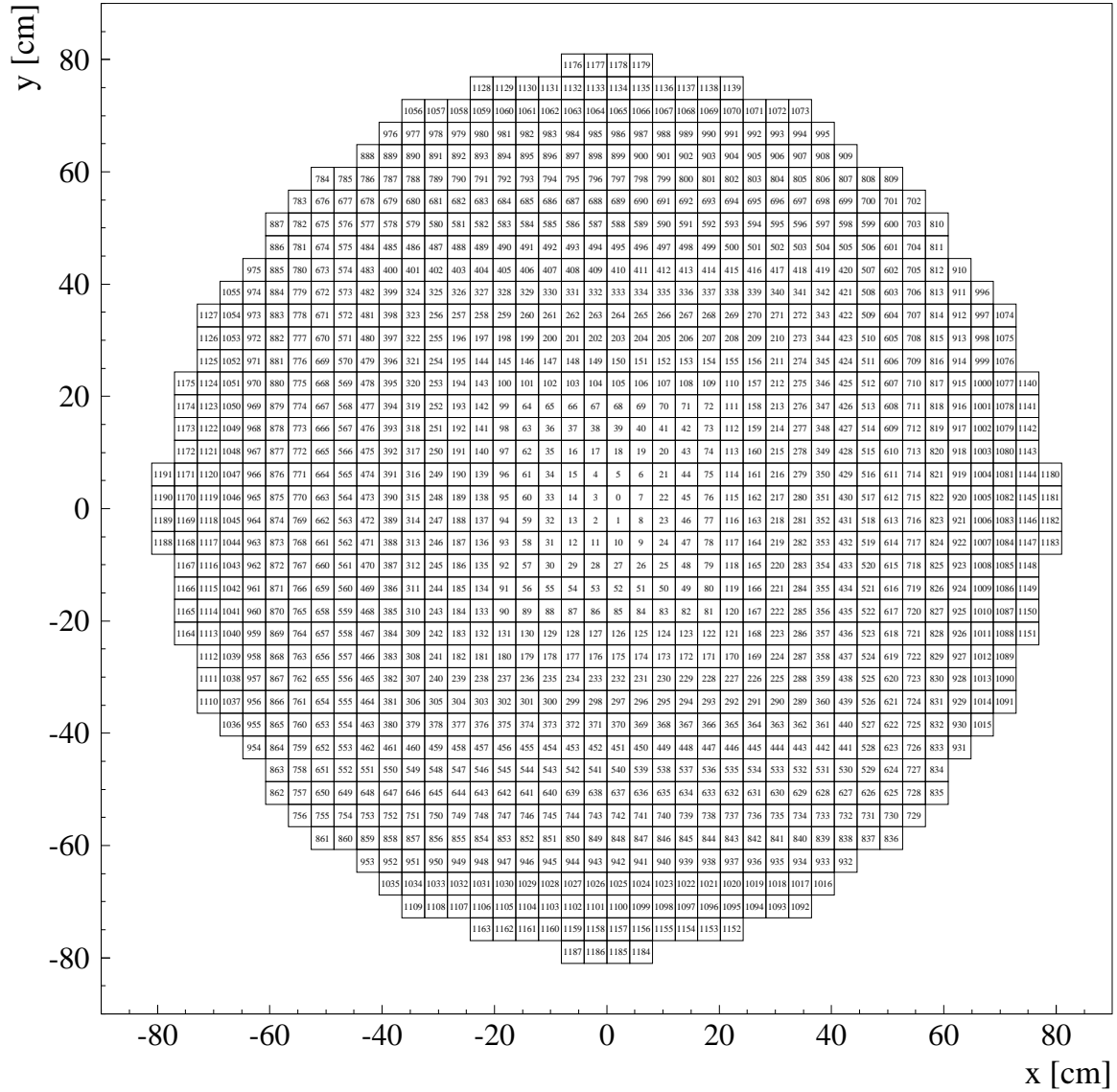
Figure B.1: *Cell numbering scheme of the SpaCal calorimeter to be compared to the actual mechanical construction depicted in figure 2.7. The cell numbers zero to three correspond to the veto cells.*

Bibliography

[Abr91]   H. ABRAMOWICZ, E. M. LEVIN, A. LEVY and U. MAOR, *A Parametrization of $\sigma_T(\gamma^* p)$ above the Resonance Region $Q^2 \geq 0$*, Phys. Lett. **B269** (1991), 465.

[Abr97]   H. ABRAMOWICZ and A. LEVY, *The ALLM Parameterization of $\sigma_{tot}(\gamma^* p)$: An Update* (1997), hep-ph/9712415.

[Abt93]   I. ABT et al. (H1 Collaboration), *Measurement of the Proton Structure Function $F_2(x, Q^2)$ in the Low x Region at HERA*, Nucl. Phys. **B407** (1993), 515.

[Abt97a] I. ABT et al. (H1 Collaboration), *The H1 Detector at HERA*, Nucl. Instrum. Meth. **A386** (1997), 310.

[Abt97b] I. ABT et al. (H1 Collaboration), *The Tracking, Calorimeter and Muon Detectors of the H1 Experiment at HERA*, Nucl. Instrum. Meth. **A386** (1997), 348.

[Adl97a] C. ADLOFF et al. (H1 Collaboration), *Diffraction Dissociation in Photoproduction at HERA*, Z. Phys. **C74** (1997), 221, hep-ex/9702003.

[Adl97b] C. ADLOFF et al. (H1 Collaboration), *A Measurement of the Proton Structure Function $F_2(x, Q^2)$ at Low x and Low Q^2 at HERA*, Nucl. Phys. **B497** (1997), 3, hep-ex/9703012.

[Adl01a] C. ADLOFF et al. (H1 Collaboration), *Deep-Inelastic Inclusive ep Scattering at Low x and a Determination of α_s*, Eur. Phys. J. **C21** (2001), 33, hep-ex/0012053.

[Adl01b] C. ADLOFF et al. (H1 Collaboration), *On the Rise of the Proton Structure Function F_2 towards Low x*, Phys. Lett. **B520** (2001), 183, hep-ex/0108035.

[Adl03]   C. ADLOFF et al. (H1 Collaboration), *Measurement and QCD Analysis of Neutral and Charged Current Cross Sections at HERA*, Eur. Phys. J. **C30** (2003), 1, hep-ex/0304003.

[Ahm94]   T. AHMED et al. (H1 Collaboration), *Deep Inelastic Scattering Events with a Large Rapidity Gap at HERA*, Nucl. Phys. **B429** (1994), 477.

[Ahm95]   T. AHMED et al. (H1 Collaboration), *Experimental Study of Hard Photon Radiation Processes at HERA*, Z. Phys. **C66** (1995), 529.

[Aid96]   S. AID et al. (H1 Collaboration), *A Measurement and QCD Analysis of the Proton Structure Function $F_2(x, Q^2)$ at HERA*, Nucl. Phys. **B470** (1996), 3, hep-ex/9603004.

[Akt04]   A. AKTAS et al. (H1 Collaboration), *Measurement of the Proton Structure Function F_2 at Low Q^2 in QED Compton Scattering at HERA*, Phys. Lett. **B598** (2004), 159, hep-ex/0406029.

[Alb69]   W. ALBRECHT et al., *Separation of σ_L and σ_T in the Region of Deep Inelastic Electron-Proton Scattering*, DESY Report 69-046 (1969).

[Alt77]   G. ALTARELLI and G. PARISI, *Asymptotic Freedom in Parton Language*, Nucl. Phys. **B126** (1977), 298.

[Alt79]   G. ALTARELLI, R. K. ELLIS and G. MARTINELLI, *Large Perturbative Corrections to the Drell-Yan Process in QCD*, Nucl. Phys. **B157** (1979), 461.

[And83a]   B. ANDERSSON, G. GUSTAFSON, G. INGELMAN and T. SJÖSTRAND, *Parton Fragmentation and String Dynamics*, Phys. Rept. **97** (1983), 31.

[And83b]   B. ANDERSSON, G. GUSTAFSON and B. SÖDERBERG, *A General Model for Jet Fragmentation*, Z. Phys. **C20** (1983), 317.

[And89]   B. ANDERSSON, G. GUSTAFSON, L. LONNBLAD and U. PETTERSSON, *Coherence Effects in Deep Inelastic Scattering*, Z. Phys. **C43** (1989), 625.

[And93]   B. ANDRIEU et al. (H1 Calorimeter Group Collaboration), *Results from Pion Calibration Runs for the H1 Liquid Argon Calorimeter and Comparisons with Simulations*, Nucl. Instrum. Meth. **A336** (1993), 499.

[And94]   B. ANDRIEU et al. (H1 Calorimeter Group Collaboration), *Beam Tests and Calibration of the H1 Liquid Argon Calorimeter with Electrons*, Nucl. Instrum. Meth. **A350** (1994), 57.

[And96]   V. ANDREEV, *Acceptance Determination of Electron Tagger (ET44) in 1995*, H1 Internal Note H1-10/96-493 (1996).

[App97]   R. D. APPUHN et al. (H1 SPACAL Group Collaboration), *The H1 Lead/Scintillating-Fibre Calorimeter*, Nucl. Instrum. Meth. **A386** (1997), 397.

[Arb96]   A. ARBUZOV et al., *HECTOR 1.00 - A Program for the Calculation of QED, QCD and Electroweak Corrections to ep and $l^{\pm}N$ Deep Inelastic Neutral and Charged Current Scattering*, Comput. Phys. Commun. **94** (1996), 128, hep-ph/9511434.

[Ark00]   V. V. ARKADOV, *Measurement of the Deep-Inelastic ep Scattering Cross Section Using the Backward Silicon Tracker at the H1 Detector at HERA*, Ph.D. thesis, Humboldt-Universität zu Berlin (2000), DESY-THESIS-2000-046.

[Arn95] C. ARNDT, *Kalibration des H1 Spaghetti Kalorimeters mit Halo Myonen*, Ph.D. thesis, Universität Hamburg (1995).

[Awe92] T. C. AWES et al., *A Simple Method of Shower Localization and Identification in Laterally Segmented Calorimeters*, Nucl. Instrum. Meth. **A311** (1992), 130.

[Bai01] A. BAIRD et al. (H1 Collaboration), *A Fast Track Trigger for the H1 Collaboration*, Nucl. Instrum. Meth. **A461** (2001), 461.

[Bal94] R. D. BALL and S. FORTE, *Double Asymptotic Scaling at HERA*, Phys. Lett. **B335** (1994), 77, hep-ph/9405320.

[Bar78] W. A. BARDEEN, A. J. BURAS, D. W. DUKE and T. MUTA, *Deep Inelastic Scattering beyond the Leading Order in Asymptotically Free Gauge Theories*, Phys. Rev. **D18** (1978), 3998.

[Bar02] J. BARTELS, K. GOLEC-BIERNAT and H. KOWALSKI, *A Modification of the Saturation Model: DGLAP Evolution*, Phys. Rev. **D66** (2002), 014001, hep-ph/0203258.

[Bas95a] U. BASSLER and G. BERNARDI, *H1KINE : Reconstruction of Kinematic Variables inside H1REC: User's Guide*, H1 Software Note 51-06/95 (1995).

[Bas95b] U. BASSLER and G. BERNARDI, *On the Kinematic Reconstruction of Deep Inelastic Scattering at HERA: The Sigma Method*, Nucl. Instrum. Meth. **A361** (1995), 197, hep-ex/9412004.

[BDC00] BDC GROUP, *BDC Hardware Status*, URL: https://www-h1.desy.de/h1det/tracker/bdc/poster.html (2000).

[Bet34] H. BETHE and W. HEITLER, *On the Stopping of Fast Particles and on the Creation of Positive Electrons*, Proc. Roy. Soc. Lond. **A146** (1934), 83.

[Bil89] P. BILLOIR, *Progressive Track Recognition with a Kalman like Fitting Procedure*, Comput. Phys. Commun. **57** (1989), 390.

[Biz92a] J. C. BIZOT, *Hardware Study for a Topological Level 2 Trigger*, H1 Internal Note H1-09/92-240 (1992).

[Biz92b] J. C. BIZOT, *Status of Simulation for a Topological Level 2 Trigger*, H1 Internal Note H1-02/92-212 (1992).

[Biz98] J. C. BIZOT et al., *SpaCal-Based L2TT Trigger Elements*, H1 Internal Note H1-04/98-538 (1998).

[Bjo69a] J. D. BJORKEN, *Asymptotic Sum Rules at Infinite Momentum*, Phys. Rev. **179** (1969), 1547.

[Bjo69b] J. D. BJORKEN and E. A. PASCHOS, *Inelastic Electron-Proton and γ-Proton Scattering, and the Structure of the Nucleon*, Phys. Rev. **185** (1969), 1975.

[Blo69]   E. D. BLOOM et al., *High-Energy Inelastic ep Scattering at 6° and 10°*, Phys. Rev. Lett. **23** (1969), 930.

[Bor92]   K. BORRAS, *Aufbau und Kalibration eines Flüssig-Argon Kalorimeters im H1 Detektor*, Ph.D. thesis, Universität Dortmund (1992).

[Bou95]   V. BOUDRY, *The Inclusive Electron Trigger for the SpaCal: Design and CERN-Test Results*, H1 Internal Note H1-03/95-430 (1995).

[Bre69]   M. BREIDENBACH et al., *Observed Behavior of Highly Inelastic Electron-Proton Scattering*, Phys. Rev. Lett. **23** (1969), 935.

[Bre99]   J. BREITWEG et al. (ZEUS Collaboration), *ZEUS Results on the Measurement and Phenomenology of F_2 at Low x and Low Q^2*, Eur. Phys. J. **C7** (1999), 609, hep-ex/9809005.

[Bre00]   J. BREITWEG et al. (ZEUS Collaboration), *Measurement of the Proton Structure Function F_2 at Very Low Q^2 at HERA*, Phys. Lett. **B487** (2000), 53, hep-ex/0005018.

[Bro95]   R. BROCK et al. (CTEQ Collaboration), *Handbook of Perturbative QCD*, Rev. Mod. Phys. **67** (1995), 157.

[Bru87]   R. BRUN et al., *GEANT3 User's Guide*, CERN DD/EE/84-1 (1987).

[Buc91]   W. BUCHMÜLLER and G. INGELMAN, eds., *Proceedings of the Workshop Physics at HERA*, volume 1, Hamburg (1991).

[Cal69]   J. CALLAN, CURTIS G. and D. J. GROSS, *High-Energy Electroproduction and the Constitution of the Electric Current*, Phys. Rev. Lett. **22** (1969), 156.

[Cap94]   A. CAPELLA, U. SUKHATME, C.-I. TAN and J. TRAN THANH VAN, *Dual Parton Model*, Phys. Rept. **236** (1994), 225.

[Che61]   G. F. CHEW, S. C. FRAUTSCHI and S. MANDELSTAM, *Regge Poles in $\pi\pi$ Scattering*, Phys. Rev. **126** (1961), 1202.

[Col89]   J. C. COLLINS, D. E. SOPER and G. STERMAN, in A. MUELLER, ed., *Perturbative Quantum Chromodynamics*, World Scientific (1989), 1.

[Der93a]   M. DERRICK et al. (ZEUS Collaboration), *Measurement of the Proton Structure Function F_2 in ep Scattering at HERA*, Phys. Lett. **B316** (1993), 412.

[Der93b]   M. DERRICK et al. (ZEUS Collaboration), *Observation of Events with a Large Rapidity Gap in Deep Inelastic Scattering at HERA*, Phys. Lett. **B315** (1993), 481.

[Der96]   M. DERRICK et al. (ZEUS Collaboration), *Measurement of the Proton Structure Function F_2 at Low x and Low Q^2 at HERA*, Z. Phys. **C69** (1996), 607, hep-ex/9510009.

[Dev04]   R. DEVENISH and A. COOPER-SARKAR, *Deep Inelastics Scattering*, Oxford University Press (2004).

[Dir95]   M. DIRKMANN, *Untersuchungen an einem Spaghetti-Kalorimeter unter besonderer Berücksichtigung des inneren Randbereiches und des Nachweises von π Mesonen*, Ph.D. thesis, Universität Dortmund (1995).

[Dir96]   M. DIRKMANN, *Calibration of the SpaCal with Cosmics*, H1 Internal Note H1-05/96-477 (1996).

[Dir97]   M. DIRKMANN and K. PFEIFFER, *Improved Position-Reconstruction in the SpaCal's Inner Region*, H1 Internal Note H1-01/97-512 (1997).

[Dok77]   Y. L. DOKSHITZER, *Calculation of the Structure Functions for Deep Inelastic Scattering and e^+e^- Annihilation by Perturbation Theory in Quantum Chromodynamics*, Sov. Phys. JETP **46** (1977), 641.

[Don92]   A. DONNACHIE and P. V. LANDSHOFF, *Total Cross-Sections*, Phys. Lett. **B296** (1992), 227, hep-ph/9209205.

[Don94]   A. DONNACHIE and P. V. LANDSHOFF, *Proton Structure Function at Small Q^2*, Z. Phys. **C61** (1994), 139, hep-ph/9305319.

[DR74]   A. DE RUJULA et al., *Possible Non-Regge Behavior of Electroproduction Structure Functions*, Phys. Rev. **D10** (1974), 1649.

[Dre85]   A. DRESCHER et al., *The Argus Electron-Photon Calorimeter. III. Electron-Hadron Separation*, Nucl. Instrum. Meth. **A237** (1985), 464.

[Eck01]   D. ECKSTEIN, in G. BRUNI, G. IACOBUCCI and R. NANIA, eds., *Proceedings of the IX DIS Workshop*, Bologna (2001), 376–379.

[Eck02]   D. ECKSTEIN, *Messung der Longitudinalen Strukturfunktion $F_L(x, Q^2)$ mit dem HERA-Experiment H1*, Ph.D. thesis, Humboldt-Universität zu Berlin (2002), DESY-THESIS-2002-008.

[Els93]   E. ELSEN, *The H1 Trigger and Data Acquisition System*, H1 Internal Note H1-01/93-262 (1993).

[Eng96]   R. ENGEL and J. RANFT, *Hadronic Photon-Photon Interactions at High Energies*, Phys. Rev. **D54** (1996), 4244, hep-ph/9509373.

[Erd96]   M. ERDMANN, *The Partonic Structure of the Photon: Photoproduction at the Lepton-Proton Collider HERA*, DESY Report 96-090 (1996).

[Fey69]   R. P. FEYNMAN, *Very High-Energy Collisions of Hadrons*, Phys. Rev. Lett. **23** (1969), 1415.

[Fox74]   D. J. FOX et al., *Test of Scale Invariance in High-Energy Muon Scattering*, Phys. Rev. Lett. **33** (1974), 1504.

[Fri73]   H. Fritzsch, M. Gell-Mann and H. Leutwyler, *Advantages of the Color Octet Gluon Picture*, Phys. Lett. **B47** (1973), 365.

[Gay06]   J. Gayler, private communication (2006).

[GB99a]   K. Golec-Biernat and M. Wüsthoff, *Saturation Effects in Deep Inelastic Scattering at Low Q^2 and its Implications on Diffraction*, Phys. Rev. **D59** (1999), 014017, hep-ph/9807513.

[GB99b]   K. Golec-Biernat and M. Wüsthoff, *Saturation in Diffractive Deep Inelastic Scattering*, Phys. Rev. **D60** (1999), 114023, hep-ph/9903358.

[Gin57]   E. L. Ginzton, *Proposal for a Two-Mile Linear Electron Accelerator at Stanford University*, unpublished (1957).

[Gla98a]   A. A. Glazov, *Measurement of the Proton Structure Functions $F_2(x, Q^2)$ and $F_L(x, Q^2)$ with the H1 Detector at HERA*, Ph.D. thesis, Humboldt-Universität zu Berlin (1998), DESY-THESIS-1998-005.

[Gla98b]   A. A. Glazov and R. Wallny, Presentation at the 'H1 Thursday Meeting', 22.01.98 (1998).

[Gla05a]   A. A. Glazov, Presentation at the 'Low Q^2 nELAN Meeting', 28.06.05 (2005).

[Gla05b]   A. A. Glazov, Presentation at the 'nELAN Meeting', 27.09.05 (2005).

[Gla05c]   A. A. Glazov, Presentation at the 'Low Q^2 nELAN Meeting', 30.08.05 (2005).

[Gla06]   A. A. Glazov, private communication (2006).

[Glü92]   M. Glück, E. Reya and A. Vogt, *Parton Distributions for High-Energy Collisions*, Z. Phys. **C53** (1992), 127.

[Glü98]   M. Glück, E. Reya and A. Vogt, *Dynamical Parton Distributions Revisited*, Eur. Phys. J. **C5** (1998), 461, hep-ph/9806404.

[GM64]   M. Gell-Mann, *A Schematic Model of Baryons and Mesons*, Phys. Lett. **8** (1964), 214.

[Gog96]   N. Gogitidze and S. Levonian, *An Offline Luminosity Determination for the 1995 e^+p Data*, H1 Internal Note H1-02/96-471 (1996).

[Gre64]   O. W. Greenberg, *Spin and Unitary Spin Independence in a Paraquark Model of Baryons and Mesons*, Phys. Rev. Lett. **13** (1964), 598.

[Gri72]   V. N. Gribov and L. N. Lipatov, *Deep Inelastic ep Scattering in Perturbation Theory*, Sov. J. Nucl. Phys. **15** (1972), 438.

[Gri81]   L. V. Gribov, E. M. Levin and M. G. Ryskin, *Singlet Structure Function at Small x: Unitarization of Gluon Ladders*, Nucl. Phys. **B188** (1981), 555.

[Gri83]   L. V. GRIBOV, E. M. LEVIN and M. G. RYSKIN, *Semihard Processes in QCD*, Phys. Rept. **100** (1983), 1.

[Gri90]   G. GRINDHAMMER, M. RUDOWICZ and S. PETERS, *The Fast Simulation of Electromagnetic and Hadronic Showers*, Nucl. Instrum. Meth. **A290** (1990), 469.

[Gro73a] D. J. GROSS and F. WILCZEK, *Asymptotically Free Gauge Theories*, Phys. Rev. **D8** (1973), 3633.

[Gro73b] D. J. GROSS and F. WILCZEK, *Ultraviolet Behavior of Non-Abelian Gauge Theories*, Phys. Rev. Lett. **30** (1973), 1343.

[Gus86]   G. GUSTAFSON, *Dual Description of a Confined Color Field*, Phys. Lett. **B175** (1986), 453.

[Gus88]   G. GUSTAFSON and U. PETTERSSON, *Dipole Formulation of QCD Cascades*, Nucl. Phys. **B306** (1988), 746.

[H1]   H1 COLLABORATION, *Measurement of the DIS Cross Section at Low Q^2 at HERA*, to be published.

[Han63]   L. N. HAND, *Experimental Investigation of Pion Electroproduction*, Phys. Rev. **129** (1963), 1834.

[Han65]   M. Y. HAN and Y. NAMBU, *Three-Triplet Model with Double SU(3) Symmetry*, Phys. Rev. **139** (1965), B1006.

[Ing91]   G. INGELMAN, in W. BUCHMÜLLER and G. INGELMAN, eds., *Proceedings of the Workshop Physics at HERA*, Hamburg (1991), 1366–1394.

[İşs96]   Ç. İŞSEVER, *Entwicklung eines alternativen Gewichtsverfahrens für das H1-Kalorimeter*, Diploma Thesis, Universität Dortmund (1996).

[İşs00]   Ç. İŞSEVER, *Messung der Protonstrukturfunktionen $F_2(x, Q^2)$ und $F_L(x, Q^2)$ bei HERA in radiativer ep-Streuung*, Ph.D. thesis, Universität Dortmund (2000), DESY-THESIS-2001-032.

[Jac79]   F. JACQUET and A. BLONDEL, in U. AMALDI, ed., *Proceedings of the Study for an ep Facility for Europe*, Hamburg (1979), 391–394.

[Jan94]   J. JANOTH et al., *Response of Mesh-Type Photomultiplier Tubes in Strong Magnetic Fields*, Nucl. Instrum. Meth. **A350** (1994), 221.

[Jan95]   J. JANOTH et al., *An Algorithm to Calibrate the New H1 Backward Calorimeter 'SPACAL' Using the Kinematic Peak*, H1 Internal Note H1-11/95-464 (1995).

[Jan96]   J. JANOTH, *Das Kalibrationssystem CAM für das neue Kalorimeter SpaCal des Detektors H1 bei HERA und Analyse der ersten Daten*, Ph.D. thesis, Universität Heidelberg (1996).

[Kar91]   V. KARIMAKI, *Effective Circle Fitting for Particle Trajectories*, Nucl. Instrum. Meth. **A305** (1991), 187.

[Kar96]   S. KARSTENSEN, *Report Proton Pick Up*,
URL: http://www.desy.de/~sven/Projects/projects.html (1996).

[Kat97]   J. M. KATZY, *Messung der Strukturfunktion F_2 bei kleinen Bjorken-x und kleinen Impulsüberträgen am H1 Experiment bei HERA*, Ph.D. thesis, Universität Heidelberg (1997).

[Kat06]   J. M. KATZY, private communication (2006).

[Kel98]   N. KELLER et al., *Status of the BDC Analysis*, H1 Internal Note H1-08/98-550 (1998).

[Kle06]   C. KLEINWORT, private communication (2006).

[Köh97]   J. KÖHNE, *Realization of a Second Level Neural Network Trigger for the H1 Experiment at HERA*, H1 Internal Note H1-01/97-509 (1997).

[Krä98]   T. KRÄMERKÄMPER, *Messung der Gluondichte im Photon und Entwicklung eines neuronalen Triggers*, Ph.D. thesis, Universität Dortmund (1998).

[Krü06]   K. KRÜGER, private communication (2006).

[Küs91]   H. KÜSTER, *ASCALE User Guide*, H1 Software Note 24-08/91 (1991).

[Kwi92]   A. KWIATKOWSKI, H. SPIESBERGER and H. J. MOHRING, *HERACLES: An Event Generator for ep Interactions at HERA Energies Including Radiative Processes*, Comp. Phys. Commun. **69** (1992), 155.

[Laš02a] T. LAŠTOVIČKA, in A. ESKREYS, J. KWIECIŃSKI and J. SZWED, eds., *Proceedings of the X DIS Workshop*, Cracow (2002), 2835–2840.

[Laš02b] T. LAŠTOVIČKA, *Self-Similar Properties of the Proton Structure at Low x*, Eur. Phys. J. **C24** (2002), 529, hep-ph/0203260.

[Laš04a] T. LAŠTOVIČKA, Presentation at the 'nELAN Meeting', 15.06.04 (2004).

[Laš04b] T. LAŠTOVIČKA, *Measurement of the Inclusive Deep Inelastic Scattering Cross Section at Low Q^2*, Ph.D. thesis, Humboldt-Universität zu Berlin (2004), DESY-THESIS-2004-016.

[Len99]   V. LENDERMANN, *Simulation of Passive Material in the Backward Region of the H1 Detector*, H1 Internal Note H1-08/99-575 (1999).

[Len01]   V. LENDERMANN, *Measurement of the QED Compton Scattering Cross Section with the H1 Detector at HERA*, Ph.D. thesis, Universität Dortmund (2001), DESY-THESIS-2002-008.

[Len06]   V. LENDERMANN, private communication (2006).

[Lev95] S. LEVONIAN and A. PANITCH, *Treatment of the Proton Satellite Bunches in 1994 Data*, H1 Internal Note H1-09/95-454 (1995).

[Lev06] S. LEVONIAN and Y. SOLOVIEV, private communication (2006).

[LM05] G. LAŠTOVIČKA-MEDIN, A. GLAZOV and T. LAŠTOVIČKA, in A. DE ROECK and H. JUNG, eds., *HERA and the LHC: A Workshop on the Implications of HERA for LHC Physics* (2004-2005), 79–83, CERN-2005-014.

[Łob03] E. M. ŁOBODZIŃSKA, in V. T. KIM and L. N. LIPATOV, eds., *Proceedings of the XI DIS Workshop*, St. Petersburg (2003), 93–98.

[Lön92] L. LÖNNBLAD, *ARIADNE Version 4: A Program for Simulation of QCD Cascades Implementing the Color Dipole Model*, Comput. Phys. Commun. **71** (1992), 15.

[Mar98] A. D. MARTIN, R. G. ROBERTS, W. J. STIRLING and R. S. THORNE, *Parton Distributions: A New Global Analysis*, Eur. Phys. J. **C4** (1998), 463, hep-ph/9803445.

[Mar02] A. D. MARTIN, R. G. ROBERTS, W. J. STIRLING and R. S. THORNE, *MRST2001: Partons and α_s from Precise Deep Inelastic Scattering and Tevatron Jet Data*, Eur. Phys. J. **C23** (2002), 73, hep-ph/0110215.

[Mar03] A. D. MARTIN, R. G. ROBERTS, W. J. STIRLING and R. S. THORNE, *Uncertainties of Predictions from Parton Distributions. I: Experimental errors*, Eur. Phys. J. **C28** (2003), 455, hep-ph/0211080.

[Mer05] J. MERKEL, *Systematische Studien zur Ausrichtung der rückwärtigen Detektoren von H1 für die Messung der Protonstrukturfunktion F_2*, Diploma Thesis, Universität Dortmund (2005).

[Mey96] A. MEYER, *Adjustment of the High Voltage for the H1 Spacal*, H1 Internal Note H1-08/96-486 (1996).

[Mey97] A. MEYER, *Measurement of the Structure Function $F_2(x, Q^2)$ of the Proton at Low Q^2 with the H1 Detector at HERA Using the New Detector Components SpaCal and BDC*, Ph.D. thesis, Universität Hamburg (1997).

[Moc04] S. MOCH, J. A. M. VERMASEREN and A. VOGT, *The Three-Loop Splitting Functions in QCD: The Non-Singlet Case*, Nucl. Phys. **B688** (2004), 101, hep-ph/0403192.

[Mon00] C. MONTAG and J. KLUTE, in J.-L. LACLARE et al., eds., *Proceedings of EPAC 2000*, Vienna (2000), 1534–1536.

[Müc00] A. MÜCKE, R. ENGEL, J. P. RACHEN, R. J. PROTHEROE and T. STANEV, *Monte Carlo Simulations of Photohadronic Processes in Astrophysics*, Comput. Phys. Commun. **124** (2000), 290, astro-ph/9903478.

[Nau02]   J. NAUMANN, *Entwicklung und Test der dritten H1-Triggerstufe*, Ph.D. thesis, Universität Dortmund (2002).

[Nav94]   H. NAVELET, R. PESCHANSKI and S. WALLON, *On the Singular Behavior of Structure Functions at Low x*, Mod. Phys. Lett. **A9** (1994), 3393, hep-ph/9402352.

[New04]   P. NEWMAN, *Deep Inelastic Lepton Nucleon Scattering at HERA*, Int. J. Mod. Phys. **A19** (2004), 1061, hep-ex/0312018.

[Nic96]   T. NICHOLLS et al. (H1 SPACAL Group Collaboration), *Performance of an Electromagnetic Lead/Scintillating Fiber Calorimeter for the H1 Detector*, Nucl. Instrum. Meth. **A374** (1996), 149.

[Nic98]   T. NICHOLLS et al., *Concept, Design and Performance of the Second Level Trigger of the H1 Detector*, IEEE Trans. Nucl. Sci. **45** (1998), 810.

[Ohl92]   M. OHLSSON, C. PETERSON and A. L. YUILLE, *Track Finding with Deformable Templates: The Elastic Arms Approach*, Comput. Phys. Commun. **71** (1992), 77.

[PB00]   H. PLOTHOW-BESCH, *PDFLIB: Proton, Pion and Photon Parton Density Functions, Parton Density Functions of the Nucleus, and α_s Calculations*, User's Manual - Version 8.04, W5051 PDFLIB, CERN-ETT-TT 2000.04.17 (2000).

[Per75]   D. H. PERKINS, in W. T. KIRK, ed., *Proceedings of the International Symposium on Lepton and Photon Interactions at High Energies*, Stanford (1975), 571–603.

[Pet04]   A. PETRUKHIN, in D. BRUNCKO, J. FERENCEI and P. STRÍŽENEC, eds., *Proceedings of the XII DIS Workshop*, Štrbské Pleso (2004), 372–376.

[Pet06]   A. PETRUKHIN, private communication (2006).

[Pit06]   D. PITZL, private communication (2006).

[Pol73]   H. D. POLITZER, *Reliable Perturbative Results for Strong Interactions?*, Phys. Rev. Lett. **30** (1973), 1346.

[Pös96]   R. PÖSCHL, *Untersuchung der Ortsauflösung des H1-Spaghetti-Kalorimeters unter besonderer Berücksichtigung großer Einschußwinkel der Primärteilchen*, Diploma Thesis, Universität Dortmund (1996).

[Pum02]   J. PUMPLIN et al., *New Generation of Parton Distributions with Uncertainties from Global QCD Analysis*, JHEP **07** (2002), 012, hep-ph/0201195.

[Reg59]   T. REGGE, *Introduction to Complex Orbital Momenta*, Nuovo Cim. **14** (1959), 951.

[Reg60]   T. REGGE, *Bound States, Shadow States and Mandelstam Representation*, Nuovo Cim. **18** (1960), 947.

[SC99] H. C. SCHULTZ-COULON et al., *A General Scheme for Optimization of Trigger Rates in an Experiment with Limited Bandwidth*, IEEE Trans. Nucl. Sci. **46** (1999), 915.

[Sch91] G. A. SCHULER and H. SPIESBERGER, in W. BUCHMÜLLER and G. INGELMAN, eds., *Proceedings of the Workshop Physics at HERA*, Hamburg (1991), 1419–1432.

[Sch96a] S. SCHLEIF, *SpaCal Reconstruction*, H1 Software Note 56-03/96 (1996).

[Sch96b] B. SCHWAB, *Das Rückwärtsdriftkammersystem des H1-Experiments*, Ph.D. thesis, Universität Heidelberg (1996).

[She96] V. SHEKELYAN and A. ZHOKIN, Presentation at the meeting 'Towards F_2', 07.05.96 (1996).

[Sjö94] T. SJÖSTRAND, *High-Energy Physics Event Generation with PYTHIA 5.7 and JETSET 7.4*, Comput. Phys. Commun. **82** (1994), 74.

[Spi91] H. SPIESBERGER et al., in W. BUCHMÜLLER and G. INGELMAN, eds., *Proceedings of the Workshop Physics at HERA*, Hamburg (1991), 798–839.

[Sta98] R. STAMEN, *Analyse quasireeller QED-Compton-Ereignisse*, Diploma Thesis, Universität Dortmund (1998).

[Ste99] J. STEINHART, *Die Messung des totalen $c\bar{c}$-Photoproduktions-Wirkungsquerschnittes durch die Rekonstruktion von Λ_c-Baryonen unter Verwendung der verbesserten dE/dx-Teilchenidentifikation am H1 Experiment bei HERA*, Ph.D. thesis, Universität Hamburg (1999).

[Tay69] R. E. TAYLOR, in D. W. BRABEN, ed., *Proceedings of the International Symposium on Lepton and Photon Interactions at High Energies*, Liverpool (1969), 251–260.

[Tlu99] M. TLUCZYKONT, *Z-Kalibration der zentralen Spurenkammer des H1-Detektors bei HERA*, Diploma Thesis, Universität Hamburg (1999).

[Urb05] K. URBAN, *Triggerstudien für eine Messung der Protonstrukturfunktion F_2 bei H1*, Diploma Thesis, Universität Dortmund (2005).

[Var06] A. VARGAS, *Determination of the Energy Scale Uncertainty for the Measurement of F_2 at Low Values of Q^2 with the H1 Detector*, Ph.D. thesis, Universität Dortmund (2006).

[Ver05] J. A. M. VERMASEREN, A. VOGT and S. MOCH, *The Third-Order QCD Corrections to Deep-Inelastic Scattering by Photon Exchange*, Nucl. Phys. **B724** (2005), 3, hep-ph/0504242.

[Vog04] A. VOGT, S. MOCH and J. A. M. VERMASEREN, *The Three-Loop Splitting Functions in QCD: The Singlet Case*, Nucl. Phys. **B691** (2004), 129, hep-ph/0404111.

[Wei73] S. WEINBERG, *Non-Abelian Gauge Theories of the Strong Interactions*, Phys. Rev. Lett. **31** (1973), 494.

[Wel94] H. P. WELLISCH et al., *Hadronic Calibration of the H1 LAr Calorimeter Using Software Weighting Techniques*, H1 Internal Note H1-02/94-346 (1994).

[Wis98] CH. WISSING, *Bestimmung der Charakteristika des Flugzeitsystems des H1-Detektors zur Messung des Strahluntergrundes*, Diploma Thesis, Universität Dortmund (1998).

[Yui90] A. L. YUILLE, T. YANG and D. GEIGER, *Robust Statistics, Transparency and Correspondence*, Harvard Robotics Laboratory Technical Report 90-7 (1990).

[ZEU03] ZEUS COLLABORATION, *Measurement of the Proton Structure Functions F_2 and F_L Using Initial State Radiative Events at HERA*, Contributed Paper to EPS 2003, Aachen, Abstract 502 (2003).

[Zho95] A. ZHOKIN and V. EFREMENKO, Minutes of the 'ELAN Meeting', 28.07.95 (1995).

[Zwe64] G. ZWEIG, CERN preprints TH401, TH412 (1964).

Danksagung

Es ist vollbracht. Am Freitag, den 25. August 2006 um 4:37 Uhr beginnt der Drucker damit, die vollständige Version des Werkes zu Papier zu bringen. Vollständig? Nein, der wichtigste Teil fehlt noch: An dieser Stelle sei all denjenigen Dank ausgesprochen, die maßgeblich zum Gelingen dieses Projektes beigetragen haben.

Mein besonderer Dank gilt meinem Doktorvater, Herrn Prof. Dr. D. Wegener, für die große Unterstützung, die er mir während der gesamten Promotionszeit hat zuteil werden lassen.

Herr Prof. Dr. H.-C. Schultz-Coulon hat die Analyse stets mit großem Enthusiasmus verfolgt und für die nötige Motivation in schwierigen Zeiten gesorgt. Einen Telefonjoker in Heidelberg zu wissen, war stets ein beruhigendes Gefühl. Ich bin sehr froh, daß ich ihn als Zweitgutachter gewinnen konnte.

Großer Dank für die herausragende Betreuung dieser Arbeit sei drei Personen ausgesprochen: Katja Krüger, Victor Lendermann und Sasha Glazov. Ohne die zahlreichen Diskussionen über die vielen Details der Strukturfunktionsmessung hätte die Arbeit in der vorliegenden Form nicht enstehen können. Durch die sorgfältige Korrektur von Katja und Sasha hat das Manuskript deutlich an Lesbarkeit gewonnen. Das Theoriekapitel hat durch Christiane Risler wertvolle Impulse erfahren, Paul Newman hat seine Nachtschicht damit zugebracht, in liebevoller Kleinarbeit der Einleitung und dem Ergebniskapitel mein „disturbed English" auszutreiben.

Für eine tolle Zeit in der Dortmund-Heidelberg Kollaboration am DESY danke ich: Andrea, Andreas, Christoph, Christopher, Çigdem, Daniel, Dirk, Jesko, Jörg, Jürgen, Katja, Klaus, Kristin, Marc-Oliver, Michael, Mitch, Moritz, Rainer, Roman, Stephan und Victor. Hier sei Andrea besonders hervorgehoben: Wir haben die Höhen und Tiefen der Analyse gemeinsam durchlebt. Dem aufmerksamen Leser wird nicht entgangen sein, daß ihre Arbeit die meistzitierte ist (zur Erinnerung: [Var06]). Abseits der Analyse blieb immer Zeit für Gespräche über Gott und die Welt, die ich sehr genossen habe. Marc-Oliver danke ich für die nette Bürogemeinschaft.

Dank für die gute Zusammenarbeit sei Ewelina Łobodzińska, Nataša Raičević, Jan Kretzschmar und Alexey Petrukhin ausgesprochen.

Daheim in Dortmund danke ich Herrn Prof. Dr. B. Spaan für die freundliche Aufnahme an seinem Lehrstuhl. Seine Weisheiten wie „Keine Doktorarbeit über 100 Seiten!" werden mir in Erinnerung bleiben. Leider konnte ich seinen Ansprüchen nicht gerecht werden: Meine Arbeit ist nun doch zwei Seiten länger als seine. Matthias Domke danke ich für seine Verdienste um die Rechnerfarm, die die umfangreichen Simulationsrechnungen ermöglicht haben. Der ordnenden Hand von Frau E. Lorenz ist es zu verdanken, daß sich alle Formalitäten reibungslos aus dem fernen Hamburg erledigen ließen.

Einige Konferenzbesuche waren mir erst dank der finanziellen Unterstützung durch das Graduiertenkolleg „Physik der Elementarteilchen an Beschleunigern und im Universum" der Universitäten Dortmund und Bochum möglich.

Auch abseits der Physik hat eine Reihe von Menschen mein Leben bereichert. An erster Stelle seien meine Eltern genannt, die mir stets alle erdenkliche Unterstützung haben zukommen lassen und ohne die ich es nicht bis hierher geschafft hätte. Spannende Nachmittage durfte ich mit meinen Patenkindern Jakob und Louis sowie ihren Brüdern verbringen. Meinen Freunden danke ich für den Sonnenschein, den sie verbreiten.

Ana und Christiane verdanke ich eine schöne Zeit in Hamburg. Ana pünktlich zum großen Finale an meiner Seite zu haben, davon hätte ich nie zu träumen gewagt. Danke, daß es Dich gibt.